# Low-Energy Signals in the LUX-ZEPLIN (LZ) Experiment and Spectral Measurements of Xenon Luminescence

IMPERIAL

A thesis presented for the degree of

Doctor of Philosophy

Albert Baker

Department of Physics

Imperial College London

# Abstract

A significant proportion of the Universe is believed to be composed of some unknown substance known as dark matter. The leading candidate for this dark matter are weakly interacting massive particles (WIMPs). The LUX-ZEPLIN (LZ) experiment, housed one mile underground in the Sandford underground research facility (South Dakota, USA), is currently searching for these particles using a 7 tonne liquid xenon target. In this thesis the evidence for dark matter is presented alongside how liquid xenon time projection chambers are expected to detect WIMP dark matter via low energy nuclear recoils. This methodology is brought to life through LZ's first WIMP search. This analysis, which found no WIMP candidates in its 5.5 tonne · 60 day exposure, imposes the most stringent upper limits to the spin-independant WIMP–nucleon cross-section to date.

The calibration of the PMTs to VUV light using $^{83m}$Kr is detailed alongside a comparison to previous dedicated measurements performed at Imperial. This in-situ calibration is exploited as part of a $^{8}$B sensitivity study which uses the double photoelectron emission (DPE) effect and the time profile of xenon scintillation to reduce the scintillation threshold of LZ, improving its sensitivity to low energy interactions such as CE$\nu$NS.

Alternatively, liquid xenon (LXe) detectors can completely forgo scintillation signals in an effect to explore even lower energy phenomena. A current limitation of these "S2-only" analyses is our ability to calibrate detectors in this ultra-low energy regime. Several methods to calibrate this region using existing sources are studied assuming a 50–150 eV region of interest.

Finally, measurements of the xenon luminescence spectra are presented for warm gas, saturated vapour, and liquid states. These results, which include the first measurement of saturated xenon vapour spectra and the first simultaneous measurement of liquid and vapour spectra, observe that S1 light is consistently of longer wavelength than S2 light.

# Statement of originality

I, the author of this work, affirm that the work contained within this thesis constitutes work conducted by the author. It is acknowledged that the work described here relies on or is otherwise connected to works performed by others within the LUX-ZEPLIN collaboration and Imperial dark matter group. Such works and any other works referred to in this thesis, are appropriately acknowledged and referenced where applicable.

For the chapters relating to LZ, I include a brief acknowledgement of specific instances where my work builds upon or extends previous works by members of LZ.

Chapter 3 details the design and operation of LZ, whilst Chapter 5 details LZ's first WIMP search using the SR1 dataset. This chapter almost exclusively details work carried out and lead by the wider LZ collaboration. My contributions to the WIMP search are largely detailed in Chapter 4 though some software work I performed is detailed in Chapter 3.

Chapter 4 details the calibration of the LZ PMTs to VUV light. The primary data was acquired and processed by the LZ collaboration. The results presented in this section were the analyses that I myself performed. These results were then compared to measurements taken previously at Imperial, these measurements were performed prior to my PhD at Imperial and as such I had no involvement in the Imperial measurements.

Chapter 6 describes a study of LZ's sensitivity to $^{8}$B neutrinos and is a re-implementation and augmentation of a previous LZ sensitivity study. The data used to measure PMT timing offsets in this chapter was acquired by the wider LZ collaboration.

The xenon spectra measurements were performed by a small group at Imperial with each member having a wide remit. For this reason I provide a more detailed description of my contributions to this work below.

Chapter 8 details the measurement of xenon spectra using proto-Xenia. The chamber was primarily built by Kelsey Oliver-Mallory at Imperial College, though the author worked on commissioning the monochromator and LP Hg systems. The slow control software was originally created as part of the ZEPLIN-III experiment but has been updated by the author for use with proto-Xenia. The DAQ and primary analysis frameworks were written by colleagues in Coimbra as part of the MIGDAL experiment but have been updated by the author for use with proto-Xenia. Data presented in this chapter were acquired by the Imperial laboratory group, which includes the author. All analyses and results presented in this chapter were performed by the author.

# Licence

The copyright of this thesis rests with the author. Unless otherwise indicated, its contents are licensed under a Creative Commons Attribution-NonCommercial-ShareAlike 4.0 International Licence (CC BY-NC-SA).

Under this licence, you may copy and redistribute the material in any medium or format. You may also create and distribute modified versions of the work. This is on the condition that; you credit the author, do not use it for commercial purposes and share any derivative works under the same licence.

When reusing or sharing this work, ensure you make the licence terms clear to others by naming the licence and linking to the licence text. Where a work has been adapted, you should indicate that the work has been changed and describe those changes.

Please seek permission from the copyright holder for uses of this work that are not included in this licence or permitted under UK Copyright Law.

# Open data access

The data acquired by the LUX-ZEPLIN (LZ) collaboration and its member, which includes the author, are processed according to the LZ data management plan.

The data taken within the Liquid Xenon Laboratory at Imperial College London will be published under an Open Access licence at a later date pursuant to publication in a journal under similar terms.

# Acknowledgements

Whilst I may not have achieved all that I would have wished during my PhD, I am nevertheless proud of what I have managed to accomplish. Achieving what I have done would not have been possible without either support from the Imperial group or my numerous colleagues past and present without whom LZ would neither exist nor achieve the world-leading results it has and hopefully continues to produce.

I would like to thank my supervisor, Henrique Araújo, for both obtaining this studentship on LZ and xenon R&D and providing guidance throughout. Whilst I may not have taken all of his guidance on board at the time I hope that I can continue to learn from the experiences encountered during my PhD. I would also like to thank Tim Sumner, my second supervisor, for the productive discussions throughout my PhD.

I would like to acknowledge and thank Andrew Stevens, Elisa Jacquet, and Kelsey Oliver-Mallory without whom the xenon luminance measurements would not be possible or nearly as enjoyable; The long summer days in the lab were, at times, some of the most enjoyable days that I can recall.

I would like to thank the computing team at Imperial, namely Simon Fayer, Daniela Bauer, and Dan Whitehouse, for their invaluable assistance and advice in relation to LZ software, laboratory computing infrastructure, and general computing support.

During my PhD I had the opportunity to visit colleagues at Universidade de Coimbra. I would like to thank Paulo Brás, Alexandre Lindote, Guilherme Pereira, and Claudio Silva for the welcoming atmosphere during my stay. Whilst it may have rained for almost the entirety of my visit, I still very much enjoyed my time in Portugal.

Through my PhD I have learnt the importance of small victories and brief moments of respite. Being part of LZ had provided me both the opportunity to explore new places and spend time with a variety of individuals; be it exploring the Smithsonian (Ewan Fraser), complaining about everything under the sun (Sam Eriksen), or exploring Portugal on my own. I have grateful for these times and opportunities and look back on them fondly.

I would like to thank the wider Imperial particle physics group. My interactions with everyone, both professional and social, were enjoyable and a privilege.

During a PhD it is very easy to become obsessed with a small area of research. I am grateful to the wider LZ collaboration for reminding me that the work we do, whilst normal to us, is extraordinary.

This work was supported by the Science and Technology Facilities Council (STFC) and used computing resources provided by the Imperial College Research Computing Service.

# Table of Contents

**List of Figures** 10

**List of Tables** 14

**1 Introduction** 15

**2 Detection of Dark Matter and Neutrinos** 19

2.1 Dark Matter . . . 20

2.1.1 Astrophysical evidence . . . 20

2.1.2 Cosmological evidence . . . 23

2.1.3 Dark matter candidates . . . 26

2.2 Detecting Dark Matter . . . 29

2.2.1 Dark matter scattering kinematics . . . 31

2.3 Solar Neutrinos . . . 36

2.4 Signal Generation in Liquid Xenon Detectors . . . 39

2.4.1 Excitation, ionisation and heat . . . 39

2.4.2 Ionisation and scintillation yields in liquid xenon (LXe) . . . 41

2.5 Two-phase noble element time-projection chambers . . . 42

2.6 The WIMP dark matter landscape prior to LZ . . . 47

2.7 Conclusion . . . 49

**3 The LUX-ZEPLIN (LZ) Experiment** 51

3.1 The LZ experiment . . . 52

3.1.1 TPC design and operation . . . 53

3.1.2 PMT Design and Operation . . . 57

3.2 Particle Detection in LZ . . . 63

3.2.1 Offline Software . . . 64

3.2.2 Computing centres . . . 66
3.2.3 Software distribution . . . 67
3.3 Data Centre and User Analysis Study . . . 68
3.4 Conclusion . . . 72

**4 Measurement of double photoelectron PMT response using $^{83m}$Kr 73**
4.1 The double photoelectron emission (DPE) effect . . . 74
4.1.1 Modelling photon detection as a Poisson process . . . 76
4.2 Calibrating with $^{83m}$Kr . . . 77
4.2.1 Detector conditions . . . 78
4.2.2 Pulse-level event selection . . . 78
4.2.3 PMT-level event selection . . . 83
4.3 Fitted DPE probabilities and their comparison with previous measurements . . . 84
4.4 Conclusion . . . 89

**5 First WIMP search with LZ 91**
5.1 Commissioning . . . 92
5.2 Science run 1 (SR1) . . . 92
5.3 WIMP Search Methodology . . . 93
5.3.1 Detector Operations . . . 93
5.3.2 Data Processing & Selection . . . 93
5.3.3 Detector Model & Simulations . . . 94
5.3.4 Simulating the detector response . . . 95
5.3.5 Statistical Analysis . . . 95
5.3.6 Detector Operations . . . 96
5.3.7 Detector Calibration . . . 96
5.3.8 Characterising the ER and NR bands . . . 98
5.3.9 Data Selection . . . 99
5.3.10 Result . . . 101
5.4 Conclusion . . . 106

**6 Using the DPE effect to improve $^{8}$B sensitivity 107**
6.1 Analytic reanalysis of previous study . . . 109
6.1.1 Discriminating with double photoelectron emission (DPE) . . . 109

6.1.2 Discriminating with time separation . . . 109
6.1.3 Optimising median sensitivity in a counting experiment . . . 111
6.1.4 Adding variables . . . 113
6.1.5 Re-evaluation of the sensitivity . . . 115
6.2 Improving LZ's photon timing reconstruction . . . 116
6.2.1 Inter-array difference in photon time-of-flight . . . 116
6.2.2 Measuring individual PMT timing offsets with $\alpha$-decays . . . 121
6.3 Conclusion . . . 122

**7 Low Energy Calibration in Liquid Xenon Detectors 125**
7.1 Introduction . . . 126
7.2 Coherent Gamma Elastic Scattering . . . 126
7.3 Compton Scattering . . . 129
7.4 $^{127}$Xe Orbital Electron Capture . . . 133
7.4.1 The orbital electron capture process . . . 133
7.4.2 Relaxation of the daughter atom . . . 135
7.4.3 LUX's measurement of $^{127}$Xe . . . 138
7.5 Conclusion . . . 140

**8 Xenon Luminescence Spectroscopy 143**
8.1 Xenon luminescence spectra . . . 145
8.2 Triggered Time-Resolved Photon Counting Spectroscopy . . . 148
8.3 Proto-Xenia . . . 149
8.3.1 Wavelength dependant corrections . . . 152
8.3.2 Detector operations . . . 154
8.4 Internal radioactive source – $^{228}$Th . . . 156
8.5 Computing and software infrastructure . . . 156
8.5.1 Slowcontrol and Detector Monitoring . . . 157
8.5.2 Data Acquisition (DAQ) . . . 158
8.5.3 Dead-time . . . 159
8.5.4 Data processing . . . 159
8.6 In-situ Calibration Using an LP Hg lamp . . . 161
8.7 Xenon vacuum ultraviolet (VUV) Luminescence Measurements . . . 166

8.7.1 Data selection . . . . . 167
8.7.2 Spectra acquisition . . . . . 169
8.8 Xenon Spectra Results . . . . . 171
8.9 Discussion of Observed Xenon Spectra . . . . . 174
8.10 Conclusion . . . . . 180

**9 Conclusion** **183**

**Bibliography** **187**

# List of Figures

**2 Detection of Dark Matter and Neutrinos**

2.1 The galactic rotation curve of the Milky Way. . . . . 22
2.2 A map of the temperature anisotropies in the CMB as observed by Planck. . . . 25
2.3 The CMB temperature power spectrum as measured by the Planck experiment 25
2.4 The dark matter relic abundance for a freeze-out candidate . . . . . 29
2.5 Schematic of the three methods by which dark matter could interact with the Standard Model. . . . . 30
2.6 The differential recoil spectra of WIMPs on xenon and argon. . . . . 35
2.7 The production mechanism of solar neutrinos via the proton-proton (PP) chain. 36
2.8 The differential recoil spectra of solar and atmospheric neutrinos on xenon. . . 38
2.9 Diagram of quanta ($\gamma$, $e^-$) production via excitation, recombination, and ionisation of recoiling xenon atoms . . . . . 40
2.10 Charge and light yields for NR and $\beta$-particle ER interactions in LXe. . . . . 43
2.11 LXe-TPC design and operation . . . . . 45
2.12 pre-LZ limits on the WIMP interaction cross-section and the neutrino fog . . . . 48

**3 The LUX-ZEPLIN (LZ) Experiment**

3.1 CAD visualisations of the LZ experiment focusing on the central TPC detector system and its interfaces to the detector control and operating systems and the outer detector which is employed primarily as a neutron veto system. . . . . 54
3.2 Possible photon detection mechanisms for PMT photosensors. . . . . 59
3.3 The probability of producing a fake S1 from dark count pile-up and the associated rate of accidental single scatter events . . . . . 63
3.4 A 14 keV tritium decay interaction recorded by LZ. . . . . 65
3.5 A standard LZ workflow used for benchmark tests. . . . . 70

3.6 The results of LZ benchmarks for several UK institutions, NERSC and Coimbra. 71

**4 Measurement of double photoelectron PMT response using $^{83m}$Kr**

4.1 $^{83m}$Kr's two-stage decay scheme including transition types, energies, and probabilities. . . . 78
4.2 Summed and channel-level waveforms for a $^{83m}$Kr decay in LZ. . . . 79
4.3 The temperature of the LZ top and bottom PMT arrays during the $^{83m}$Kr calibration 79
4.4 Spatial distribution of $^{83m}$Kr events. . . . 80
4.5 Fitted distribution of the decay time of the $^{83m}$Kr meta-stable state as measured by the separation between the $S1_a$ and $S1_b$ pulses. . . . 81
4.6 Distribution of $S1_a$, $S1_b$, $S1_{total}$, and S2 corrected pulse areas for $^{83m}$Kr decay events. . . . 82
4.7 The channel amplitude and area parameters for one of the LZ PMTs alongside the measured channel area distribution used to perform the DPE measurement. 83
4.8 Fitted single photon distribution for a single LZ TPC PMT. . . . 84
4.9 Measured DPE probabilities from $^{83m}$Kr $S1_b$ light and quantum efficiencies. . . . 86
4.10 Comparison of the DPE probabilities measured in LZ, at Imperial, and according to the linear model. . . . 87
4.11 Comparison of DPE probabilities as measured at Imperial, in LZ, and according to the linear model observed at Imperial. . . . 88

**5 First WIMP search with LZ**

5.1 Simplified schematic of the first WIMP search. . . . 94
5.2 Calibration of LZ's ER and NR bands, within the WIMP ROI, during SR1. . . . 99
5.3 The events remaining after all data quality cuts for SR1 alongside relevant signal and background PDFs. . . . 102
5.4 Current limits on the spin-independant WIMP-nucleon cross-section. . . . 105

**6 Using the DPE effect to improve $^{8}$B sensitivity**

6.1 Distribution of the largest channel area metric using MC and analytic methods. 110
6.2 Signal efficiency and background leakage for a two-fold analysis using the maximum channel area and difference in photon detection times. . . . 112

6.3 Optimisation of the Asimov test-statistic for detecting $^{8}$B neutrinos using a two-fold coincidence. . . . 113
6.4 The photon and $^{8}$B detection probabilities calculated per array. . . . 114
6.5 Marginalised S2 PDFs for simulated $^{8}$B events and observed accidental events. 116
6.6 The Asimov test statistic when including electron drift-time and S2 area for a two-fold $^{8}$B discovery against a dark-count S1 accidental background. . . . 117
6.7 An $\alpha$-decay single scatter observed near the top of LZ. . . . 118
6.8 The relationship between electron drift-time (depth) and the difference in photon arrival time between LZ's two PMT arrays . . . 119
6.9 Summed waveforms for maximal difference in photon time-of-flight in LZ and XLZD. . . . 120
6.10 Average of the measured intra-array PMT timing offsets with respect to each array's central PMT. . . . 122

**7 Low Energy Calibration in Liquid Xenon Detectors**

7.1 Theoretical differential cross-sections for coherent gamma elastic-scattering on xenon . . . 127
7.2 The recoil spectra of xenon atoms due to coherent gamma elastic-scattering. . 128
7.3 The Klein-Nishina (angular) differential cross-section as a function of scattering angle. . . . 130
7.4 The Compton electron's recoil energy as a function of scattering angle. . . . 131
7.5 The cross-sections for photons interacting with liquid xenon . . . 132
7.6 The expected per shell electron capture probabilities for $^{127}$Xe and $^{123}$I. . . . 134
7.7 The electron capture decay mechanism including the Auger and fluorescence relaxation processes. . . . 135
7.8 The atomic structures and energies of $^{127}$Xe and $^{127}$I. . . . 137

**8 Xenon Luminescence Spectroscopy**

8.1 Morse potential curves of $Xe_2^\star$ as a function of interatomic separation. . . . 147
8.2 Averaged waveforms for $\alpha$-particle interactions in proto-Xenia alongside a photon detected in the monochromator PMT . . . 149
8.3 CAD diagram of proto-Xenia. . . . 150

8.4 CAD cross-section of proto-Xenia highlighting the electrode grids, $^{228}$Th source, liquid surface, Hg lamp and monochromator. . . . . 151
8.5 The wavelength-dependant transmission efficiencies of several materials used in proto-Xenia. . . . . 153
8.6 Decay diagram of $^{228}$Th . . . . . 156
8.7 Schematic of data flow, computing resources, software, and hardware sensors . 157
8.8 DAQ dead-time as measured with $\alpha$-particle triggered data. . . . . 160
8.9 The observed spectrum from the LP Hg lamp. . . . . 162
8.10 Dead-time corrected LP Hg calibration. . . . . 163
8.11 Calibration of the monochromator system using a linear model . . . . . 164
8.12 Observed LP Hg spectrum converted to wavelength using the calibration values 165
8.13 Resolution of the 184.95 nm LP Hg line as a function of slit-width . . . . . 165
8.14 The phase diagram of xenon below the critical point and the density of xenon vapour and gas as a function of pressure. . . . . 166
8.15 Data selection cuts for $\alpha$ interactions . . . . . 167
8.16 S1–S2 distribution of event associated with $\alpha$-decays . . . . . 168
8.17 The S1 and S2 time coincidence cuts used to measure the luminescence spectra. 170
8.18 Detector state during xenon data acquisition . . . . . 172
8.19 Spectra of xenon vapour and liquid at 1.7 bar . . . . . 173
8.20 Spectra of xenon vapour as a function of S2 (temperature) at 1.7 bar . . . . . 174
8.21 Spectra of GXe/LXe (S2/S1) xenon at 2.2 bar . . . . . 175
8.22 Spectra of GXe/LXe (S2/S1) xenon at 1.3 bar . . . . . 175
8.23 Comparison of S1 and S2 light in warm xenon gas. . . . . 176
8.24 Electroluminescence spectra of warm gaseous xenon at 0.3 bar and 2.2 bar . . . 176
8.25 Comparison between measurements of xenon spectra performed at Imperial. . 177
8.26 Comparison of xenon spectra measurements to results in the literature. . . . . 178

# List of Tables

**5 First WIMP search with LZ**

5.1 The number of events remaining in the SR1 WIMP search dataset after each set of applied cuts. . . . . 101

5.2 Expected and best fit number of events for signal and background components for the 60 days·5.5 tonne SR1 exposure. . . . . 103

**8 Xenon Luminescence Spectroscopy**

8.1 Measurements of the scintillation spectra of gaseous and liquid xenon. . . . . 181

# 1

# Introduction

From measurements at the astronomical and Cosmological scales it is apparent that a significant fraction of the Universe is composed of some unknown substance. This "dark matter", present in the early Universe, interacts gravitationally with conventional matter and was instrumental in creating the Universe in its present form. A natural question to ask of such a substance is 'what is it made of?'. Extensions to the Standard Model of particle physics provide multiple candidates for dark matter including weakly interacting massive particles (WIMPs). This thermal relic from the early Universe should interact with normal matter via some interaction at or below the weak scale. The hunt for such a dark matter particle, once a fringe area of research, has developed into a compelling and wide-ranging field of research in the particle physics community.

The majority of this thesis is dedicated to searching for WIMPs as part of the LUX-ZEPLIN (LZ) experiment. Additional R&D work measuring the luminescence spectra of xenon, the target medium of LZ, is also presented.

**Chapter 2** outlines the motivation for dark matter at the astronomical and Cosmological scales. With the foundations set, the required properties of a dark matter candidate are described and possible detection methods outlined. An introduction to WIMPs is provided detailing the expected detection mechanism via coherent elastic scatter off nuclei. This detection mechanism is compared to neutrino coherent elastic neutrino-nucleus scattering (CE$\nu$NS) scattering, an irreducible background for any experiment searching for WIMPs. With the expected signal described, the liquid xenon (LXe) time projection chamber (TPC) detector design is outlined including details of the signal production mechanism. This chapter culminates with a review of the field prior to the current generation of experiments.

**Chapter 3** describes the design, operation, and calibration of the LZ experiment. Specific emphasis is placed on the operation of the photomultipler tube (PMT) photosensors used in the TPC due to their relevance to Chapters 4 and 6. A review of LZ's offline computing is provided alongside a study comparing UK and US computing resources from the perspective of analysers.

**Chapter 4** details the in-situ measurement of the double photoelectron emission (DPE) probability for LZ's TPC PMTs using $^{83m}$Kr. In the process of this calibration, a measurement of the half-life of the intermediate state encountered in $^{83m}$Kr's two-stage decay is presented.

Finally, the results of these in-situ measurements are compared to dedicated measurements performed at Imperial College London.

**Chapter 5** encompasses LZ's first WIMP search using the SR1 dataset. Using LZ's significantly larger target mass this is the most sensitive WIMP dark matter analysis to date with a total exposure of 5.5 tonne · 60 days. This analysis, the key-note work of the experiment, was centrally orchestrated by senior members of the collaboration. My primarily contribution to this analysis was the in-situ calibration of the LZ TPC PMTs as described in Chapter 4. During this analysis I also studied scintillation backgrounds at threshold, not discussed here, and contributed to the development of parts of the core analysis framework.

**Chapter 6** describes a study of LZ's sensitivity to $^{8}$B neutrinos from the sun using analytic methods. These methods simplify the computation of signal and background PDFs and allow for greater exploitation of the full detector response model. The signal and background models are then augmented though the addition of two discriminating parameters, the interaction depth and ionisation signal (S2) strength, improving signal–background discrimination.

In addition to the above study, measurements of the PMT timing offsets are performed both within and between the two PMT arrays using waveforms from $\alpha$-decay. The results of these measurements are then extrapolated for the 3 m detector proposed by the XLZD consortium.

**Chapter 7** details several methods to calibrate LZ TPCs at the ultra-low energies relevant for ionisation-only (S2-only) analyses. The first two methods investigate whether photo-nucleus coherent gamma elastic-scattering (CGES) or Compton scattering could produce interaction of the required energy and rate for calibration. Orbital electron capture is studied in detail to investigate how $^{127}$Xe electron capture should be interpreted and exploited in this ultra-low energy regime.

**Chapter 8** presents spectral measurements of xenon luminance using the proto-Xenia chamber housed at Imperial. Using a LXe TPC design, these measurements provide the first simultaneous measurement of liquid xenon scintillation and xenon vapour electroluminescence, with the latter also the first measurement of its kind.

**Chapter 9** provides a review of the work and results presented in this thesis.

# 2

# Detection of Dark Matter and Neutrinos

From astrophysical and cosmological observations there is strong evidence for the existence of an as yet unobserved dark matter component of the Universe. This dark matter is expected to account for approximately 85% of the matter density of the Cosmos. Whilst there have been numerous observations from the astrophysical to cosmological scales consistent with the dark matter hypothesis, no convincing evidence of a particle compatible with dark matter has yet been observed. A dark matter candidate of particular interest to the physics community is the weakly interacting massive particle (WIMP). These hypothesised thermal relics from the early Universe provide a solution to the dark matter problem and have been the preferred candidate for direct detection dark matter experiments for several decades. The most successful detection technology for WIMPs, in the mass range 10 GeV to 10 TeV, has been two-phase (liquid/gas) xenon time projection chambers.

In this chapter astrophysical and cosmological evidence for dark matter will be reviewed and the required characteristics of a dark matter particle outlined. Focusing exclusively on WIMP dark matter, the coherent elastic nuclear scattering mechanism used for the detection of WIMPs and neutrinos will be described. Subsequently, the physics of liquid xenon as a detector medium will be discussed including its use in the highly successful two-phase time projection chamber (TPC) design. Finally, the state of the field, prior to the current generation of tonne-scale liquid xenon (LXe) experiments, will be presented.

## 2.1 Dark Matter

In this section several pieces of evidence for the existence of dark matter at the astrophysical and then cosmological scale will be provided, roughly in chronological order. Here only a few specific results will be described focusing on key or otherwise standard examples. For a much more thorough monograph of the history of evidence for dark matter the reader is referred to the following review [1].

### 2.1.1 Astrophysical evidence

The first evidence for dark matter originates from astrophysical observations. Here a very brief description of evidence for dark matter at the galaxy and galaxy cluster scales is provided focusing on galaxy cluster rotations, galaxy rotation curves, and gravitational lensing of galaxy clusters.

In 1933, Zwicky used the virial theorem, which states that the time-averaged kinetic energy of a system in equilibrium should equal minus one-half of the time-averaged gravitational potential energy of the system, to compare the visible and inferred masses of galaxy clusters. Using this relationship Zwicky observed that the quantity of visible matter within the Coma Cluster was insufficient to support the velocities of its constituent galaxies. To replicate these observations, Zwicky proposed that the Coma Cluster had approximately 400 times more mass than can optically observed [2, 3].

Through the mid-to-late $20^{th}$ century the observation and study of individual galaxies led to many measurements of galactic rotation curves. These curves, measured as the rotational velocity of galaxies as a function of radius, consistently observe a constant rotational velocity out to large radii [4, 5]. According to Newtonian dynamics, in these outer regions the rotational velocity should decrease as square root of the radius. The observed deviation from this law hints that there is non-visible matter following a different spatial distribution to normal matter, suggesting it must also interact differently to normal matter. Freeman went as far to say [5]:

> "[If the results are correct then] there must be in these galaxies additional matter which is undetected, either optically or at [a wavelength of] 21 cm. Its mass must be at least as large as the mass of the detected galaxy, and its distribution must be quite different from the exponential distribution which holds for the optical galaxy."

The most recent measurement of the galactic rotation curve for the Milky Way, the galaxy in which we live, using data from GAIA [6, 7], WISE [8], APOGEE [9], and 2MASS [10], are shown in Figure 2.1. The observed rotation curve is fitted using a model composed of normal matter components alongside dark matter following an Einasto density profile [11]. The best fit parameters of this model finds a local dark matter density of $0.425 \pm 0.004\,\mathrm{GeV/cm^3}$ equivalent to one proton per two cubic centimetres [12].

In conclusion, it is clear that ordinary matter cannot explain the observed dynamics of galaxies, including our own. To reconcile the above observations with our current understanding of physics requires an additional component of dark matter in quantities far exceeding that of ordinary matter.

In 2004, non-visible matter which interacts very differently to ordinary matter was observed in the Bullet Cluster [15]. Produced from the collision of two galaxy clusters, the cluster was studied

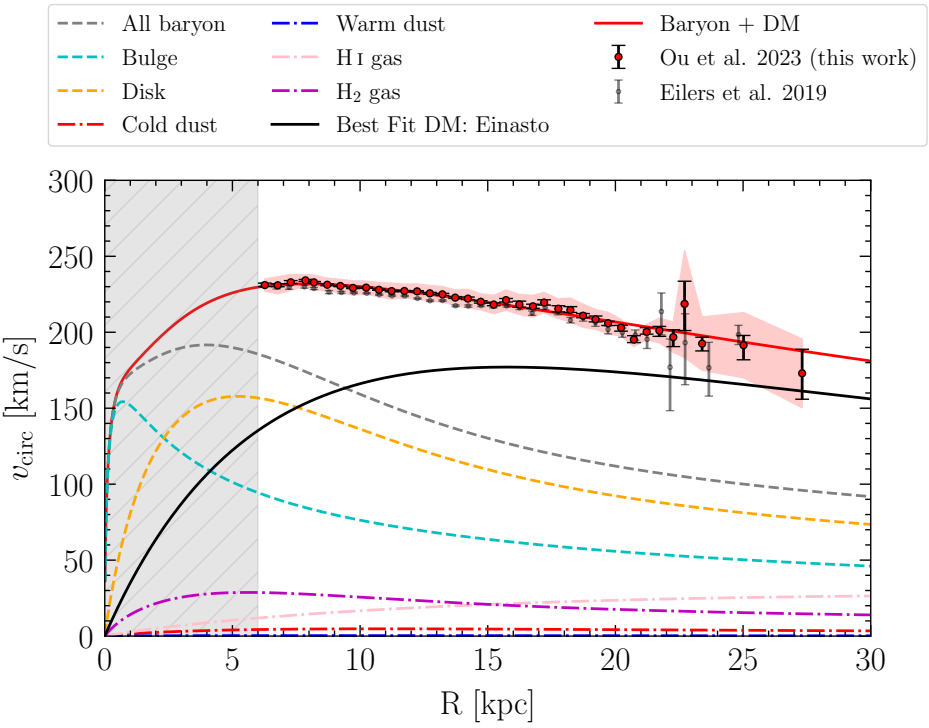



Figure 2.1: The Galactic rotation curve of the Milky Way as measured by Ref [12] using datasets from the GAIA [6, 7], WISE [8], APOGEE [9], and 2MASS [10] experiments. A previous measurement, Ref [13], is shown as black circles. A model of the Milky Way galactic rotation curve is shown (red line), using the baryon model from Ref [14] and a substantial dark matter component following an Einasto dark matter profile [11]. Figure reproduced from Ref [12] by permission of Oxford University Press on behalf the Royal Astronomical Society who retain the copyright of this reproduced figure.

using optical imaging, x-ray astronomy and weak gravitational lensing. The x-ray images provide the location of the galaxies and gas, which contains most of the visible mass, of the two constituent galaxy clusters. Weak gravitational lensing, where the potential well produced by mass bends light around said mass, was used to locate and "weigh" the total mass between the source and observer. When the two galaxy cluster collided to form the Bullet Cluster, the galaxies passed one another without interaction whereas the gas of the two systems slowed down due to ram pressure. This led to the majority of the visible mass density, which originates from the gas, being close to the collision point. Weak gravitational lensing measurements instead demonstrated that the majority of mass of the Bullet Cluster was surrounding the galaxies that passed though the collision unimpeded. This observation demonstrated that there is a significant non-visible dark matter component with a low interaction cross-section both with itself and with normal matter.

This observation was, and remains, the most striking example of a system where the dark and baryonic components of a galactic object can be spatially resolved and distinguished.

### 2.1.2 Cosmological evidence

The cosmological evidence for dark matter is strongly coupled to the understanding of the early Universe and how it has evolved to the present day. For this reason a brief review of the early Universe is provided prior to a discussion of the evidence for dark matter arising from it.

#### 2.1.2.1 The early Universe

At the end of the radiation-dominated era (371,000 years after the Big Bang), the cosmos was filled with a hot charged plasma of baryons, photons and dark matter. Any over-density fluctuations in this plasma would lead to gravitational potential wells which would attract the massive baryons and dark matter. The photons, which are largely ignorant of the gravitational potential, undergo frequent scattering on the charged (baryon) constituents within the opaque plasma, leading to an outward radiation pressure acting on the baryons. The combination of the inward (restoring) gravitational potential and outward (driving) radiation pressure leads to the baryon component of the plasma acting as a driven oscillator. A consequence of the oscillating plasma are waves of baryon over-densities, analogous to sound waves, known as baryon acoustic oscillations (BAOs).

The shape (relative and absolute heights) of the BAO modes contains information on the relative abundances of dark matter and baryons. As a simplification, if the Universe has more dark matter then the oscillator would have a stronger gravitational restoring force leading to smaller oscillations overall, whereas if the Universe had more baryons then the amplitude of the oscillations would be larger. In particular the odd modes, which originate from the compression of the plasma, are particularly sensitive to the relative amounts of baryons and dark matter [16].

As the Universe cooled though expansion the charged plasma eventually neutralised forming hydrogen in what is known as decoupling or recombination.[1] In the absence of the charged plasma, the photons, which contain information about the Universe at the time of decoupling, are free to propagate through the now transparent Universe. This decoupling led to the cessation of the radiation pressure and by extension the end of baryon acoustic oscillations. The photons from the surface-of-last-scattering, the radiation emitted at decoupling, should be detectable today, with substantial red shift, and would contain information about the Universe at the point of decoupling, including the relevant energy and matter densities and BAOs.

#### 2.1.2.2 Observing the relics of the early Universe

In 1965, the hypothesis of the surface-of-last-scattering existing as a black-body spectrum was proposed alongside an unexpected measurement of just such a spectrum with a temperature of $3.5 \pm 1.0\,\mathrm{K}$ which came to be known as the cosmic microwave background (CMB) [17, 18]. Successive experiments improved their measurements of the CMB, including the addition of spatial sampling with increasingly precise angular resolution and most recently the inclusion of polarisation maps, with the most recent results obtained by the Planck experiment [19]. The results from Planck demonstrate remarkable homogeneity in the universe, ($-\Delta T | < 300\,\mu\mathrm{K}$) at the time of decoupling, and provide high-quality measurements of BAOs, as can be seen in Figures 2.2 and 2.3 respectively.

By analysing the observed BAO spectrum, Figure 2.3, Planck was able to measure the dark

[1] Strictly speaking, this is not recombination as the proton and electron were never previously bound.

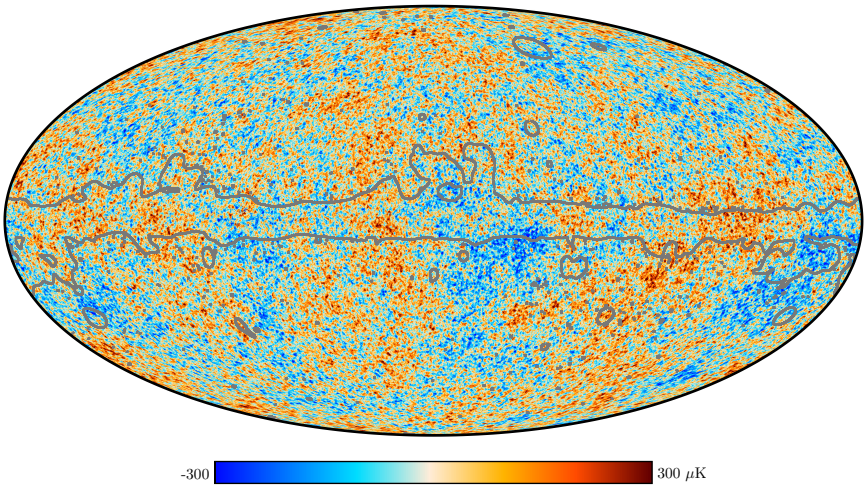



Figure 2.2: A map of the temperature anisotropies in the CMB as observed by Planck in their 2018 analysis. Figure provided by ESA and the Planck Collaboration [19].

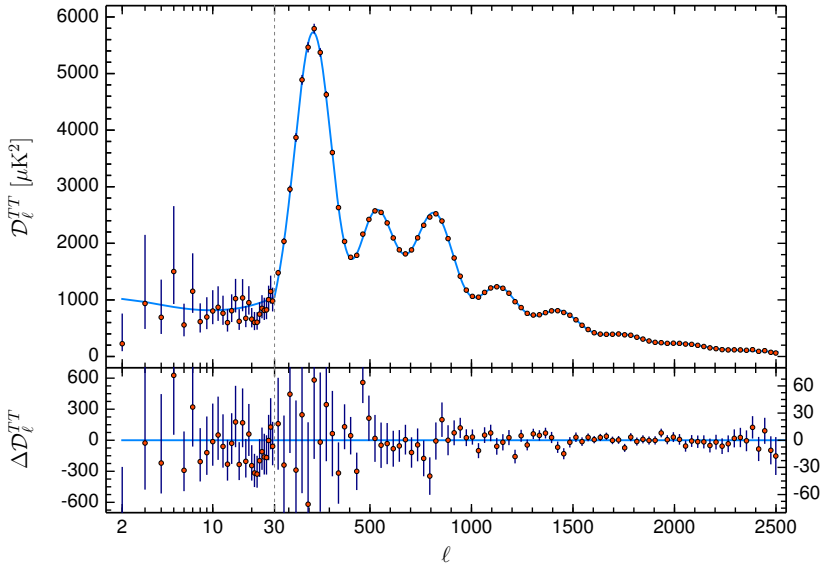



Figure 2.3: The CMB temperature power spectrum (red) as measured by the Planck experiment. The multipole moment $l$ is a proxy of the angular scale over which anisotropy occurs. The multidimensional best fit of the base-$\Lambda$CDM model is shown in blue. Figure from Planck Collaboration, A&A, volume 641, A6, 2020, reproduced with permission © ESO [20].

matter and baryon energy densities in the early Universe as

$$\begin{aligned} \Omega_b &= 0.022{,}33 \pm 0.000{,}15 \qquad \text{(baryons)} \\ \Omega_c &= 0.119{,}8 \pm 0.001{,}2 \qquad \text{(cold dark matter)} \end{aligned} \tag{2.1}$$

where $\Omega$ is the energy density normalised to the critical density of the Universe $\rho_c$, the energy density required for a flat Universe in the absence of dark energy [20].

Through the cosmological inference of dark matter in the early Universe, it is clear that dark matter is not only unlikely to originate from an unaccounted for astrophysical effect but that it has existed within the Universe over its life-time. Any convincing candidate/model for dark matter must then be valid over the life-time of the Universe and exist within the early Universe.

### 2.1.3 Dark matter candidates

From the evidence described previously over a wide range of scales it is clear that there is dark matter in the Universe. Naturally, the next question is, what is it? Within constraints derived from the observed evidence numerous dark matter models can be made. Here a brief overview of these constraints will be given alongside a detailed description of the weakly interacting massive particle (WIMP) dark matter model most relevant to this thesis. For a more general overview of dark matter candidates the reader is referred to Refs [21, 22].

The first key assumption made within this thesis is that the astrophysical/cosmological dark matter originates from an as-of-yet undiscovered particle outside the Standard Model of particle physics. If such a particle existed in the early Universe, as might be expected in the high-energy plasma, and then decoupled from it with some relic abundance, it could explain both the current astrophysical and the primordial cosmological observations.

**Electric charge:** As no evidence of dark matter has been obtained via the electromagnetic interactions it is commonly assumed that dark matter is electrically neutral. However, if the electrical millicharge of dark matter was suitably small it is possible that the effect of the dark matter charge would be insufficient to be detected in previous measurements. From astrophysical observations and experimental exclusions limits it has been shown that dark matter of mass 1 GeV (10 TeV) must have a millicharge less than $10^{-6}$ ($10^{-4}$) relative to the charge of an electron. From the same calculations it is also expected that any such charged

dark matter particle would have been ejected from the Galactic disc due to the Galactic magnetic field and shockwaves from supernova explosions [23].

**Self interactions:** The observations from the Bullet Cluster impose some limitation on the dark matter self-interaction cross-section. If the dark matter is treated as a particle of mass $m_\chi$ with some self-interaction cross-section $\sigma_\chi^{self}$, then $\sigma_\chi^{self}$ must be suitably low such that the two dark matter halos, one for each galaxy cluster, passed through one another without significant impediment. Using this logic an order of magnitude limit on $\sigma_\chi^{self}$ can be calculated as [24]

$$\frac{\sigma_\chi^{self}}{m_\chi} < 1 \left[\frac{cm^2}{g}\right]. \tag{2.2}$$

**Non-baryonic:** Observations from the CMB using the $\Lambda$CDM model demonstrate that the dark matter component should be non-baryonic in nature and therefore not interact via the strong force.

**Low interaction strength with Standard Model:** For the dark matter to remain in the configuration expected from galactic rotation curves and the Bullet Cluster requires the dark matter particle to have a low interaction cross-section with Standard Model particles. If the dark matter frequently scattered on normal matter its spatial distribution would be significantly altered. If the dark matter interacted with the gas during the Bullet Cluster collision then the dark matter would have settled within a similar spatial distribution to the gas and not the constituent galaxies.

**Stable:** Dark matter is required to explain both recent astrophysical observations and cosmological observations of the early Universe. For a particle to explain both observations requires the particle to either stable or at least long-lived over the lifetime of the Universe.

#### 2.1.3.1 Thermally produced WIMPs

Arguably the most popular class of dark matter candidates are known as weakly interacting massive particles (WIMPs) which exist as thermal relics from the early Universe [25].

Consider a particle $\chi$ of mass $m_\chi$ which is in equilibrium with the plasma in the hot early Universe. If this particle were to decouple from the plasma, such that it could no longer

annihilate, it would provide a dark matter relic density $\rho_\chi$ in the early Universe. The density of this species would decrease as the Universe expands with the energy density obeying

$$\rho_\chi = m_\chi n_\chi = \frac{m_\chi n_{\chi_0}}{R^3} \equiv \Omega_\chi \rho_c, \tag{2.3}$$

where R is the cosmological scale factor distance, $n_\chi$ ($n_{\chi_0}$) is the time-evolving (current) particle number density, $\rho_c$ is the critical energy density required for a flat (zero-curvature) universe, and $\Omega_\chi$ is the ratio of the dark matter energy density to the critical energy density. Using this equation the relationship between the abundance of dark matter particles, of some fixed mass, and the energy density is clear. To explain the observed dark matter energy density requires the correct particle number density 13.7 GYr after $\chi$ leaves thermal equilibrium with the plasma. This number can be calculated by solving the following Boltzmann equation:

$$\dot{n}_\chi = -3Hn_\chi - \langle \sigma v \rangle \left( n_\chi^2 - n_{\chi,eq.}^2 \right), \tag{2.4}$$

where $H \equiv \dot{R}/R$ is the Hubble parameter, $\dot{R}$ is the first time derivative of R, $\langle \sigma v \rangle$ is the thermally-averaged total annihilation cross-section and $n_{\chi,eq.}$ is the equilibrium number density. An approximate solution to Equation 2.4 is shown in Figure 2.4. As the Universe expands, eventually it becomes impossible for the $\chi$ particles to find one another to annihilate. This process, known as freeze-out, is fulfilled when

$$H(t) \geq n_\chi \langle \sigma v \rangle . \tag{2.5}$$

As the co-moving number density of $\chi$ can no longer increase via production (as the temperature is too low) nor can it decrease ($\chi$ can no longer find one another) the number of $\chi$ in the Universe will remain constant; The present abundance of this thermal relic is given by

$$\Omega_\chi h^2 \approx \frac{2.4 \times 10^{27}}{\langle \sigma v \rangle}, \tag{2.6}$$

where h is the dimensionless Hubble constant, when ignoring the mass dependence in several parameters for a non-relativistic $\chi$ [26]. From Equation 2.6 we can see that the final relic abundance is, to first-order, inversely proportional to the self-annihilation cross-section. This is expected since higher self-annihilation cross-sections leads to the decoupling of the $\chi$ at a

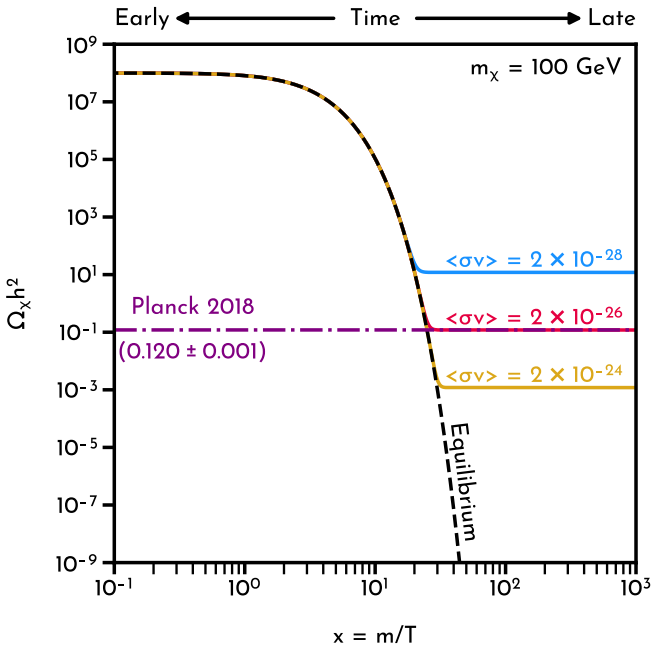



Figure 2.4: The temperature (time) evolution of the $\chi$ dark matter relic abundance. Plot created from relic abundance calculations and results Refs [26, 27] alongside the observed dark matter density observed by Planck [20].

later time at which point the relic abundance is lower. If one chooses a cross-section at the weak scale, a reasonable first guess for a particle with a low interaction cross-section, a relic abundance approximately equal to the observed value from cosmological measurements is obtained, this is sometimes referred to as the 'WIMP miracle'.

## 2.2 Detecting Dark Matter

Dark matter can be detected though three detection channels, shown in Figure 2.5 which are called direct detection, indirect detection, and collider production.[2] This thesis focuses exclusively on direct detection, but the other two methods are briefly outlined here.

**Direct detection ($\chi + \text{SM} \rightarrow \chi + \text{SM}$)** is where a dark matter particle scatters off, or otherwise interacts with, a Standard Model particle. Using this methodology particle physics observations are intrinsically connected to astrophysical dark matter, allowing direct statements of its particle nature to be made alongside measurements of some galactic dark matter halo parameters. Examples of experiments looking for dark matter is this way include two-phase time projection

[2]The definitions of the "direct" and "indirect" channels differ from those used in the collider community.

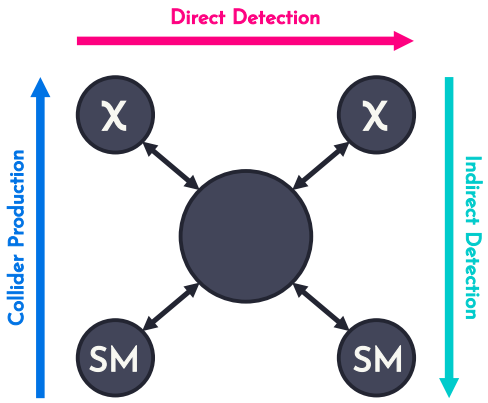



Figure 2.5: Schematic of the three methods by which dark matter could interact with the Standard Model.

chambers (TPCs), such as the ZEPLIN-III experiment [28], cryogenic bolometers, for example CRESST [29], scintillating crystal detectors, which includes the DAMA/LIBRA experiment [30], and directional detectors such as DRIFT [31].

**Indirect detection ($\chi + \chi \rightarrow \mathrm{SM} + \mathrm{SM}$)** is where experiments search for Standard Model products from dark matter annihilation. Examples of experiments looking for dark matter is this way include gamma-ray telescopes, such as the large area telescope (Fermi/LAT) [32], and neutrino detectors, such as the IceCube experiment [33]. See Ref. [34] for a thorough review on indirect detection.

**Collider production ($\mathrm{SM} + \mathrm{SM} \rightarrow \chi + \chi$)** is where two Standard Model particles produce dark matter particles which, like neutrinos, exfiltrate the detector without detection. A standard methodology to study such interactions is to look for missing transverse momentum from proton-proton collisions at the Large Hadron Collider (LHC). If dark matter particles could be created in this way precision measurements of the particle mass and interaction cross-sections could be studied, but these dark matter consistent particles could never unequivocally be connected to the astrophysical dark matter observations unlike the above processes. Examples of experiments searching for dark matter at colliders include the LHC general purpose detectors, ATLAS [35] and CMS [36]. See Refs. [37, 38] for detailed reviews of dark matter production in particle colliders.

### 2.2.1 Dark matter scattering kinematics

The computation of recoil spectra and scattering rates of galactic WIMPs on targets such as xenon are relativity straight forward under certain assumptions. Here the key results of the aforementioned calculations are made using the conventions outlined by Smith and Lewin [39].

To compute the recoil spectrum and rate of WIMPs elastic scattering on a xenon target requires two components: a velocity distribution of the incoming dark matter particles (astrophysics) and a kinematic model for the WIMP-nucleus interaction (particle physics). Using these two components the differential WIMP nuclear recoil spectrum can be calculated as

$$\frac{dR}{dE_r} = \overbrace{\frac{\sigma_{\chi A}}{2\, m_\chi \mu_{\chi A}^2} F^2(q)}^{\text{Particle Physics}} \times \overbrace{\rho_\chi \int_{v_{min}}^{v_{max}} \frac{f(\vec{v})}{v} d^3v}^{\text{Astrophysics}}, \tag{2.7}$$

where $\sigma_{\chi A}$ is the WIMP-nucleus cross-section, $\rho_\chi$ is the energy density of dark matter, $\mu_{\chi A}$ is the WIMP-nucleus reduced mass, $F^2(q)$ is the scattering form-factor for a momentum transfer q, and $f(\vec{v})$ is the velocity distribution of the dark matter with respect to the Earth reference frame.

**Dark matter velocity profile:** a common model of the dark matter velocity profile is the standard halo model (SHM). In the galactic reference frame the dark matter vector velocity obeys a 3D Gaussian profile centred about the origin and truncated at the galactic escape velocity $v_{esc}$ [40]. In the laboratory (Earth) frame the velocity profile is boosted by $\vec{v}_\oplus$: the sum of the velocities of the sun around the galactic centre and the Earth around the Sun. Using these assumptions the un-normalised velocity probability-density function (PDF), in the laboratory frame, can be written as

$$f(v \mid v_\oplus, v_{esc}) \propto \exp\left(-\frac{|\,\vec{v}+\vec{v}_\oplus\,|^2}{2v_0}\right) \times \theta\left(|\,\vec{v}+\vec{v}_\oplus\,| - v_{esc}\right), \tag{2.8}$$

where $v_0$ is the modal circular rotational speed and $\theta$ is the Heaviside step function. Recent observation of localised dark matter structures in the Milky Way by Gaia, have led to the proposal of an updated SHM++ dark matter velocity distribution [41, 42]. This update model better represents our current understanding of the velocity profile of our Galaxy but is not commonly used in the dark matter community.

**WIMP scattering kinematics:** The kinetic energy of non-relativistic WIMPs can be written as

$$E_\chi = \frac{1}{2} m_\chi v_\chi^2, \tag{2.9}$$

with the most probable WIMP kinetic energy $E_0$ occurring for $|v| = v_0$. By treating the WIMP-nucleus interaction as a classical elastic scattering process the recoil energy of the nucleus can be written

$$E_r = E_\chi r \left( \frac{1 - \cos(\theta)}{2} \right) \tag{2.10}$$

where $\theta$ is the scattering angle in the centre-of-mass frame and $r = 4\, m_\chi m_A / (m_\chi + m_A)^2$, where $m_A$ is the mass of the target nucleus. Assuming isotropic WIMP-nucleus scattering this recoil energy is uniformly distributed with $0 \leq E_r \leq E_\chi r$.

**WIMP scattering rate:** By ignoring the velocity of the Earth, the Galactic escape velocity, and the WIMP-nucleus form-factor the differential recoil rate can be approximated as

$$\left. \frac{dR}{dE_r} \right|_{v_{esc} = \infty}^{v_\oplus = \vec{0}} \approx \frac{R_0}{E_0 r} e^{-E_r / E_0 r}, \tag{2.11}$$

where $R_0$ is the total integrated-rate and $E_0$ is the most probable WIMP energy. The WIMP-nucleus differential recoil rate for argon and xenon targets is displayed in Figure 2.6. Here we can see how the choice of target nucleus affects the recoil rate with a heavier target having a quicker decay in the recoil rate as a function of recoil energy.

Using Equation 2.10 the maximum nucleus recoil energy encountered in backscattering interactions can be calculated as $E_r^{max} = E_\chi\, r$. In the detection of dark matter there are two important limits: what is the fastest (the highest energy) WIMP within the Galaxy?, and what is the lowest energy recoil we can detect? For a WIMP to be detected it must be gravitationally bound to the Galaxy requiring the WIMP to have a speed less than the escape velocity with respect to the galactic rest frame. In the boosted earth frame this allows a WIMP to have a maximum velocity of

$$v_{max.} = v_{esc} + v_0 \tag{2.12}$$

with respect to the detector. The energy threshold of the detector $E_{thres}$, the lowest energy detectable recoil, is a detector parameter independent of the hypothetical dark matter particle. The combination of these two limits defines the lowest mass WIMP that can be detected. If a

recoil must be above $E_{thres}$ to be detected and largest recoil is from a WIMP with a velocity of $v_{max}$ then the lowest mass WIMP that can be detected is

$$m_{\chi}^{min.} = \left( \frac{E_{thres}\, m_A}{2\, v_{max}^2} \right)^{-1/2} \tag{2.13}$$

in the limit that $m_{\chi} \ll m_A$. This $m_{\chi}^{min.} \propto m_A^{-1/2}$ dependence highlights that a lighter target nucleus is kinematically preferential for searching for lower mass WIMPs in the absence of detector efficiency considerations.

**WIMP interaction cross-section:** The interaction cross-section of WIMPs on atoms can be split into two main categories: spin-dependant (SD) and spin-independent (SI), here only the spin-independent case will be discussed. The WIMP-nucleus spin-independent cross-section $\sigma_{SI,0}$ is partitioned into proton and neutron components

$$\sigma_{SI,0} = \frac{4\mu_{\chi A}^2}{\pi} \Big( Z \times f_{proton} + (A - Z) \times f_{neutron} \Big)^2, \tag{2.14}$$

where $f_{proton}$ ($f_{neutron}$) describes the WIMP–proton (WIMP-neutron) coupling strength. Often WIMP's are assumed to couple equally to protons and neutrons ($f_{proton} = f_{neutron}$) leading WIMPs to scatter coherently off all the target nucleons resulting in the total cross-section scaling as the square of the target's atomic number. The above expression of the scattering cross-section is often simplified as

$$\sigma_{SI,0} \approx A^2 \times \left( \frac{\mu_{\chi A}}{\mu_{\chi,nucleon}} \right)^2 \times \sigma_{nucleon}, \tag{2.15}$$

where $\mu_{\chi,nucleon}$ is the WIMP-nucleon reduced mass. An advantage of this formalism is that is allows the WIMP-nucleus cross-section to be written in terms of a WIMP-nucleon cross-section. Using the $\sigma_{nucleon}$ WIMP-nucleon cross-section results from different experiments using with different targets can be easily compared.

The approximation that the WIMP coherently scattering off the entire nucleus is only true at low momentum transfer $q = \sqrt{2 m_A E_r}$. To take into account the non-zero momentum transfer the full scattering cross-section is often written as

$$\sigma_{SI}(E_r|A) = \sigma_{SI,0} \times F^2(q, r_n), \tag{2.16}$$

where $r_n$ is the effective nuclear radius and $F^2(q, r_n)$ is the momentum-transfer dependant form-factor. There are several choices for the form-factor, a common form-factor used in dark matter direct detection is the Helm form-factor

$$F(q, r_n) = 3\frac{j_1(q\, r_n)}{q\, r_n} \times e^{-(qs)^2/2}, \tag{2.17}$$

where s is a numerical constant and $j_1$ is the spherical Bessel function of the first kind [43]. The effect of the Helm form-factor reducing the scattering cross-section, and thus also the observed recoil rate, can be seen in Figure 2.6. For low-energy recoils ($E_r \leq 100\,\text{keV}$) this can have a significant effect on the recoil rate for heavier nuclei, such as xenon, but has less impact on lighter targets, such as argon.

**Different targets:** The choice in target medium affects the rate of interactions, due to the $A^2$ scaling, and the shape of the expected recoil spectrum, from the nuclear form factor and WIMP-target kinematic conservation laws. Two common targets for direct dark matter searches are argon and xenon. In Figure 2.6 the expected observable recoil rates of xenon and argon detectors are compared for several WIMP masses.

The first observation is that xenon has a much higher recoil rate per unit mass compared to argon, this is due to xenon having a much higher atomic number. The decay in recoil rate for xenon is much quicker than argon due to the heavier target quickly becoming kinematically unfavoured by the $e^{-1/r}$ term in Equation 2.11. For this reason the sensitivity of a xenon target is much more dependent on the detection threshold that of an argon experiment. One of the most striking differences between the two targets is the effect of the nuclear form factor. In the xenon this leads to a substantial reduction in recoil rate for recoils of approximately 90 keV.

Detector and analysis effects also have a significant affect of the detectable recoils rate and spectrum. For this reason the expected observable recoil rate of the LZ (xenon) and DEAP-3600 (argon) experiments are shown. Due to LZ's substantially lower detection threshold it is much more sensitive to low mass WIMPs when compared to DEAP-3600. This is unexpected from the purely kinematic comparison of xenon and argon targets above.

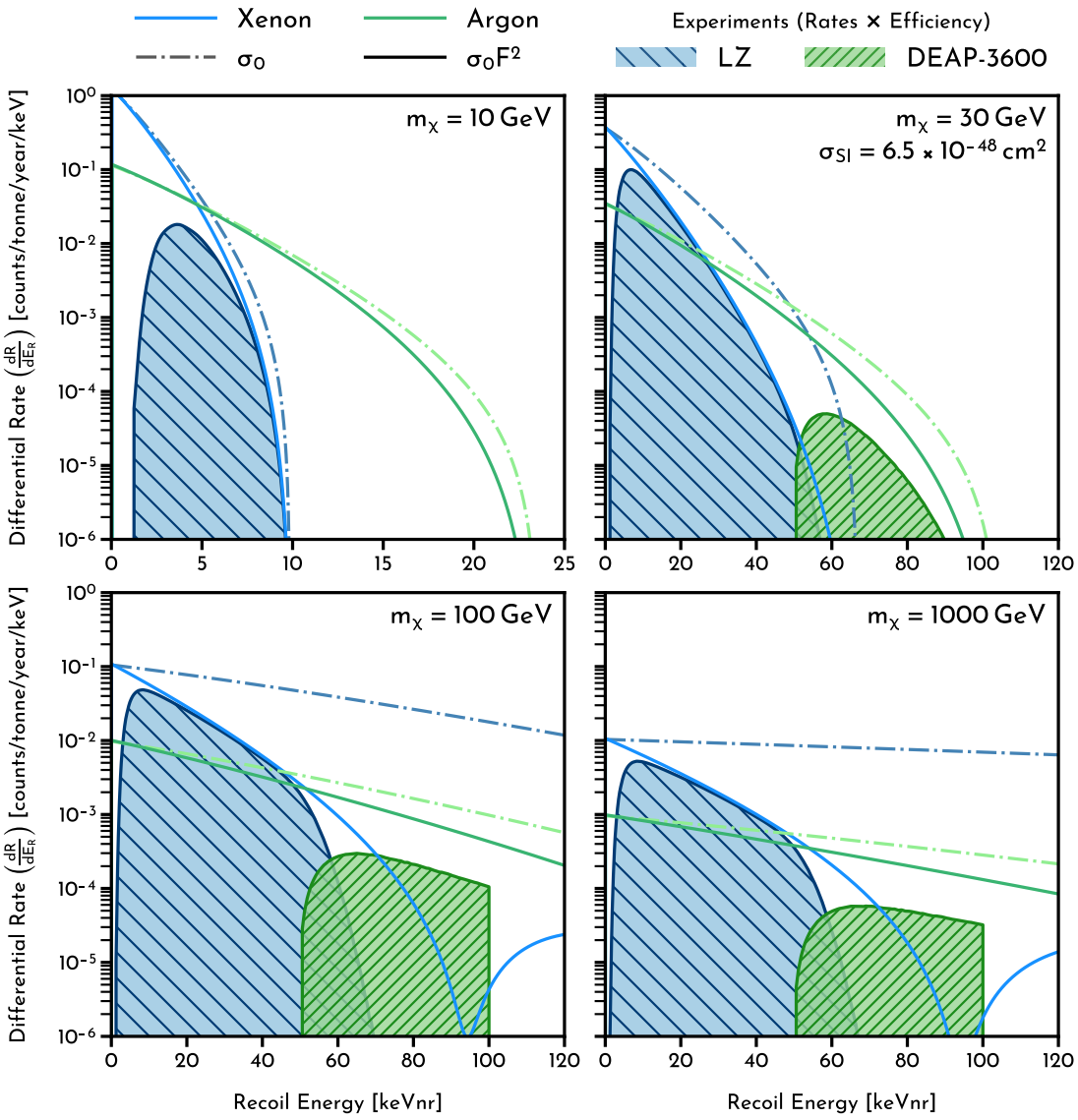



Figure 2.6: The expected differential recoil spectra of 10 GeV, 30 GeV, 100 GeV, and 1000 GeV WIMPs on argon and xenon targets assuming a WIMP-nucleon cross-section of $6.5 \times 10^{-48}$ cm$^2$. Here the lighter dashed (darker solid) lines denote the cross-section before (after) applying the Helm form-factor correction. The filled regions show the expected observed rate from the LZ (xenon) and DEAP-3600 (argon) experiments which include detector efficiencies and region-of-interest (ROI) cuts [44, 45]. The rates prior to the application of the Helm form-factor ($\sigma_0$) are calculated using code from Ref. [46].

## 2.3 Solar Neutrinos

Solar neutrinos can interact with target nuclei via coherent elastic neutrino-nucleus scattering (CE$\nu$NS). In this process the neutrino coherently scatters off all the nucleons within the nucleus, similar to the coherent scattering expected for WIMPs. This process was recently observed for the first time by the COHERENT collaboration, who detected man-made neutrinos from the Spallation Neutron Source in the Oak Ridge National Laboratory, using both CsI and liquid argon targets [47, 48].

Solar neutrinos are produced via nuclear fusion process occurring within the sun. The high-flux component produced by the proton-proton (PP) chain is shown in Figure 2.7. These neutrinos scatter off target nuclei via a similar kinematic process as WIMPs and thereby constitute an irreducible background.

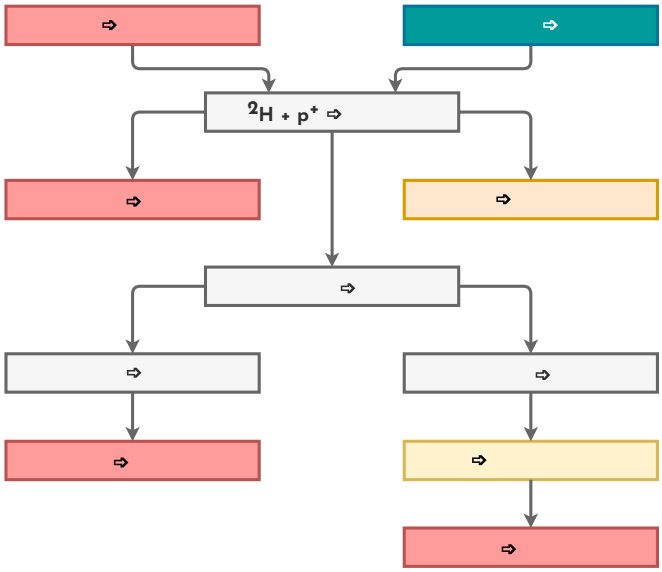



Figure 2.7: Production mechanism for solar neutrinos via the proton-proton (PP) chain alongside associated ranching fractions. Figure adapted from Ref [49].

The differential rate of this irreducible CE$\nu$NS background can be calculated as

$$\frac{dR}{dE_r} = \frac{1}{M_T} \times \int \overbrace{\left(\frac{dN}{dE_\nu}\right)}^{\text{Astrophysics}} \times \overbrace{\frac{d\sigma\left(E_\nu, E_r\right)}{E_r}}^{\text{Particle physics}} dE_\nu, \tag{2.18}$$

where the neutrino flux is a fixed astrophysical quantity and the cross-section is a calculable

particle physics quantity described by the Standard Model. The CE$\nu$NS scattering cross-section can be calculated as

$$\frac{d\sigma\left(E_\nu, E_r\right)}{dE_r} = \frac{G_F^2}{4\pi} Q_w^2 m_A \left(1 - \frac{m_A}{2}\frac{E_r}{E_\nu^2}\right) F^2\left(E_r\right), \tag{2.19}$$

where $G_F$ is the Fermi coupling constant; $Q_w = N - (1 - 4\sin^2\theta_w)\, Z$ where N (Z) is the number of neutrons (protons); and $\theta_w$ is the weak mixing angle [50]. The differential and integrated detection CE$\nu$NS rates, calculated using the method above, are calculated for a xenon target and displayed in Figure 2.8.

The addition of these WIMP-like interactions impairs an experiment's ability to claim discovery though statistical inference, known as being within the "neutrino fog", and is primarily quantified by the reduction in the rate of improving sensitivity per unit time. In principle an extremely sensitive detector could still detect WIMPs below the CE$\nu$NS scale by either: slowly traversing through the neutrino fog and observing WIMPs as an excess on the neutrino background, or by observing annual modulation consistent with the Earth traversing the dark matter halo. In reality the requirements and scale of such a liquid noble gas detector is impractical. For this reason, in practise the ultimate liquid noble gas dark matter detector is one that is sensitive enough to discover dark matter up to the neutrino fog.

A particularly interesting source of astrophysical neutrinos are those from $^8$B decay. Due to the high energy and flux of these neutrinos these will be the first neutrinos detected by a WIMP detector. The differential rate of these neutrinos closely matches that of a 6 GeV WIMP, as shown in Figure 2.8. Because of this, the detection of $^8$B neutrinos acts as a validation that the detector should be able to detect WIMPs if they have a suitably high interaction cross-section. The detection of $^8$B via CE$\nu$NS is interesting in its own right as this would be the first observation of astrophysical neutrinos via CE$\nu$NS. The current generation of tonne-scale LXe are expected to be sensitive to these interactions and such a search is a central analysis of these detectors secondary only to a WIMP search.

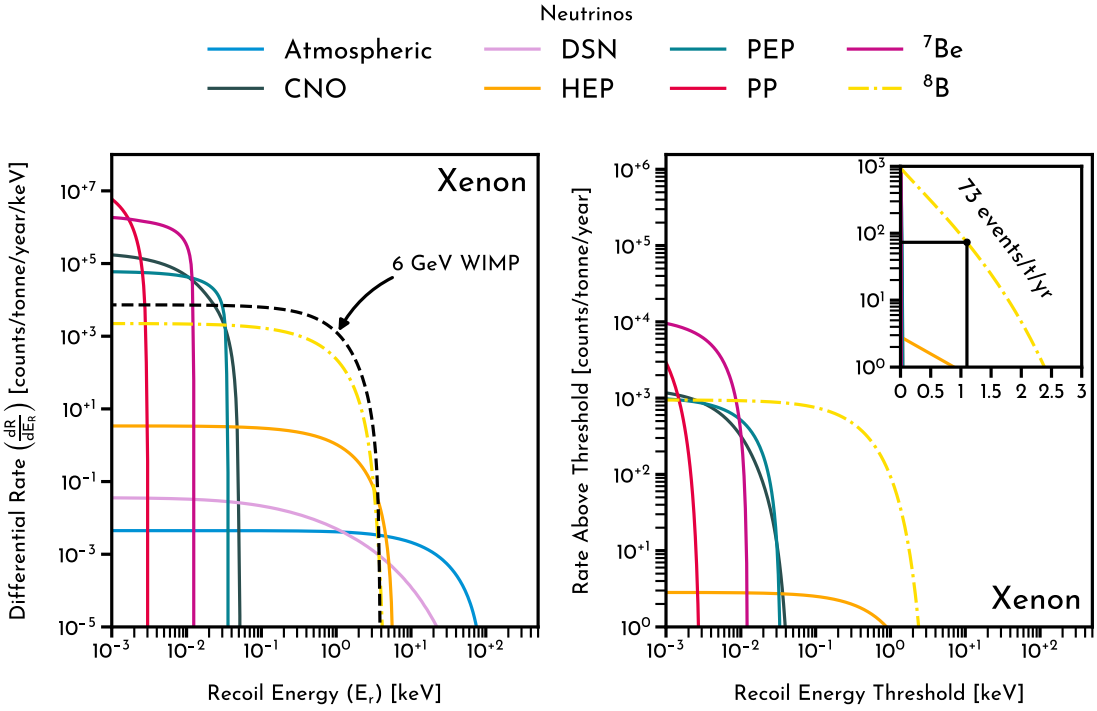



Figure 2.8: The differential recoil spectra of solar and atmospheric neutrinos on xenon. The most interesting neutrino spectrum to two-phase noble gas TPC detectors, like LZ, is $^{8}$B, due to its relatively high differential rate above/near nominal detector thresholds. To demonstrate the accessibility to $^{8}$B interactions in xenon detectors the differential recoil rate of 6 GeV WIMPs is also plotted. Figure created using fluxes and formalisms from Billard et al. [50]. For ease of comparison the colours match those in the proton-proton chain diagram above (Figure 2.7).

## 2.4 Signal Generation in Liquid Xenon Detectors

### 2.4.1 Excitation, ionisation and heat

The elastic scattering of liquid noble gas nuclei deposits energy into the liquid. This energy is partitioned into excitation, ionisation, and sub-excitation electrons[3] as described by the Platzman equation [51]:

$$E = n_i E_i + n_{ex} E_{ex} + n_i \epsilon, \tag{2.20}$$

where $n_i$ ($n_{ex}$) is the number of ionised (excited) atoms, each of which requires a mean energy of $E_i$ ($E_{ex}$) to produce, and $\epsilon$ is the mean energy of the liberated sub-excitation energy electrons. As the sub-excitation electrons cannot be detected this term is usually ignored, leaving the more familiar

$$E = n_i E_i + n_{ex} E_{ex}. \tag{2.21}$$

Signal production in LXe is controlled by two processes, impact excitation and recombination. A schematic of these two processes, including how they relate to one another, is shown in Figure 2.9. In this section a brief review of these two processes is given based upon the more complete reviews provided by Refs [52, 53].

Impact excitation of xenon atoms (A) leads to the production of excited dimers, known as excimers, which can exhibit electronic ($A_2^\star$) or electronic-and-vibrational ($A_2^{\star,\nu}$) excitation. The electronic excitation can be of either the singlet or triplet state. The relaxation of the $A_2^{\star,\nu}$ excimer is the source of vacuum ultraviolet (VUV) emission in LXe and is defined by a 3 ns (27 ns) time constant for the singlet (triplet) state. The full chain of interactions for primary VUV emission can be written as:

$$\begin{aligned} e^- + A &\rightarrow A^\star + e^- && \text{(impact excitation)} \\ A^\star + A &\rightarrow A_2^{\star,\nu} && \text{(excimer formation)} \\ A_2^{\star,\nu} + A &\rightarrow A_2^\star + A && \text{(relaxation)} \\ A_2^{\star,(\nu)} &\rightarrow A + A + \gamma && \text{(VUV emission)} \end{aligned} \tag{2.22}$$

where $A^\star$ ($A^{\star\star}$) denotes a weakly (strongly) excited atom.

[3] These are electrons with insufficient energy to ionise the target and are thus an end stage of the energy deposition process

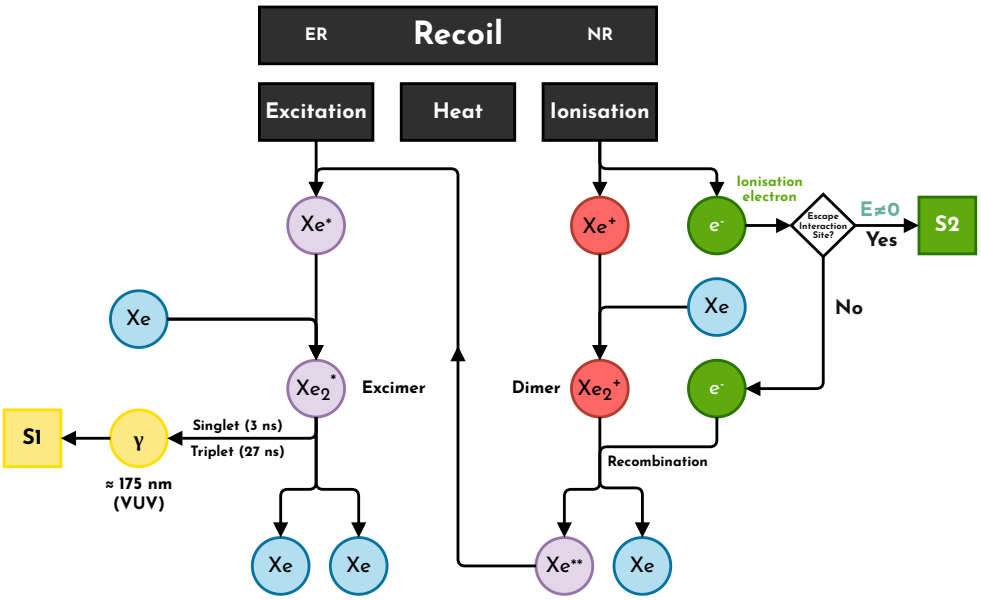



Figure 2.9: Diagram of quanta (optical photons $\gamma$, ionisation electrons $e^-$) production via excitation and recombination of recoiling xenon atoms. The energy partitioned into heating the target via nuclear scatters cannot be observed in xenon detectors and is thus not detailed here and must be accounted for during energy reconstruction. Blue represents Xe atoms, red represents Xe ions and dimers, purple represents Xe excimers, yellow represents scintillation, and green represents ionisation electrons.

If the ionisation electrons are unable to escape the interaction site they will recombine with the surrounding xenon ions leading to VUV emission. Specifically, these electrons can combine with molecular xenon ions ($A_2^+$) to produce strongly excited xenon atoms. These excited xenon atoms can then produce VUV photons via thermionic de-excitation, excimer formation, and finally VUV emission as described by

$$\begin{aligned} e^- + A &\rightarrow A^+ + e^- + e^- && \text{(impact ionisation)} \\ A^+ + A + A &\rightarrow A_2^+ + A \\ e^- + A_2^+ &\rightarrow A^{**} + A && \text{(recombination)} \\ A^{**} + A &\rightarrow A^* + A + \text{heat} \\ A^* + A + A &\rightarrow A_2^* + A + \text{heat} \\ A_2^* &\rightarrow A + A + \gamma && \text{(VUV emission)} \end{aligned} \quad . \tag{2.23}$$

Recombination influences how many of the initial ionisation electrons are detected as electrons

or photons. This effect can be succinctly written as

$$\begin{aligned} n_\gamma &= n_{ex} + n_i r \\ n_e &= (1-r)\, n_i, \end{aligned} \tag{2.24}$$

where $n_\gamma$ ($n_e$) is the number of photons (electrons) that are able to escape from the interaction site. In the absence of a drift fields ultimately most of the electrons will recombine. Using Equations 2.21 and 2.24 the interaction energy in noble liquids can be written in terms of the number of observable quanta:

$$E = W\left(n_\gamma + n_e\right), \tag{2.25}$$

where W is the W-value to produce either a photon or an electron in the noble liquid. The above equation does not take into account energy lost to heat; insignificant for electronic recoils but significant for nuclear recoils. To take into account this missing energy the full energy partition formula can be written as

$$E = \frac{W}{\mathcal{L}(E)}\left(n_\gamma + n_e\right), \tag{2.26}$$

where $\mathcal{L}(E)$ is the Lindhard factor [54]. This additional consideration leads to an ambiguity when reconstructing energy from the total number of observed quanta as the reconstruction depends on whether the interaction is deemed to be electron recoil (ER) or nulcear recoil (NR) in nature. For this reason reconstructed energy in LXe is sometimes quoted in units of keVnr and keVee which explicitly denote the reconstructed energy under the NR and ER hypothesis respectively.

### 2.4.2 Ionisation and scintillation yields in LXe

In the previous section we established the physics behind quanta production in liquid xenon. Experimentally the metrics of interest are the energy dependant charge and lights yields, defined as the quanta produced per unit energy

$$\begin{aligned} L_y(E) &= \frac{n_\gamma}{E} \qquad \text{(light yield)} \\ Q_y(E) &= \frac{n_e}{E} \qquad \text{(charge yield)} \end{aligned}, \tag{2.27}$$

which are displayed in Figure 2.10 for NR and ER interactions. The anti-correlation in the average number of photon and electron quanta produced is present within these two yield models, with the total ER yield constrained to 1/W and the total NR constrained to L(E)/W.

## 2.5 Two-phase noble element time-projection chambers

The most successful noble gas detectors for dark matter searches have been two-phase TPCs. These detectors are able to locate interactions in (x, y, z) and measure both the ionisation electrons and scintillation photons from interactions. Using these two signals two-phase TPCs are able to discriminate between NR and ER interactions.

#### 2.5.0.1 The TPC design

Single-phase liquid noble gas detectors have been, and indeed continue to be, used to search for dark matter, with examples including the 3.7 kg (fiducial) ZEPLIN-I and 97 kg (fiducial) XMASS-I detectors [65–67]. One difficulty with such scintillation-only detectors is their limited ability to discriminate between ER and NR events.

To improve the discrimination and background rejection capabilities of the single phase detectors, the two-phase TPC design developed in the early 1970s [68]. By reading out signals from both scintillation photons and ionisation electrons, two-phase xenon TPCs are able to effectively discriminate between NR (signal) and ER (background) events using the difference in their yields, as seen in Figure 2.10. The first two-phase xenon detector used to search for dark matter was the ZEPLIN-II detector [69] which was developed in parallel with ZEPLIN-III [70].

Two-phase TPCs use a liquid noble gas (usually argon or xenon) as the bulk target alongside a thin gaseous vapour for electroluminescent amplification of ionisation electrons. The extraction and amplification of the ionisation electrons requires the application of a strong external electric field. To produce the required electric fields a three or four electrode grid configuration is often used. To detect both the primary scintillation and the secondary electroluminescence photons a pair of photomultipler tube (PMT) arrays located at the top and bottom of the detector are often used. A schematic diagram of this design is displayed in Figure 2.11a.

The three key electrodes used in electric field production are the cathode, gate, and anode grids. The cathode-gate pair is used to generate an $\mathcal{O}$(100 V/cm) E-field to drift ionisation

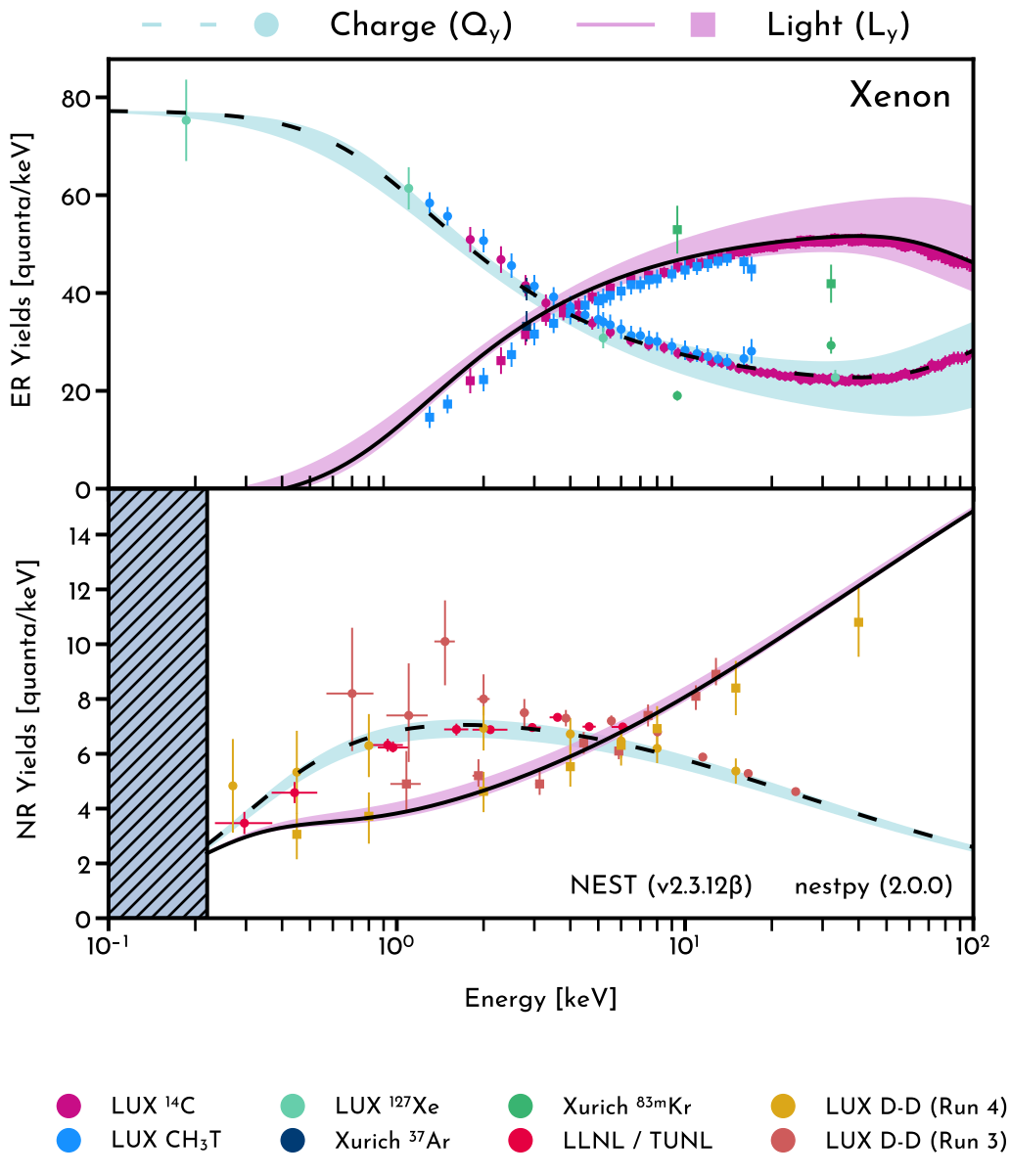



Figure 2.10: Charge and light yields for β-particle ER interactions (top) and NR interactions (bottom) in LXe as calculated using the Noble Element Simulation Technique (NEST) framework [53, 55–57]. Measurements from multiple experiments, operating at different drift fields, are also plotted for comparison with the NEST model. ER data includes results from LUX [58–60] and Xurich [61]. NR data includes results from LUX [62, 63] and LLNL/TUNL [64]. The E-field dependant yields are shown assuming a drift-field of 50 V/cm, 180 V/cm (black), and 500 V/cm, where the charge (light) yield is (inversely) proportional to the electric field. The central 180 V/cm line was chosen for comparison with the tritium data which was acquired at 180 V/cm.

electrons to the liquid surface. The gate-anode pair is used to generate an $\mathcal{O}$(kV/cm) E-field for the extraction and electroluminescent amplification of the ionisation electrons. In addition to the above electrodes, an additional fourth bottom grid is often added to protect the bottom PMT array from the strong electric field generated by the cathode.

#### 2.5.0.2 Quanta detection in two-phase TPCs

The generation and observation of quanta from a WIMP interactions in a two-phase liquid noble -gas detector is illustrated in Figure 2.11b. This single scatter event topology is the expected signal from a WIMP interacting with the target due to the low interaction cross-section. If an event is detected with multiple scatters this is a sign of a non-WIMP particle such as a neutron.

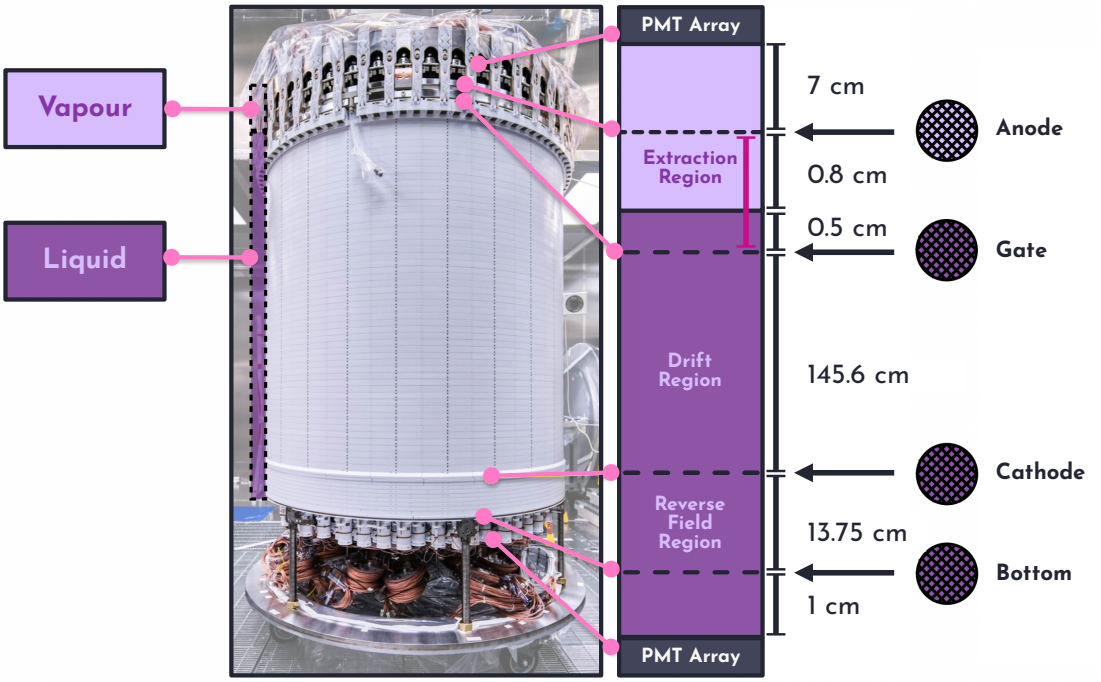
Scintillation photons from the interaction site, produced both by impact excitation and recombination, can be directly detected using the two PMT arrays. This signal, detected by the PMTs as a short pulse, is known as a S1 pulse. Due to detector effects, such as geometry, photon interactions, and the PMT quantum efficiency (QE), only some fraction of the generated photons are detected. These effects are usually absorbed into a single scintillation gain, known as $g_1$, allowing the observed S1 signal to be written as

$$S1 = g_1 n_\gamma. \tag{2.28}$$

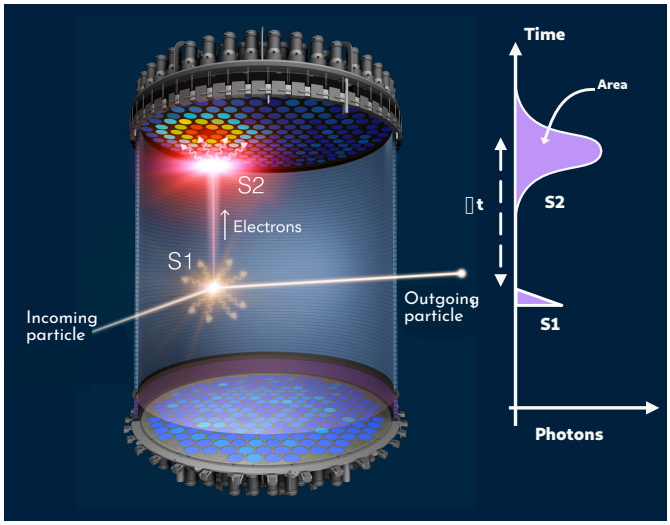
Ionisation electrons are drifted by the drift electric field upwards to the liquid surface. As the electrons drift they have some probability of being captured on electronegative impurities leading to only a fraction of the electrons reaching the liquid surface. This can be modelled by an exponential decay

$$n_e(t_{drift}) = n_e(0) \times \frac{1}{\tau} e^{-t_{drift}/\tau} \tag{2.29}$$

where $t_{drift}$ is the time over which the electrons drifted, known as the drift-time, and $\tau$ is known as the free electron lifetime. At the liquid surface the electrons are extracted into the vapour with some probability $P_{extract}$. Within the vapour the ionisation electrons produce electroluminescence thorough repeated impact ionisation and recombination which is detected by the TPC PMTs as a broad pulse known as an S2 signal.




(a) Annotated photograph of LZ with its four grid design. Figure adapted from Ref [71].




(b) Diagram of a LXe TPC detector showing a single scatter event leading to the production of S1 and S2 pulses. Figure adapted from Ref [72].

Figure 2.11: LXe-TPC design and operation

.

The S2 pulse is detected at a time $t_{drift}$ after the S1 pulse and is localised in the (x, y) plane within the top array, as seen in Figure 2.11b. This time delay allows the z position of the interaction to be reconstructed as $z = \int_0^{t_{drift}} v_z(\vec{x}(t))\,dt$. The (x, y) localisation of the S2 pulse in the upper array allows the (x, y) position of the interaction to be reconstructed. The absolute size of the S2 pulse is defined as

$$S2 = g_2\, n_e, \tag{2.30}$$

where $g_2$is the charge gain. This charge gain is a detector parameter which can be modelled by

$$g_2 = \frac{1}{\tau} e^{-t_{drift}/\tau} \times P_{extract} \times S_{SE} \tag{2.31}$$

where $S_{SE}$ is the signal from a single extracted electron, which is also a detector parameter.

The combination of the S1 and S2 pulses provides additional information about the primary interaction which can be used for signal/background discrimination. In the S2-S1 parameter space NR and ER interaction produce two distinct bands with the ER band having a higher S2 for a given S1. Using these bands the discrimination power of a detector can be qualified as the percentage of ER events that leak below the NR band median. In this parameter space LXe TPCs provide excellent discrimination, with LUX and ZEPLIN-III rejecting 99.9% and 99.99% respectively [28, 73].

The backgrounds in liquid noble gas detector originate from radioactive isotopes within the target liquid and detector components alongside external radiation including $\gamma$-rays from the environment and interactions induced by cosmic rays. These backgrounds can be mitigated via: detector siting, detector design, material selection, target purification and data analysis.

To reduce the rate of muons passing though the detector WIMP detection experiments are usually located deep underground within mines or under mountains. Housing a detector within such a facility can reduce the muon flux by a factor of a million or more. Several facilities exist around the world to house such experiments, including Boulby Underground Laboratory [UK], Sanford underground research facility (SURF) [US], Laboratori Nazionali del Gran Sasso (LNGS) [IT], SNOLAB [CA] and China Jinping Underground Laboratory (CJPL) [CN].

The liquid's non-noble contaminants can be removed via chemical processes. Any noble contaminants, such as krypton, must be removed using other means such as charcoal chroma-

tography [74]. Even after this processing radioactive isotopes of the desired noble gas can be present in the liquid due to cosmogenic activation. In xenon a key activation isotope is the short-lived $^{127}$Xe isotope ($\tau_{1/2}$ = 36.4 day) which decays away quickly during detector commissioning and operation [59]. For argon detectors the long-lived $^{39}$Ar isotope ($\tau_{1/2}$ = 268 year) from atmospheric argon is more problematic lingering in the detector almost indefinitely. The argon dark matter community is planning to use argon from underground sources which is naturally lower in $^{39}$Ar to remove this background contamination [75].

The finite interaction lengths of neutrons and $\gamma$-rays leads to the external and detector component backgrounds scattering near the TPC walls and not near the centre. This self-shielding of the central TPC volume leads to a much quieter environment for a WIMP search. Using the detectors 3D reconstruction capabilities the analysis (fiducial) volume can be optimised to maximise WIMP sensitivity with respect to these backgrounds.

## 2.6 The WIMP dark matter landscape prior to LZ

The search for a particle consistent with dark matter has been of great interest to the particle physics community. Several technologies have been used for dark matter searches, as shown in Figure 2.12, with the most successful being two-phase xenon detectors. Experimental exclusion limits, driven by threshold at low masses and constrained by the measured dark matter density $\rho_\chi$ at high masses, have steadily excluded WIMPs at increasingly feeble cross-sections.

The current generation of tonne-scale LXe detectors, LUX-ZEPLIN (LZ) and XENONnT, are expected to begin probing the neutrino fog at the $^8$B ridge but will remain firmly outside the fog for most WIMP masses. A future LXe detector, proposed by the XLZD consortium [76], is being designed to test the WIMP hypothesis up to the neutrino fog; this detector, likely the last, would have adequate sensitivity to observe WIMPs at 3$\sigma$ up to the neutrino fog for masses greater than ~6 GeV.

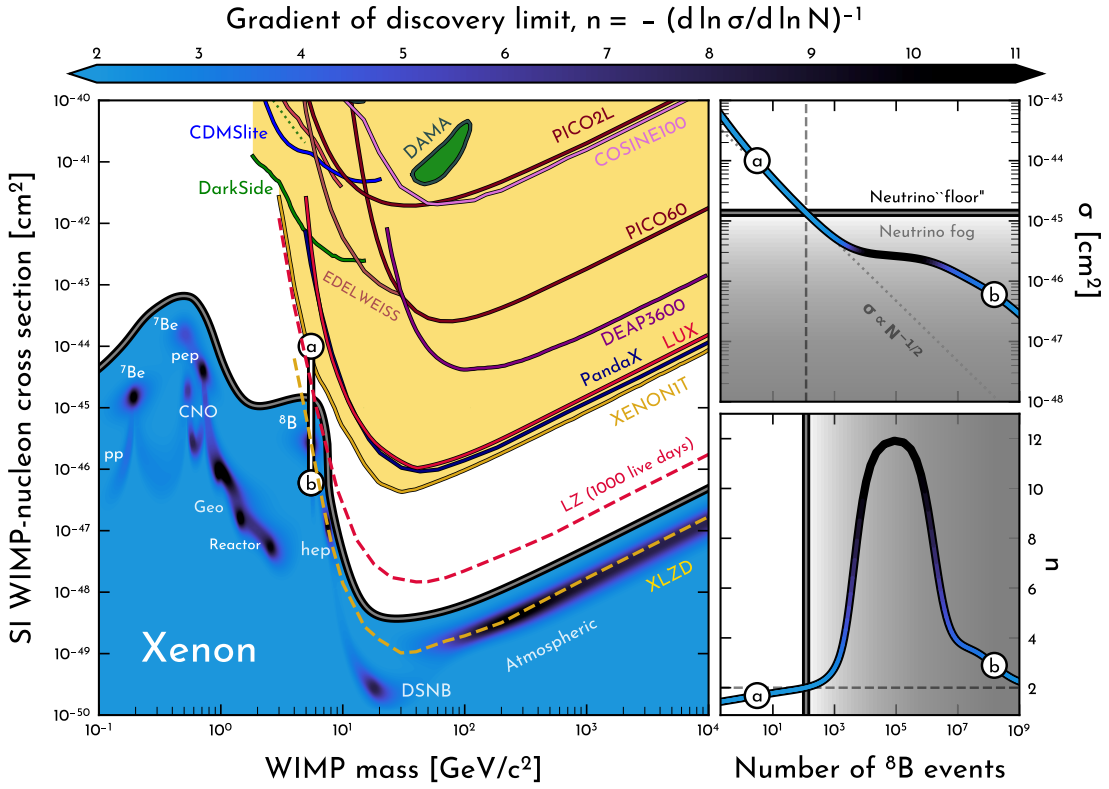



Figure 2.12: (left) The pre-LZ WIMP dark matter exclusion curves are shown alongside the neutrino fog for xenon. (top right) The improvement in sensitivity as a function of exposure from position (a) to (b) in the left plot's parameter space. A steeper gradient effectively indicates that an experiment will exclude more parameter space per unit time. The flat dark region, encountered as the detector has sufficient exposure to detect CE$\nu$NS interactions, indicates a plateau of diminishing returns which must be endured until sufficient exposure it obtained such that WIMP interactions can be observed as an excess over the CE$\nu$NS background. (bottom right) the number of neutrino events detected between points (a) and (b) in the parameter space. This plot shows that the rate of excluding parameter space is minimal between $\mathcal{O}(100)$ and $\mathcal{O}(10^7)$ $^8$B CE$\nu$NS interactions. Figure reproduced from Ref [77] using code modified under a MIT licence [78] with experimental limits taken from Refs [76, 79–89].

## 2.7 Conclusion

In this chapter the evidence for dark matter, a missing component of the Universe, at astrophysical and cosmological scales is presented. To explain these observations an as-of-yet undetected particle, known as a WIMP, which could exist in the Cosmos as a thermal relic from the early Universe is described. Using classical scattering kinematics the differential recoil spectra of such a particle is calculated assuming a spin-independent interaction. The relative performance of argon and xenon detectors to detect WIMPs is naively compared for serval WIMP masses by computing their relative interaction cross-sections and recoil spectra including DEAP-3600's and LZ's measured signal efficiencies. The CE$\nu$NS process by which neutrinos can coherently scatter of nuclei is discussed focusing on its presence as an irreducible background and how it can be used to validate the performance of WIMP detectors through the observation of $^{8}$B solar neutrinos.

With the presence of dark matter established and the physics goals of WIMP detectors outlined, the two-phase noble gas TPC detector is introduced, focusing on its design and operation. This discussion focuses on the scintillation (S1) and ionisation (S2) signals produced in these detectors, culminating in a discussion of the charge and light yields of xenon detectors, their ability to discriminate nuclear and electronic recoils, and how they can reconstruct events in 3D.

Finally, the state of the field prior to the current generation of tonne-scale LXe TPCs is presented alongside a discussion of how the neutrino fog will affect ever larger and more sensitive detectors.

# 3

# The LUX-ZEPLIN (LZ) Experiment

This chapter gives a general overview of the design, operation and current status of the LZ experiment including the recent world-leading WIMP result. Topics of broad relevance, such as those outlined above, are only outlined whereas areas connected to, or necessary for, the work detailed later in the thesis (such as PMT operation, software, and calibrations) are described in greater detail.

Naturally this section details work carried out by the whole LZ collaboration. I contributed to the skimming framework outlined within this chapter, performed the double photoelectron emission (DPE) calibration discussed here, and is the focus of Chapter 4, and was responsible for designing and performing the Data Centre study in Section 3.3.

## 3.1 The LZ experiment

LZ is a currently operating direct detection dark matter experiment hosted by SURF. The successor of the highly-successful LUX and ZEPLIN-III experiments [70, 90], LZ is a multi-tonne two-phase xenon TPC and is the largest such detector to date. LZ has been designed to search for WIMP dark matter but is also sensitive to other physics including neutrinoless double-$\beta$ decay ($0\nu\beta\beta$), axion-like particles (ALPs), and astrophysical neutrinos [91–95].

To reduce the muon flux reaching LZ, the experiment is situated 4850 ft underground within the Davis cavern. At this depth the vertical overburden of 4.3 ± 0.2 km w.e reduces the muon flux by a factor of $3 \times 10^6$ relative to that at the surface [72]. Recent measurements by the Majorana demonstrator experiment, also at the 4850 ft level, have observed a muon flux of $(5.31 \pm 0.17) \times 10^{-9}$ μ/s/cm$^2$ which is similar to previous calculated rates [96, 97].

The experiment is composed of three detector systems: the inner LXe TPC, the LXe skin, and the gadolinium-loaded liquid scintillator (GdLS) outer-detector (OD), shown in Figures 3.1a and 3.1b. The TPC is used to detect WIMPs scattering off xenon atoms whereas the skin and OD are anti-coincidence veto systems for background mitigation and characterisation. To optimise LZ's sensitivity to WIMPs significant effort was made to reduce the background rate originating from detector components though material assay and selection. This campaign facilitated the use of low background materials in construction and informed the expected background model of the detector [98].

The operation and monitoring of the LZ experiment requires several additional subsystems including xenon circulation, xenon purification, detector calibration, high-voltage equipment, conduits, data acquisition equipment, and detector cooling apparatus.

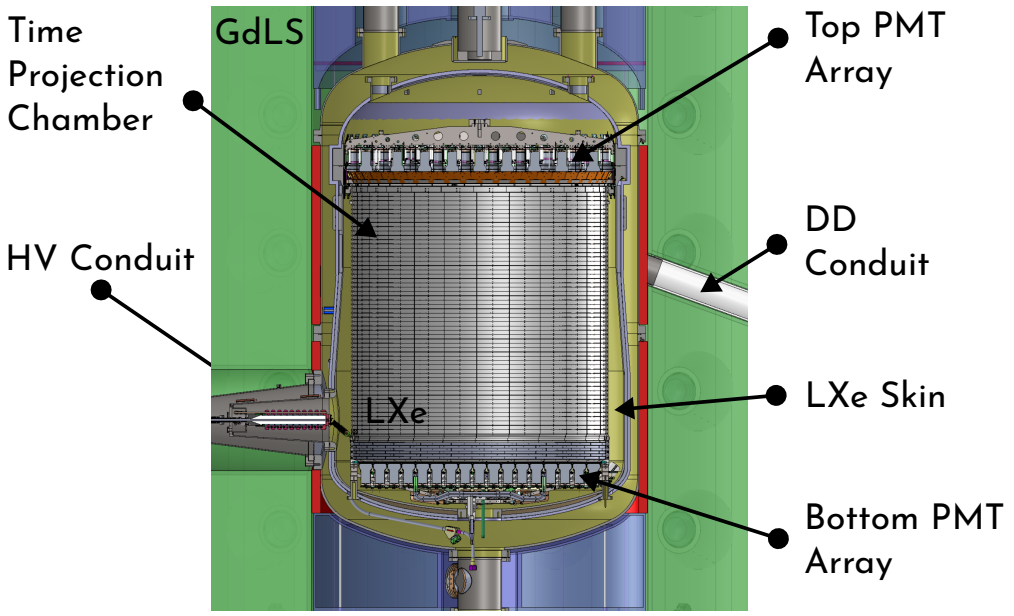
### 3.1.1 TPC design and operation

The xenon detector system is composed of a LXe TPC housed within an ultrapure titanium vessel, henceforth referred to as the inner cryostat vessel (ICV). To maintain the detector at the low temperatures (~175 K/—100 °C) required to liquify xenon, the ICV is thermally decoupled from the environment. This decoupling is achieved by operating the ICV within a vacuum space inside an outer cryostat vessel (OCV), also built from ultrapure titanium.

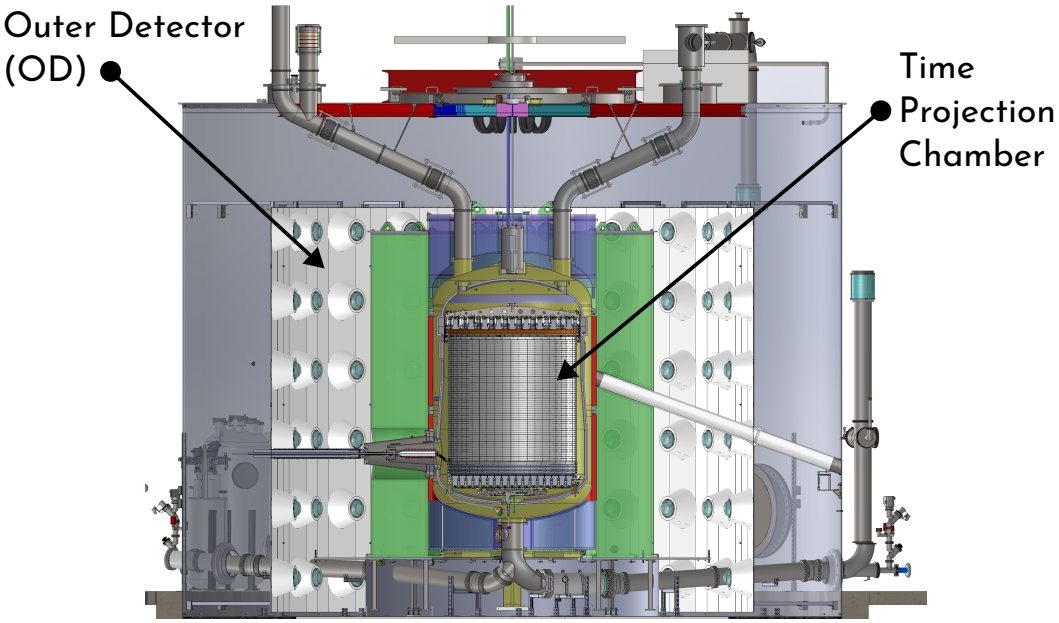
The central TPC contains approximately 7 tonnes of active LXe within a ~1.5 m tall × ~1.5 m diameter cylinder. The design of LZ is most similar to its predecessor LUX: with a large bulk volume; Polytetrafluoroethylene (PTFE) walls, which are highly reflective to VUV light [99]; two arrays of ultra low-background PMTs; and four custom-made woven stainless steel electrode grids.

The upper pair of grids (anode, gate), which define the extraction region, are used to generate a strong electric field to extract ionisation electrons across the liquid surface and produce electroluminescence in the vapour. To maintain the position of the liquid surface between the gate and anode, a weir system is used which spills any excess xenon into an external xenon handling system for purification. The middle pair of grids (gate, cathode), which define the drift region, generate an electric field to drift electrons to the liquid surface. The final (bottom) grid provides a grounding plane above the bottom array PMTs to negate the electric field across the photosensors. More details of the design, construction, and testing of these electrode grids can be found in Ref [71].

To maintain the xenon target in the liquid state the TPC is operated at approximately 172 K (—101 °C). To maintain this temperature the thermally decoupled ICV is cooled using a set of thermosyphons mounted at the liquid level. These syphons remove heat from the ICV to a liquid nitrogen bath housed above the water tank. The nitrogen boil-off from the bath, produced from the added heat, is condensed using a cryocooler thereby storing the heat into a chilled water system.




(a) CAD visualisation of the LZ TPC, skin, OCV, and GdLS filled acrylic tanks. To connect the heavily shielded TPC to the lab control systems (Data Acquisition (DAQ), high-voltage power supplies) and deuterium-deuterium (D-D) neutron generator requires several interfaces and conduits including the HV and acdd conduits labelled here.




(b) CAD visualisation of the LZ experiment highlighting the external water tank and the gadolinium loaded liquid scintillator outer detector. This GdLS filled acrylic vessels' acts as a neutron veto system by detecting $\gamma$-rays produced during neutron capture on hydrogen and gadolinium using PMTs mounted on the water tank walls. The rest of the OD is composed of a water tank which provides extra shielding.

Figure 3.1: CAD visualisations of the LZ experiment focusing on the central TPC detector system and its interfaces to the detector control and operating systems and the outer detector which is employed primarily as a neutron veto system.

Due to electrostatic considerations, a dielectric stand-off is required between the TPC and grounded ICV. In LZ, this volume, known as the skin, is filled with liquid xenon due to its high density and purity. The xenon within the skin will produce scintillation light from particles such as neutrons and $\gamma$-rays. To improve external background rejection of such particles, the skin was instrumented with 131 PMTs to act as an anti-coincidence veto system.

Research grade xenon is usually contaminated with 100 parts-per-billion of $^{85}$Kr, a radioactive fission product present within natural Kr. To remove the contaminants, the xenon is purified using a charcoal chromatography system operated at the SLAC National Accelerator Laboratory (SLAC). Using this krypton removal system the xenon was purified to a $^{85}$Kr contamination of 0.3 parts-per-trillion [72, 100].

The xenon can also be contaminated with electronegative impurities such as $H_2O$ and $O_2$. These impurities capture drifting electrons leading to a reduction in the S2 signal size as a function of drift time/length, as described in Equation 2.29. If the electron lifetime, the mean electron capture length, is short low energy signals, with small S2s, may be completely captured and never detected.

To improve the electron lifetime in LZ the xenon is purified continuously of electronegative impurities with a circulation time of around 2.4 days for the total 10 tonnes xenon payload. In LZ this is accomplished by recirculating the xenon though a zirconium getter, operated at 400 °C, which captures impurities with a single-pass efficiency of greater than 99% (depending on flow rate and temperature) though chemical bonding [101]. Recirculation is achieved by removing liquid the detector via the top of the TPC using a weir system. The liquid, now outside the detector, is then passed through a two-phase heat exchanger coupled to a zirconium getter used to purify the vaporised xenon. The purified vapour is then condensed by the heat exchanger and injected into the TPC and skin with the flow to each system controlled independently.

Detector components, such as PMT cables and feedthoughs, within the detector will emanate $^{222}$Rn, the progenitor of the dominant backgrounds in LZ. As the zirconium getter, outlined above, removes contaminants via chemical bonding it has no power to remove inert noble elements, such as $^{222}$Rn, from the xenon. In LZ an activated carbon trap is used to remove radon, with a design efficiency of 90%, from gaseous xenon, via physical adsorption, using the

methodology demonstrated by XMASS [74]. This in-situ radon removal is applied to gaseous xenon syphoned from the xenon vapour at the top of the TPC. The syphoned gaseous xenon is passed though the charcoal trap and into the recirculation system, outlined above, before the zirconium getter and injected back into the detector via the recirculation system.

As the TPC resides within several layers of material designed to shield the detector from external backgrounds several calibration systems are required to access the central detector. Calibration sources in LZ exist in four categories: internal, radioactive isotopes mixed into the liquid; calibration source deployment (CSD), $\gamma$-ray and neutron sources deployed between the inner and outer cryogenic vessels; external, sources situated outside the water tank; and optical, LED located within the TPC, skin, and OD to monitor PMT performance.

The internal sources are injected into the xenon circulation line and allowed to mix with the xenon inside the TPC. These calibration sources are used to map out the entire TPC geometry to develop the LZ detector response model. Injected sources include tritiated methane ($CH_3T$), $^{83m}$Kr and $^{220}$Rn.

The external sources in LZ are composed of two types: a deuterium-deuterium (D-D) generator and a YBe photo-neutron source. The D-D source, which sits outside the water tank, is primarily used to calibrate LZ's NR response model. To permit neutrons to travel from outside the water tank to the TPC two conduit systems were built. Each conduit system connects the water tank wall to the OCV and during WIMP search (D-D calibration) the conduits are filled with (evacuated of) water. Two conduit systems are built to calibrate different parts of the TPC: the first connects horizontally to the TPC just below the liquid surface, and the second connects to the TPC at a greater depth at a shallow inclination angle. Each of these conduit systems has two input tubes with different diameters allowing optimisation of neutron flux or collimation. The photo-neutron source is used to perform low-energy (at threshold) neutron calibrations of the detector. Housed within a tungsten alloy 'pig', the source is deployed directly above the OCV by evacuating the water in a small volume above the detector. Due to the short mean free path of low energy neutrons this source can only be used to calibrate the top of the detector.

The CSD sources are deployed between the OCV and ICV using three conduits accessible from above the upper deck of the Davis cavern. Operated using a stepper motor controlled cable

and laser range finder, the CSD tubes are used to deploy neutron and $\gamma$-ray sources including AmLi, $^{22}$Na and $^{228}$Th. Applications of these sources include calibrating the OD energy scale, synchronising the skin and TPC detectors, performing high-energy calibration of the TPC for $0\nu\beta\beta$ searches, and performing neutron calibrations at any height relative to the TPC.

To measure each PMT's single photoelectron (SPE) response and to monitor any degradation in PMT performance each detector has a blue (470 nm) LED calibration system. The TPC contains 48 LEDs with 24 located in each array each of which points to the opposite array. The skin contains 25 LEDs with 12 in the top side array and 13 in the bottom side array. The OD contains 35 LED driven optical fibres, known as the Optical Calibration System (OCS), split between the PMT support structs (30 fibres) and below the bottom tank (5 fibres). To enable triggered analysis of LED data the synchronised LED trigger is passed to the Data Acquisition (DAQ) to be recorded alongside the PMT data.

### 3.1.2 PMT Design and Operation

Photomultipler tubes (PMTs) are used as the sole photosensor LZ. Between the three detector systems (TPC, Skin, and OD) four PMT models are used. In this section a brief overview of the LZ TPC PMTs is given including a description of photon detection using PMTs.

#### 3.1.2.1 Choice of TPC PMT and their design

The TPC PMTs used in LZ are custom Hamamatsu R11410-22 PMTs which are based upon the commercially available R11410-20 model designed for radiopurity and operation at low temperature [102]. This PMT has been popular in the field having been used in XENON1T and acts as the base for XENONnT's R11410-21 PMTs [103, 104]. The R11410-20 base model was chosen for LZ due to its ultra-low background design and high (32 ± 3%) QE for VUV at LXe temperatures [72, 105]. To achieve this the R11410-20 PMTs are fitted with quartz windows, which provide good sensitivity to VUV light, and bialkali photocathodes optimised for operation at low temperatures [106]. The LZ specific R11410-22 model, developed in partnership with Hamamatsu, was designed for minimal radioactive contamination (factor of 1,000 less radioactivity than the base model) and to reduce spurious photon emission from internal structures [72]. For these reasons the XENON1T and XENONnT experiments' also based their R11410-21 PMTs on the R11410-20 model. Between the LZ and XENON experiments the R11410-20 derivatives PMTs have been subject to a variety of quality control and characterisation

measurements including: after-pulsing, gain, single photoelectron (SPE) resolution, double photoelectron emission probability, dark rate, and background rate measurements at both ambient and LXe temperatures [104, 105, 107–109].

#### 3.1.2.2 Detection Principles of PMTs

Figure 3.2 shows several detection topologies for PMTs. The standard detection topologies for PMTs are SPE and DPE emission, where a single photon is detected though the production of one or two photoelectrons from the photocathode. Sometimes the photon can miss the PMT's photocathode and strike a dynode or the photoelectron can scatter within the PMT, these rare topologies cause non-standard detection responses and are normally ignored in most analyses. Finally, it is possible for PMTs to record signals without an incident photon, called dark counts, or from ions of residual gases within the PMT; called afterpulsing. These effects are measured and accounted for in LZ analyses.

In the next few sections the standard response of PMTs to photons (SPE and DPE) are detailed alongside the dark count and afterpulsing topologies.

#### 3.1.2.3 Single photoelectron emission response

PMTs detect photons using the photoelectric effect. When a photon hits the photocathode it can produce a photoelectron with some QE, here denoted by $\eta$. Using a series of dynodes the initial photoelectron is amplified via secondary electron emission. At the end of the dynode chain, the amplified signal is read out from the anode. Standard methods to quantify the observed signal include quoting the integrated charge of the signal or to return the voltage as a function of time at some fixed sampling rate.

The measured integrated charge from SPE detection in R11410-22 PMTs can be modelled as a positively truncated normal PDF, $f(x|\mu_{SPE}, \sigma_{SPE})$, which can be written as

$$f(x|\mu_{SPE}, \sigma_{SPE}) = \begin{cases} \frac{1}{1-\text{erf}\left(\frac{-\mu_{SPE}}{\sqrt{2}\sigma_{SPE}}\right)} \times \mathcal{N}(x|\mu_{SPE}, \sigma_{SPE}) & x \geq 0 \\ 0 & x < 0 \end{cases} \tag{3.1}$$

where $\mathcal{N}(x, \mu_{SPE}, \sigma_{SPE})$ is the normal distribution PDF, $\mu_{SPE}$ is the mean integrated charge of an SPE response, and $\sigma_{SPE}$ is the standard deviation of the integrated charge. Typically,

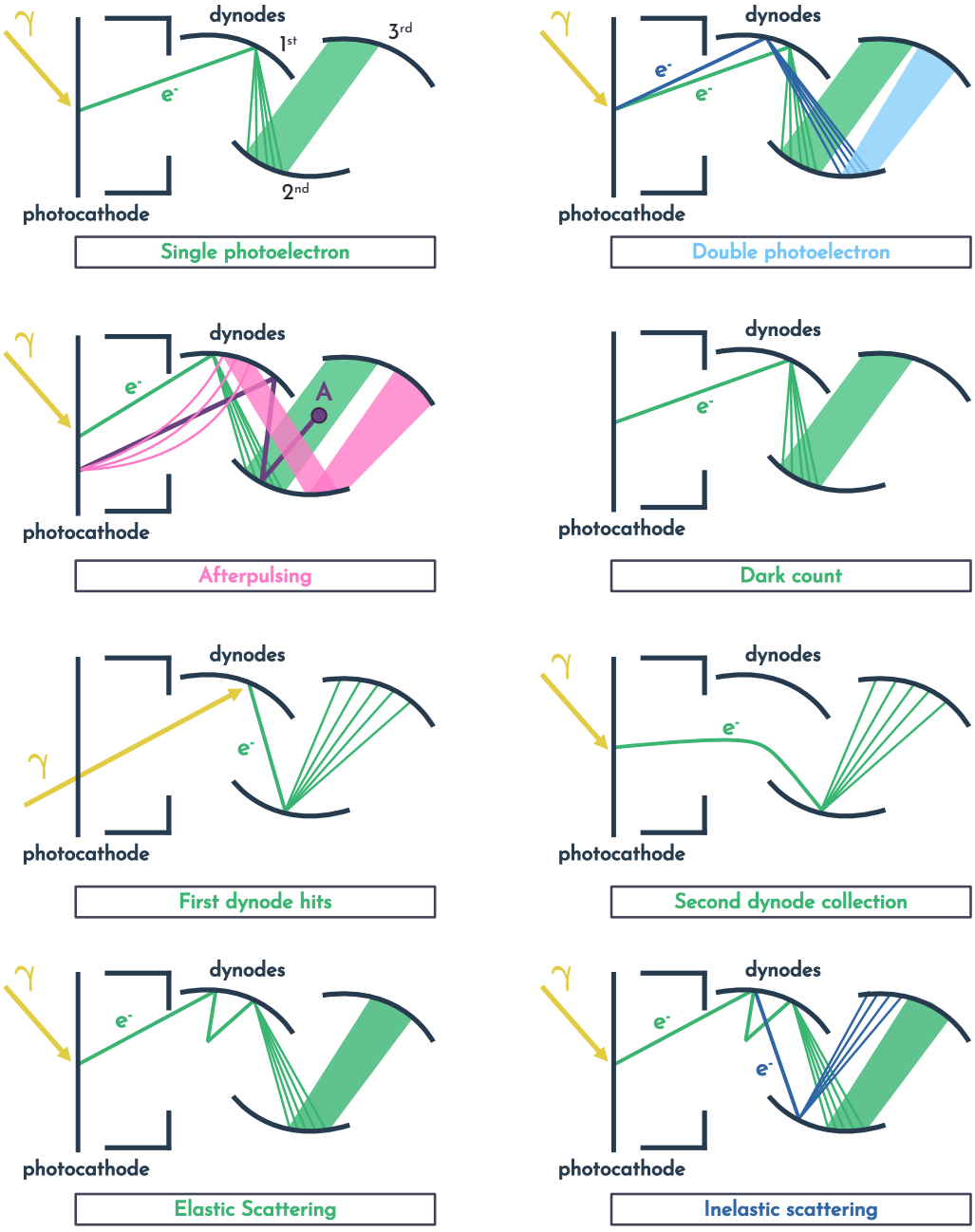



Figure 3.2: Possible photon detection mechanisms for PMT photosensors. The first row shows the standard detection mechanisms considered in LZ. The second row shows two sources of background/contamination taken into account in LZ analyses. The third and fourth rows show other detection mechanisms not typically considered in LZ. Figure adapted, with permission, from Ref [110].

though not in LZ, the PMT pulse area (integrated charge) is quoted in units of photoelectrons (phe), where $\mu_{SPE} = 1\,\text{phe}$, and not integrated charge (pVs).

#### 3.1.2.4 Double photoelectron emission response

Whilst it is commonly assumed that a single photon striking the photocathode will produce zero or one photoelectrons, this is not universally true. In 1988, it was observed that single VUV photons incident on multialkali photocathodes can lead to the emission of two electrons in what is now called the DPE effect [111]. The first photoelectron is produced via the photoelectric effect, as is the case for SPE production, and the second "photoelectron"[1] is produced by impact ionisation

$$e^- + A \rightarrow A^+ + e^- + e^- \tag{3.2}$$

where a charged particle imparts enough energy to liberate a bound electron.

This process, which occurs with a probability $P_{DPE}$, was largely unnoticed by the HEP community until it was recently observed in Hamamatsu's R8778, R8520, and R11410 PMT; these models have or will be used in the LZ, LUX, Panda-X, XENON10, XENON100, XENON1T, and XENONnT experiments PMTs [112]. With knowledge of this process, dedicated measurements of the DPE probabilities of several LZ R11410-22 PMTs operated at LXe temperature, were performed at Imperial [108].

If a photon is detected via DPE emission, the two photoelectrons will be emitted almost simultaneously from the same point on the photocathode leading to simultaneous detection. The observed signal from a PMT DPE detection has, on average, twice the amplitude and integrated area of a SPE detection. This leads to a more complicated double truncated normal pdf for the PMT single photon response

$$g(x|\mu_{SPE}, \sigma_{SPE}, P_{DPE}) = (1 - P_{DPE}) \times f(x|\mu_{SPE}, \sigma_{SPE}) + P_{DPE} \times f(x|2\mu_{SPE}, \sqrt{2}\sigma_{SPE}), \tag{3.3}$$

where the first (second) term denotes the SPE (DPE) response. The DPE term is defined as having double the mean and variance of the SPE response. As the DPE effect breaks the one-to-one correspondence of detected photon to photoelectron this effect should be taken into account to when reconstructing the number of detected and initial quanta. In LZ this is

[1] This electron is not truly a photoelectron as it is not produced though the photoelectric effect

accomplished by quoting pulse areas in units of the mean integrated charge of an incident photon. This area, in units of photons detected (phd), is defined as

$$A[\text{phd}] = \frac{A[\text{phe}]}{1 + P_{DPE}}, \tag{3.4}$$

where $1 + P_{DPE}$ is the mean number of photoelectrons emitted per photon.

Measurements of the DPE probability as a function of wavelength were performed at Berkeley for three PMT models, including the R11410-20 design adapted for LZ. This study, conducted using a single PMT of each model, demonstrated a smooth transition between SPE-only and SPE–DPE responses for wavelengths below ~250 nm [109].

Due to the DPE effect there is ambiguity in Hamamatsu's quoted QE measurements. Hamamatsu define QE as the 'number of photoelectrons emitted from the photocathode divided by the number of incident photons' [113]. By this definition the probability of detecting an incident photon is not the Hamamatsu QE ($\eta_H$) but is instead

$$\eta = \frac{\eta_H}{1 + P_{DPE}}. \tag{3.5}$$

Because of this the Hamamatsu quoted QE must be corrected for use in LZ and other LXe detectors. In the absence of the DPE effect, which is the standard case in most experiments, these two definitions are equivalent.

During the LZ quality control programme, a dedicated measurement of the DPE probability for a subset of 35 LZ PMTs was performed at Imperial. Each PMT had its DPE probability measured both at room temperature and at −94.4 °C (LXe temperature). The DPE probability of each PMT, at low temperature, was found to loosely follow a linear model,

$$P_{DPE} = \alpha + \beta \times \eta_H \tag{3.6}$$

where $\alpha$=0.048 ± 0.003 and $\beta$=0.54 ± 0.01, with a sample mean 22.6 ± 0.2% [108].

#### 3.1.2.5 Afterpulsing

Afterpulsing occurs when a photoelectron ionises residual gas atoms inside the PMT. Ions produced close to the input optics drift along the electric field and strike the photocathode

producing many "photoelectrons". These coincident "photoelectrons" are amplified back down the dynode chain producing a very large, ion dependant, pulse with the same shape and width as photon detection. In the LZ PMTs the time between the atom being ionised and striking the photocathode is a constant dependent on the mass/charge ratio of the ion [114]. Using these characteristic ion dependant time delays, $\mathcal{O}(\mu s)$, and pulse areas, afterpulsing events can be selected, characterised, and separated from the initial detected photon.

#### 3.1.2.6 Dark Counts

Dark counts are the random emission of single photoelectrons, with some rate $r_d$, from the PMT photocathode without an incident external photon. Sources of dark counts include thermionic emission and scintillation from internal PMT components [113]. Dark counts perfectly mimic photon detection via SPE emission, but cannot mimic DPE emission. If several dark counts are detected in coincidence they will mimic an S1 pulse.

If a fake S1 pulse from dark count pile-up across several PMTs is accidentally paired with an unrelated S2 the event will be reconstructed as an accidental single scatter. The number of these accidental events within a specific time-window can be calculated using Poisson and binomial statistics. If there are N PMTs each with a dark rate $r_d$ of $\mathcal{O}$(10 Hz), then each PMT should on average observe $r_d t$ events over a time period t. This $r_d t$ term defines Poisson distribution $P(n|s = r_d t)$, where the probability of detecting at least one dark count within a time t is

$$P(DC|t) = 1 - P(0|s = r_d t) = 1 - s\, e^{-s}. \tag{3.7}$$

By treating the event window as M contiguous blocks of time t, the probability of observing one-and-only-one fake S1, with a coincidence of at least K PMT hits, within one drift length before an S2 can be calculated, using a binomial model.

The probability of producing a fake S1 from dark count pile-up before an isolated S2, assuming three different full drift-lengths, is shown in Figure 3.3. By assuming an isolated S2 rate of 1 mHz, consistent with the 0.5 mHz and 2.6 mHz observed in LUX [115] and XENON1T [116] respectively, the expected rate of fake single scatters can be calculated. Using a 3-fold S1 requirement we expect less than one event per 1000 live-days from dark count pile-up accidentals for all but the most pessimistic and unrealistic of models.

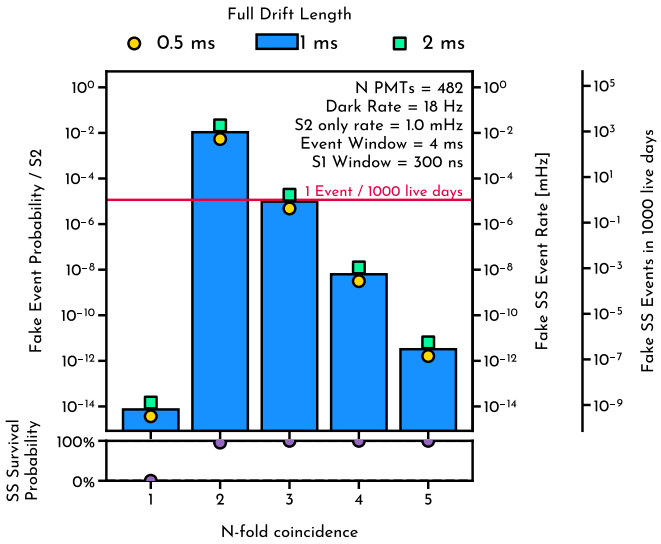



Figure 3.3: (Top panel) The probability of a fake single scatter event due to S1s from dark count pile-up per S2 pulse. Calculated assuming 482 operational LZ PMTs each with a dark rate of 18 Hz for 0.5 ms (yellow circle), 1 ms (blue bar), and 2 ms (green square) full drift-lengths. By multiplying by an assumed isolated S2 rate of 1 mHz the rate of fake single scatter events is calculated alongside the number of fake events in 1000 live days. (Bottom panel) The probability of a genuine single scatter event not being contaminated by a fake S1 which would exclude the event from being a WIMP candidate.

## 3.2 Particle Detection in LZ

As detailed in Section 2.5, two-phase xenon TPCs detect interactions via two signals: scintillation and ionisation. Both of these signals are detected using the amplified readout voltage of the TPC PMTs housed in the two PMT arrays. To improve the dynamic range of the LZ TPC PMTs they are readout using a dual-gain system. The low gain amplifies the signal by a factor of four with a 30 ns shaping-time constant; whilst the high gain amplifies the signal by a factor of 40 with a 30 ns shaping-time constant. The amplified PMT signals are constantly written to circular buffers at a rate of 100 MHz (10 ns sampling) at a resolution of 14-bits. The current contents of these circular buffers can be written to disk on request if a trigger condition is met. The most common trigger employed in LZ is an S2 filter trigger which activates for S2 signals larger than a few electrons. Other triggers include a periodic (1 Hz) and random triggers which enable the study of the background behaviour of the detector.

To reduce the amount of data written to disk LZ, like LUX [117], only writes out PMT responses from the circular buffer above some threshold in what is known as pulse-only digitisation

(POD). In LZ this reduces the data volume by a factor of 50 [72]. For analysis and visualisation the sum of all PMT POD waveforms are used, though channel level PODs are available for analyses if required.

Figure 3.4 shows a 14 keV single scatter event from tritium decay inside the TPC. Column A in Figure 3.4 shows the raw TPC signals observed by LZ. The top panel shows the characteristic S1-S2 single scatter pattern alongside the time separation between the two pulses which is the drift time of ionisation electrons from the interaction site to the liquid surface. The bottom panel focuses on the individual summed S1 and S2 pulses. Here the difference in shape between the two types of pulse is obvious: the S1 pulse defined by a sharp rise time followed by a long tail; the S2 pulse defined by a broad symmetric pulse produced by the convolution of the electroluminescence region response(approximately a rectangular pulse) with the normally distributed longitudinal diffusion of the ionisation electrons. In columns B and C, the ability to reconstruct the position of the event in 3D is demonstrated. Column B shows the spread of the detected S2 light across both PMT arrays. Using the distribution of light in the upper array the (X, Y) position of the event can be reconstructed using the PMT weighted centroid position or using the Mercury algorithm originally developed for ZEPLIN-III [118]. In column C, the drift-time (Z) and S2 (X, Y) reconstructions are used to locate the interaction vertex in (X, Y, Z) for the purpose of background rejection via financialisation.

### 3.2.1 Offline Software

Data taken by the LZ DAQ system is stored as raw digitised POD waveforms in units of ADC counts. The offline software handles the conversion of the data into more analyser-friendly formats which includes the application of various software-level corrections.

#### 3.2.1.1 LZap

LZap is an event processing tool built on the Gaudi [119] framework and is used to convert raw LZ waveform data into analyser friendly observables called reduced quantitys (RQs). First, each channel POD waveform has time and amplitude/area corrections applied. The former is to time align every PMT, the latter converts the waveform amplitude from units of ADC counts to mV and then into phd/ns using calibration values. With each POD in phd/ns the pulse finder is applied returning contiguous POD samples that pass an S1 or S2 filter. The pulse parameteriser then calculates various pulse level quantities (amplitude, widths, integrated areas etc.) and

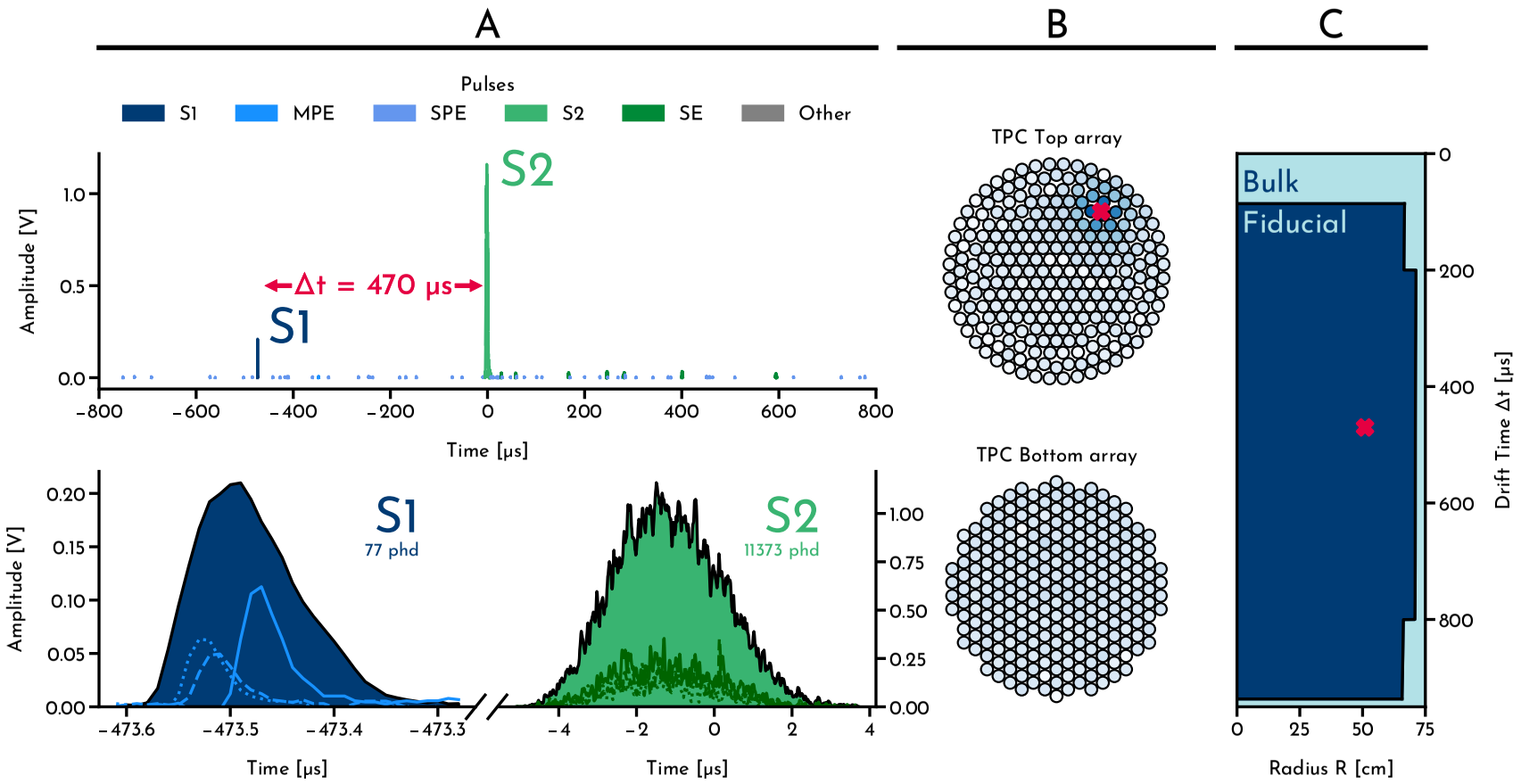



Figure 3.4: A 14 keV tritium decay interaction recorded by LZ including position reconstruction information (red). Column A shows the TPC response within 800 µs of the trigger. The top panel shows the summed waveforms from the TPC PMTs with the S1 (blue) and S2 (green) pulses labelled alongside the measured drift-time, a proxy for the Z position of the interaction. The bottom panel shows the summed S1 and S2 pulses in detail including individual PMTs waveforms which have been scaled up by a factor of ×10 for the S1 PMTs and ×2 for the S2 PMTs. Column B shows how the S2 light spread across the top array can be used for (X, Y) spatial reconstruction. Column C combines the depth (Z) and transverse (X, Y) position reconstructions to locate an interaction in 3D for the purpose of background rejection.

then classifies the pulse as one of six classifications: SPE, multiple photoelectron (MPE), single electron (SE), S1, S2 and other. Using these parameterised pulses the event builder constructs single and multiple scatters events. If an event has one significant S1 and one significant S2 then the event is a single scatter. If there is one significant S1 and multiple S2s then the event is a multiple scatter. The event builder then applies event level corrections including position-dependant S1 and S2 area corrections alongside more sophisticated corrections using the Mercury algorithm originally developed for ZEPLIN-III [118].

### 3.2.2 Computing centres

LZ data is stored and processed at two data centres: The United Kingdom data-centre (UKDC), hosted at Imperial, and the United States data-center (USDC), hosted by the national energy research scientific computing center (NERSC) at the Lawrence Berkeley National Laboratory in the USA. The two centres are based on different computational models: the UKDC uses grid computing where analyses are spread over many remote non-interactive compute nodes and sometimes spread over a large geographical area (e.g., across a country) and the USDC uses a high-performance computing (HPC) system where many compute nodes are directly attached to a login node. To provide computational redundancy, in case of shutdown (expected or otherwise) or degraded performance, all LZ analysis and data processing software has been designed to run at either data centre. In practice the two data centres are generally used for different purposes. The USDC is responsible for storing LZ's raw data to tape (long term storage), performing prompt (real time) LZap processing of data transferred from SURF, and most user data analyses. The UKDC is responsible for large-scale data reprocessing (running a new version of LZap over all acquired data) and large scale simulations however does also support user analysis.

#### 3.2.2.1 UKDC

Using the UK's existing GridPP infrastructure, the UKDC is based upon the highly successful distributed (grid) computing model [120, 121]. In this model the data is stored on an Imperial managed server, within a commercial data centre, and can be streamed from anywhere in the world using the XROOTD protocol and GridPP certificate authentication [122]. This storage solution had provided excellent uptime enabling continuous access to LZ data.

In addition to data-storage, GridPP enables users to perform large scale computations easily

and efficiently across the UK's GridPP compute nodes, including some dedicated nodes owned by LZ, via a job submission interface. To submit these jobs to GridPP compute nodes the DIRAC grid middleware is used [123]. Because the UKDC data-storage and computational nodes can be accessed from anywhere in the world the UKDC works on a bring-your-own basis where researchers will use their local university computing resources or computer to access and use the UKDC.

#### 3.2.2.2 USDC

For US computing needs, LZ uses the NERSC computing facility which maintains several HPC systems. During operations LZ has used the now decommissioned Cori and recently launched Perlmutter systems. As HPC systems are designed to run a wide variety of software for many research communities some virtualisation software is required to use standard high-energy physics (HEP) computing workflows on HPC systems. The uptime of the USDC has proved problematic at points with users experiencing frequent and sometimes unplanned outages validating LZ's support of two independent data centres.

### 3.2.3 Software distribution

As these two data centres use significantly different models there is the potential for significant differences in software deployment between the two centres. To minimise any difference LZ designed its software to work within a CENTOS-7 environment, common in the HEP community, and distribute official software releases using the CERN virtual machine file system (*/cvmfs/*) [124]. Using these systems users of UK computing resources can easily run official software without installing any software or requiring a specific local environment beyond CENOTS-7. The USDC cannot natively access /cvmfs/ nor is it compatible with any LZ software deployments built against a CENTOS-7 system. To provide a comparable environment virtualisation software packages such as Shifter or Singularity/Apptainer are used to run a CENTOS-7 docker image with /cvmfs/ access thereby mimicking the more standard setup found in the UK.

## 3.3 Data Centre and User Analysis Study

At the end of LZ's first science run (SR1), detailed in Chapter 5, a study of the UK computing resources was commissioned to better understand and compare the two centres from an analysers' perspective. This study, conducted in 2022, had two purposes: to document any and all differences in usability between the two data-centres and to benchmark the performance of interactive computing across LZ institutions in the UK. Interactive computing in this context refers to using a remote cluster's login node, rather than using the GridPP compute nodes via the DIRAC middleware. This workflow is common for the tuning and development of analyses and does not describe the workflow for large scale analyses using the UKDC and its GRID computing model. For current datasets LZ complete datasets can be analysed in an interactive mode at the USDC but not at the UKDC. As LZ collects data it is likely that US analyses will also have to use the local batch system bringing it in line with the UKDC.

Due to LZ's use of /cvmfs/ there is only one difference in running software at each data centre; on the UKDC users must have a valid grid proxy whilst on the USDC users must be within the required docker image. The real separation in user experience between these two data centres arises when scaling up analyses to larger datasets. In the USDC analysers are limited to using the same batch system whereas in the UKDC you can either use your local batch system or the GridPP compute nodes via Dirac. The extra steps required for the UKDC, either learning a batch system unique to your instruction or the Dirac middleware, has lead to some frustration for UK analysers. During in-person analysis workshops designed it became clear that a significant reason for users choosing to use one data centre over the other is their institutions local induction, with users staying with whatever they used first.

With the emergence of python as the language of choice amongst analysers an important aspect of a user's perception of usability is the ease of running Jupyter notebooks. The USDC provides an online portal to access Jupyter notebooks via Jupyter hub. Using this it is very easy for analysers to start working as soon as they join the experiment with almost no training. In contrast, users of the UKDC mostly have to run their own Jupyter lab server and forward the port to their computer. This extra step, whilst trivial provided the necessary experience, creates a significant barrier for new users thereby deterring users from using the UKDC more generally. The introduction of native Jupyter support within modern integrated development environments (IDEs) even across a secure shell (SSH) connection should lead to a natural

reduction of this barrier with time.

The simplest method to quantify UK interactive performance was to run the WIMP search data-selection and data processing steps at various sites, including NERSC, using $CH_3T$ calibration data. This tested several pieces of the LZ software stack and benchmarked the actual time taken to perform each part of the WIMP search analysis. The specific workflow for this study is shown in Figure 3.5.

First the list of files to be analysed was found using LZ's data catalogue. Next the first science run (SR1) WIMP analysis (skimmer) is run over the input file-list producing two files: The first file, known as a skim file contains the RQs (IDs) of all events passing the science-run one (SR1) WIMP-search cuts; the second file contains the raw file path and IDs of all events passing the cuts and can be used as an input for LZap to generate a new RQ file with the most recent LZap version. By using these two file the affect of any change in LZap can be easily studied using a Python script.

To execute this workflow on multiples clusters across the UK, at NERSC and in Coimbra (Portugal), the *snakemake* workflow management system was used [125, 126]. Snakemake allows the organisation of complicated workflows using a simple YAML description file and can produce benchmark statistics. Subjects in this study were required to: clone the analysis code, run the snakemake executable, and report the results for their cluster. There were only two differences between running this workflow at NERSC and at UK clusters: first, NERSC requires users to use Shifter to emulate a CENTOS-7 system; second, streaming data from the UKDC requires users to have a valid GRID proxy.

The results of the benchmarking study are shown in Figure 3.6. The Imperial cluster using XROOTD streaming and the NERSC facility (specifically the now decommissioned CORI computer) performed similarly for all tests. This is to be expected as both computer systems are accessing the data locally. The other UK and Portugal based clusters performed worse than Imperial when streaming data via XROOTD. This reduction in performance is approximately proportional to the distance from the Imperial cluster, located in a commercial data centre west of London.

The reduction in performance with distance from Imperial is more pronounced for the skimming framework than for LZap. This is attributed to the skimmer processing many low data-volume

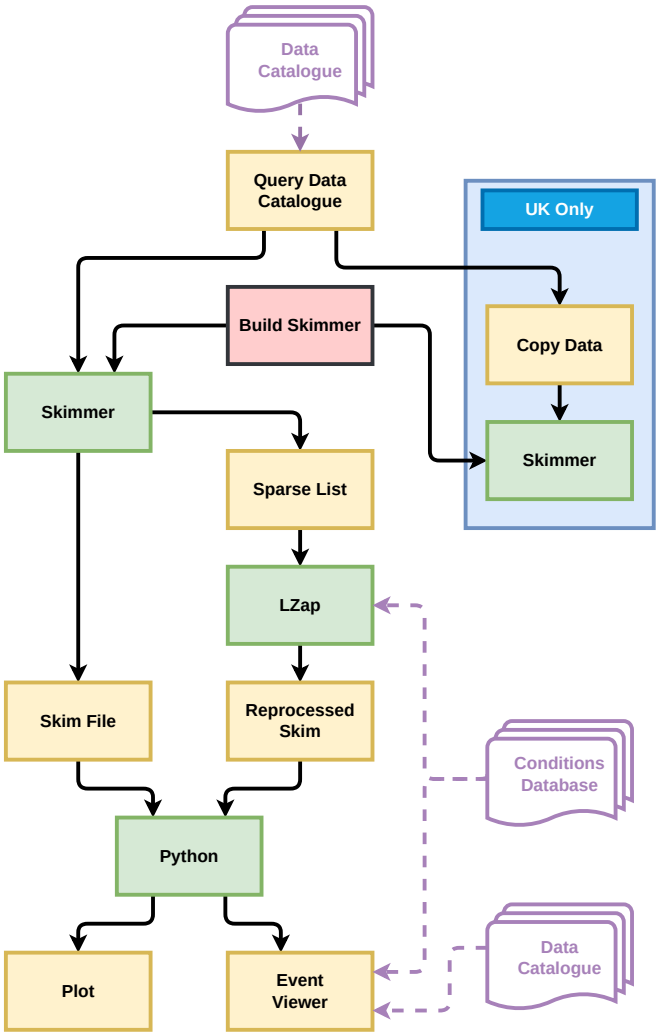



Figure 3.5: A standard LZ workflow used for benchmark tests. First tritium ($CH_3T$) calibration data is first found using the data catalogue and saved into a file. Next the filelist is analysed using the S1 WIMP search skimmer which produces two files a skimmed ROOT file and a LZap sparse list. This sparse list is then processed using LZap to produce a version of the ROOT skim file using the latest LZap version. Finally, the two versions of the skim files are compared in Python. For UK tests the analysis skimmer was also applied to data copied locally to investigate the effect of streaming data via XROOTD. To automate this workflow easily and efficiently on multiple computing clusters the *snakemake* package was used [125, 126]

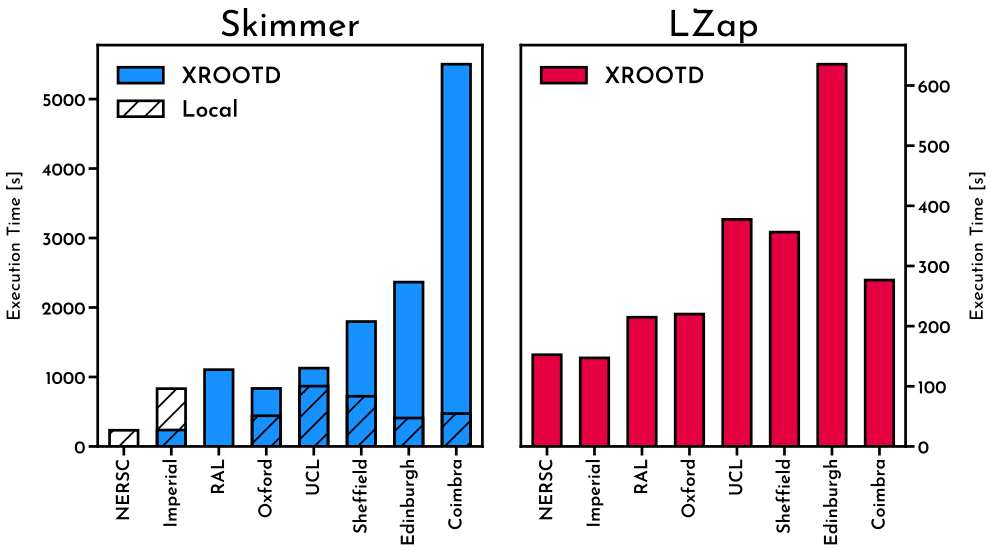



Figure 3.6: The results of the LZ benchmarks for several UK institutions, NERSC and Coimbra (Portugal). In the left plot the skimmer execution time is plotted for each site when accessing the data locally (black hatch) or via XROOTD from Imperial (blue) for the UK institutions and Coimbra. All the sites, apart for Imperial, are slower when streaming via XROOTD due to the slower network link to the DIRAC storage element than to the local high-volume network file system. In the right plot the execution time of the LZap stage is shown. For LZap the execution time varies less due to LZap being CPU dominated.

events, which quickly leads to the skimmer becoming network I/O limited. In contract, LZap spends far more time in significantly more complicated C++ analysis code limiting the impact of I/O on the execution time. When comparing the performance of different UK-based clusters using the skimmer with local data it is clear any differences in computation speed, due to local hardware and network speeds, are minor.

In this study it was demonstrated that there is only one minor difference for interactively running official LZ software between the two data centres. This was expected due to LZ's software deployment strategy but is none-the-less an import conclusion. Any difference in a user's perception of each data centres usability thereby originates from their initial training with analysers tending to use whatever centre is being used within the local group. When it comes to non-LZ software, the most significant difference in user experience is the ease of using Jupyter at each site. Currently, this is much easier at the USDC with its Jupyter hub deployment though modern IDEs should reduce this difference in time.

The raw (local data) performance of each UK cluster was found to be slightly slower than

the USDC but not enough to meaningful slowdown analysis. However, it is clear that some members of LZ in the UK encounter significantly worse performance when using streaming the data to their local computing resource. To improve the interactive analysis environment for these users located far away from London, LZ requested access to the Rutherford Appleton laboratory (RAL) cluster which provides a significantly quicker interactive environment than some of the more distance clusters. Using this cluster users are able to more efficiently perform data exploration to inform large scale computations using either Dirac or the USDC and have a contingency platform for analysis when the USDC is offline.

## 3.4 Conclusion

In this chapter the design and operation of the LZ experiment was described. Particular emphasis was placed on the TPC including details of the detector construction, xenon circulation and purification systems, and calibration systems. The TPC PMTs are described in greater detail with particular focus given to the possible photon detection topologies within PMTs. The DPE effect was described in particular detail due to its relevance to Chapters 4 and 6. With the detector described, the single scatter (S1–S2) event topology was discussed using a 14 keVee tritium decay as an example.

In addition to the physical detector and its operation, LZ's offline computing infrastructure is outlined, including relevant pieces of software, alongside a study comparing and contrasting UK and US computing resources. This study, designed and implemented by the author, demonstrates how LZ has managed to support both the HPC and GRID computing paradigms using /cvmfs/ and containerisation. In addition, this study established the core analysis software can become I/O limited when streaming data interactively. A recommendation of this study, which has since be implemented, was the procurement of interactive nodes at the Rutherford Appleton laboratory for specific institutions.

# 4

# Measurement of double photoelectron PMT response using $^{83m}$Kr

## 4.1 The DPE effect

It is usually the case that the response of a PMT to low light levels involves at most one photoelectron per incident photon. Each of these photoelectrons will produce a signal with some integrated area X sampled from some distribution $\mathcal{D}(\mu, \sigma)$ of mean $\mu$ and standard deviation $\sigma$. This function depends on the PMT model and has previously been approximated using Gaussian and Crystal Ball functions [108]. The number of photons detected by a PMT can be estimated as

$$\hat{N}_\gamma = \hat{N}_{phe} = X[phe] = \frac{X[pVs]}{\mu_{SPE}[pVs]}, \tag{4.1}$$

where $\mu_{SPE}$ is the mean response for SPE detections, and X[phe] is the integrated pulse area measured in units of $\mu_{SPE}$. Because of the above one-to-one correspondence the integrated area of a signal is often quoted as X[phe] as this directly provides the estimator of the number of detected photons.

When detecting VUV photons with PMTs this one-to-one relationship breaks down with $P_{DPE}$ of photons simultaneously producing two "photoelectrons" in what is known as the double photoelectron emission (DPE) effect [109]. In this mechanism, the first electron is a true photoelectron produced via the photoelectric effect, whilst the second electron is produced via impact ionisation ($e^- + A \rightarrow A^+ + e^- + e^-$) and it thus not a true photoelectron. With the addition of this effect the average number of photoelectrons emitted from the photocathode per $N_\gamma$ detected photons is

$$\langle N_{phe} \rangle = N_\gamma \times (1 + P_{DPE}). \tag{4.2}$$

By combining Equations 4.1 and 4.2, the estimator of the number of detected VUV photons can be written as

$$\hat{N}_\gamma = \frac{\hat{N}_{phe}}{1 + P_{DPE}} = \frac{X[phe]}{1 + P_{DPE}} = X[phd]. \tag{4.3}$$

In this form integrated areas quoted in units of "phd" naturally provide the estimator of the number of detected photons, analogous to using "phe" for detecting photons outside the VUV. For this reason LZ quotes all TPC and skin signals in units of "phd".

Like any other PMT parameter, $P_{DPE}$ can vary significantly from one PMT to the next, even for PMTs of the same make, model, and batch. This sample variation means the increase in the number of detected photoelectrons cannot be absorbed into a single detector level

correction, such as increasing the $g_1$ and $g_2$ parameters without some smearing of the detector response. Thus, event reconstruction must correct for this effect on a PMT-by-PMT basis. Unfortunately, PMT manufacturers do not measure this parameter during quality control, they instead measure an inflated quantum efficiency, $\eta_{\text{manu.}} = (1 + P_{\text{DPE}}) \times \eta_{\text{true}}$, only appropriate for photons below VUV energies.

To remedy these issues, the DPE probability has to be directly measured for all TPC and skin PMTs. Prior to installation all LZ PMTs underwent quality control assessment. For a subset of the TPC PMTs, henceforth referred to as the "golden" PMTs, this assessment included a dedicated measurement of the DPE probability at Imperial College London. This study observed a sample mean DPE probability of 22.6 ± 2.0% for PMTs operated at LXe temperatures (−97.4 °C) using recombination light from α-particle interactions in xenon gas [108]. As part of this study the DPE probability measured was observed to loosely depend on the manufacturer's, room temperature measured, QE as

$$P_{\text{DPE}} = m\eta + c, \tag{4.4}$$

where m = 0.45 ± 0.03 and c = 4.8 ± 0.1 %. This model enabled LZ to correct for the DPE effect in a reasonable manner prior to the in-situ measurement presented here. The remainder of this chapter will detail the in-situ measurement of the DPE probability for the TPC PMTs. All quantities in units of "phd" contained within this chapter use DPE probabilities calculated using Equation 4.4.

The simplest method to measure the DPE probability is to fit the magnitude of a PMTs response to single VUV photons using some model based upon Equation 4.7. In principle, either the amplitude or integrated area of the PMT response can be used: in practice, integrated area is almost always used as it suffers less from DAQ digitisation as integration averages out signal fluctuations. Naively, the simplest option would be to use pulses where only one PMT registers a response, however such detections are overwhelmingly originate from dark counts which do not produce DPE responses. The next best option is to use pulses which can be positively attributed to interactions in the xenon that produce few photons. For an interaction which produces some number of photons there is a probability $P_{\text{pile-up}}$ that multiple photons are detected at once. As the integrated area of two coincident SPE responses would perfectly mimic a DPE response, $P_{\text{pile-up}}$ must be both minimised and well understood.

### 4.1.1 Modelling photon detection as a Poisson process

Pile-up and the calculation of $P_{DPE}$ can be best discussed using a hypothetical "standard candle" source which always produces the same number of scintillation photons from exactly the same location. For a given PMT observing this candle, the number of photons detected within a time interval T is a random variable sampled from a Poisson distribution $P(n|\nu)$, where $\nu$ is the mean number of detected photons for that specific PMT. This parameter $\nu$, a proxy of the photon flux through the PMT, is proportional to the number of scintillation photons produced per event and the solid-angle containing the PMT window, effectively the proximity of the candle to the PMT.

To properly monitor and control photon pile-up requires the measurement of $\nu$. Due to their limited resolution, PMTs are unable to accurately count the number of individual photoelectrons emitted from the photocathode purely from a signal's integrated area. However, they are very successful at distinguishing between the presence and absence of photoelectric emission. Mathematically, this means the probability $P(n = 0|\nu)$, and its complement $P(n > 0|\nu)$, can be calculated but any other probability $P(n \neq 0|\nu)$ cannot be accurately obtained. Fortunately, the probability of zero detections,

$$P(0|\nu) = e^{-\nu}, \tag{4.5}$$

is sufficient to calculate the estimator of the mean number of detected photons,

$$\hat{\nu} = -\ln\left(P(0|\nu)\right) = -\ln\left(\frac{M}{N}\right), \tag{4.6}$$

for a population of N trials sampled from a "standard candle" source where M trials observe zero photoelectrons.

As Equation 4.6 is valid only for standard candle populations great care must be made to select a source of events with a small systematic variation in $\nu$. This in combination with minimising pile-up means that this analysis requires a low-energy source within a small volume far away from the PMT in question. Here, the low energy and far away volume minimise $\nu$ whilst the choice of a small volume minimises the spatial variation of $\nu$. This standard candle would enable photon detection to be treated as a Poisson process where for each event a single PMT sees either one or zero photons with the higher coincidence component heavily suppressed.

The best available calibration source to fulfil these requirements is $CH_3T$. This suitability was demonstrated in LUX where $CH_3T$ was used to measure the DPE probability after this effect was understood towards the end of operations [127]. Unfortunately, at the time of this study no $CH_3T$ calibrations had been performed and none were planned for the near future. The next best option available for this study was the $^{83m}$Kr source which was used for this work.

## 4.2 Calibrating with $^{83m}$Kr

$^{83m}$Kr is 41.9 keV monoenergetic calibration source which, when mixed throughout the LXe volume, permits the study of spatially dependent detector response at low energies near the WIMP signal region [128]. The LUX collaboration made prodigious use of this source using it to study the electric field; the relationship between the S2 reconstructed and real interaction vertices; and measure S1 and S2 spatially dependent correction maps [129]. The dispersed, monoenergetic, and low-energy nature of this source allows $^{83m}$Kr to approximate a standard candle when using spatial data-selection cuts to minimise the magnitude and spatial variation in $\nu$ on a PMT-by-PMT basis.

The $^{83m}$Kr source, produced by the decay of $^{83}$Rb, is added to the xenon circulation line by injecting xenon gas through a radon-pure charcoal infused with $^{83}$Rb. As a noble gas the $^{83m}$Kr passes though the circulation system unimpeded whereas any contaminants, including $^{83}$Rb, will be rejected by the getter.

$^{83m}$Kr decays via a two-stage process, as shown in Figure 4.1. The initial state decays with a 1.83 h half-life and deposits 32.1 keV as conversion electrons, Auger electrons and x-rays. The intermediate state has a half-life of 154 ns and deposits 9.4 keV via a pair of conversion and Auger electrons or via a $\gamma$-ray. Due to the short half-life of the intermediate state, the two de-excitations occur within the same event window with the two S1 signals often overlapping and the S2 signals always merged. For the fraction of events in which the two S1s can be time-resolved the first, higher energy, S1 is called $S1_a$ and second, lower energy, S1 is called $S1_b$. In LZ the mean $S1_b$ signal has an integrated area of 70 phd which when spread over the 482 PMTs leads to a naturally low $\nu$ per PMT.

To prevent $^{83m}$Kr events beings split into two datasets, one with one S1 and another with two S1s, the LZ analysis chain treats both cases (2 S1s & 1 S2 and 1 S1s & 1 S2) as single scatter

events. For standard analyses, in the absence of $^{83m}$Kr, the double S1 population can be trivially removed.

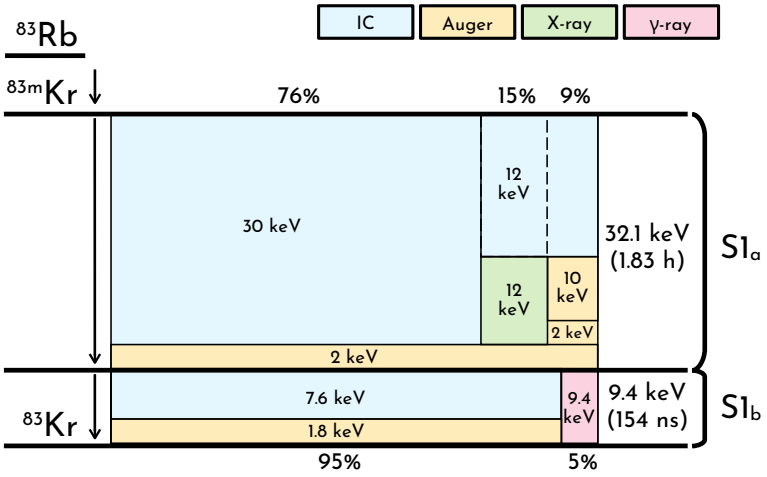



Figure 4.1: $^{83m}$Kr's two-stage decay scheme including transition types, energies, and probabilities. Figure adapted from Ref [129].

Waveforms from the decay of a $^{83m}$Kr radioisotope in LZ are shown in Figure 4.2. In this event the two S1s can be clearly time resolved. For each of the S1s the coloured individual PMT waveforms demonstrate that the majority of PMTs detect no more than one photon per S1, substantiating that $^{83m}$Kr is an eligible source for this study.

### 4.2.1 Detector conditions

During this $^{83m}$Kr calibration the detector was under stable operating conditions. At this time the average temperature of the top (bottom) PMT array was stable at −95 °C (−99 °C) with a full range variation of 0.04 °C (0.4 °C) as seen in Figure 4.3. The increased variation associated with the bottom array is due to the injection of warmer xenon into the bottom of TPC when deploying the $^{83m}$Kr source.

### 4.2.2 Pulse-level event selection

The spatial distribution of $^{83m}$Kr events used in this work, within a central volume of the TPC, is shown in Figure 4.4. In this calibration the $^{83m}$Kr remained close to the TPC walls throughout deployment with comparably few decays occurring within the central volume. This effect is in part due to the liquid flow configuration established early in operations and to the short half-life of $^{83m}$Kr leading to atoms decaying prior to reaching the centre of the detector.

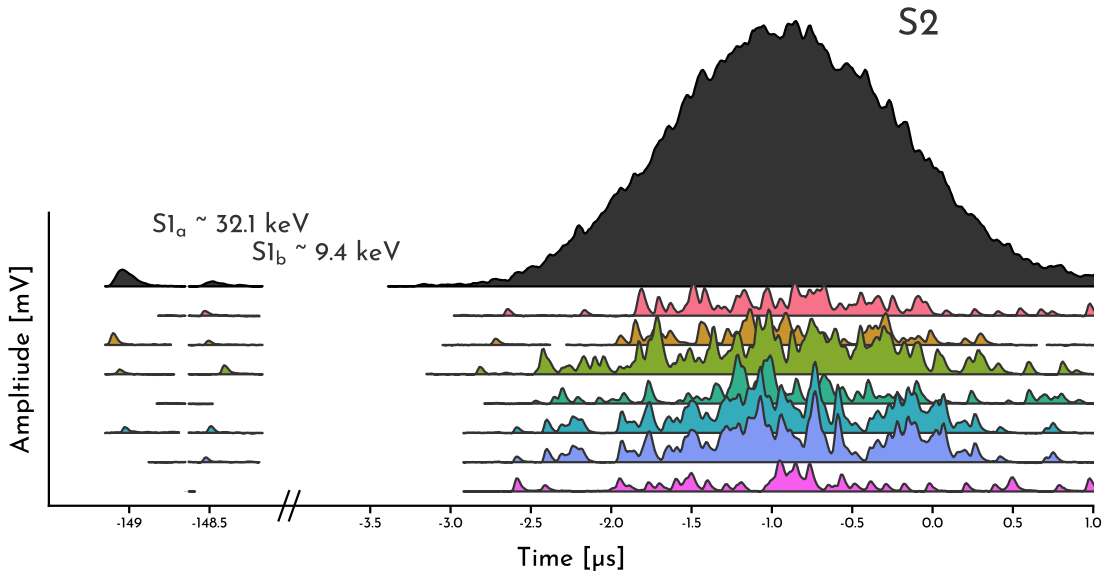



Figure 4.2: Summed (black) and individual channel-level (coloured) waveforms for a $^{83m}$Kr decay in LZ. Within the two S1 pulses the individual PMTs observe single photons which are used to characterise each PMT's single photon detection response.

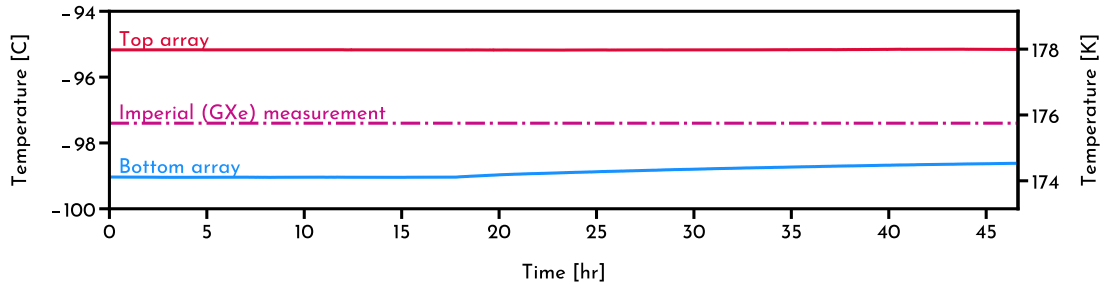



Figure 4.3: The temperature of the LZ top and bottom PMT arrays during the $^{83m}$Kr calibration, alongside the Imperial measurement's operation temperature.

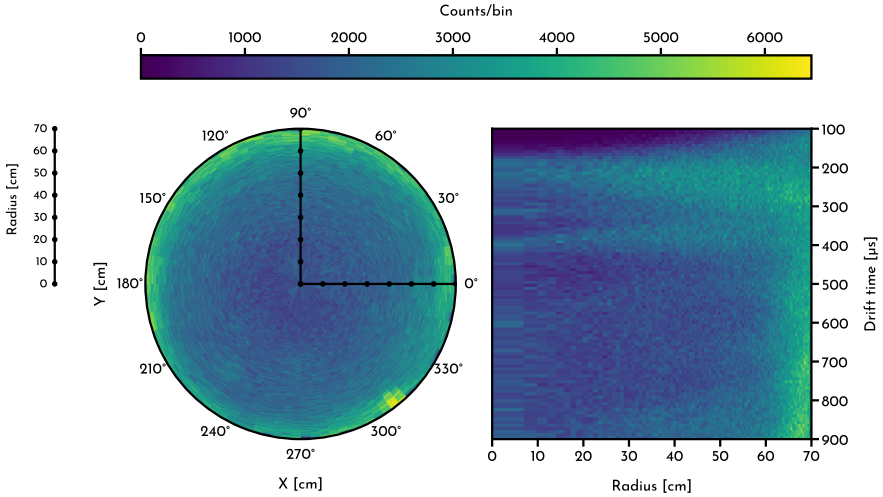



Figure 4.4: Spatial distribution of $^{83m}$Kr events used in this work. The region shown here is a central volume of the TPC. The spatial distribution observed here, with the events predominantly located at the large radii and in a band between 200 µs and 400 µs, is due to the physical distribution of the injected source. Whist the light detection efficiency does vary in position in LZ for interactions of these energies this only changes the relative size of detected signals and is insufficient to effect the overall S1 detection efficiency and measured spatial distributions.

As the majority of events are located at the bottom of the detector near the TPC wall, most of the S2s in this dataset require a maximal drift-time correction from the finite electron life-time and a large (X, Y) correction due to charge loss and reduced electroluminescence amplification at large radii. The S1 signals also have relatively large corrections due to the specific geometric effects originating from being near the corner of the TPC.

The half-life of the metastable state can be measured from the time between the $S1_a$ and $S1_b$ pulses as shown in Figure 4.5. This distribution obeys the exponential decay of the intermediate state's half-life multiplied by the efficiency of resolving the two pulses. Events with a separation less than 500 ns were removed from this analysis to remove any systematic effect originating from the pulse finding algorithm. By fitting this distribution the half-life of the intermediate state was measured as 154.5 ± 0.2 ns. This result, which only quotes a statistical error, agrees with previous measurements as shown in the right panel of the same figure.

The corrected and uncorrected $S1_a$, $S1_b$, and S2 signals from $^{83m}$Kr events are shown in Figure 4.6. For each population the distribution is fitted using a 2D Gaussian model shown in black. The uncorrected population represents the average number of photons detected per event. From this 0.14 (0.38) were detected on average per PMT for an $S1_a$ ($S1_b$) pulse. This spatially and

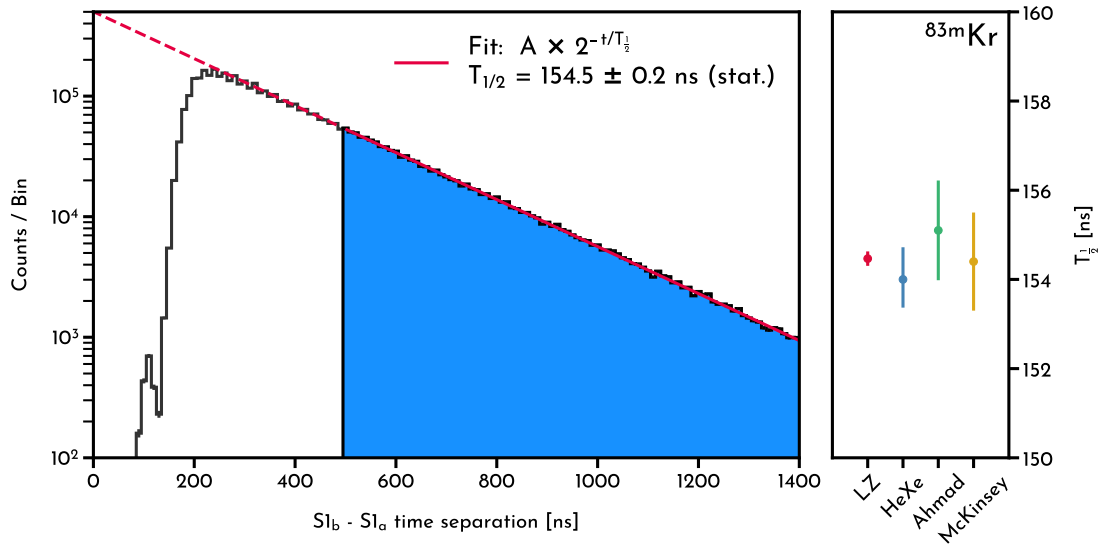



Figure 4.5: (Left panel) Fitted distribution of the 154.5 ± 0.2 ns half-life of the $^{83m}$Kr meta-stable state as measured by the separation between the $S1_a$ and $S1_b$ pulses. (Right panel) Comparison of LZ's measurement of the intermediate state's half-life (red) to previous results [128, 130, 131].

PMT averaged $\nu$ demonstrates than only 0.9% of PMTs are expected to detect more than one photon per $S1_b$ pulse according to the simple Poisson model.

Through the application of data-driven S1 and S2 correction maps the energy resolution of the $^{83m}$Kr population can be improved through the reduction of S1 and S2 variances. These more compact populations, also fitted using a 2D Gaussian model, enable a superior selection criterion for $^{83m}$Kr events.

To select the $^{83m}$Kr population two event-level data selection cuts were applied. First, an event must have two S1s and one S2, the corrected areas of which must reside within the all three populations shown in Figure 4.6. Second, the two S1s must be fully resolved with minimal overlap to produce a constant number of photons per pulse. This was achieved by requiring the two pulses to be separated by at least 300 ns and that the width of the $S1_b$ was near maximal.

On inspecting the $S1_b$ PMT level waveforms it was quickly apparent that many of the channels which where listed as having detected a photon (measuring an integrated channel area greater than 0.1 phd) had in fact detected nothing. This is somewhat surprising as PODded readout should only write out PMTs which observe a signal above the baseline noise. On closer inspection all of these fake detections were in PMTs which had detected a photon within the

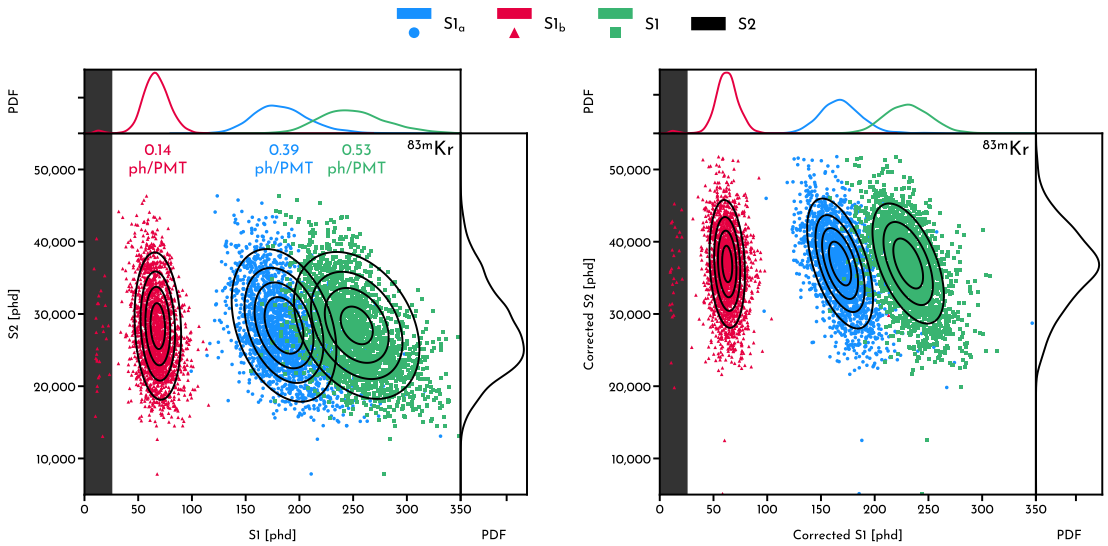



Figure 4.6: Distribution of $S1_a$ (blue), $S1_b$ (red), $S1_{total}$ (green), and S2 corrected pulse areas for $^{83m}$Kr decay events. The left set of panels show uncorrected pulse areas and represent the number of photon detected by the PMTs, whereas the right panels show the corrected areas taking into account geometric and other effects. The small $S1_b$ signals, located to the far left, are from the incorrect splitting of merged S1 pulses leading to much shorter, and smaller, $S1_b$ pulses.

preceding $S1_a$ pulse, suggesting that the baseline after detecting photons occasionally remains at some elevated value for some modest time period. The only guaranteed method to remove such reconstruction errors was to only use PMT signals from $S1_b$ pulses if the PMT observed nothing in the preceding $S1_a$ pulse. This leads to a sizable, though not overwhelming, reduction in statistics for each PMT.

Through the application of the additional stringent data-selection cuts on decay vertex position the value of $\hat{\nu}$ could be reduced to acceptable levels. However, due to the limited dataset a reasonable large selection volume was required to achieve the necessary statistics required for least-squares fitting. Over this volume a variation in $\hat{\nu}$ sufficient to produce a 1% absolute systematic variation in $P(2|\hat{\nu})$ was observed, with the effect more pronounced for the bottom array where the light detection efficiency is higher. This variation in $\nu$ leads to an anti-correlated variation in any estimate of $P_{DPE}$, thereby preventing this Poisson pile-up model from being used for this study. Instead, a cut specially targeting photon pile-up was devised as described in the next section.

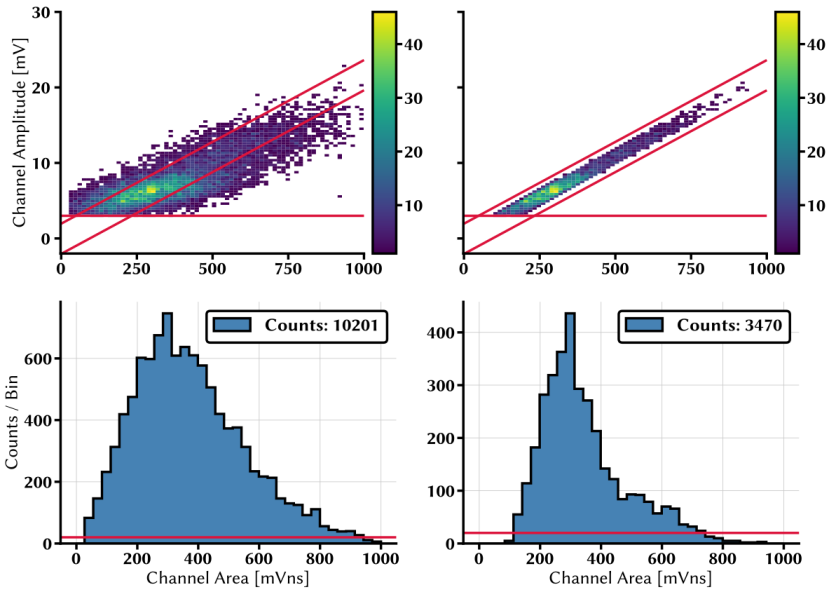
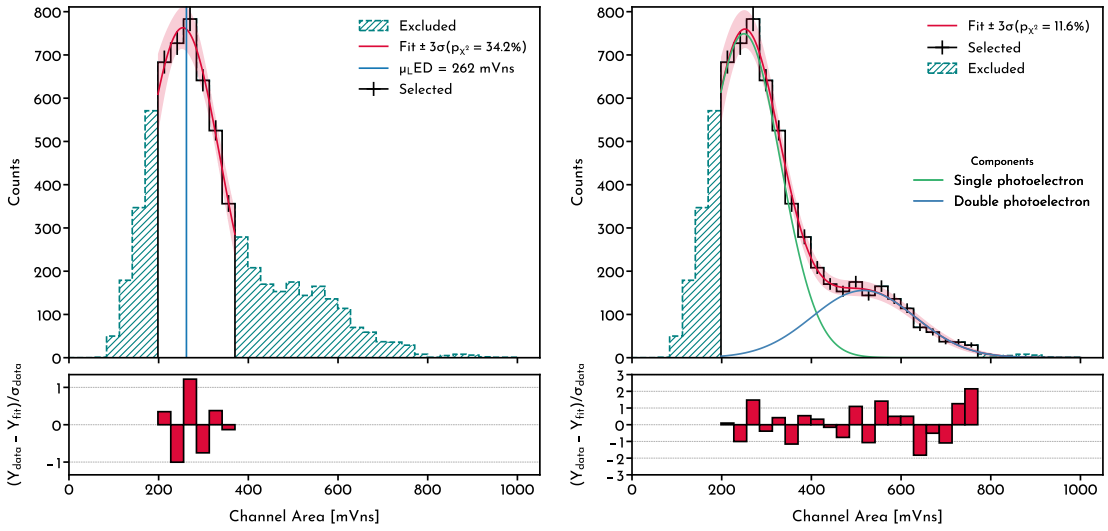



Figure 4.7: The channel amplitude and area parameters for one of the LZ PMTs alongside the measured channel area distribution used to perform the DPE measurement.

### 4.2.3 PMT-level event selection

To design a cut to preferentially remove photon pile-up the distributions of zero, one, two, and three photon occupancy signals, classified by a peak-finding algorithm, were investigated. This was done in the (channel area, channel amplitude) parameter space, shown in Figure 4.7. In this space zero occupancy channels were found to produce baseline noise, as expected, and time-resolvable multiple occupancy signals were found to produce signals with a smaller amplitude per unit area, consistent with the response of several smaller SPE peaks rather than one large DPE peak.

To remove the photon pile-up populations a linear model was developed for each photon occupancy dataset, see Figure 4.7. This model describes the linear relationship between pulse amplitude and pulse area in each PMT. PMT responses from multiple photons that are not exactly coincident should be wider than single photon detection, irrespective of SPE or a DPE response, leading to a shorter amplitude per unit area. Using this logic, single-photon detections were selected by requiring the difference between a PMT's measured and expected amplitude, according to its measured integrated area and the linear model, be less than 1 mV.




(a) Fit to the SPE response with a single Gaussian model.

(b) Fit to the single photon (SPE & DPE) distribution with a two Gaussian model. The best fit value for $P_{DPE}$ was 22.7%.

Figure 4.8: Fitted single photon distribution for PMT 419. (Top panel) The observed distribution (black) and fitted model (red). (Bottom panel) The residuals of this fitted model to the data.

## 4.3 Fitted DPE probabilities and their comparison with previous measurements

Using the definitions outlined in Sections 3.1.2.3 and 3.1.2.4, the single photon response can be written as

$$g(x-\mu, \sigma, P_{DPE}) = (1 - P_{DPE}) \times f(x-\mu, \sigma) + P_{DPE} \times f(x-2\mu, \sqrt{2}\sigma), \tag{4.7}$$

where the first (second) term denotes the SPE (DPE) response and $\mu$ ($\sigma$) is the mean (standard deviation) of the SPE response.

The measurement of the DPE probability was performed from a PMTs area distribution in three steps. First, the low area region of the channel area distribution was excluded as the lower detection efficiency for small signals distorts the distribution's shape. Second, the channel area distribution was fitted using a single truncated Gaussian model about the first peak to measure the SPE mean and variance. Finally, using the DPE model value and SPE parameters as initial guesses the double truncated-Gaussian model was fitted over a wider region encompassing both the SPE peak and DPE shoulder. As cuts were applied specifically to remove channel responses from photon pile-up no coincident term is included in this model. The application of

this fitting procedure to PMT 419 is shown in Figure 4.8 and was repeated for all operational PMTs in the TPC.

The above procedure worked for the vast majority (476/480) of active TPC PMTs. The remaining four PMTs exhibited responses which could not be adequately fitted: two of these PMTs had an abnormal SPE response shape post cuts and the other two produced distributions with the expected shape which could not be fitted using the algorithm above. For these four PMTs the DPE probabilities calculated using the linear model developed at Imperial, Equation 4.4, were used.

The measured DPE probabilities for all active TPC PMTs, including those with unsatisfactory fits, are shown as a spatial map in Figure 4.9 alongside the associated PMT quantum efficiencies. The pattern visible in the DPE map is consistent with QE pattern placed intentionally across the arrays for optimum sensitivity.

The measured DPE probabilities are mostly in good agreement with model developed from the Imperial measurements, as shown in Figure 4.10. The large variance in LZ results compared to the model is unsurprising as similar behaviour was observed in the data used to create this model at Imperial.

A direct comparison of the measured DPE probabilities for the golden PMTs operated at LXe temperatures at Imperial and within LZ is displayed in Figure 4.11 separated by array. For both arrays the mean DPE probability agrees with the previous measurement within errors, with the upper (lower) array 0.6 $\sigma$ (0.4 $\sigma$) above (below) the Imperial result on average.

As the temperature of two PMTs arrays, top = −95 °C and bottom =−99 °C, were slightly different to that present at Imperial (−97.6 °C) some small systematic effect on the DPE probability is expected. The polarity of this effect will be opposite for each of the arrays as the top (bottom) array is warmer (cooler) than the temperature used at Imperial.

The results presented within this work are used in all LZ analyses including, but not limited to, the core WIMP search [132], low-energy electron recoil [133], background determination [134], and effective field theory [135] publications.

Since the conclusion of this work several high statistic tritium calibrations have been performed. It would be advantageous to repeat this analysis using the low-energy component of these

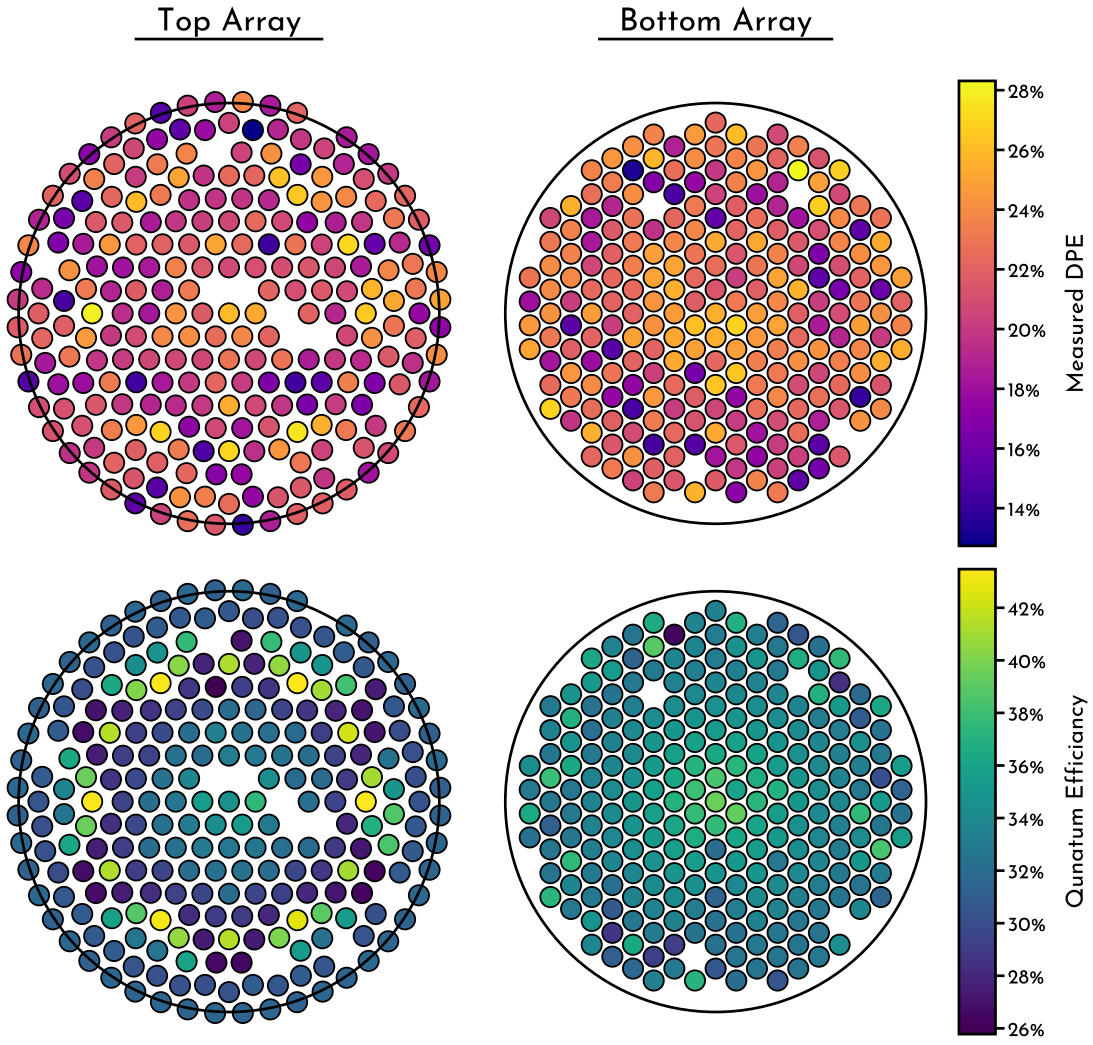



Figure 4.9: Measured DPE probabilities from $^{83m}$Kr $S1_b$ light (top) and quantum efficiencies (bottom). The geometric pattern visible within the DPE measurements is consistent with that of the quantum efficiency, as expected. Disabled PMTs are not shown in these maps. The large black circle represents the full radius of the TPC.

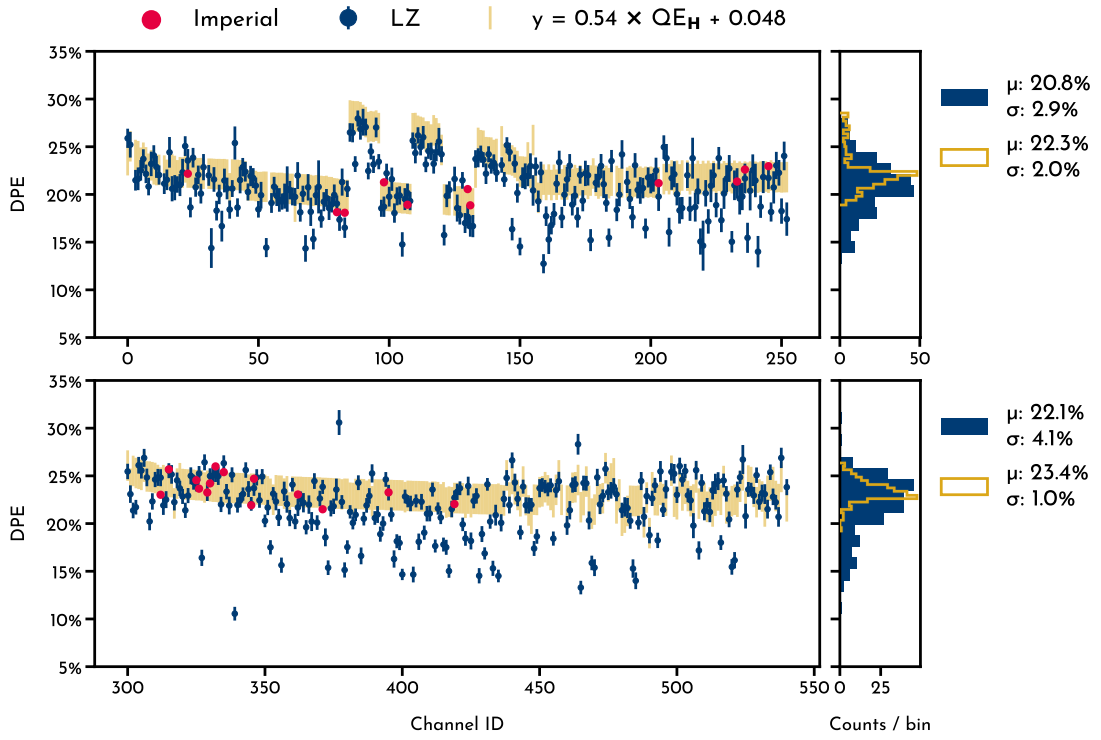



Figure 4.10: Measurements of the DPE probability for every active TPC PMT (blue), previous measurements performed at Imperial College London (red) and the expected DPE probability expected from the linear model found at Imperial.

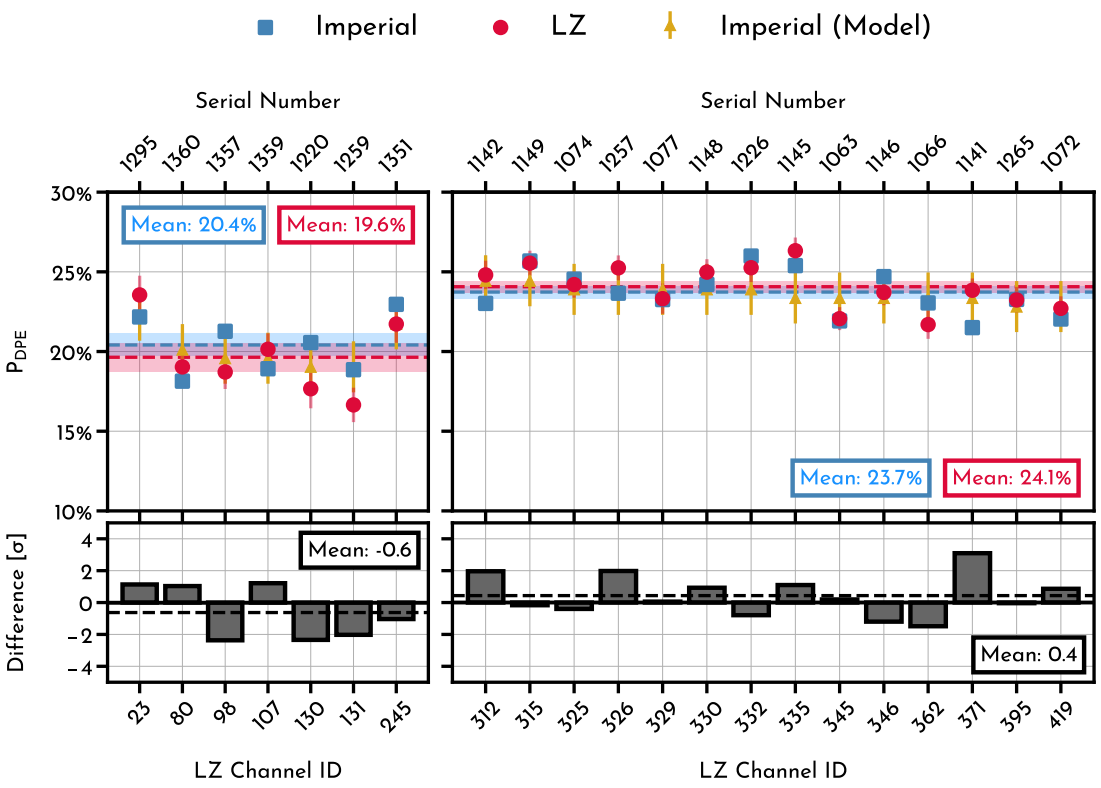



Figure 4.11: Comparison of DPE probabilities as measured at Imperial (blue), in LZ (red), and according to the linear model observed at Imperial (yellow). The left (right) panel contains PMTs mounted in the upper (lower) array.

calibrations to reduce the systematic uncertainties present within the Poisson modelling and better constrain the measurement of the per-PMT DPE probability. It would also be interesting to measure the DPE probability for S2 light. Due to the large number of photons produced per electron emitted into the saturated vapour, this measurement would be best performed using a population of single electron pulses to measure the DPE for the bottom array only.

## 4.4 Conclusion

In this chapter a procedure to measure the DPE probability using a hypothetical "standard candle" source was outlined. The number of photons detected by a given PMT using this source, which produces a low and fixed number of scintillation photons, would follow a Poisson model. The dispersed $^{83m}$Kr source is then suggested as a candidate for such a candle due to the low scintillation yield of the $S1_b$ produced in the two-stage decay process. Whilst characterising this source, the half-life of the meta-stable state was measured at 154.5 ± 0.2 ns, in agreement with previous measurements.

Whilst studying individual PMT responses from this source it became apparent that the reconstructed PMT response of $S1_b$ PMT pulses were being contaminated by signals induced from the preceding $S1_a$ pulse. This contamination was removed during this study by only using PMTs which did not detect a photon in the preceding $S1_a$ pulse.

Unfortunately limited statistics coupled with an $O(\%)$ spatial systematic on the measured DPE probability precluded the use of the Poisson model method. Instead, a simpler model which selects single photon responses using the PMT area v.s. amplitude parameter space was used. By fitting the resulting PMT area distribution for each PMT using a double truncated-Gaussian model the DPE probability was obtained for 476 of the 480 active TPC PMTs. The remaining PMTs could not be fit using this method and instead use the linear model developed at Imperial to calculate their DPE probabilities.

The measured DPE probabilities were found to be in reasonable agreement with the linear model developed at Imperial. It should be noted that the linear model does not fully capture the broadness of the measured DPE probabilities in either the LZ or Imperial measurements. Finally, a direct comparison of the Imperial and LZ measurements was performed for the "golden" PMTs present in both datasets. Good agreement was found between both measurements

though a systematic effect between the two arrays was observed. The sample mean of the upper array golden PMTs was found to be 0.4 σ below the Imperial average for the same PMTs, whilst the lower array average was 0.6 σ above the equivalent Imperial sample mean for the same PMTs. This effect is not wholly unexpected as the probability is known to increase at lower temperatures and the upper (lower) PMTs are operated a couple of degrees above (below) the temperature used in the Imperial measurements.

These measurements are important for accurately reconstructing the energy of interactions within the detector and improving the energy resolution of the detector by reducing the systematic error inherent from different PMT having slightly different response models. Measuring the DPE probability for a PMT is also important when developing cuts based on the measured channel response as this can affect the signal efficiency for a given PMT. For example, if a cut is developed which requires the integrated area of a PMT response be less than some global constant defined as a function of the SPE response, then a PMT with a larger DPE probability will have a lower signal efficiency than a PMT with a lower DPE probability as the average signal is proportional to the DPE probability.

The measured DPE probabilities presented in this chapter are used within all LZ analyses including, but not limited to, the core WIMP search [132], low-energy electron recoil [133], background determination [134], and effective field theory [135] publications.

# 5

# First WIMP search with LZ

This chapter details LZ's first WIMP search using data taken during the first science run (SR1). This discussion encompasses the commissioning of LZ, its calibration, its first science run, and the WIMP search result. This analysis was directed and managed by senior members of the LZ experiment as it was both the first and primary analysis of the experiment. My chief contribution to this analysis was the in-situ calibration of the LZ TPC PMTs, described in detail in Chapter 4, alongside work investigating scintillation (S1) backgrounds at threshold with particular focus on waveform analyses, not discussed here, and developing and validating parts of the data analysis framework.

## 5.1 Commissioning

LZ was commissioned during the second half of 2021. Whilst full of low pressure xenon gas the TPC PMTs were calibrated and characterised, including measurements of afterpusling, before having their gains matched and regularly monitored. During this commissioning 482/494 of the TPC PMTs, 129/131 of the skim PMTs, and 120/120 of the OD PMTs were operational and suitably stable for LZ's requirements, a pass rate above the minimum requirement of 96% set for the TPC and skin.

Between August and September the detector was filled and levelled ensuring the liquid surface was perpendicular to the TPC's vertical axis. In October the grids were biased with the first S1-S2 events observed on the sixth of October. The main S2 trigger logic was then tuned with 100% efficiency achieved for pulses of at least six extracted electrons.

Initial calibrations where performed (AmLi, $^{83m}$Kr, $^{220}$Rn YBe, $^{57}$Co, and $^{22}$Na) to understand the detector response, develop spatial light correction maps for the S1 and S2 signals, and to tune the position reconstruction which achieved a 4 mm planar resolution and 0.7 mm depth resolution for S2 signals of 30 electrons.

## 5.2 Science run 1 (SR1)

The first science run was designed to fulfil two purposes: to facilitate the full characterisation of the detector over an extended period, and ,if possible, achieve world-leading sensitivity to WIMPs. Sensitivity studies suggested a 60 day exposure to reliably achieve this goal.

Data for LZ's first science run was acquired between the 23$^{rd}$ of December 2021 and the 18$^{th}$ of April 2022, totalling 116 days. In January, $^{83m}$Kr calibrations were performed to update the S1 and S2 light correction maps. Later the same month, four days of D-D calibrations data was acquired to measure the NR response of the detector including characterisation of the NR band. In February and April, LED calibrations were performed to measure the evolution in PMT gains. Excluding the above calibrations, detector maintenance, DAQ dead-time and period of anomalous conditions the total live-time, prior to data quality cuts, was 89 live days. Acquired over 804 separate runs, this dataset comprises approximatly 110 million events spread across 441,000 raw data files and totals just under 150 TiB of disk space.

Immediately after SR1 a more intense calibration campaign was conducted. Two rounds of $^{83m}$Kr calibrations were performed to measure the S1 and S2 correction maps. A week of $CH_3T$ calibrations ($\sim$ 7million events) was performed to measure the ER band to high accuracy. This was followed by more D-D calibrations to measure the NR band. Finally, six days of AmLi data was acquired, totalling approximately 21 million events, as an alternative NR dataset.

## 5.3 WIMP Search Methodology

The core methodology of a WIMP search with a two-phase LXe-TPC can be split into six components: detector operations, WIMP data selection, detector modelling, signal model generation, background model generation, and performing the statistical analysis of choice. These components and how they relate to one another are shown in Figure 5.1.

### 5.3.1 Detector Operations

To acquire a dataset to perform a WIMP search analysis requires operating the detector in stable conditions for extended periods of time. This requires in-person and remote detector monitoring, including performing periodic calibrations, such as the LED calibrations, and maintenance of detector components.

### 5.3.2 Data Processing & Selection

To effectively analyse LZ data requires processing the raw POD waveforms into simple user-friendly data structures called RQs. For LZ this requires: finding and classifying pulses, parametrising pulses (calculating pulse areas and widths etc.), applying detector corrections,

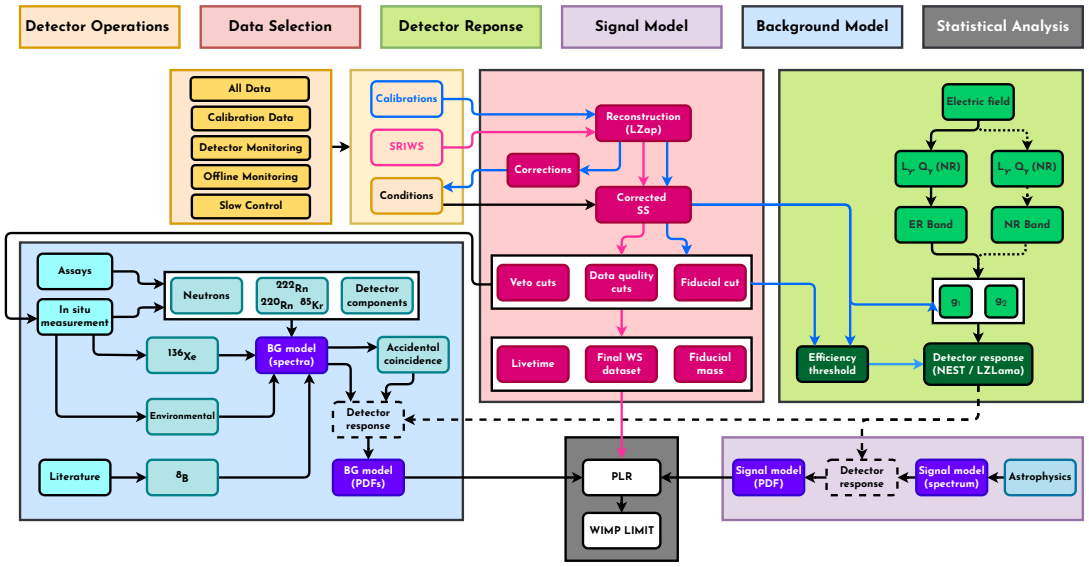



Figure 5.1: Simplified schematic of the first WIMP search. The analysis is split into six sections: detector operations, WIMP data selection, detector response modelling, signal modelling, background modelling and the final PLR statistical analysis. Note: some of these sections are more closely connected than shown here; for instance, the detector model is used as part of the in-situ measurement of backgrounds.

and building physically-motivated events such as single and multiple scatters. The LZap software, detailed in 3.2.1.1, was written to perform these data processing tasks.

To analyse these RQ files a data analysis, selection, and skimming framework, henceforth know as the ALPACA was written. This framework, designed to consolidate all data selection cuts, was used to perform all data selection cuts for the primary WIMP analysis.

### 5.3.3 Detector Model & Simulations

To be able to perform statistical tests comparing experimental observations to various physical models requires detailed simulations based upon a tuned and accurate detector model. For a detailed description of the detector model and simulation framework used in LZ the reader is referred to Ref [136]. Here, only the parts of the simulation framework required for the SR1 WIMP search will be outlined.

To produce accurate simulations of TPC requires three steps. One, an analytic or Monte-Carlo (MC) energy deposition model. Two, a yield model which details how many scintillation photons and ionization electrons are produced from energy deposition in the target. Three, a detector

model including optical transport, photon detection, electron-lifetime and pulse clustering of simulated signals.

#### 5.3.3.1 Signal model

The WIMP differential recoil spectrum are calculated numerically using the procedure as described by Smith and Lewin in Ref [39] and briefly outlined in Section 2.2.1. For the LZ signal model the standard halo model (SHM) from Ref [42] was chosen as agreed in Ref [137]. Using this model the WIMP signal recoil energy PDF is approximately exponential with a decay contestant of $-\frac{m_\chi}{m_A}$, where $m_\chi$ is the dark matter mass and $m_A$ is the target atoms mass.

#### 5.3.3.2 Background model

The background models are primarily generated using BACCARAT [136], an internal Geant4 [138, 139] based simulation framework, which records the energy deposits within all the detectors systems. Using this software a variety of radiogenic and external backgrounds can be simulated.

### 5.3.4 Simulating the detector response

The LXe-specific element of simulations in LZ use the Noble Element Simulation Technique (NEST) framework [53, 55–57]. Using NEST, energy depositions are used to generate primary quanta (photon & electrons) using scintillation and ionisation yields models tuned on calibration data from a variety of experiments. See section 2.4 for a brief overview of LXe physics and Figure 2.10 for details on the NEST yield models. The NEST framework has the ability to perform quick and accurate simulations out-of-the-box, however LZ chose to write a simulation package, using NEST as a library, called LZlama. This package provides greater flexibility when tuning the detector model, for instance running clustering algorithms and using observed correction maps, and allows simulation results to be written out in a RQ-like data format, facilitating seamless comparison between data and simulation.

### 5.3.5 Statistical Analysis

To search for WIMPs LZ employs the profile likelihood ratio (PLR) method [140–142], following the conventions outlined in Ref [137].[1] Specifically LZ uses S1–$\text{Log}_{10}$(S2) template PDFs

[1] Some conventions in this white paper were applied incorrectly and have been corrected in LZ implementation.

generated using the LZlama package to calculate signal and background likelihoods for the PLR.

No software-level bias mitigation was applied in science-run one (SR1). This was to allow the proper diagnostic study of the TPC. The tuning of data selection cuts was based on either sidebands of WIMP search data or calibration data so as not to bias the analysis. In future science runs LZ plans to embed fake signal events into the raw data stream. These fake events, known as "salt", will be generated by stitching together S1 and S2 pulses from calibration data. Using *salting* as a bias mitigation has been successfully applied using software and hardware injection methods in the LUX [87] and the laser interferometer gravitational-wave observatory (LIGO) experiments [143].

### 5.3.6 Detector Operations

LZ's first science run was conducted between the 23$^{rd}$ of December 2021 and the 12$^{th}$ of May 2022, totalling 141 days. During this period the drift (extraction) field was maintained at 193 V/cm (7.3 kV/vm), and the temperature and pressure of the detector were stable, within 0.2%, at 174.1 K and 1.791 bar(a) respectively. The electron lifetime varied between 5000 µs and 8000 µs over the course of SR1 far in excess of the 951 µs maximum drift time. Prior to SR1 twelve of the TPC and two of the skin PMTs were disabled due to them exhibiting excessive noise or other malfunctioning behaviour during detector commissioning.

### 5.3.7 Detector Calibration

LZ uses a variety of calibration sources including internal dispersed sources, closed external sources and a neutron generator. Here three of the calibration sources relevant to or directly used in this thesis are outlined: LED calibration used periodically calibrate the PMTs; $CH_3T$, a dispersed ER source, used to tune the detector model to replicate the observed ER band; and D-D, used to observe and characterise the NR band response, crucial for observing the NR interactions expected from WIMPs. The $^{83m}$Kr source, discussed in detail during previous chapter, has been omitted from this discussion in the interests of brevity and to avoid repetition.

#### 5.3.7.1 LED calibration

Blue (470 nm) LEDs are used to measure the SPE response of the PMTs and monitor any degradation in PMT performance, for example increased afterpulsing. Due to the comparably long wavelength LED photons cannot be used to measure the DPE effect as this does not occur at these wavelengths.

Each detector system has its own LED calibration system each driven using pulsers located in the cavern. The TPC contains 48 LEDs with 24 located in each array each of which point towards the opposite array. The skin contains 25 LEDs with 12 in the top side array and 13 in the bottom side array. The OD contains 35 LED driven optical fibres, known as the OCS, split between the PMT support structs (30 fibres) and below the bottom tank (5 fibres). To enable triggered analysis of LED data the synchronised LED trigger is passed to the DAQ to be recorded alongside the PMT data.

#### 5.3.7.2 Electronic recoil band (tritium) calibration

The ideal ER calibration source for a LXe TPC is one that: has a low mean energy, is spatially uniform and poses no risk to future operations. Tritium $\beta$-decays provides a solution to the first two points: tritium has the second lowest known $\beta$-emission energy (18.6 keV), after $^{187}$Re (2.5 keV) [144, 145]; and exists in a molecular form which can be injected into the detector and allowed to mix into the xenon [146]. Unfortunately, molecular tritium ($T_2$) adsorbs onto surfaces and is liable to embed itself into the detectors plastic components via diffusion, effectively poisoning the detector [58]; tritium's long half-life ($T_{\frac{1}{2}}$ =12.3 years) necessitates the moderation of both effects. Even in the absence of these effects molecular tritium will linger within the xenon, its noble nature making it immune from the getter. LUX overcame these impediments by bonding tritium into a methane ($CH_4$) molecule which can be efficiently removed by the getter. Using this triturated methane ($CH_3T$), LUX pioneered the low energy calibration of the ER band in LXe [58].

Even using this validated methodology there are still risks. The PandaX-2 experiment successfully calibrated their detector with $CH_3T$ but was unable to completely remove the $CH_3T$. In an attempt to expunge the remaining $CH_3T$, the PandaX collaboration removed and distilled the xenon from their detector and flushed the detector with warm xenon gas prior to refilling; after this process PandaX-II was left with a residual $CH_3T$ contamination of 40 nBq/kg [147].

Due to the potential risks of poisoning the detector with tritium both the LZ and LUX experiments approached such calibrations with caution. For LZ this required both the careful purification of the $CH_3T$ source, to remove any $T_2$ contaminants, and validation of the deployment procedure. This validation included injecting the TPC with pure methane to prove that the stable carrier molecule could be removed as expected by the getter, performing table-top validations of the procedure in the lab, and performing a low activity calibration to validate that the getter removed the contaminants as expected.

The $CH_3T$ calibration was performed after SR1 with the aim of calibrating the ER band with approximately 5500 events between 2 keV and 8 keV within the 5.6 tonne fiducial volume. This quantity of events, 20 times the background observed within SR1's ER band, requires 19,600 decays accounting for an overall selection efficiency of 28%. To achieve this an initial activity of 65 mBq was required which was approximatly 340 times the measured background rate.

#### 5.3.7.3 D-D (NR band) calibration

Arguably the most important calibration is the characterisation of the NR band as this is where WIMP signals will be observed. Using this calibration the signal PDF for WIMP interactions and neutron backgrounds can be generated and the signal acceptance of the detector to WIMPs, the most important metric for such a detector, can be assessed.

In LZ the NR band is measured using a D-D neutron generator which emits monoenergetic 2.45 MeV neutrons. These neutrons, emitted by the generator in the cavern, traverse the water tank and OD via one of two conduits which link the cavern and the TPC outer-vessel (OV) specially at a height just below the liquid surface. Within the TPC these neutrons produce a continuum of nuclear recoils up to a maximum energy of approximately 74 keV, well above the region-of-interest (ROI) considered in LZ. The distribution of these recoils peaks towards low energies well within the ROI and provides good coverage of the entire WIMP signal region for most candidate particle masses.

### 5.3.8 Characterising the ER and NR bands

The ER and NR bands, as measured with $CH_3T$ and D-D, are shown alongside simulated percentile bands in Figure 5.2. From this a clear separation between the two bands is observed.

The detector response, the solid lines, was tuned using the tritium dataset to reproduce the median, 10% percentile, and 90% percentile bands and then validated against the D-D dataset achieving a better than 1% agreement in the mean and 4% in the width. The resulting detector model has been made publicly available as part of the NEST software [148].

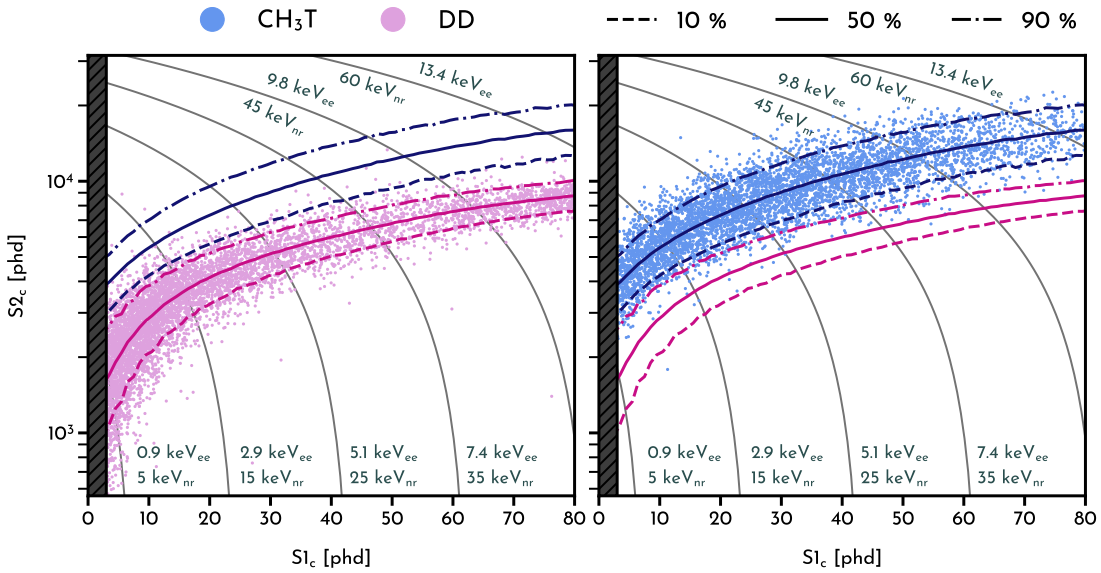



Figure 5.2: Calibration of the ER and NR bands, within the WIMP ROI, during SR1. The NR (ER) band, shown as pink (blue) points was observed using a D-D ($CH_3T$) source. The NEST detector response, plotted as 10%, 50% and 90% percentiles, was tuned to the $CH_3T$ ER band and then validated against the D-D NR band. Figure adapted from Ref [45].

A nuance of these bands is that they are not universally applicable to all ER and NR interactions. Due to the energy dependent anti-correlation between the S1 and S2 signals, PDFs is this parameter space implicitly depend on the underlying energy spectrum. By deriving the above bands using the known $CH_3T$ and D-D spectra the underlying model parameters obtained above can be applied to the WIMP spectra to create a signal PDF however the D-D "NR" band itself it not truly applicable to the signal model of any WIMP candidate.

### 5.3.9 Data Selection

To produce the final WIMP search datasets requires numerous data selection cuts. These can be split into five main categories: ROI selection, fiducial volume selection, exclusion period removal, data quality cuts, and anti-coincidence veto rejection.

The ROI is defined as all single scatter events with a corrected S1 area between 3 phd and

80 phd and a corrected S2 area between 600 phd and $1 \times 10^5$ phd. The fiducial volume is approximately defined as the volume at least 4 cm from the TPC walls, 22.8 cm below the gate, and 2.2 cm above the cathode. Three additional volumes exhibiting elevated background rates were removed: regions less than 5.2 cm from the top (drift-times $<$ 200 µs) wall; regions less than 5 cm from the bottom (drift-times $>$ 800 µs) wall; and a 6 cm radius about the field-cage resistor chain embedded in the at the 9 o'clock position. The heightened background rate near the TPC corners is expected due to greater ingress of external backgrounds due to the higher surface area to volume ratio whilst the resistor chain activity is attributed to radioactive emission from detector components.

Whilst SR1 was a very stable campaign there are nevertheless periods which cannot be used due to transient operational anomalies and periods of elevated background rate. The most significant operational exclusion period is due to elevated rates of localised grid emission which are removed using simple time exclusion periods totalling 3.1% of the total livetime. The single largest contributor to the exclusion periods is the delayed emission of electrons, and their associated S2s, from large S2 signals; high energy S2s affect the following $\mathcal{O}$(100 ms) whilst muons affect the following $\mathcal{O}$(10 s) [149, 150]. These periods of elevated activity are excluded by applying an energy dependent hold off period after large S2 signals leading to a 29.8% livetime loss in SR1.

To reject events with anomalous S1 and S2 shapes a battery of pulse level cuts are applied to the S1 and S2 pulses individually. The majority of these cuts focus on the shape of the pulses for instance checking if two S2 pulses have been merged into one pulse or checking if the time profile of the S1 is consistent with xenon scintillation. To reject accidental events, where isolated S1 and S2 pulses happen, by chance, to be detected within a drift time of one another, further cuts are applied to test if the S1 and S2 pulses are consistent with the reconstructed single scatter. Examples of such cuts include: checking that the fraction of S1 light detected an array, which is inversely proportional to the propagation distance, is consistent with the measured drift time and seeing if the diffusion of the S2, as inferred by its width, is consistent with drifting for measured drift time. These cuts were created and tuned using calibration data and events with an unphysical drift time (drift time $>$ maximum drift length) which can only arise from accidental coincidence.

Finally, an anti-coincidence cut is applied using the skin and OD detectors to remove $\gamma$-ray and

Table 5.1: The number of events remaining in the SR1 WIMP search dataset after the accumulation of each cut.

| Accumulated cuts | Remaining events | Percentage |
|---|---|---|
| all events | $1.1 \times 10^8$ | 100% |
| & exclusion periods | $6.0 \times 10^7$ | 54.25% |
| & single scatters | $1.0 \times 10^7$ | 9.10% |
| & region-of-interest | $1.8 \times 10^5$ | 0.17% |
| & S2 quality cuts | $3.5 \times 10^4$ | 0.03% |
| & S1 quality cuts | $3.1 \times 10^4$ | 0.03% |
| & fiducial volume | 416 | 0.0004% |
| & vetoes | 335 | 0.0003% |

neutron interactions. To reject $\gamma$-rays events with a skin (OD) signal within 0.3 µs (0.5 µs) of the S1 are rejected. Similarly, to reject neutrons, any event which has an OD signal consistent with neutron capture on hydrogen or gadolinium less than 1.2 µs after the S1 is vetoed. The position averaged efficiency of this neutron veto was measured to be 89 ± 3% using an AmLi source deployed using the three CSD tubes at several heights [132]. The majority of the events in removed by this cut in the SR1 dataset were located outside the fiducial volume, as expected from external backgrounds. The minority of events rejected within the fiducial volume are removed by the skin veto and are located near fiducial volume perimeter.

The accumulated application of these cuts on the SR1 dataset is tabulated in Table 5.1. From the initial 110 million events only 10 million are single scatters. Of these single scatters only 0.03% are within the ROI and pass the battery of S1 and S2 cuts. The final dataset, after applying the fiducial volume and veto cuts, contains only 335 events.

### 5.3.10 Result

The distribution of the remaining 335 events remaining in the SR1 WIMP search dataset are displayed in Figure 5.3 using the S1–S2 and radius–drift-time parameter spaces. The majority of the events present originate from Rn daughter $\beta$-decays and electron capture of $^{37}$Ar. The $^{37}$Ar contamination was expected due to cosmogenic activation and will be suppressed in future campaigns due to the isotopes short half-life [151] .

Using the PLR statistical test the upper limit of the spin-independent WIMP-nucleon cross-section was calculated at the 90% confidence level for several WIMP masses. The result of

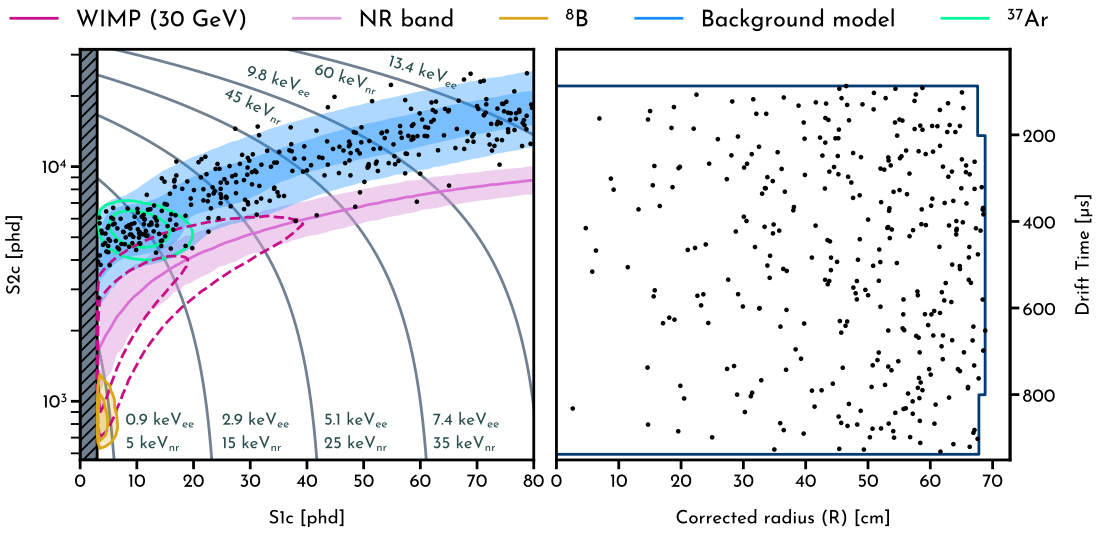



Figure 5.3: The events remaining after all data quality cuts for SR1 alongside relevant signal and background PDFs. Here the background model is the total weighted PDF from detector ERs, detector NRs, $\nu$ ERs, $\beta$-decay, $^{124}$Xe, $^{127}$Xe, $^{136}$Xe, and $^{37}$Ar. (Left) The S1-S2 distribution used in the PLR analysis. (Right) Position of the surviving events and the definition of the fiducial volume (blue). Figures adapted from Ref [45].

these calculations is shown in Figure 5.4 alongside limits from other experiments. LZ has set the strongest limits on the spin-independent WIMP-nucleon interaction cross-section to date for masses above 9 GeV reaching a minimum cross-section of $9.2 \times 10^{-48}$ cm$^2$ for a 36 GeV/c$^2$ WIMP.

When quoting the exclusion limits for LZ a power constrained limit (PCL) at the $-1\,\sigma$ level was used. Power-constrained limits, part of the 'Recommended conventions for reporting results from direct dark matter searches' [137], prevent statistical tests from excluding parts of the parameter space where an experiment's power to reject the null hypothesis is limited [152]. In practise this is designed to prevent the test from rejecting hypotheses where the expected signal is suitably small compared to the background that the detector effectively is not sensitive to the signal. In this case the power constrained limit will return a weaker limit of some predefined power instead of the erroneous overly ambitious limit naively returned by the test.

Unfortunately the procedure contained in the agreed recommended conventions incorrectly constrained the discovery-power and not rejection-power leading to a lack of consensus on the "correct" power constraint to use when publishing results. LZ chose to publish limits constrained at the $-\sigma$ (16%) level whereas XENONnT have published their limits constrained to the median

Table 5.2: Expected and best fit number of events for signal and background components for the 60 days·5.5 tonne exposure. The expected number of $^{37}$Ar events were assumed to be between zero and three times the calculated value owing to large uncertainties in this calculation. Each of these results was used as a constraint within the combined fit, with all components having a Gaussian prior apart from the uniform $^{37}$Ar and asymmetric detector neutron priors. Table reproduced from Ref [132].

| Component | Expectation | Best fit |
|---|---|---|
| β-decay + Detector (ER) | 215 ± 36 | 222 ± 16 |
| ν (ER) | 27.1 ± 1.6 | 27.2 ± 1.6 |
| $^{37}$Ar | [0, 288 ] | $52.5^{+9.6}_{-8.9}$ |
| $^{124}$Xe | 5.0 ± 1.4 | 5.2 ± 1.4 |
| $^{127}$Xe | 9.2 ± 0.8 | 9.3 ± 0.8 |
| $^{136}$Xe | 15.1 ± 2.4 | 15.2 ± 2.4 |
| $^{8}$B CEνNS | 0.14 ± 0.01 | 0.15 ± 0.01 |
| Accidentals | 1.2 ± 0.3 | 1.2 ± 0.3 |
| Detector neutrons | $0.0^{+0.2}$ | $0.0^{+0.2}$ |
| WIMP (30 GeV) | – | $0.0^{+0.6}$ |
| Total | – | 333 ± 17 |

(50%) level [153].

The background PDFs considered in this analysis are β-decay, detector ER, $^{37}$Ar, $^{124}$Xe, $^{127}$Xe, $^{136}$Xe, $^{8}$B (CEνNS), accidentals, and detector neutrons. Here the β-decay component refers to $^{212}$Pb, $^{214}$Pb, and $^{85}$Kr decays. The estimated Pb activity ($^{212}$Pb = 0.14 µBq/kg, $^{214}$Pb=3.26 µBq/kg) was estimated by fitting energy spectra outside the ROI whist the Kr activity was calculated assuming a 144 ± 22 ppq concentration of $^{nat}$Kr as measured from in situ mass spectroscopy. The $^{37}$Ar, produced by cosmogenic activation of the xenon whilst above ground, was expected to produce 96 events during SR1 [151]. The expected number of counts for each component was computed using assay measurements and/or sideband datasets.

The sharp dip in LZ's observed exclusion limit is because LZ observed fewer events than expected in low-energy low-S2 region of the ER band, as can be seen in Figure 5.3. To prove this is a genuine statistical fluctuation, and not an analysis bias, this quiet region was investigated using $CH_3T$ and D-D calibration data. This study found no evidence for any unexpected analysis bias preferentially removing events within this region demonstrating that the stronger

limit for 30 GeV WIMPs is simply a statistical fluctuation.

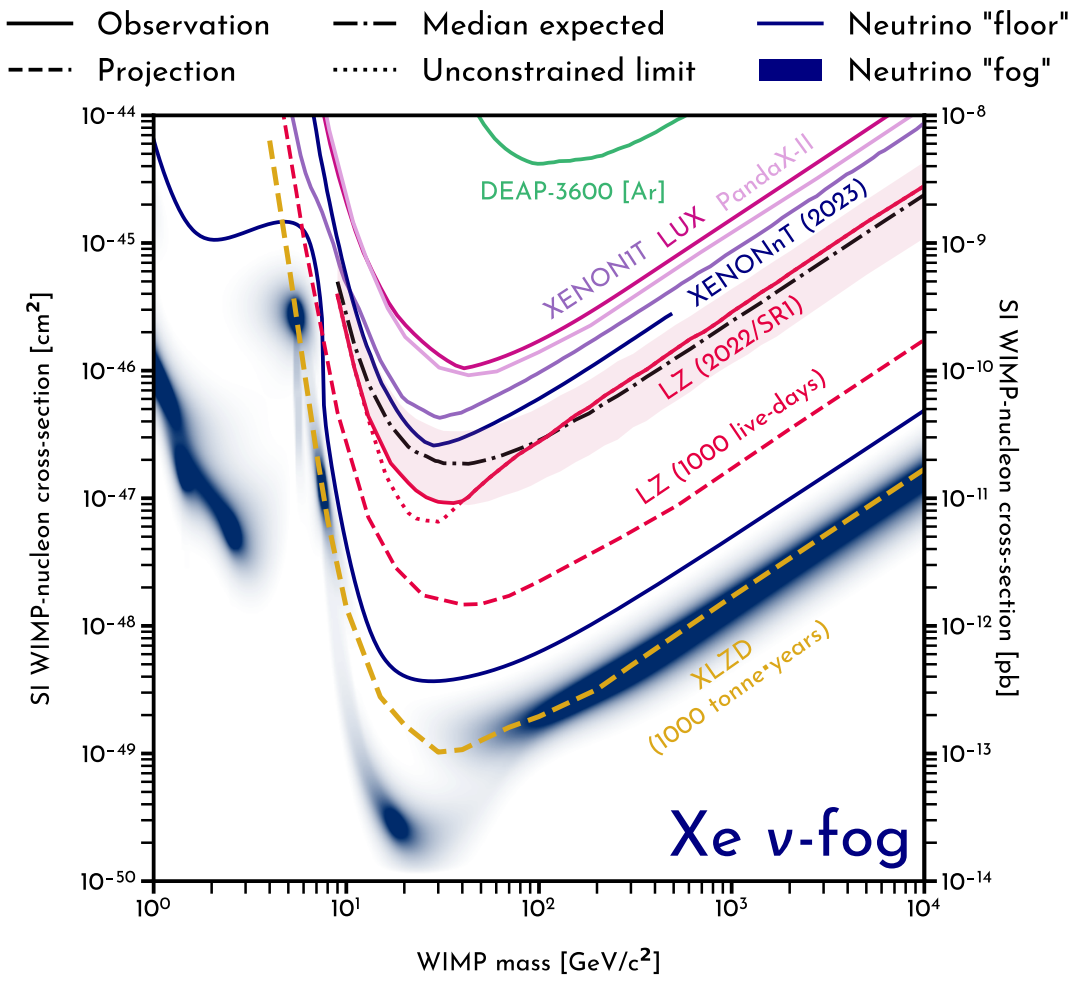



Figure 5.4: Current limits on the WIMP-nucleon cross-section. The power-constrained exclusion limit observed by LZ in its first science run, described in this chapter, is plotted as a solid red line with the unconstrained limit shown by the red double-dashed line [45]. The median sensitivity is represented by the black dot-dashed line and its accompanying 1 σ error band. The exclusion limits of several other xenon experiments, LUX [87], PandaX-II [89], XENON1T [116], and XENONnT [153], are displayed alongside DEAP-3600, a single phase, scintillation-only argon experiment [154]. Projections of the full LZ exposure (1000 live-days) [91] and the xenon detector proposed by the XLZD consortium (1000 tonne-years) [76] are shown as dashed lines. The "neutrino fog", where experiments start observing neutrinos via CEνNS, is shown for xenon detectors by the solid black line and the blue contours using the calculations performed in Ref [77].

## 5.4 Conclusion

In this chapter the LZ SR1 WIMP search analysis was motivated, outlined and described. This short engineering run, designed to study and characterise the detector over a 116 calender-day period, produced world-leading upper limits on the spin-independent WIMP-nucleon cross-section for WIMP masses above 9 GeV/$c^2$ at the 90% confidence level using a 60 days·5.5 tonne exposure. This analysis achieved a peak sensitivity of $9.2 \times 10^{-48}$ cm$^2$ for a 36 GeV/$c^2$ WIMP.

To achieve this result required: a stable detector state over the 116-day run duration; reliable data processing; rigorous calibration of the detector's ER and NR responses; the careful tuning of the detector model to said detector response; a well understood background model informed by side-band analyses and assays; and finally the application of a statistical test, in this case a PLR.

With the understanding developed during this short run, encompassing only 6% of the expected 1000 live-day dataset, LZ can continue to operate and eat into new parameter space as its strives to achieve its projected sensitivity of $1.4 \times 10^{-48}$ cm$^2$ for a 40 GeV/$c^2$ WIMP.

My most significant contribution to this analysis was the in-situ measurement of the DPE probabilities for all of LZ's TPC PMTs alongside validating these measurements against dedicated measurements performed at Imperial. These measurements were, and remain, instrumental in taking into account the DPE effect and are important for minimising the systematic error during energy reconstruction, particularly at threshold. Using my expertise of studying low energy signals and the PMT response I also studied scintillation backgrounds encountered at threshold, more notably backgrounds from Cherenkov emission in the PMT windows. This work is not presented within this thesis. Finally, I contributed to the development of the core analysis framework which was integral to performing this analysis.

# 6

# Using the DPE effect to improve $^{8}$B sensitivity

Boron-8 solar neutrinos scattering via CE$\nu$NS produce events close to, if not below, the nominal scintillation threshold achieved in the current generation of tonne-scale LXe TPCs. This threshold, driven by the presence of S1s from dark-count pile-up, can be reduced by including parameters that discriminate between Xe scintillation and dark-count pile-up. In this chapter a sensitivity study is described which exploits Xe scintillation characteristics and the LZ detector response to reduce the scintillation threshold from three-fold S1s, defined by three PMTs registering a response, to two-fold.

This technique was successfully applied in the LUX experiment, where the coincidence requirement was reduced from two-fold S1s to single-fold S1s [127]. A sensitivity study evaluating the sensitivity of such an analysis in LZ, where the coincidence requirement in reduced from three-fold to two-fold, has previously been performed and can be found in Ref [95]. In that work the discriminating variables were limited to the largest of the two PMT response (integrated area), henceforth called $X_{max}$, and the time-seperation between the two photon detections.

Here, a study similar in scope to the aforementioned work is presented with two noteworthy modifications. Firstly, the PDFs of the two discriminating variables were calculated analytically trivialising the computation of the signal and background PDFs. By treating the $X_{max}$'s PDF analytically this new method can include the variation in PMT parameters—mainly the mean, standard deviation, and DPE probabilities—for all 121524 unique PMT pairs, whereas the previous study was limited to using an average PMT response for all photon detections. Secondly, several additional discriminating variables, electron drift-time and S2 area, were added, increasing the median sensitivity for detecting $^8$B neutrinos in LZ.

These analytic PDFs can be directly used within the *Flamedisx* framework being developed within the LXe dark matter community [155, 156]. By using explicit profile likelihoods, opposed to MC generated template PDFs, *Flamedisx* can perform statistical tests multidimensional parameters spaces without the curse of dimensionality experienced by standard Monte Carlo methods. By adding in the additional parameter spaces outlined above *Flamedisx* should be an ideal method to exploit the observations described within chapter for a $^8$B search in LXe TPCs such as LZ.

## 6.1 Analytic reanalysis of previous study

### 6.1.1 Discriminating with DPE

Dark counts are unlikely to produce DPE responses in a single PMT, thus if any two-fold S1 has a large PMT response consistent with DPE in one channel then this two-fold S1 is more likely to be from VUV light produced from a Xe interaction. The simplest metric to quantify the "VUV-ness" of a two-fold S1 is the largest PMT integrated area response. As the signal and background models are based on the same fundamental process, with the background model effectively a special case of the signal model ($P_{DPE} = 0$), the PDF of the metric of interest for both can be calculated simultaneously.

The PMT response is a random variable (RV), $X_i$, sampled from some PDF $g(x|\mu_i, \sigma_i, p_i)$. For each event there are two RVs, $X_0$ and $X_1$, each sampled from a different PMT distribution function. The metric of interest, the maximum of the two responses, is computed as $X_{max} = \max(X_0, X_1)$ and is itself a RV sampled from

$$P_{max}(x|\mu_1, \sigma_1, p_1, \mu_2, \sigma_2, p_2) = g_1(x|\mu_1, \sigma_1, p_1)\, G_2(x|\mu_2, \sigma_2, p_2) \tag{6.1}$$

$$+ g_2(x|\mu_2, \sigma_2, p_2)\, G_1(x|\mu_1, \sigma_1, p_1), \tag{6.2}$$

where $g_j$ is the PDF of a PMT integrated area, as described in Equation 4.7, and $G_j$ is the corresponding cumulative-density function (CDF). Using this equation, the distribution of $X_{max}$ under either the signal ($p = P_{DPE}$) or background ($p = 0$) hypotheses can be easily computed for any of the 121524 unique PMT pairs. The PDFs of $X_{max}$ for signal (VUV photons) and background (SPEs) events are shown in Figure 6.1 alongside MC estimates of the PDFs. The shape of each distribution is similar to the underlying PMT response PDF with a bias towards larger values, as expected from the application of the maximum operator.

### 6.1.2 Discriminating with time separation

The fundamentally different production mechanisms for signal (Xe scintillation) and background (dark-count pile-up) events leads to very different photon detection timing PDFs. The simplest metric to describe the underlying distributions of the detected signals is the absolute time separation between the two PMTs: $\delta T = |T_0 - T_1|$, where $T_j$ is a RV sampled from the detection time PDF. Because of their fundamentally different production mechanisms the signal and

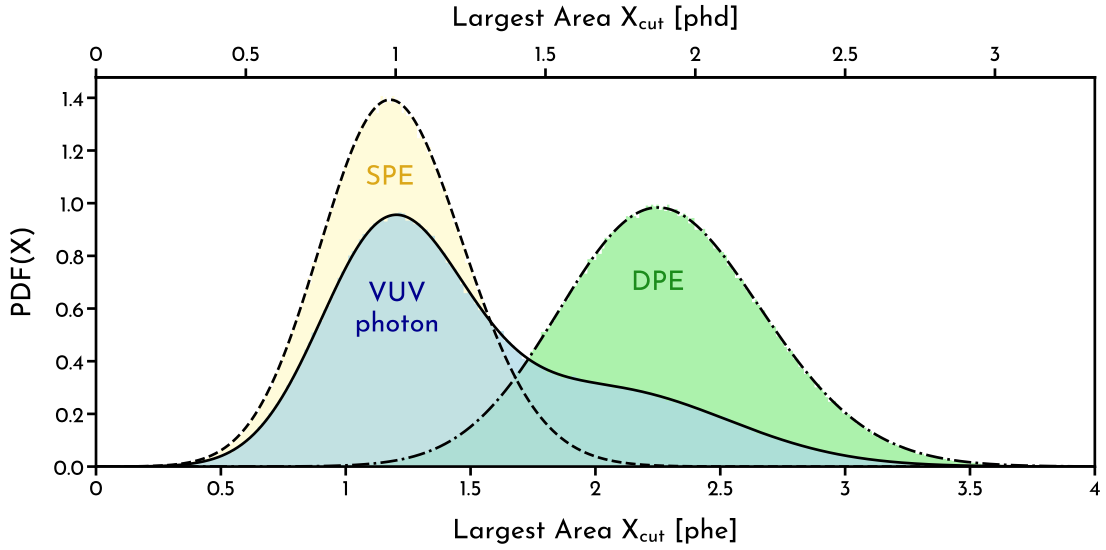



Figure 6.1: Distribution of the largest channel area metric using MC (solid colour) and analytic (black line) methods. Due to the selecting the largest of the two PMT responses the mean of the distribution are biased to the right.

background models are very different, Xe scintillation versus accidental coincidences, meaning the signal and background PDFs must be computed independently.

First let us consider the dark-count pile-up. Dark-counts within a PMT are randomly distributed in time with no-correlation with preceding dark-counts or detected photons and occur independently of any interaction in any other PMT. Such processes are known to follow a Poisson model where the time difference between responses follows

$$f_{dark}(t) = Re^{-Rt} \tag{6.3}$$

for uniformly distributed random variables of mean detection rate R. Assuming uniform dark rate of 18 Hz, as used in the previous study, leads to an $O(100\text{ ms})$ exponential decay function.

Now let us consider the more complicated Xe scintillation case. The time profile of Xe scintillation produced in low-energy interactions, where there is negligible recombination, follows a double exponential model

$$f(t) = \alpha \cdot \frac{1}{\tau_1} e^{-t/\tau_1} + (1-\alpha) \cdot \frac{1}{\tau_3} e^{-t/\tau_3}, \tag{6.4}$$

where $\tau_1$=3.27 ns ($\tau_3$=23.91 ns) is the decay constant for the singlet (triplet) state occupied with a probability of 37% (63%) [157].

The PDF of the time statistic of interest at two-fold, $\delta T = |T_0 - T_1|$ can be computed as

$$f_{Xe}(t) = \frac{1}{\tau_1 + \tau_3}\left[\left\{\tau_3\alpha^2 + \tau_1\left(2\alpha - \alpha^2\right)\right\}\frac{e^{-t/\tau_1}}{\tau_1} + \left\{\tau_1(1-\alpha)^2 + \tau_3\left(1-\alpha^2\right)\right\}\frac{e^{-t/\tau_3}}{\tau_3}\right] \tag{6.5}$$

which upon simplification reveals essentially the same double exponential PDF with a different singlet-triplet ratio

$$f_{Xe}(t) = \beta \cdot \frac{1}{\tau_1}e^{-t/\tau_1} + (1-\beta)\cdot\frac{1}{\tau_3}e^{-t/\tau_3}, \tag{6.6}$$

where the singlet exponential occurring with a probability of $\beta$=19.3%. This result is not as surprising as it may first appear. Consider the second photon from the biased perspective of the first photon, the second must occur later and must be sampled from either the singlet or triplet exponential. This means that the time difference between the first and second photons must be the sum of the singlet and triplet components each occurring with an updated probability accounting for each photon being emitted by either the singlet or triplet state.

### 6.1.3 Optimising median sensitivity in a counting experiment

The search for $^8$B neutrinos undergoing CE$\nu$NS in LZ can be treated as a counting experiment. In this experiment we observe a total number of events N equal to the sum of signal (S) and background (B) components. Each separate trial of such an experiment will observe a different number of signal and background events, with each being sampled from a Poisson distribution. To encapsulate the typical sensitivity of such an experiment to the signal process the *Asimov* dataset, which best represents the underlying statistical process, is used; more formally this dataset will always return the true values of the underlying parameters using the method of maximum likelihood [140].

For a counting experiment where the number of background events is known the median sensitivity is given by

$$Z = \sqrt{2\left[(S+B)\ln\left(1+\frac{S}{B}\right) - S\right]}, \tag{6.7}$$

which returns the typically quoted result $Z = S/\sqrt{B}$ when $S << B$.

To optimise the sensitivity of this analysis, cuts on $\delta T$ and $X_m$ are used. As the PDF of these parameters are independent, we can construct the joint signal and background PDFs as the product of the two separate PDFs. The independence of these parameters similarly allows the

use of orthogonal cuts on each parameter,

$$\delta T < \Delta T_{cut} \tag{6.8}$$

$$X_{max} > X_{cut}, \tag{6.9}$$

with no sensitivity loss.

The signal efficiency and background leakage as a function of the cut parameters in this 2D space are shown in Figure 6.2. The shapes of the two distribution are qualitatively similar,

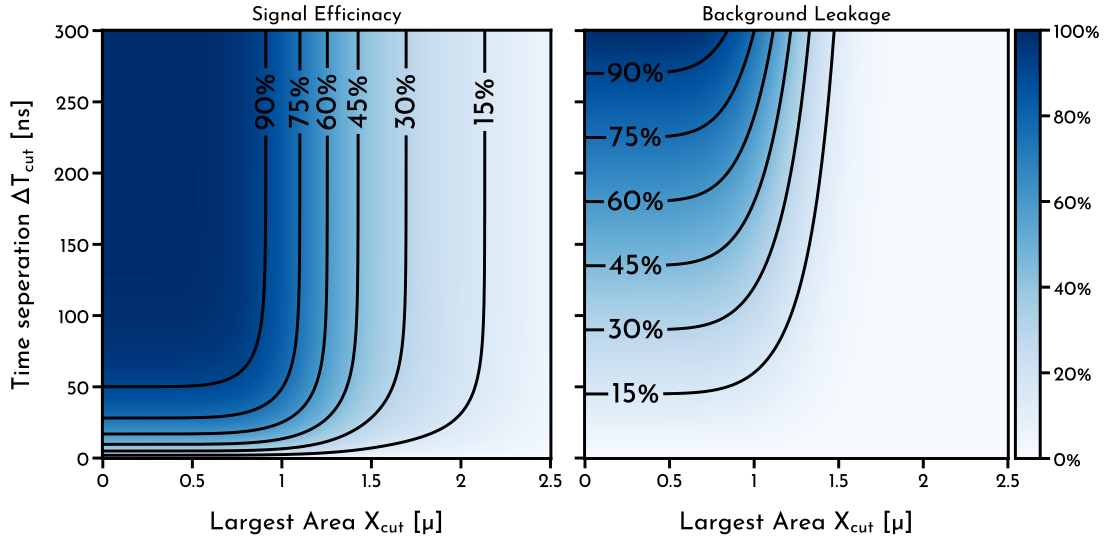



Figure 6.2: Signal efficiency (left) and background leakage (right) for a two-fold analysis using the maximum channel area and difference in PMT response times as discriminating parameters.

greater efficiency for a longer $\Delta T_{cut}$ and smaller $X_{cut}$, as expected. By weighting these 2D spaces by the number of expected events and using them as input values to Equation 6.7 the median sensitivity can be calculated and optimised.

For a live-time of 1000 days we assume that before cuts we will observe the expected number of events according to the Poisson processes. For this study we assume 960 accidental events and 100 two-fold $^8$B events as was considered in the previous study. The Z-score in the 2D space, shown in Figure 6.3, prefers a large $X_{cut}$ and short $\Delta T_{cut}$. Using the *iminuit* minimisation package [158] an optimum median sensitivity of Z = 10.3 was found for $X_{cut}$ = 2.2 phe and $\Delta T_{cut}$ = 57.3 ns.

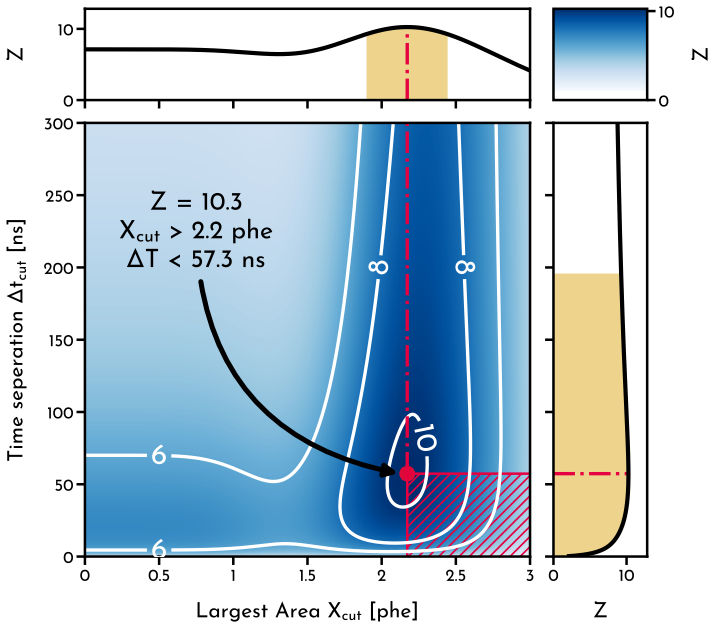



Figure 6.3: Optimisation of the Asimov test-statistic for detecting $^8$B neutrinos using a two-fold coincidence. The optimal event selection, A $\geq$ 2.2 phe and $\Delta$T $\leq$ 64.9 ns, is shown in red.

### 6.1.4 Adding variables

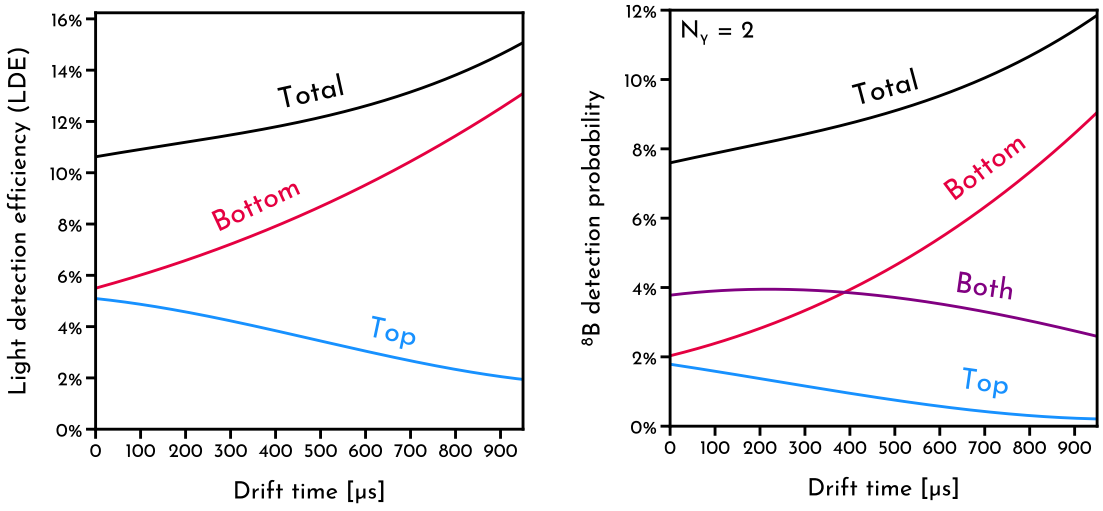
To further increase the sensitivity of this analysis additional discriminating parameters can be added. Two of the most useful are the electron drift-time and the corrected S2 area. Here the signal and background models for each parameter are discussed after which an improved projected sensitivity is calculated.

#### 6.1.4.1 Adding depth (electron drift-time) information

The light detection efficiency (LDE), the probability of detecting a photon from some position $\vec{x}$, in LZ is not spatially uniform and can differ significantly between the two arrays. For medium to high-energy interactions, where the S1 detection probability is approximately 100%, this leads to a spatial variation in the size (integrated area and amplitude) of S1 signals. At low energies, such as those expected from $^8$B, the spatial variation in LDE leads to a similar spatial variation in S1 detection efficiency. Simply put, low-energy events at the scintillation threshold are more likely to be detected in regions of high LDE, leading to these uniformly distributed interactions being observed to follow a spatially dependant PDF.

A detector's LDE map is most easily measured using a dispersed monoenergetic calibration

source which produces a known number of scintillation photons. By taking the ratio of S1 integrated area per array, measured in phd, with the known number of primary scintillation photons the LDE per array can be calculated. The measured LDE per array in LZ measured using the total S1 from $^{83m}$Kr decay is shown in Figure 6.4a.




(a) Photon detection probability.

(b) 2-fold $^8$B detection probability.

Figure 6.4: The photon and $^8$B detection probabilities calculated per array.

LZ's spatially averaged LDE is much higher in the lower array—this effect chiefly originates from total internal reflection at the liquid-vapour boundary at the top of the detector. The spatial variation in the bottom array's LDE has a much larger absolute dependence on electron drift-time (depth) than that of the top array. From this measurement it is clear that $^8$B events are more likely to be detected near the bottom of the detector by the bottom array.

To better capture the variation of the signal PDF with electron drift-time, the probability of detecting two-fold events via BB, TB, BT, and TB combinations, where T (B) represents detecting a photon in the top (bottom) array, should be used. This probability can be computed by summing the binomial probability of successfully detecting two photons from $N_\gamma$ scintillations photons, where the mean probability of producing $N_\gamma$ photons from $^8$B is calculated using NEST:

$$P = \sum B(2|N_\gamma, p_{array}) \times P(N_\gamma|^8B). \tag{6.10}$$

By using the LDE shown in Figure 6.4a the $^8$B signal PDF in Figure 6.4b was produced. We observe that the detection probability in the bottom array is both significant higher and has

significantly greater spatial variation than any other detection topology.

In contrast, accidental backgrounds, the most significant background at low energies, should not exhibit the same spatial dependence and will exhibit a different top-bottom asymmetry profile. These occur for two reasons depending on the source of the accidental S1 pulse. If the accidental S1 is from genuine xenon scintillation will have a different detection profile than would be expected for the observed interaction depth. If the accidental S1 originates from PMT effects, such as dark counts, it will have a much more uniform distribution across the PMT arrays compared to scintillation light. For these reasons, the inclusion of this spatial dependence and the fraction of light detected in each array should reduce the dominant accidental backgrounds in this analysis.

By performing this analysis using only the bottom array without position dependence reduces the number of dark-count pile up events from 960 to 240 (75% rejection) whilst retaining 53% of the 100 $^8$B events leading to an improvement in the expected median sensitivity. By including spatial signal and background PDF the strong variation in the $^8$B signal with depth against the uniformly distributed accidental background should lead to further improvements in median sensitivity.

#### 6.1.4.2 Adding corrected S2 area information

Low-energy $^8$B interactions will produce small S2 signals, whereas LZ's observed accidental background S2 spectrum which extends to larger S2s, as seen in Figure 6.5. By selecting event with an S2 smaller than a given size the signal/background ratio can be further improved with a S2 $< 10^{3.25}$ selection achieving 100% signal efficiency with ~65% background rejection.

### 6.1.5 Re-evaluation of the sensitivity

The optimal median sensitivity for $^8$B neutrinos against an accidental background driven by dark-count pile-up, using the (maximum channel area, channel time separation, corrected S2, electron drift-time) parameter space in the bottom array is Z = 13.7, as shown in Figure 6.6.

The addition of the corrected S2 area produces a highly selective cut against accidental backgrounds. From this study the addition of an electron drift-time cut has limited impact, the sensitivity preferring to maximise signal acceptance. A more sophisticated PLR analysis may be able to make better use of the electron drift-time parameter and combine the three TT, BB,

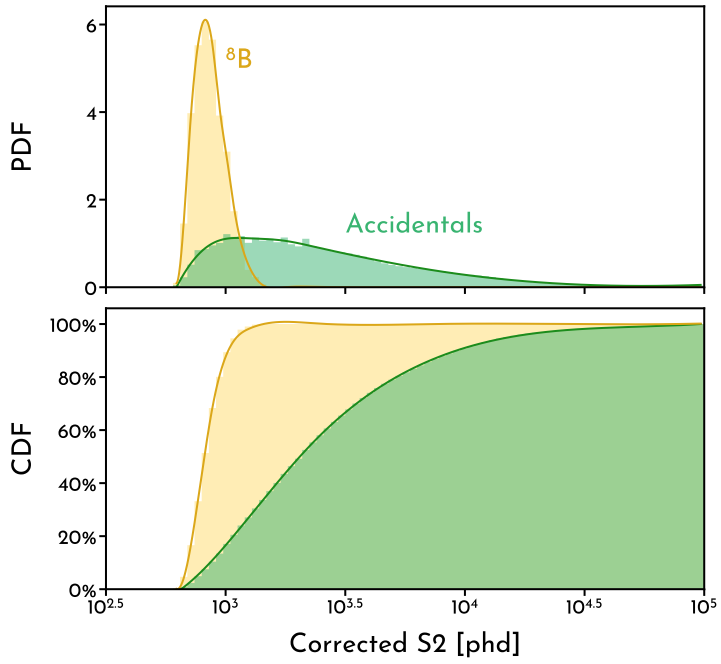



Figure 6.5: Marginalised S2 PDFs for simulated $^8$B events and observed accidental events. By selecting events with smaller S2 signals the signal/background ratio can be further increased.

and TB/BT combinations instead of only using BB as done here, to attain a greater median sensitivity.

## 6.2 Improving LZ's photon timing reconstruction

Using the difference in PMT detection times to select $^8$B neutrinos requires all the TPC PMTs to be well synchronised and the photon time-of-flight (TOF) accounted for as a function of interaction vertex position. In this section measurements of the depth dependant TOF corrections are presented alongside PMT timing offsets both between and within the arrays. These measurements were performed using high-energy $\alpha$-particle waveforms which allow for the study of spatially dependant systematic effects.

### 6.2.1 Inter-array difference in photon time-of-flight

It takes a small, but non-negligible, amount of time for scintillation photons to reach a PMT from the interaction site. This TOF can be modelled assuming a VUV photons velocity of 0.6 c, this value has been calculated assuming a refractive index of 1.69 within the VUV and measured experimentally in Refs [159, 160]. Due to the compact design of LXe TPCs the difference in

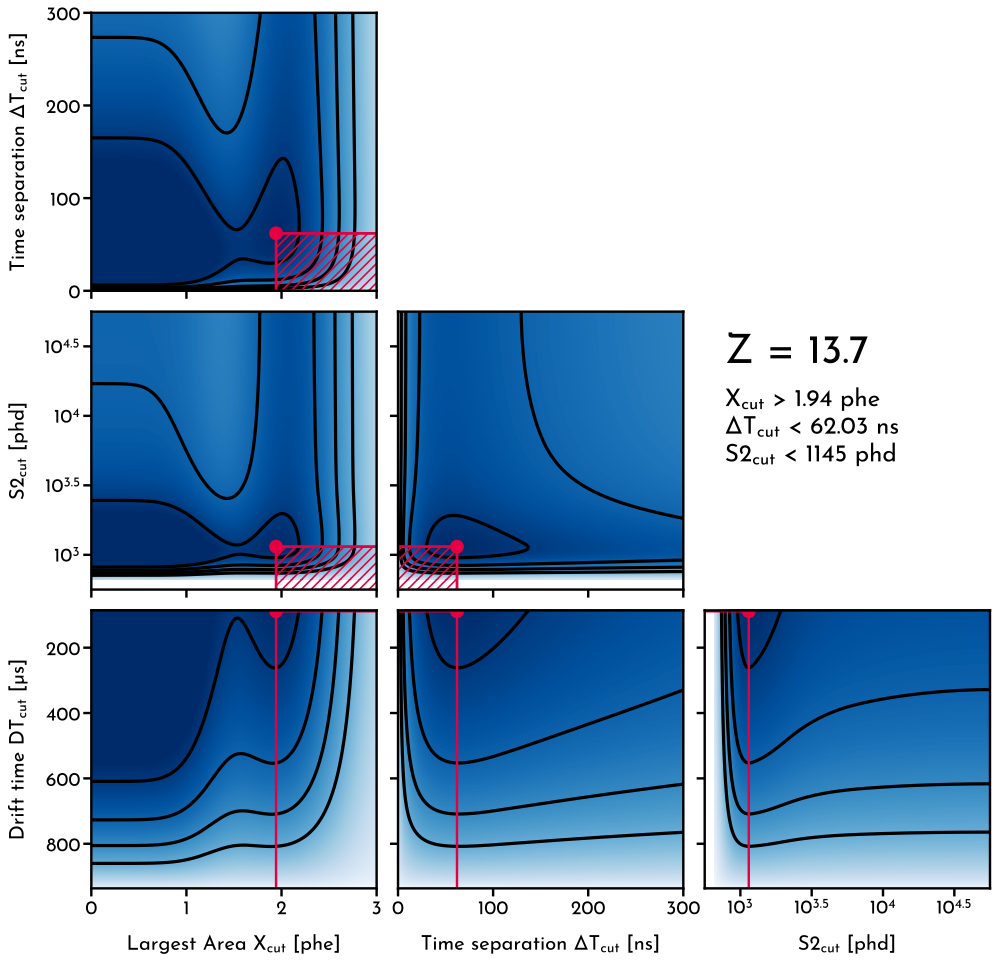



Figure 6.6: The Asimov test statistic for a two-fold $^{8}$B discovery against a dark-count S1 accidental background. This result includes electron drift-time and integrated S2 area as discriminating parameters to the result shown in Figure 6.3.

photon TOFs between the two PMT arrays is often ignored. With the emergence of tonne-scale detectors the difference in TOF across the TPC can be noticeable; in LZ the inter-array photon TOF can be clearly seen for high energy interactions, such as those produced in α-decay, as shown in Figure 6.7. By modelling the shape of the summed waveforms with an exponentially extended Gaussian[1], the TOF correction can be measured with a greater resolution than the 10 ns (100 MHz) sampling used in LZ.

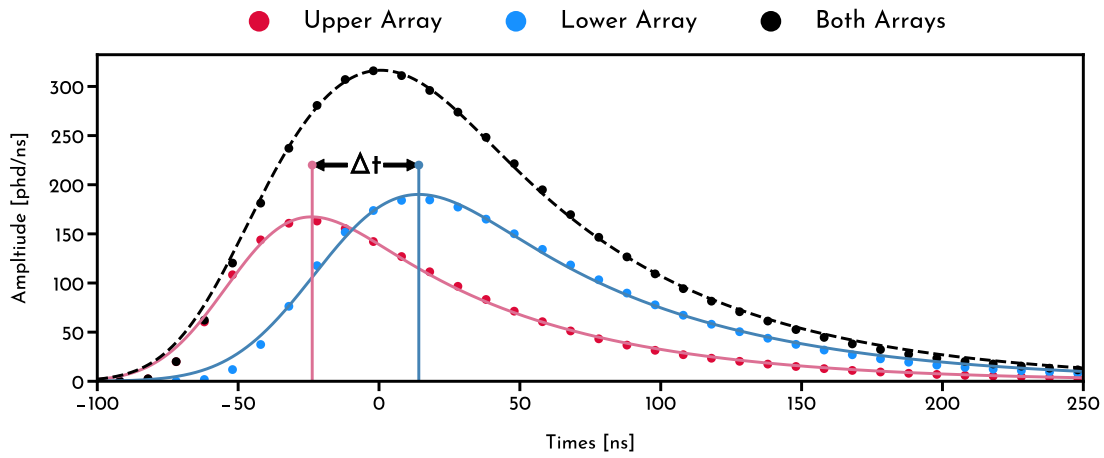



Figure 6.7: An α-decay single scatter observed near the top of LZ. The per array summed waveforms are shown in blue (lower array) and red (upper array) alongside the total TPC summed waveform in black. The points represent LZ observed amplitudes whilst the lines represent a fitted model. Here the difference in photon TOF (Δt) can be observed with the upper array detecting the photons before the lower array.

This difference in photon arrival time is expected to grow linearly with vertical displacement from the midpoint between the two PMT arrays. By fitting multiple α-decay events with the aforementioned model the relationship between the TOF correction and the depth of an interaction can be mapped, as shown in Figure 6.8. By fitting the relationship between the Z coordinate and the difference in photon arrival times a correction factor of

$$\Delta t\ [\text{ns}] = \frac{\text{electron drift-time}[\mu\text{s}] - 652.14}{14.30} \tag{6.11}$$

is obtained. In LZ this leads to a maximum Δt between the two arrays of approximately 40 ns, which can be ignored for most analyses but should be taken into account when exploiting pulse-shape discrimination (PSD), and a global offset of 7.3 ns between the two arrays attributed to the difference in signal cable lengths. An interesting application of this result is the depth

[1]This model is not physically motivated but is adequate to parametrise the pulse shape.

reconstruction of large isolated S1 pulses using the $\Delta t$ between the two arrays. Using this reconstruction accidental events can be removed by comparing the observed $\Delta t$ to that expected from Equation 6.11.

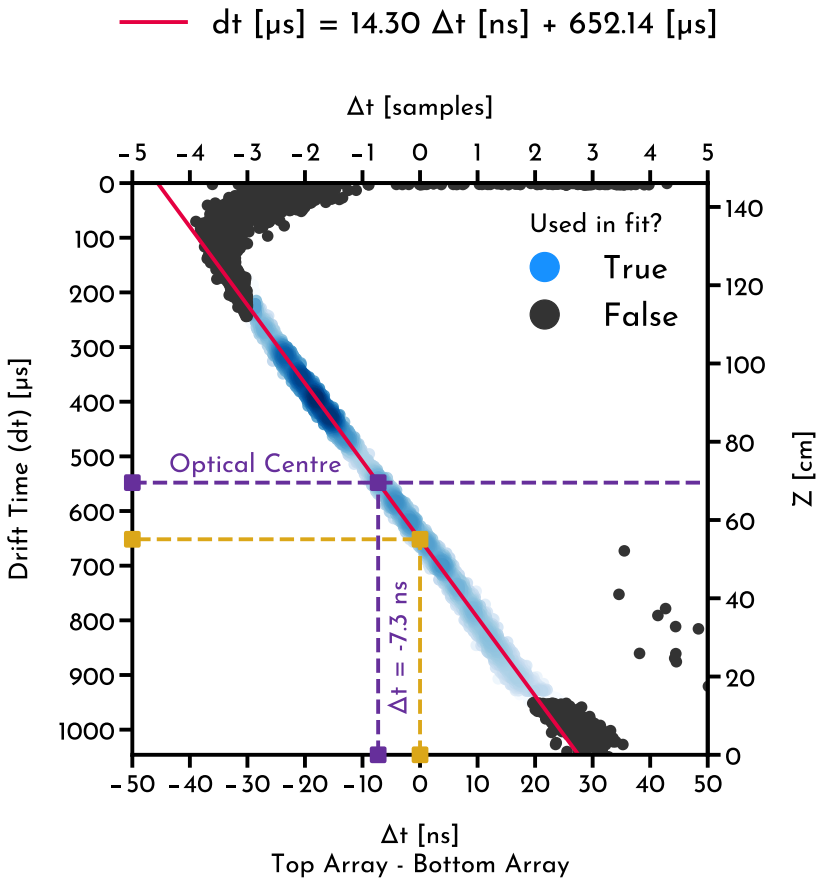



Figure 6.8: The relationship between electron drift-time and the difference in photon arrival time between LZ's two PMT arrays. The scatter points, coloured by the local data density, are observations in LZ, the purple line is the optical centre of the TPC, the yellow line in the depth at which the two arrays observe the light simultaneously. By fitting the observations a linear model, visualised by the red line, was observed which demonstrates a 7.3 ns offset between the two arrays.

Whilst this effect can still be mostly ignored in LZ the effects is expected to be much more significant in the 3 m TPC proposed by the XLZD consortium [76]. Extrapolating the result sound in Figure 6.7 leads to a projected maximum $|\Delta t|$ of approximately 80 ns at the top or bottom of the TPC. By applying this projected offset to LZ data the expected S1 pulse shape for interactions near the top and bottom arrays in a 3 m can be calculated, as shown in Figure 6.9.

The distortion of the S1 shape at maximal TOF difference in LZ leads to a minor broadening

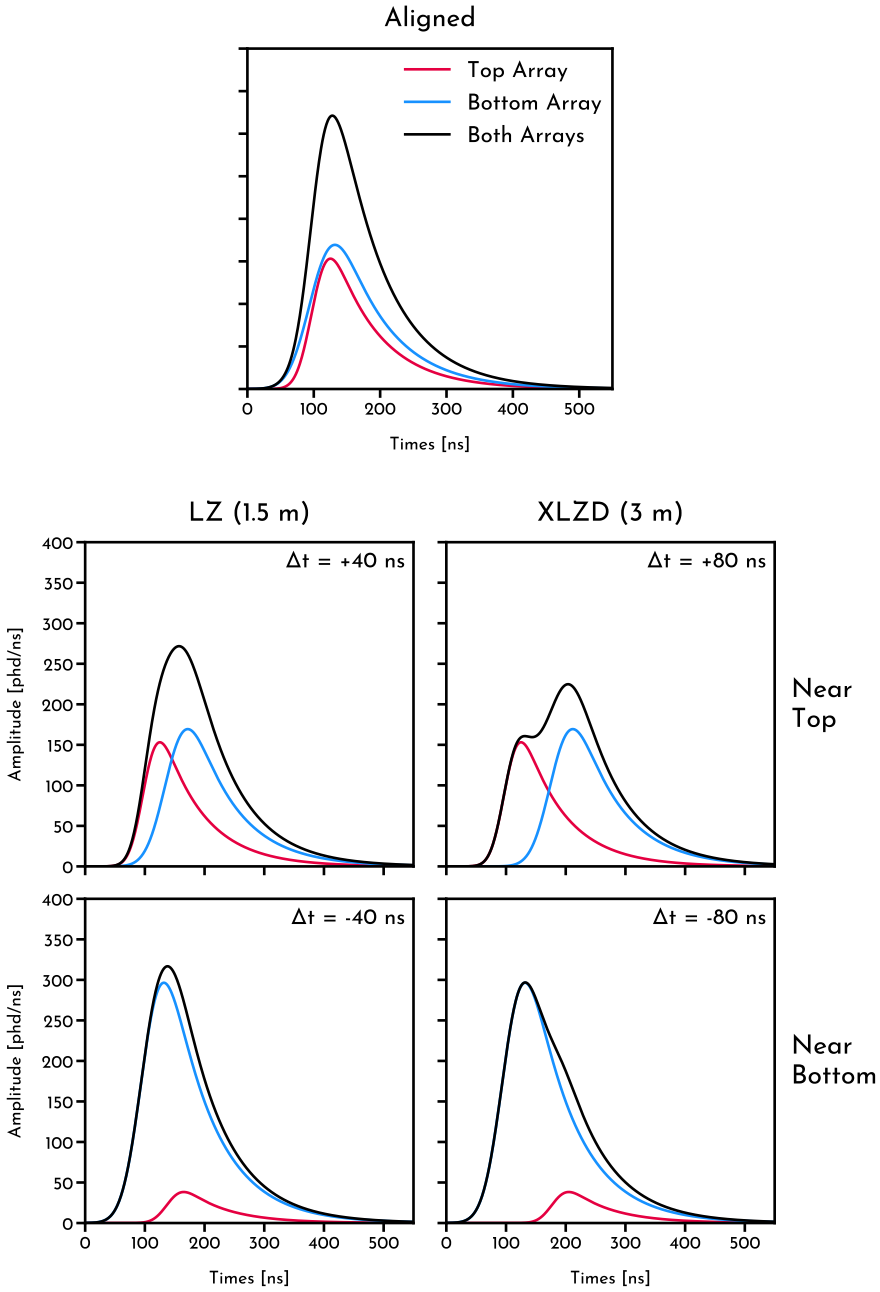



Figure 6.9: Summed waveforms for the top (red) and bottom (blue) arrays alongside the total TPC summed waveform (black) for several interaction depths. The singular top panel shows how an S1 in the centre of a TPC will be observed with the two arrays detecting photons simultaneously leading to a new narrow pulse width. The bottom two-by-two grids shows how the total S1 shape is distorted by the maximal difference in photon TOF, with the left columns displaying measured LZ (1.5 m) waveforms and the right column showing waveforms extrapolated for XLZD (3 m). The S1 pulses shown in the top (bottom) row show events near the top (bottom) of the TPC. The difference in array amplitudes between the top and bottom panels originate from the measured top-bottom asymmetry measured in LZ which exists due to geometric effects and reflection at the liquid surface.

of the S1 pulse. When this effect is scaled up to a 3 m detector the S1 response from pulses near the top array become so malformed as to become unrecognisable as xenon scintillation, without correction this will lead to difficulties in pulse classification. The distortion experienced near the bottom array, which adds a shoulder to S1 tails, is much weaker as the majority of S1 light is detected in the bottom array, assuming XLZD has the same top-bottom asymmetry (TBA) as LZ's. From these observations it is clear that these corrections must be applied for all analyses in a future 3 m detector whereas they are only needed in LZ for analyses exploiting PSD, such as the $^8$B analysis discussed previously.

### 6.2.2 Measuring individual PMT timing offsets with $\alpha$-decays

The timing offset between individual PMTs can be obtained using the above fitting methodology applied to the individual PMT signals. A photon emitted at some true time $\phi$ is detected by some PMT, labelled i, at a time

$$t_i = \phi + \frac{L_i}{v} + \tau_{i,k}, \tag{6.12}$$

where $L_i$ is the distance the photon travels before being detected by the PMT, v is the photon velocity, and $\tau_{i,k}$ is the temporal offset of the PMT to some other reference PMT labelled k. The difference in photon detector time between two PMTs can be written as:

$$t_i - t_j = (\phi - \phi) + \left(\frac{L_i - L_j}{v}\right) + \left(\tau_{i,k} - \tau_{j,k}\right) \tag{6.13}$$

allowing the PMT timing offset to be written as

$$\tau_{i,j} \equiv \tau_{i,k} - \tau_{j,k} = \left(t_{i,k} - t_{j,k}\right) - \left(\frac{L_i - L_j}{v}\right) \equiv \Delta t_{i,j} - \frac{\Delta L_{i,j}}{v}. \tag{6.14}$$

Using this equation, the offset between PMTs i and j, $\tau_{i,k}$, can be measured for each event using the 3D vertex reconstructed afforded by the S1-S2 pair.

For this measurement three considerations were made: firstly, only PMT housed in the same array will be compared due to the inter-array offset observed in Figure 6.8; secondly, event near the TPC walls were rejected as these would have a maximal difference in TOF between PMTs housed in the same array and could lead to anomalous waveform shapes due to geometric effects; and finally, the offset between PMTs i and j will be calculated as the average of the

offsets measured for all other PMTs housed in the same array to account for any minor errors in the TOF correction.

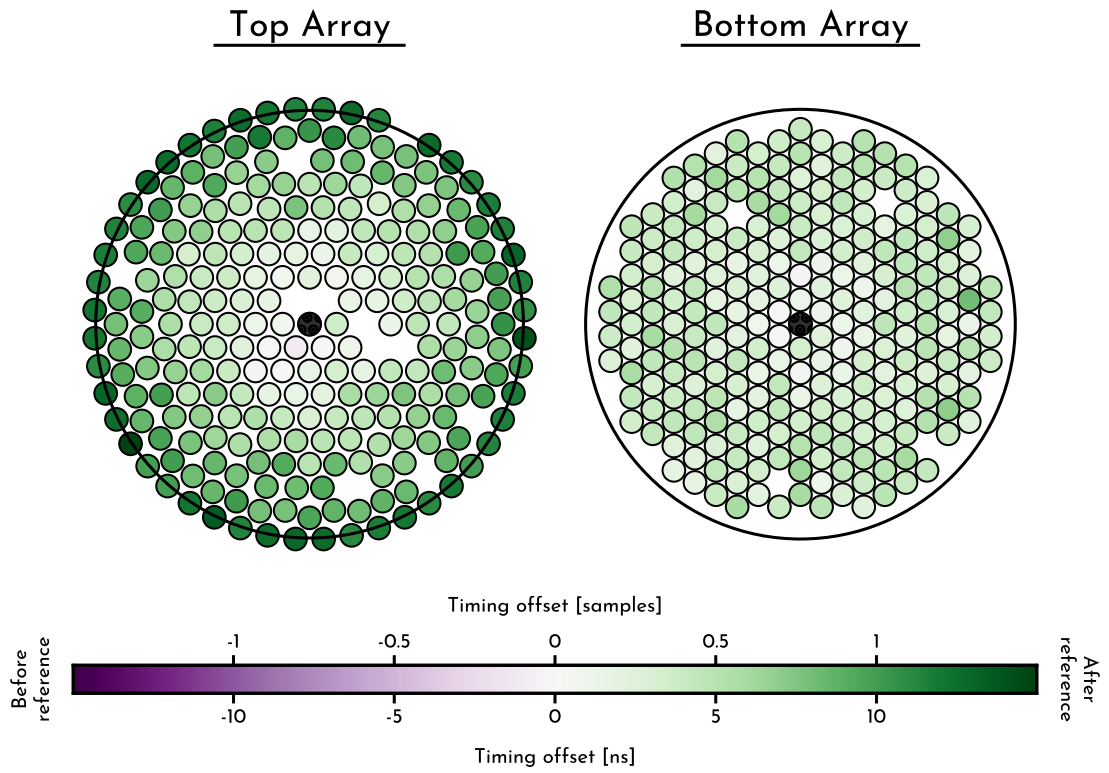



Figure 6.10: Average of the measured intra-array PMT timing offsets with respect to arrays central PMT.

Using this method the PMT timing offsets, shown in Figure 6.10, were calculated. These results demonstrate that the asynchronicity of the PMTs within each array is minimal with most offsets being less than one 10 ns sample. Some spatial dependence was observed in the upper array. The origin of this is not yet known but has been observed in LED timing measurements and is currently attributed to the difference in PMT signal cable lengths.

## 6.3 Conclusion

In this chapter a sensitivity study of LZ's ability to observe $^8$B neutrinos via CE$\nu$NS is presented. This study investigates the reduction of the scintillation threshold from three-fold S1s to two-fold using the DPE effect and detected photon times to reject dark count pile-up. First the outline of a previous study was re-evaluated using analytic methods, simplifying the computation of the signal and background PDFs and facilitating the exploitation of the detector response at the individual PMT level.

This study is then augmented through the inclusion of electron drift-time and S2 pulse area parameters; the former exploiting the observed signal PDF's dependence on the light detection efficiency, and the latter exploiting the difference in S2 pulse areas between the $^8$B and isolated S2s. A particularly interesting observation of this study is the significant electron drift-time dependence of the signal PDF for events where both photons are detected in the bottom array. The inclusion of these two parameters increases the median sensitivity calculated using an Asimov dataset lasting 1000 live-day by ~30%.

To understand the detector timing response, measurements of the inter and intra array PMT timing offsets were performed using waveforms from $\alpha$-decay. By fitting the offset between the summed upper and lower array waveforms, the bottom array was found to detect photons from the optical centre of the TPC 7.3 ns (0.73 PMT samples) earlier than the top array. By repeating this fitting procedure with individual PMT waveforms grouped by array, the timing offset between PMTs housed in the same array was calculated. The vast majority of these offsets are less than 10 ns (1 PMT sample) with the largest offsets located in the upper array at large radii. The measurement of these timing offsets is critical to enhancing LZ's ability to detect time resolvable backgrounds, for example S1 signals from Cherenkov emission in the windows of displayed PMTs, and has been implicitly employed in the $^8$B sensitivity presented here.

Finally, the linear TOF model developed above was applied to a 3 m detector, as proposed by the XLZD consortium, demonstrating that the TOF in such a detector would significantly distort observed S1 pulses, particularly those near the top of the detector, and would require correction.

# 7

# Low Energy Calibration in Liquid Xenon Detectors

## 7.1 Introduction

Whilst primarily designed for detecting heavy WIMPs, liquid noble-gas detectors have demonstrated world-leading sensitivity to lower mass dark matter candidates. A substantial gain in sensitivity is achieved by removing the scintillation threshold and studying interactions purely from substantial ionisation (S2) signals [83, 161]. Whilst LXe TPCs are sensitive to individual extracted electrons, S2-only analyses are limited to signals larger than a few extracted electrons to remove grid-emission backgrounds.

To date few calibrations have been performed at the lower energy frontier attainable using such analyses (taken to be 50 eV to 150 eV for this study), leading to systematic uncertainties of the ionisation yield in this regime. The propagation of these uncertainties leads to uncertainties on the modelled signal and background PDFs and the final analysis sensitivity or measured cross-section. To better understand the sensitivity of such analyses requires additional calibration close to the ionisation threshold.

This chapter describes several studies using existing calibration sources to perform yield measurements at ultra-low energies within LXe TPCs. The interaction considered within these studies are: photon-atom (coherent gamma elastic-scattering) scattering, photon-electron (Compton) scattering, and unexplored electron capture decay paths of $^{127}$Xe. These potential calibrations are not specific to LZ and could be applied to both current tonne-scale experiments and kg-scale R&D TPCs.

## 7.2 Coherent Gamma Elastic Scattering

By exploiting scattering kinematics from D-D neutrons, LUX was able to probe the low energy frontier in LXe detectors [62]. Multiple scattering events, where the scattering angle can be reconstructed, allow precise reconstruction of the deposited energy. Here the feasibility of using multiple scatter events where a photon scatters coherently off an entire xenon atom is investigated.

Typically, photon-atom scatterings are split into two categories: photo-nucleus (nuclear Thomson), and photo-electron (Rayleigh and Delbrück). If the detection mechanism is only observable in terms of the initial and final states with no information on which specific process occurred

then the scattering amplitude is the sum of the possible processes, this is termed *coherence* [162]. If the total kinematic cross-section is constant within the centre-of-mass (zero momentum) frame then the process is *elastic*.

Coherent gamma elastic-scattering (CGES) has a total scattering amplitude of

$$A_{total} = A_{Ray.} + A_{Thom.} + A_{Del.}, \tag{7.1}$$

where $A_{Ray.}$, $A_{Thom.}$, and $A_{Del.}$ represent the Rayleigh, nuclear Thompson, and Delbrück scattering amplitudes, leading to a total scattering cross-section of [163]

$$\sigma_{total} \propto A^2_{total}. \tag{7.2}$$

With this model of the CGES process, theoretical predictions of the differential scattering cross-section can be produced with the predictions for xenon displayed in Figure 7.1 alongside data for 59.54 keV photons.

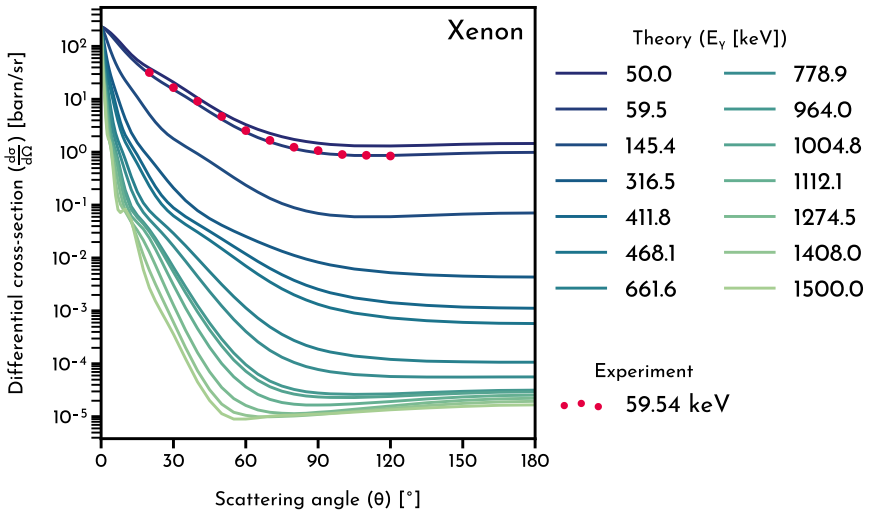



Figure 7.1: Theoretical differential cross-sections for CGES on xenon [164]. For validation measured values for 59.54 keV photons scattering on xenon are plotted in red [165].

In this process a photon of energy $E_r$ will scatter coherently off an entire atom of mass $M_A$ leading to an atomic recoil of energy

$$E_r[GeV] = E_\gamma[GeV] \times \left(1 - \left[1 + \frac{E_\gamma}{M_A} \times (1 - \cos(\theta))\right]^{-1}\right) \tag{7.3}$$

where the miniscule electron mass is ignored and natural units used. For a given target and incident photon energy, the recoil energy of the target atom is singularly dependent on the scattering angle, allowing the maximum recoil energy to be computed as

$$E_r = E_\gamma \left( \frac{2E_\gamma / M_A}{1 + 2E_\gamma / M_A} \right) \tag{7.4}$$

for back-scattering ($\theta = \pi$ rad.) interactions. By exploiting the interaction vertex reconstruction available in LXe detectors it should be possible to infer the recoil energy of such interactions allowing for specific yield measurements to be performed, similar to the D-D yield measurements performed by LUX [62].

To evaluate the feasibility of using this process to calibrate LXe detectors, such as LZ, the CGES process was simulated using the Geant4 simulation toolkit. To optimise this simulation for CGES all other photon interactions, including incoherent scattering from CGES's constituent processes outlined in Equation 7.1, were disabled so that only this comparably rare process was simulated. The results of these simulations for several photon energies are shown in Figure 7.2.

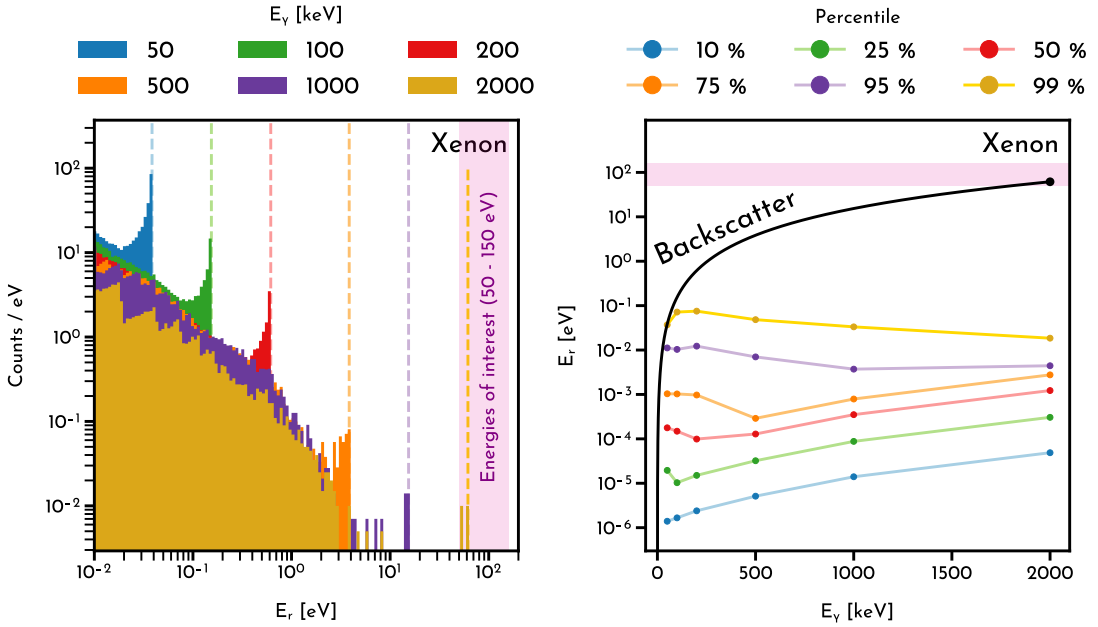



Figure 7.2: Results from a Geant4 simulation of CGES on LXe for several photon energies alongside the calibration range of interest (50–150 eV) shown in pink. (Left) Xenon recoil spectra due to CGES plotted alongside the maximum recoil energy produced though backscattering. (Right) the 10, 25, 60, 75, 95, and 99 percentiles of the xenon recoil spectra.

The recoil energy and forwardness of the scattering process are both proportional to the

incident photon energy. For the majority of photons ($E_\gamma < 2\,MeV$) the energy deposition is insufficient to calibrate LXe detectors. A 2 MeV photon would produce sufficiently energetic recoils for LXe detectors, with the back scatter energy within the region of interest as seen in Figure 7.2. Unfortunately, the strong forward nature of this process makes such interactions so unlikely as to be impractical. When taking into account the other, much more likely, scattering topologies disabled in this study it is clear CGES cannot reasonably be used as a calibration source for LXe detectors. There is the possibility of this process being of interest to other, much lighter, targets but no study of any such applicability or lack there of was performed here.

## 7.3 Compton Scattering

An alternative photon scattering process that can be used to calibrate at low energies is Compton scattering. This process, where the photon scatters off a single orbital electron, can lead to a continuum of recoil energies, which like CGES can be tagged by measuring the scattering angle. This process produces ERs which are useful for producing ionisation-only signals applicable to S2-only searches of low-mass WIMPs.

Observations by Compton in 1923 demonstrated that x-rays scattered off atomic electrons have a longer wavelength than the incident x-ray. This change in the x-ray wavelength is a function of the scattering angle and obeys

$$\Delta\lambda = \frac{2h}{m_e c}\sin^2(\theta/2) \tag{7.5}$$

where $\Delta\lambda$ is the shift in x-ray wavelength, $\theta$ is the scattering angle, and $m_e$ is the mass of the electron [166]. In a particle scattering context this one-to-one mapping of scattering angle to recoil energy is more naturally expressed as

$$\frac{E'_\gamma}{E_\gamma} = \left(1 + \frac{E_\gamma}{m_e}\left[1 - \cos\theta\right]\right)^{-1}, \tag{7.6}$$

where $E_\gamma$ ($E'_\gamma$) is the energy of the original (scattered) photon and natural units have been used. If we assume the electron is free and that it undergoes elastic scattering, the electron will recoil with an energy equal to the energy loss of the incident photon. Using Equation 7.6

this can be expressed as

$$E_r^{(ER)} = E_\gamma - E'_\gamma = E_\gamma \left( \frac{k(\theta)}{1+k(\theta)} \right), \tag{7.7}$$

where

$$k(\theta) = \frac{E_\gamma}{m_e}(1 - \cos\theta). \tag{7.8}$$

The angular differential cross-section for a single electron undergoing Compton scattering is described by the Klein-Nishina cross-section [167] and obeys

$$\frac{d\sigma_{KN}}{d\Omega} = \frac{1}{2} r_e^2 \left( \frac{E'_\gamma}{E_\gamma} \right)^2 \left( \frac{E'_\gamma}{E_\gamma} + \frac{E_\gamma}{E'_\gamma} + \sin^2\theta \right), \tag{7.9}$$

where $r_e$ is the classical electron radius. This cross-section can be seen in Figure 7.3 as a function of photon energy and scattering angle. A key observation of this process is that the backscatter probability is inversely proportional to the incident photon energy.

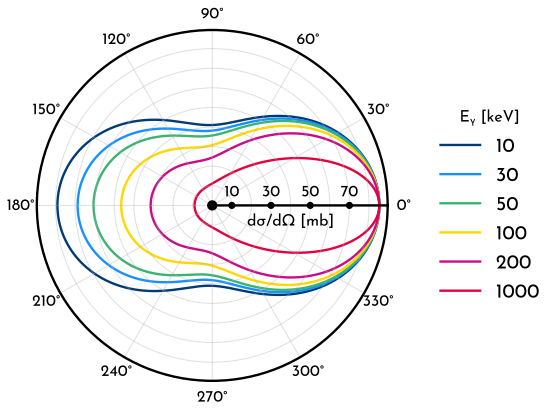



Figure 7.3: The Klein-Nishina (angular) differential cross-section as a function of scattering angle for several photon energies. The key observation of this calculation is that Compton scattering increasingly prefers shallow scattering as the photon energy increases.

Using Equations 7.7 and 7.9 the cross-section for recoils within a specific energy range ($E_{min}$, $E_{max}$), for a photon of energy $E_\gamma$ scattering between $\theta^\gamma_{min}$ and $\theta^\gamma_{max}$ degrees, can be calculated as

$$\sigma_{KN}|_{E_{min}}^{E_{max}} = 2\pi \int_{\theta_{min}(E_\gamma)}^{\theta_{max}(E_\gamma)} \left( \frac{d\sigma_{KN}}{d\Omega} \right) d\theta \tag{7.10}$$

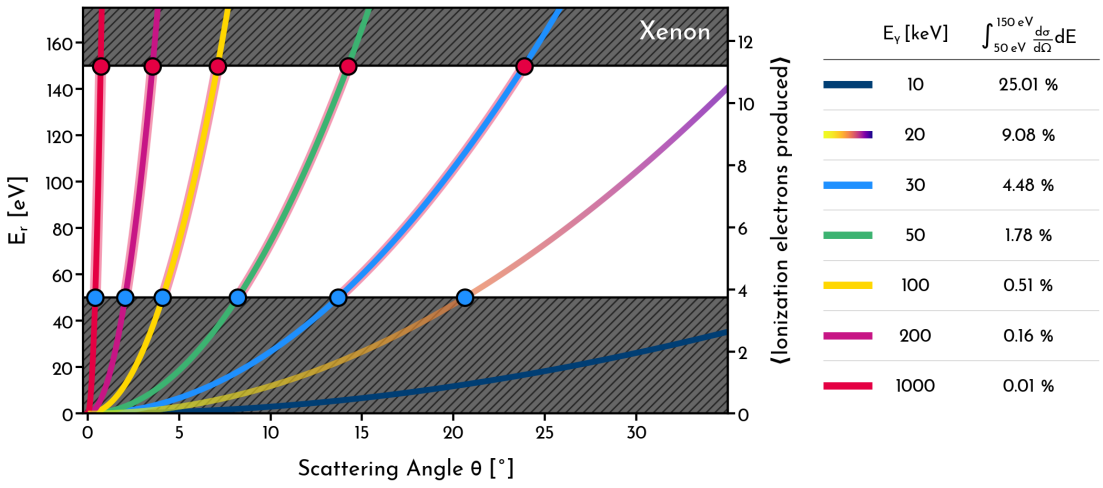
where $\theta_{m.}(E_\gamma)$ is the scattering angle required to produce an electron recoil of $E_m$, computed

as

$$\theta_r(E_\gamma) = \cos^{-1}\left(\frac{E_\gamma - E_r - \left(E_r/E_\gamma\right) m_e}{E_\gamma - E_r}\right). \tag{7.11}$$

This process can provide a source of almost arbitrarily energetic electrons, within the energy scales relevant to LXe detectors, as long as the incoming photon is of sufficient energy. Recoils via Compton scattering can be tagged using the known relationship of the incoming photon energy (from a calibration source) and the (measured) scattering angle. To evaluate the feasibility of this calibration method for a LXe target the same 50 eV to 150 eV range of interest used previously is employed.

In Figure 7.4 the electron recoil energy is plotted as a function of scattering angle for several photon energies alongside the energy ROI and its associated scattering angles. The Klein-Nishina cross-section over this angular range is calculated with the fraction of events within this energy region displayed in the accompanying table. From these calculations we observe that the percentage of events in the ROI is inversely proportional to the photon energy, and is driven by higher energy photons preferring to forward scatter.




| $E_\gamma$ [keV] | $\int_{50\,eV}^{150\,eV} \frac{d\sigma}{d\Omega} dE$ |
|---|---|
| 10 | 25.01 % |
| 20 | 9.08 % |
| 30 | 4.48 % |
| 50 | 1.78 % |
| 100 | 0.51 % |
| 200 | 0.16 % |
| 1000 | 0.01 % |

Figure 7.4: The Compton electron's recoil energy as a function of scattering angle for several photon energies (block colours). The yellow-green gradient coloured line shows the Klein-Nishina cross-section for a 20 keV photon with the colour representing the differential cross-section. The two scattering angles that define the $E_r \in (50\text{ keV}, 150\text{ keV})$ are shown by blue and red circles respectively. The table on the right contains the fraction of the interactions that will deposit energy between 50 eV and 150 eV, as calculated by integrating the differential Klein-Nihsina cross-section between the blue and red circles.

Considered in isolation Compton scattering appears an attractive form of calibration par-

ticularly by using low energy photons already present in LZ from LXe x-rays emission. To better understand the feasibility of such a calibration the cross-section for interactions in the ROI was compared to the total Compton and photo-electric cross-sections in Figure 7.5. The Compton cross-section was computed using the analytic formulas above, Geant4, and quoted from the NIST's XCOM database whilst the photo-electric cross-section is solely from the XCOM database [168].

From these calculations and simulations it is clear that such a calibration is difficult. At high energies, where we could employ $\gamma$-ray sources and thus be able to reconstruct the scattering angle from the known photon origin, we would struggle to get the required statistics due to the comparably low cross-section for the required forward facing Compton scatters. Alternatively, if we use low-energy xenon x-rays from within the xenon target we would have a higher total cross-section however, we would still face a similar low interaction probability due to the increased total Compton cross-section and would have difficulties in tagging the origin of the photon which is required for reconstructing the scattering angle and energy.

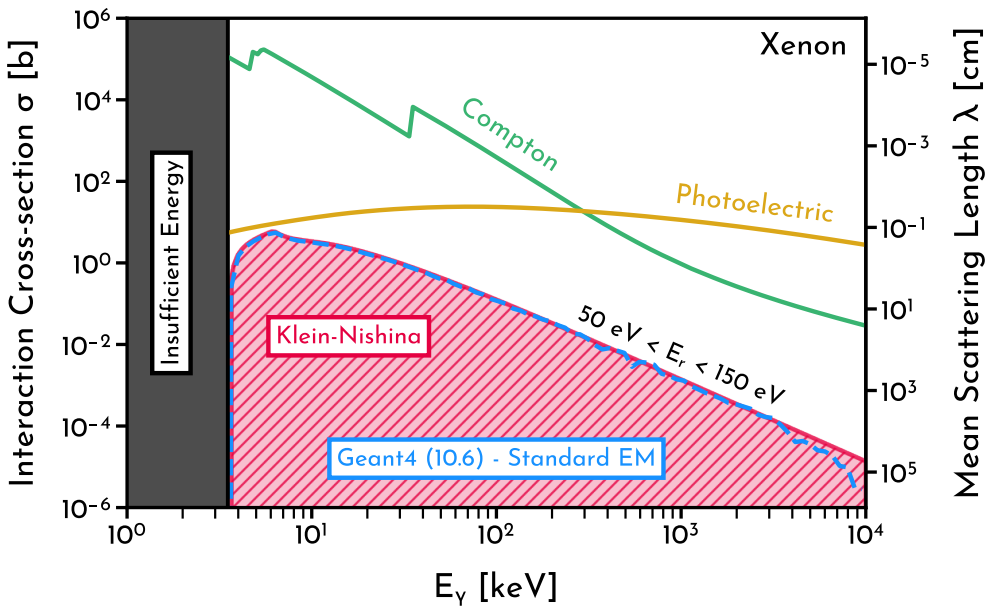



Figure 7.5: The cross-sections for photons interacting with liquid xenon. The photoelectric and Compton cross-sections are from the XCOM database [168]. The cross-section for Compton scattering depositing between 50 eV and 150 eV calculated using the Klein-Nishina formula and Geant4 are shown in red and blue.

## 7.4 $^{127}$Xe Orbital Electron Capture

Here a general overview of the electron capture (EC) processes alongside a more thorough description of $^{127}$Xe electron capture. This isotope, of interest to LZ both as a calibration source and as a source of background, decays into $^{127}$I with a 36.4 day half-life.

Electron capture is interesting within the context of two-phase xenon TPCs for two reasons: Firstly, EC provides a source of monoenergetic low-energy events which can be used for detector calibration as demonstrated by LUX [59] and XENONnT [169]; Secondly, due to its connection to the very rare double EC process. In double EC two orbital electrons interact with two nuclear protons to produce two neutrons and either two or zero neutrinos, with the neutrino-less case requiring neutrinos to Majorana in nature. The two neutrino case has been observed in $^{132}$Ba [170], $^{78}$Kr [171], and most recently in $^{124}$Xe by the XENON1T experiment which this decay being the rarest decay processes observed to date [172].

### 7.4.1 The orbital electron capture process

Isotopes with a superabundance of protons can decay via two processes: positron emission and EC of an orbital electron. Electron capture, first observed in 1922 [173], is where an orbital electron interacts with a nuclear proton producing a neutron and an electron-neutrino which at the particle level can be written as

$$ {}^{1}_{1}\mathrm{p} + {}^{0}_{-1}\mathrm{e}^{-} \rightarrow {}^{1}_{0}\mathrm{n}^{\star} + {}^{0}_{0}\,\nu_{e}. \tag{7.12} $$

In the atomic context this transforms an atom ${}^{N}_{Z}\,A$ into ${}^{N}_{Z\text{-}1}\,A^{(\star)}$, which is normally in an excited nuclear state, with a hole in one of the atomic orbitals

$$ {}^{N}_{Z}\mathrm{A} + {}^{0}_{-1}\,e^{-}_{\mathrm{orbit}} \rightarrow {}^{N}_{Z\text{-}1}\mathrm{A}^{(\star)} + \nu_{e}. \tag{7.13} $$

The probability of capturing an electron from a particular state can be most simply thought of as being proportional to the volume integral of the orbital wavefunction within the nucleus; for a more complete description of the electron capture calculations the reader is referred the review in Ref [174]. Electron capture, like other atomic transitions, obeys selection rules which determine how "forbidden" a particular transition is, in this case the selection rule requires that

$m_v = \pm 1$, where

$$m_v = \begin{cases} -(l+1) & \text{if } j = l+s \\ l & \text{if } j = l-s \end{cases}. \tag{7.14}$$

Using this rule we observe that EC is only "allowed" for the $nS_{1/2}$ and $nP_{1/2}$ orbitals leading to electron captures from other orbitals being suppressed and thus less likely, though they are not forbidden in the classical sense [175].

Electron capture in $^{127}$Xe has been observed for the K, L, M, and N shells with probabilities of 82.7 ± 2.4%, 14.1 ± 0.7%, 2.6 ± 0.2% and 0.6 ± 0.1% respectively, though capture from the O-shell is also expected [59]. This is in reasonable agreement with calculations using the BetaShape package [176–178]. To validate the BetaShape's calculations the software was compared to calculations for $^{123}$I [174] which demonstrated good agreement.

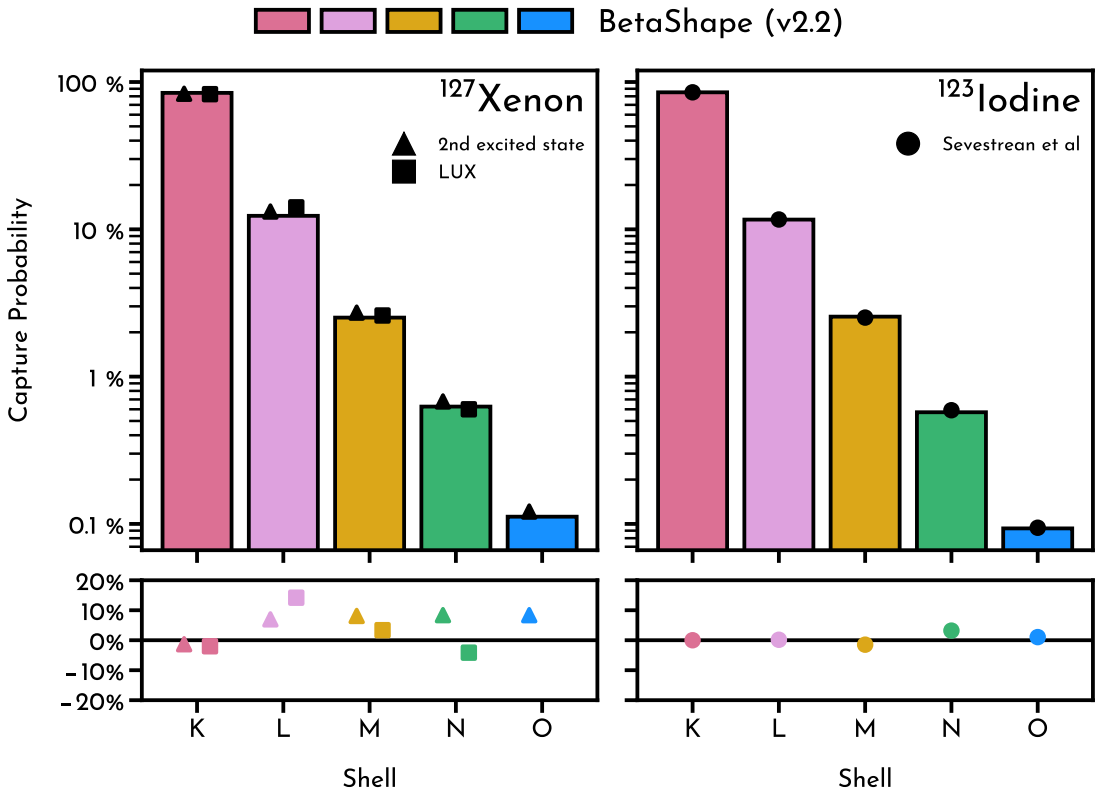



Figure 7.6: The expected per shell EC probabilities for $^{123}$I and $^{127}$Xe. The coloured bars (crosses) represent results for the first (second) excited nuclear state as calculated using BetaShape [176–178], circles represent values calculated by Sevestrean et al. [174] and squares represent results measured by the LUX experiment [59].

### 7.4.2 Relaxation of the daughter atom

The relaxation of the daughter atom to the ground state has two components: atomic de-excitation and nuclear de-excitation, which can be thought of independently.[1] The former produces the low-energy interactions of interest, while the latter allows us to tag such events. An interesting case arises if the nucleus is left in the ground state, here the decay will be detected purely from atomic de-excitation. Recent measurement of EC in $^{40}$K has observed such a decay and constituents the first observation of a third order forbidden transition [179]. This previously unobserved process has been proposed to challenge the dark matter hypothesis for results published by the DAMA/LIBRA experiment [81, 180].

#### 7.4.2.1 Atomic de-excitation

After the electron has been captured the daughter atom is left in an electrically excited state with a hole in the orbital of the captured electron. To relax the daughter must demote electrons via x-ray emission or Auger electron emission. Diagrams of these two processes, alongside the primary electron capture, are shown in Figure 7.7.

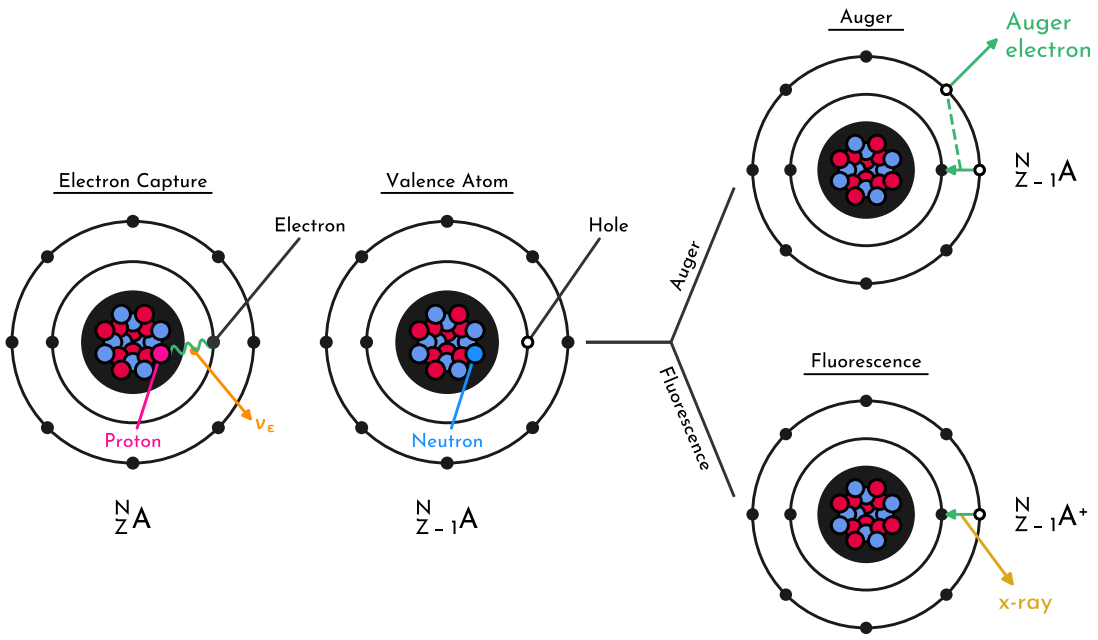



Figure 7.7: The electron capture decay mechanism including the Auger [173, 181] and fluorescence relaxation processes.

[1] The final nuclear and atomic states are related, as seen in Figure 7.6, but for this brief description of the physics this will be overlooked.

In the case of x-ray emission, where the vacancy in the $e_i^-$ orbital is filled by an electron from some higher orbital $e_j^-$, the energy of the emitted x-ray can be calculated as

$$\epsilon_{ij} = \epsilon_i - \epsilon_j, \tag{7.15}$$

where $\epsilon_{ij}$ is the x-ray energy and $\epsilon_i(\epsilon_j)$ is the ionisation energy of the i(j) orbital. As each x-ray transition transfers all the potential energy out of the atom the total detectable atomic energy for a hole in $e_i^-$ can be written as

$$E_{total} = \left( \sum_{i=hole, j>i}^{j=valance} \epsilon_{ij} \right) - \epsilon_{valance} \tag{7.16}$$

where the summation is over all transitions required to expunge the hole from the atomic structure. When quoting the total cascade energy for EC x-ray emission the final valence energy level $\epsilon_{valance}$ is often ignored as its normally negligible compared to the total emitted energy.

Auger emission was first observed by Meitner and Auger in 1922 and 1925 respectively [173, 181]. In this process a hole in the $(n,l,m)_i$ orbital is filled by an electron from the $(n,l,m)_j$ orbital causing the simultaneous emission of a $(n,l,m)_k$ orbital electron,

$$A^{\star\star} \rightarrow A^{\star+} + e^-_{ijk} \tag{7.17}$$

where $A^{\star\star}$ is the initial highly-excited atom and $A^{\star+}$ is the resulting less excited singularly-ionised atom. The observable from this process is the Auger electron, $e^-_{ijk}$, with an energy of

$$\epsilon_{ijk} = \left(\epsilon_i - \epsilon_j\right) - \epsilon_k^+, \tag{7.18}$$

where $\epsilon_i$ is the ionisation energy of the $(n,l,m)_i$ orbital and where $\epsilon_i^+$ is the ionisation energy of the $(n,l,m)_i$ orbital with a single vacancy. The modification in the binding energy of the $(n,l,m)_k^+$ orbital due to atomic ionisation is often ignored but is included in the above for completeness.

The electrons orbitals of $^{127}$Xe and $^{127}$I are displayed in Figure 7.8. For the xenon isotope the allowed EC orbitals are highlighted. Using this table the total energy deposition from fluoresce can be approximately calculated as the difference in energy between the hole orbital and the

outermost valence orbital.

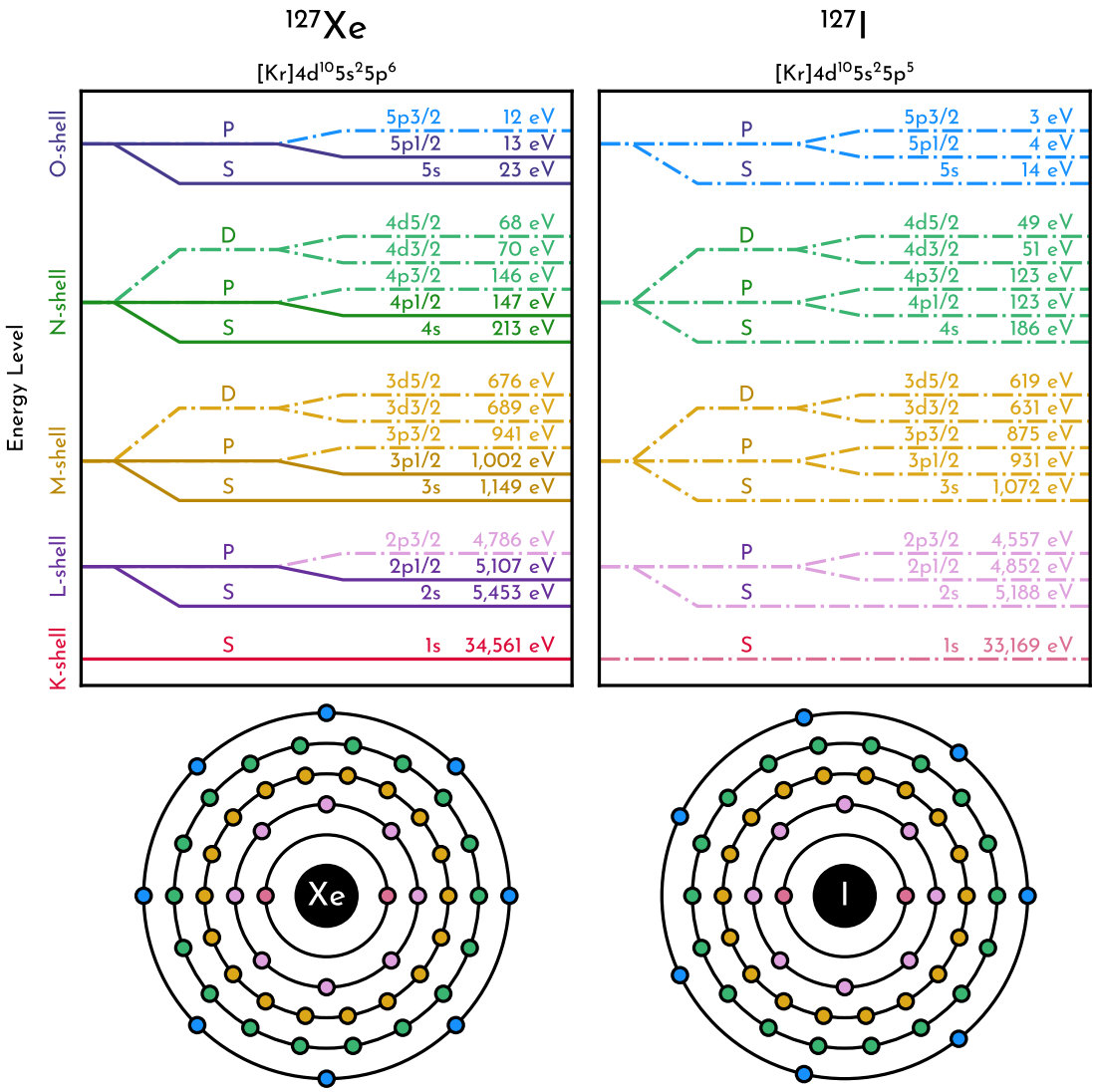



Figure 7.8: The atomic structures and energies of $^{127}$Xe and $^{127}$I. The orbitals which permit EC are displayed as dark solid lines whilst forbidden orbitals are displayed as light dashed lines. The quoted $^{127}$I energy levels are assuming the atomic ground state and not the electrically excited state produced in EC. Ionisation energies quoted from Refs [182–184].

It is difficult to accurately predict the total Auger cascade energy, $E_{Auger}$, as the atomic energy levels become increasingly distorted as the atom becomes more ionised though the ejection of Auger electrons. Recent developments in this area, such as the Jena Atomic Calculator (JAC), should make such calculations easier improving our modelling of these cascades [185, 186]. Assuming that $E_{Auger}$ can be calculated, or at least well estimated, the number of photons and

electrons produced by the EC can be written as

$$\begin{aligned} N_\gamma &= \sum Y_\gamma\left(E_{Auger}\right) \times E_{Auger} \\ N_e &= \underbrace{\sum Y_e\left(E_{Auger}\right) \times E_{Auger}}_{\text{Target scintillation/ionisation}} + N_{Auger} \end{aligned} \tag{7.19}$$

where $N_e$ ($N_\gamma$) is the number of ionisation electrons (scintillation photons) and $Y_e$ ($Y_\gamma$) is the target's charge (light) yield. In the absence of xenon luminescence and ionisation at low energies EC produces only $N_{Auger}$ electrons from the Auger cascade. This should allow extremely low energy decays, including those below the target's nominal fluorescence/ionisation threshold, such as O-shell EC of $^{127}$Xe, to be observed purely though their Auger electron response.

#### 7.4.2.2 Nuclear interactions

If the nucleus is left in an excited state it will de-excite to the ground state though the competing $\gamma$-ray and internal electron conversion processes. Using these characteristic high-energy interactions it is possible to tag low-energy interactions which otherwise could not be associated with a given process or energy; this technique was the basis of LUX's 186 eV charge yield measurement using N-shell EC of $^{127}$Xe [59].

An often overlooked part of electron capture decay is the emitted neutrino and recoiling nucleus. Assuming the total decay energy is equal to the mass difference of the parent and daughter isotopes and that the total energy is split between the nucleus and neutrino which together conserve linear momentum we can calculate the nuclear recoil energy as

$$E_{recoil} = \frac{p_\nu^2}{2m_A} \approx \frac{E_\nu^2}{2m_A} \tag{7.20}$$

for a massless neutrino. The maximum nuclear recoil energy from EC occurs for $^{7}$Be at 57 eV [175]. This effect has been observed in $^{37}$Ar decay [187], however the expected energy for xenon is simply too low, $\mathcal{O}$(eV), for detection in LXe TPCs.

### 7.4.3 LUX's measurement of $^{127}$Xe

LUX observed electron capture probabilities of 82.7 ± 2.4%, 14.1 ± 0.7%, 2.6 ± 0.2% and 0.6 ± 0.1% for the K, L, M, and N shells with no observation of O-shell decay [59]. The lack of any O-shell

observation is expected due to the low expected energy deposition (E < 14 eV) and the low expected capture probability ~0.1% leading to LUX expecting approximately 5 events for the published exposure.

The LUX experiment measured a charge yield of 75.3 ± 6.5 ± 5.2 $n_e$/keV at 186 eV using the N-shell EC of $^{127}$Xe, which is still the lowest energy calibration performed in the medium to date [59]. LUX achieved this by tagging the small S2 signal from the low energy cascade using the high energy $\gamma$-ray emitted from the nuclear de-excitation.

Through this study of the atomic de-excitation processes occurring after EC, it has become clear that the treatment of atomic cascade's made in LUX's interpretation of $^{127}$Xe may not have been wholly correct. The two assumptions of contention are: that the presence of the Auger cascades and the associated ejected electrons were ignored, and that the cascade energy from a hole in a given orbital equals the ionisation energy of said hole.

The LUX result refers to all low-energy atomic signals as being x-rays with occasional references to Auger electrons in the introduction. Not modeling the process as an Auger cascade, which for the N-shell is by far the most likely process with a fluorescence yield of $O(10^{-5})$, and ignoring the associated ionisation energy can lead to a potentially significant overestimation of the energy deposition. For example, if we capture from the innermost energy N-shell orbital (186 eV) and fill the vacancy with from the outermost N-shell orbital (49 eV) by ejecting an O-shell electron of binding energy X eV we will produce an Auger electron of energy 186 eV − 49 eV − X or more simply 137 eV − X; this is the upper limit of the N-shell Auger energy transition when filling from an N-shell orbital [188]. In addition, by ignoring the Auger cascade the emitted Auger electrons are erroneously included as ionisation quanta inflating the measured charge yield.

To evaluate the bias encountered by these two simplifications we shall compare the expected result of the measured yield with and without these assumptions for some general hypothetical decay. This decay directly produces $n_{decay}$ ionisation electrons (Auger electrons, $\beta$-particle, etc.) and $n_{target}$ electrons from the energy deposited into the target. The total deposited energy in this target E can be overestimated as $E' = E + \delta E$.

From these two statements the total number of produced photons can be written as

$$n_{total} = n_{target} + n_{decay} = Q_y(E)E + n_{decay} \tag{7.21}$$

in the absence of these two assumptions and as

$$n_{total} = n'_{target} = Q'_y(E')E' \tag{7.22}$$

when applying them.

To quantify the bias of the charge yield estimator from the application of these two assumptions the fractional bias

$$B_f(Q_y) = \frac{Q'_y - Q_y}{Q_y} \tag{7.23}$$

is used, which can be written as

$$B_f(Q_y) = -1 + \left(\frac{1}{1 - n_{decay}/n_{total}}\right)\left(\frac{1}{1 + \delta E/E}\right). \tag{7.24}$$

If the energy of the process is known ($\delta E = 0$), for instance during calibration, the bias can be written as

$$B_f(Q_y) = \frac{n_{decay}}{n_{total} - n_{decay}} = \frac{n_{decay}}{n_{target}} \tag{7.25}$$

In the case of $\beta$-decay, where $n_{primary}$=1, this bias is negligible even at low energies, (1% at approximately 2 keV). Unfortunately low energy Auger cascades can emit several Auger electrons with comparatively electrons produced from energy deposition within the xenon. In LUX's measurement of N-shell electron capture if $^{127}$Xe, where a mean response of 14 electrons was observed, this bias could be more significant though a more detailed understanding of Auger cascades in $^{127}$Xe will be required to make any robust statements.

## 7.5 Conclusion

To extend the reach of LXe detectors to ever lower detection thresholds requires a better understanding of ultra-low energy light and charge yields. This requires either deployment of new calibration sources or contriving new calibration methods using existing sources. In this

chapter several methods to calibrate a LXe detector between the 50 and 150 eV were explored, namely coherent gamma elastic-scattering, Compton scattering, and electron capture.

Coherent gamma elastic-scattering, where a photon coherently scatters off an entire atom, was found to produce recoils of insufficient energy for photons below 2 MeV. For photons above 2 MeV the process became dominated by shallow scattering making the required backscattering process vanishingly rare. For these reasons this method of calibration is deemed impractical for LXe detectors.

Compton scattering, where a photon scatters of atomic electrons, was explored using Geant4 and analytic methods. By tagging interactions by their scattering angle it should be possible to select events within a given energy range. Whilst it is possible to get a reasonable acceptance for low energy recoils, 4.5% within 50–150 eV using 30 keV x-rays, the photons in this energy regime are dominated by photoionisation making this calibration impractical.

Electron capture, the most promising of the methods considered owing to its use in LUX, was studied in detail to see how this process could be exploited in LZ. Recent developments in the calculation of the EC probabilities have demonstrated that $^{127}$Xe should undergo O-shell capture with a probability of 0.1%. This below threshold process, assumed to be undetectable in LXe detectors, could be observed in LZ by an excess of small S2s from Auger emission in coincidence with $\gamma$-rays from the excited iodine daughter.

From studying electron capture, it is apparent that LUX may have overestimated the charge yield for $^{127}$Xe N-shell electron capture. By omitting auger emission, the dominant de-excitation mechanism for this isotope, LUX ignored the energy lost to Auger ionisation and failed to subtract the primary Auger electrons which are not associated with ER response.

# 8

# Xenon Luminescence Spectroscopy

This chapter details measurements of S1 and S2 light using a LXe TPC operated at Imperial College London. Produced by the relaxation of $Xe_2^\star$ excimers, xenon VUV luminescence, which peaks at approximately 175 nm, is expected to have some dependence on the mean interatomic separation between xenon atoms. The peak emission wavelength in dense states (saturated vapour, liquid, solid), is driven by the location and slope of the potential well of the second continuum.

Current measurements appear to suggest that the peak wavelength of gaseous xenon is shorter than that of the liquid. These measurements, acquired over the past half-century, are not in total agreement with one another varying by up to several nanometres. One explanation for these discrepancies is the presence of different systematic effects between measurements that have not been correctly accounted for.

Two-phase TPC's typically use a liquid-vapour design, as described in Section 2.5. The saturated vapour, here exclusively referring to cold xenon gas in liquid equilibrium, is approximatly twice as dense as warm gas in typical operation conditions. This denser state is expected to produce luminescence that peaks as a wavelength between the warm gas and liquid modes. No measurement of xenon vapour electroluminescence spectra has been preformed to date and represents a notable omission for understanding detectors such as LZ.

The missing and sometimes conflicting xenon spectra measurements limit our ability to model the detector response of two-phase xenon detectors. Several detector and physics parameters vary as a function of wavelength: the mean scattering distance of photons is proportional to wavelength with the Rayleigh scattering length changing by 20% (or more) over a 4 nm range [189–191]; the reflectivity of detector materials, mostly PTFE in the current generation of experiment, vary as a function of wavelength and sometimes exhibit sharp absorption edges; a PMT's QE varies as a function of wavelength with the Hamamatsu R11410-10's changing by approximately 3% over a 4 nm range [114]; and photoelectric absorption by impurities and the QE of material surfaces, such as the electrode grids, both vary with wavelength affecting expected low-multiplicity electron emission backgrounds.

In two-phase xenon detectors the production mechanism for S1 and S2 luminescence is very different; S1 light is produced by particles interacting with xenon atoms in the liquid whereas S2 light is produced from electron impact electroluminescence in the saturated vapour. Mod-

elling interactions in these two-phase detectors to a sub-percent level requires additional measurements of xenon spectra as a function of state and pressure. These values are similarly required to accurately generate the S1 (LXe) and S2 (gaseous xenon (GXe)) scintillation quanta separately within an experiment's simulation framework. In particular the lack of any measurement of the emission spectra of saturated xenon vapour, outstanding over several decades, limits the accuracy of any detector model of S2 amplification signals of two-phase xenon detectors commonly employed to detect dark matter.

Here the first simultaneous measurements of xenon luminescence spectra in liquid and cold saturated vapour states are presented for several pressures (1.3 bar, 1.7 bar, 2.1 bar). These measurements using time-resolved photon-counting spectroscopy are the first measurement for cold saturated xenon vapour. By measuring the spectra simultaneously the majority of systematic effects are expected to affect the two measurements equally providing a more robust comparison between the observed spectra of the two states. In addition, several measurements for gaseous xenon are performed at high (2.2 bar) and low (0.3 bar) pressures to study the effect of density on emission spectra and observe the atomic line.

## 8.1 Xenon luminescence spectra

Xenon scintillation is produced by the relaxation of excimers (excited dimers) produced by the collision of excited and ground-state xenon atoms, see Section 2.4 for a review of these processes. When scattered xenon atoms produces $Xe_2^+$ excimers at some energy level up to and including the conduction band far above those relevant to VUV emission. The excimer then cascades towards the ground-state leading to the emission of broad spectrum infrared (IR) light, centred at 1.3 μm, before reaching the lowest energy $Xe_2^\star$ excimer [192]. The relaxation of this excimer to the ground state is the origin of the VUV luminance detected in LXe experiments such as LZ. This chapter solely details the current understanding and measurement of this VUV emission, for measurements of IR excimer emission in LXe the reader is referred to reference [192].

The potential energy contained within an excimer depends on the inter-atomic distance between the two atoms. This relationship obeys the Morse potential

$$V(r) = D_e \left( e^{-2a(r-R_e)} - 2e^{-a(r-R_e)} \right) + T_e, \tag{8.1}$$

where $D_e$ is the bond's disassociation energy, $T_e$ is atomic excitation of the dimer, $\omega_0$ is the oscillation frequency, $R_e$ is the equilibrium separation, and the constant a is $\omega_0\sqrt{2\pi^2\mu/D_e}$ for a system of reduced mass $\mu$ [193]. Like the quantum harmonic oscillator, the well of the Morse potential creates several bound energy states

$$E_\nu = T_e + h\omega_0\left(\nu + \frac{1}{2}\right) - \frac{h^2\omega_0^2}{4D_e}\left(\nu + \frac{1}{2}\right)^2 \tag{8.2}$$

defined by a vibrational quantum number $\nu$, which due to the disassociation energy at large distances, is truncated from 0 to $(2D_e/h\omega_0 - 1)$ [194]. Using these four parameters ($R_e$, $D_e$, $T_e$, and $\omega_0$) the state of a dimer can easily be modelled and the expected emission wavelength calculated.

The Morse potentials for the lowest energy $Xe_2^\star$ excimers and ground state dimer are shown in Figure 8.1. The potential energy of the excimers have three regimes: the long range ($r \geq 5$ Å) where excimers are effectively unpaired free atoms, the medium range (3.5 Å $\geq r \geq$ 5 Å) where the potential varies significantly within the well, and the equilibrium region ($r \sim 3.5$ Å) at the bottom of the well. The two most interesting excimers for this work are the $A1_1$ and $B0_u^+$ states which are the singlet and triplet states respectively. The shallow dissociative ground-state dimer leads to the dissociation of xenon dimers into two independent xenon atoms. In the absence of long-lived ground-state dimers, xenon, and other noble gases, are transparent to their own luminescence making them good scintillators.

At large separations, encountered at the low density limit where excimers are effectively free atoms, the excimer luminescence is simply atomic fluorescence (146.96 nm). If the excimer is allowed to relax slightly via atomic collisions but is still in the long range limit the photon will be of slightly longer wavelength (~150 nm) and are said to be from the first continuum. Finally, if the excimer relaxes further into the potential well before it de-excites the photon emitted will be at much longer wavelengths (~175 nm) and are said to be of the second continuum.

According to this model the triplet state produces photons with wavelengths ~2 nm longer than the singlet state. This means that photons detected earlier in an S1 pulse are expected to be of shorter wavelength than those detected closer to the end.

In addition to excimer luminescence, gaseous xenon has been demonstrated to produce photons

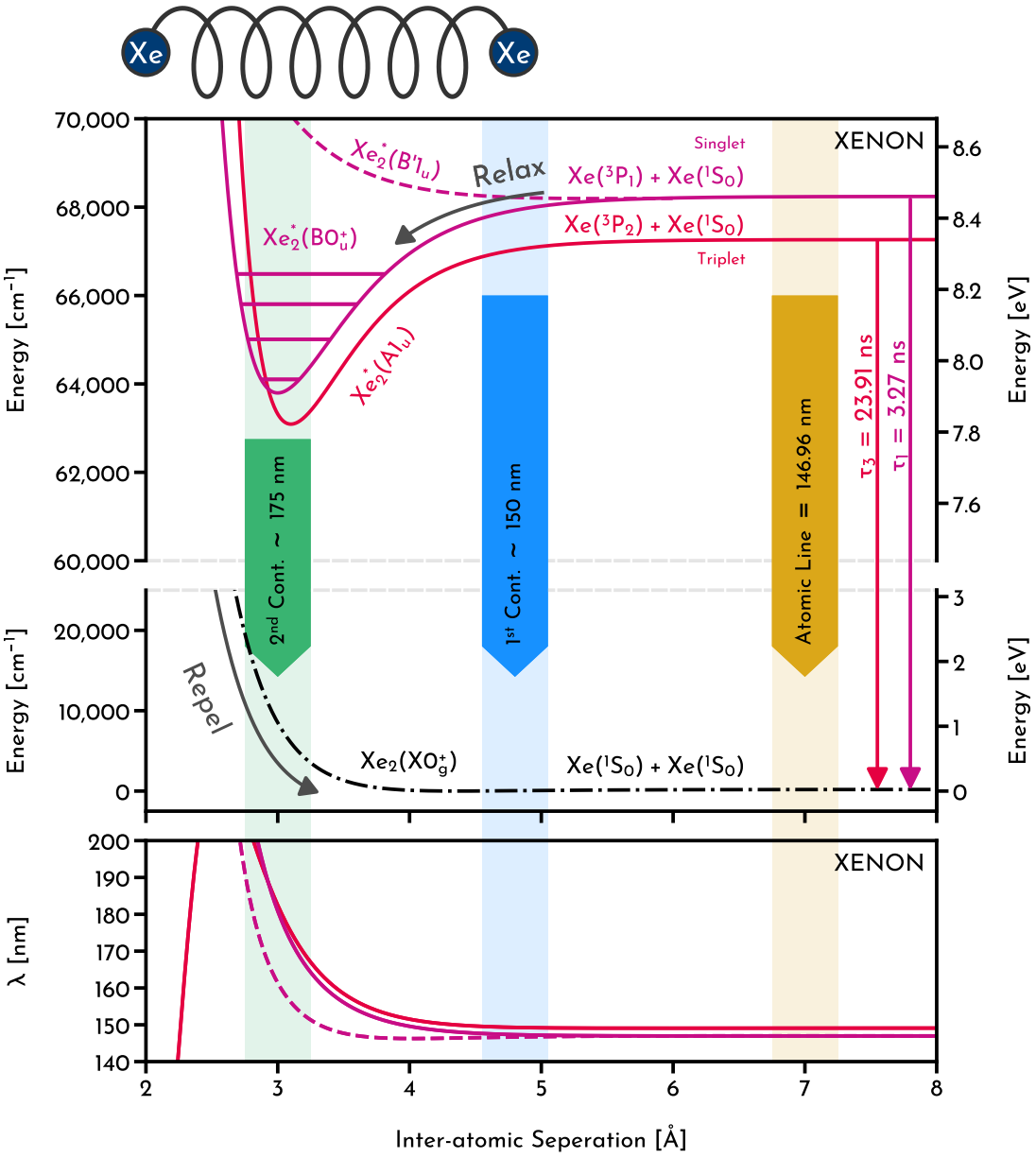



Figure 8.1: (Top panel) Morse potential curves of $Xe_2^\star$ as a function of interatomic separation. The potentials of three excimers are shown (coloured lines) alongside the dissociative ground-state potential (black dot-dashed line). From the shape of the excimer potential three main spectral regions can be identified: the atomic line where atoms are effectively uncoupled; the first continuum where a dimer relaxes before reaching its minimum energy; and the second continuum where the dimer relaxes within the potential well minimum. For the $Xe_2^\star(BO_u^+)$ state a subset of non-contiguous discrete energy levels are plotted. (Bottom panel) The wavelength of light produced from the de-excitation of a given state calculated purely from the Morse potential. Figure produced using Morse parameters from Ref. [195]

via neutral bremsstrahlung (NBrS). In this process electrons emitted into the vapour scatter off the atomic electric dipole generated in response to an external electric-field. Unlike VUV excimer luminescence, neutral bremsstrahlung produces a broad spectrum up to and possibly including the infrared. This process, first detected as visible electroluminescence at low external fields in 1969, had been largely ignored within the community who focused primarily on excimer luminescence. Recently there has been renewed interest in this process with measurements of NBrS performed in argon and xenon detectors [196, 197]. NBrS' broad spectrum has limited impact on xenon detectors, optimised for the VUV, but does directly affect argon detectors, traditionally optimised to detect visible (420 nm) light though the use of wavelength shifter [198–200]. The apparatus and methodology described within this chapter to measure VUV xenon luminescence are also being applied to observe and measure this process using dedicated gas-only datasets. This ongoing work will not be explored or detailed within this thesis.

## 8.2 Triggered Time-Resolved Photon Counting Spectroscopy

An elegant solution to make spectroscopic measurements, known as photon counting spectroscopy, is to count the number of photons detected as a function of wavelength. Photon counting spectroscopy requires three components: a light source, in this case is xenon scintillation and electroluminescence; a photo-sensor that can time-resolve single photons to a high accuracy, such as a PMT; and a device to select specific wavelengths of light, known as a monochromator. By setting the monochromator to a specific wavelength and counting number of detected photons the observed scintillation flux can be calculated. By measuring the observed flux as a function of wavelength the emission spectrum can be obtained.

Two-phase xenon TPC detectors, described in detail in Section 3.1.1, permit simultaneous observation of liquid scintillation and vapour electroluminescence as time-resolved S1 and S2 pulses. By using one PMT within the TPC to observe interactions (S1 and S2 pulses) and another PMT to detect photons behind the monochromator the emission spectrum of xenon can be measured. Using the time resolved S1, S2 and monochromator signals, shown in Figure 8.2, separate spectra for S1 (scintillation) and S2 (electroluminescence) spectra can be constructed. The narrow width of the S1 (~40 ns) and S2 (~1200 ns) pulses lead to a negligible accidental rates in the monochromator PMT, $\frac{1}{3{,}000{,}000}$ and $\frac{1}{100{,}000}$ respectively.

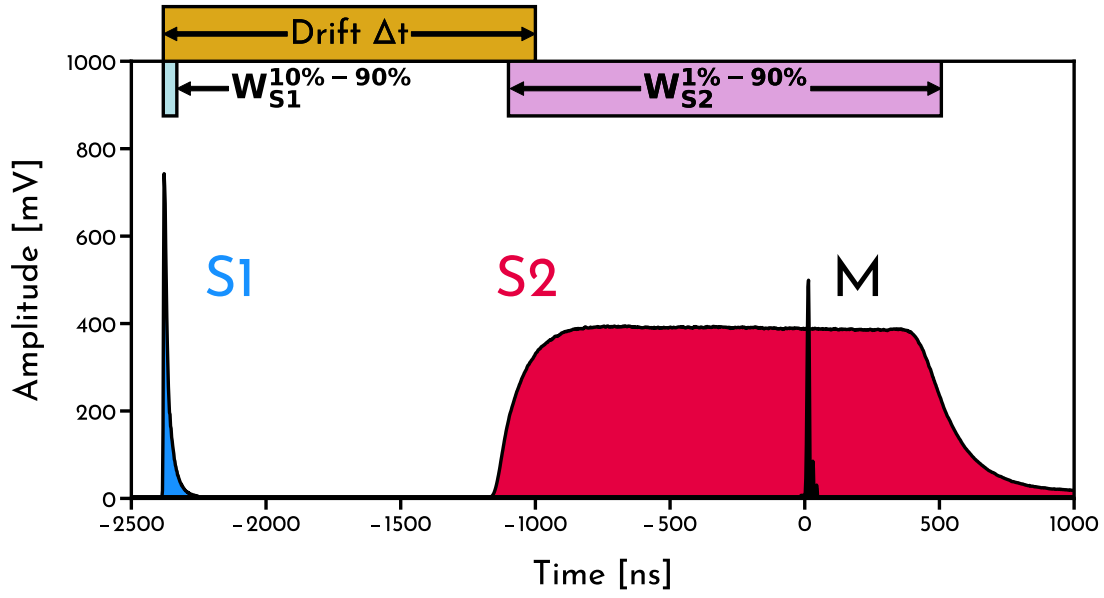



Figure 8.2: Averaged waveforms for α-particle interactions alongside a photon detected in coincidence with the S2 by the monochromator PMT. This event would be used to construct the xenon vapour electroluminescence spectra PDF.

## 8.3 Proto-Xenia

To measure the emission spectra of warm GXe, cold GXe in liquid equilibrium, and LXe states a two-phase xenon TPC known as proto-Xenia, displayed in Figure 8.3, was used. The 2.6 L TPC, which when full contains 7.7 kg of LXe at a depth of 14.5 cm, is primarily defined by its two extraction region grids (gate, anode) which are each operated at $O$(kV) generating a strong electric-field across an 11 mm region spanning the liquid surface, four pairs of optical viewports, and one internal 2-inch quartz-windowed ETEL D730/9829Q PMT. To produce localised high-energy events a thin $^{228}$Th α-source was attached to the centre of the gate. To maintain a liquid target the chamber the inner vessel was cooled to ≈−100 °C using a Gifford-McMahon cryocooler. A key element of proto-Xenia's design is the installation of four optical viewports enabling scintillation light to be detected outside the TPC and outer-vessel. The central TPC, housed within an inner-vessel (IV) and OV, is an update of a chamber previously used as a prototype for the ZEPLIN program and later to perform cathodic grid-wire studies for LZ [201].

The four viewport pairs, vertically centred around the liquid surface, facilitate two observations: the optical confirmation of the liquid height and the observation of S1, S2 and calibration light

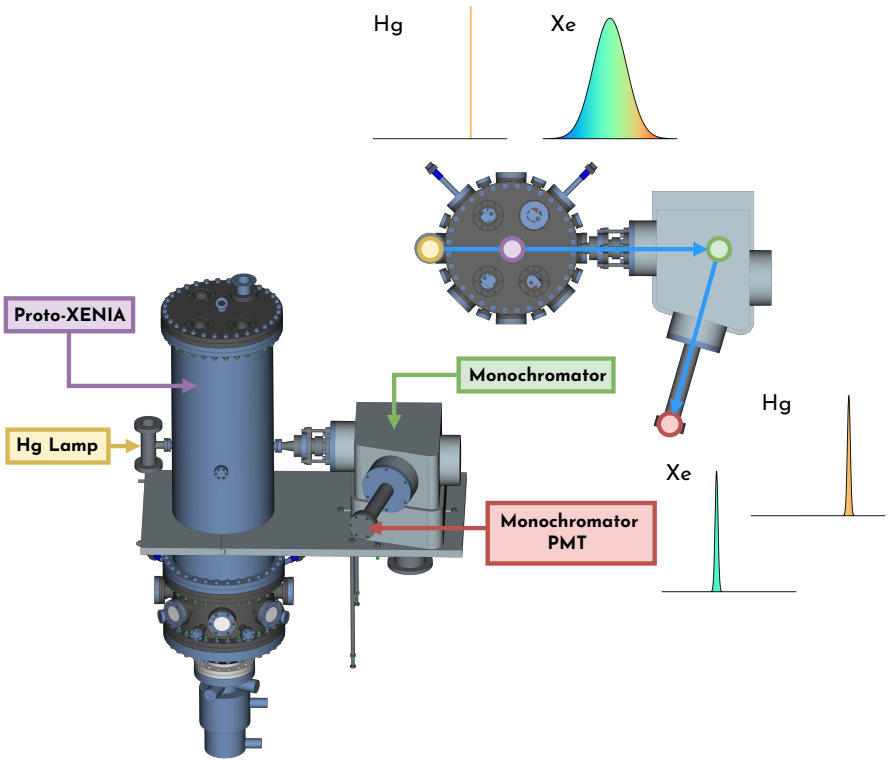



Figure 8.3: CAD diagram of proto-Xenia. The detector, in this configuration, comprises three core parts: a central LXe TPC with four viewports and a single internal PMT; a monochromator mounted with a PMT optimised for VUV light; and a low-pressure mercury lamp for calibrating the monochromator PMT. The top-down view, displayed in the top right, shows the optical path of photons (blue) from either the Hg lamp or the xenon to the monochromator PMT. In addition to this diagram sketches of the two operation modes, a Hg atomic line being detected convolved with the detector response and a xenon continuum being having a particular wavelength sampled, are displayed.

from outside the detector. The former requires at least one pair of visibly transparent viewport between the TPC and the environment. The latter requires two diametrically opposed $MgF_2$2 viewports transparent to VUV light.

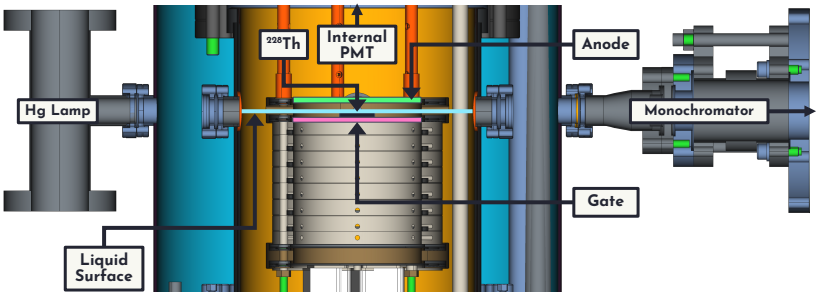



Figure 8.4: CAD cross-section of proto-Xenia. Here the gate (pink) and anode (green) grids are shown with the $^{228}$Th source braced to the gate. The liquid surface (blue) is shown with its height set at the centre of the viewports and extraction region. The internal PMT, located above the TPC, is highlighted alongside the monochromator PMT. Note: the PTFE field shaping rings (white) are part of the complete Xenia detector and were not in-place of at the time of the measurements discussed in this thesis.

One of the $MgF_2$2 viewports looks towards a Princeton Instruments Acton VM-502 vacuum monochromator mounted with a single $MgF_2$ windowed ET-9406B PMT [202]. To prevent absorption of VUV photons, the monochromator is operated within its own vacuum space. This vacuum space was stable during operations at $1.4 \times 10^{-6}$ bar measured by a gauge 1 m from the photon line-of-sight.

Using a concave holographic grating only light of a specific wavelength $\lambda$ can pass through the monochromator. By rotating the grating using a sine drive screw the wavelength can be selected linearly with angle. To have repeatable fine-tuned control of the device a stepping-motor was mounted on the device where each motor position x corresponds to some wavelength $\lambda(x)$.

The input port of the monochromator has a pair of horizontal baffles which control the quantity of light entering the device. In this work the baffles were set at 4 mm. To control the resolution and efficiency of the monochromator a pair of horizontal slits attached to the input port can be adjusted. In this work three slit-widths (0.10 mm, 0.18 mm, and 0.25 mm) were used with thinner slits leading to a finer detector resolution and a lower photon flux. The detector response from the monochromator was found to be largely Gaussian with some coma aberration, with the degree of aberration proportional to the slit-width.

The bi-alkali monochromator PMT, sensitive between 110 nm and 630 nm, was operated at −1450 V achieving an electron gain of 100 million. During operations, the measured dark-rate (~ 8 Hz) was substantially lower than the manufacturer quoted value of 100 Hz and increased slightly during the significant light exposure encountered during calibration.

The diametrically opposite viewport looks towards a low-pressure mercury (LP Hg) pencil lamp, providing a clear line-of-sight between the Hg lamp and the monochromator PMT enabling in-situ calibration of the monochromator-PMT system. The lamp, housed within a ConFlat® T-piece, was attached to and operated within the OV's vacuum space to prevent absorption of VUV light. Unable to dissipate heat to the atmosphere the lamp risks overheating, to prevent this the lamp was thermally coupled to the OV using a thin copper plate. The high photon flux produced by the lamp requires moderation to stop the monochromator PMT's photocathode charging. To limit the photon flux an oxygen-free copper plate with a $\frac{1}{2}$ mm pin-hole aperture was used in place of the copper gasket. The chosen size of the aperture was validated by calibrating the system in vacuum with a 0.10 mm horizontal slit-width, which was the width proposed for this work prior to operation.

### 8.3.1 Wavelength dependant corrections

To accurately measure the shape of spectral continua requires a good understating of the materials present in the optical path of the detected photons. Any variation in the detector's optical properties as a function of wavelength will distort the observed shape of broad spectra; monochromatic light, such as the LG Hg lamp used in this work, are immune to this distortion due to their almost infinitesimal width. For broad spectra, such as xenon luminance, these effects much be corrected for. Usually this correction can be applied by dividing by the detector's total wavelength-dependant efficiency. Several of these wavelength-dependant efficiencies are displayed in Figure 8.5.

The dominant detection efficiency for proto-Xenia is the PMT's QE. To both maximise the high-frequency QE and minimise its variation as a function of wavelength, a $MgF_2$ windowed PMT was chosen. By dividing by the PMT's QE, in this case measured by the manufacturer for a different PMT of the same model, the total PMT efficiency can be corrected for. Some care must be made to account for the DPE effect which exaggerates the QE in the VUV when using the photon counting method. An absolute calibration of the PMT used in these measurements

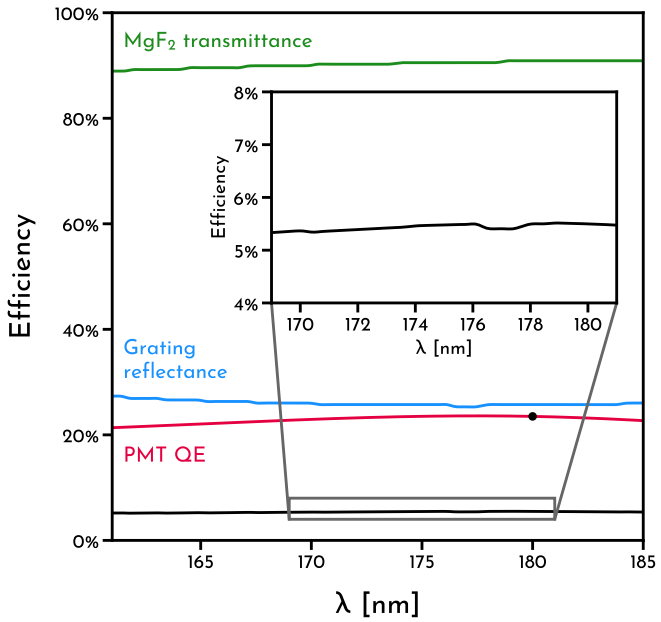



Figure 8.5: The wavelength-dependant transmission efficiencies of several materials in photons optical path alongside the QE of the monochromator PMT. $MgF_2$ and monochromator values are taken from Ref [189]. The PMT QE, displayed using a spline generated using values supplied by the manufacturer, is for a different PMT of the same model. The total efficiency of the system, calculated as the product of the coloured lines, is shown in black.

will be performed by the manufacturer at a later date with a higher granularity in the VUV.

The QE of the PMT, as approximated by a spline, was found to be reasonably flat in the region of interest for this work. Similarly, the DPE probability was found to have little effect within the known xenon luminescence region.

The transmission probability of the monochromator grating was found to be largely flat over the region of interest. The resolution of the quoted measurements does lead to a noticeable step in the transmission probability, but this should be insignificant for the measurements presented here.

Some small fraction of luminescence photons are expected to undergo reflection prior to detection. The most common reflections are expected to be off the gates, the liquid surface, and the $^{228}$Th source. The magnitude of this effect is expected to small from geometric considerations and has been ignored for the purposes of this work.

Whilst no significant changes in the wavelength-dependent efficiency are observed, the effects

outlined above are corrected for when quoting xenon spectra measurements.

### 8.3.2 Detector operations

To fill and empty the TPC a gas system built for ZEPLIN-III was used. This system allows the xenon to be released from two storage bottles into the TPC; purified via recirculation through a zirconium (Zr) getter; captured into a large volumed called the "dump" in case of an emergency / excess xenon pressure; and to be recovered back into the storage bottles at the end of operations though cryopumping the xenon with a liquid nitrogen vacuum jacket.

The gas system, designed to operate at modest pressures, has two physical control systems to relieve excess pressure: pressures exceeding 2.75 bar(a) will engage the motorised leak-valve (MLV) releasing some xenon into the dump, whilst pressures exceeding 3 bar(a) will rupture the gas-system's burst-disc rapidly expelling the xenon into the dump. If the full 7 kg LXe volume vaporises and ruptures the bust-disc the dump will reach a safe pressure of 0.6 bar(a).

To remove any contaminants from the detector the IV was evacuated to vacuum and cooled achieving a pressure of $1 \times 10^{-8}$ mbar. The presence of electronegative impurities would lead to a reduction in the number of extracted electrons thereby reducing number of photons produced in the xenon vapour. An additional consequence of impurities is that some contaminants can capture VUV photons in the xenon ROI. Water vapour is a particular contaminant of concern as $H_2O$'s absorption spectra peaks at 166 nm, with a tail that extends upwards towards the previously measured peak xenon luminescence wavelength of 175 nm [203]. An $H_2O$–LXe partial pressure of 100 ppb would lead 14% of xenon luminescence being absorbed assuming a 5 cm path length.

A residual gas analyser (RGA) was attached to the OV for real-time monitoring of any contaminants in the vacuum space and to detect any xenon leaks from the TPC. No excess of atmospheric contaminants consistent with a leak from the environment were observed during operations. A small leak of xenon gas from the IV was observed though this should have no effect on measured spectra.

The TPC was filled by condensing the gaseous xenon at approximately —100 °C. To provide the necessary cooling power a Gifford-McMahon cryocooler, which circulates cold helium (He) around a copper cold-head attached to the chamber's baseplate, was used. The chamber's

initial design had inadequate thermal coupling between the baseplate and the top of the chamber preventing full liquefaction of the vessel volume. To remedy this, two copper braids where added coupling the baseplate to the top of the chamber and three copper rods where attached to the top of the chamber protruding downwards into the liquid surface. Even with these additions there remains an $\mathcal{O}$(K) thermal gradient across the length of the TPC.

To monitor the thermal state of the detector several Pt 100 thermometers, designed and built for LZ, were used. The two main sensors used in this measurement are located ~2 cm above and below the liquid surface independently monitor the temperature of the liquid surface. To regulate the temperature of the detector a commercial proportional–integral–derivative (PID), hence forth known as the LFS, was used. By controlling the dissipated heat from resistors located around the baseplate the LFS was able to maintain the detector temperature within 0.1 °C event for the longest measurements lasting several days.

The chamber is operated using only the extraction (gate–anode) region. Using two power supplies the gate (anode) grid can be biased to a voltage of −4500 V (4500 V). Treating the grids as two infinite parallel plates equidistant to the liquid surface (5.5 mm stand-off distance) and liquid xenon as a dielectric with a relative permeability 1.96, the electric fields in the gas and liquid states can be approximated as $E_g$ = 10.8 kV/cm and $E_l$ = 0.55 kV/cm.

## 8.4 Internal radioactive source – $^{228}$Th

To generate high-energy interactions within the TPC an $\mathcal{O}$(kBq) $^{228}$Th α-source was used. Part of the thorium chain (Figure 8.6), $^{228}$Th produces several 5.5–9 MeV α-lines alongside β and γ radiation. The α-particles, with their short ~100 μm range, produce localised interactions with a large scintillation yield ($\mathcal{O}(10^5)$ photons). This high scintillation yield is necessary to maximise the probability of at least one S1 photon being detected by the monochromator. The comparatively low charge yield of α-interactions is easily mitigated by the large electroluminescence gain, $\mathcal{O}$(500) photons/electron, achievable in proto-Xenia [72]. The tight localisation of these interactions leads to a reduction on any systematic effect originating from either interaction vertex (e.g., spatial variation in E-field) or photon propagation path (e.g., angle of reflectance from the liquid surface). The β-decays are ignored for the purpose of this analysis due to their comparatively long track structures from non-monoenergetic interactions leading to greater systematic uncertainties.

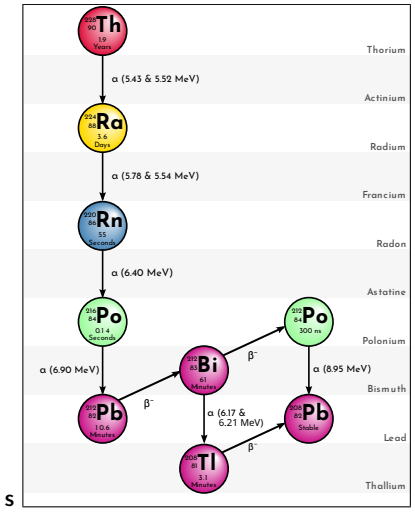



Figure 8.6: Decay diagram for the $^{228}$Th source used in proto-Xenia. Diagram edited from Ref [204] under a CC BY-SA 3.0 licence [205], α energies from Refs. [206, 207].

The $^{228}$Th, supplied by Eckert & Ziegler, was supplied as a very thin 5 mm diameter layer electroplated onto a thin (0.127–0.254 mm) platinum foil housed within a plastic housing. The source was deployed in proto-Xenia by mounting the foil onto a metal washer which was then braced to the centre of the gate using the grid wires. Some effort was made to raise the source such that it faced the monochromator window to improve the line-of-sight to the monochromator. The top of the source is highly reflective, this will lead to a small fraction of S1 and S2 photons being detected after reflecting off the source.

## 8.5 Computing and software infrastructure

The computing resources, software, and sensors used in this work, shown in Figure 8.7, are split over four computing systems each performing a specific task: the slow-control computer

monitors and controls the detector; the DAQ computer acquires raw data from the PMTs and slow-control; the Imperial HEP cluster provides long-term data storage, raw data processing and the Imperial HPC cluster is used for data storage redundancy and analysis of processed data.

The significant quantity of computing resources is driven by the large data sets required for this work. If the probability of detecting a single luminescence photon in the monochromator is 1% then only 1% of the acquired data is useful. Data could have been acquired using a coincidence trigger on both PMTs but this could lead to a bias in the acquired datasets. By using the HEP and HPC clusters the full datasets could be acquired without compromise.

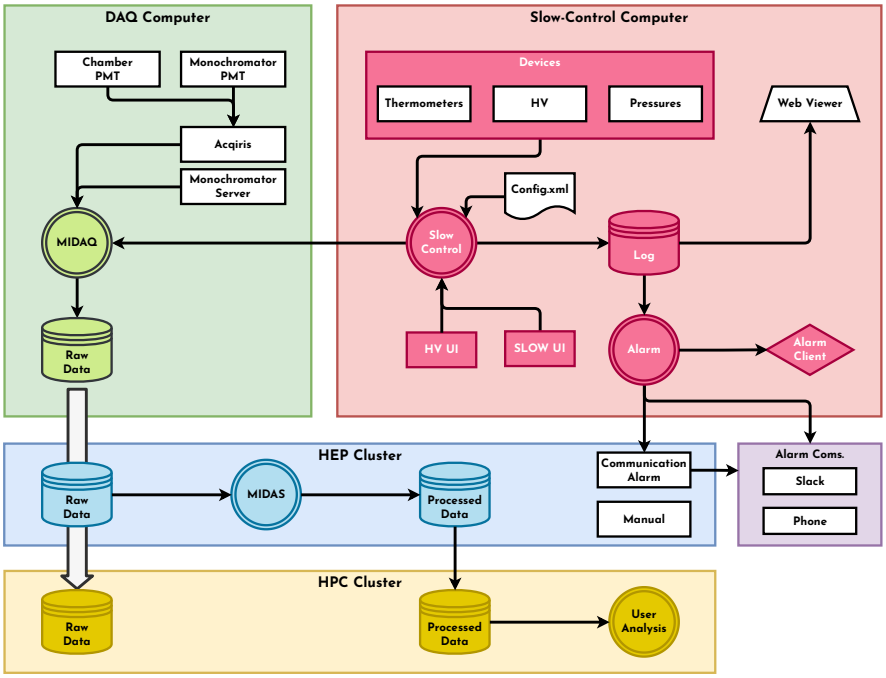



Figure 8.7: The structure of the laboratory software, detectors and monitoring systems organised over four computing resource. Each computing system: the slow-control computer (red), the DAQ computer (green), the Imperial HEP cluster (blue), and Imperial HPC cluster fulfil distinct roles. The slow-control monitors and controls the detector state; the DAQ computer writes the PMT signals and detector conditions, including monochromator positions, to disk; the HEP cluster provides long-term data storage, raw data processing; and the HPC cluster is used for data storage redundancy and user analysis.

### 8.5.1 Slowcontrol and Detector Monitoring

Proto-Xenia is monitored and controlled by a variety of software packages; collectively these pieces of software, called the slow-control, are the principal method of understanding the

current detector state. The slow-control system used for proto-Xenia is an updated version of the ZEPLIN-III slow-control and operates/monitors the high-voltage power-supplies (PMTs and grids), vacuum systems, pressure monitors and thermometers.

### 8.5.2 Data Acquisition (DAQ)

The signals from the two PMT's are each amplified using a Phillips Scientific model 770 ten-times gain amplifier NIM module. The amplified signals are then connected to an Acqiris CC108 PCI crate, henceforth referred to as the DAQ or Acqiris, mounted with two Acqiris DC270 quad-channel digitisers recording at 500 MHz (2 ns sampling).

The DAQ is controlled using MIDAQ, a software developed as part of the MIGDAL project [208], and digitises the waveforms from both PMTs at a fixed rate over a pre-defined full-range voltage. These waveforms, in contrast to LZ, are stored for the entire event window. The full range of the monochromator PMT was chosen such that the full SPE/DPE distribution of the PMT could be recorded. The full range of the chamber PMT was chosen such that the S1 from the highest energy $\alpha$-line were recorded with minimal clipping. The DAQ can be triggered using any of the digitisation channels or using an external (non-digitising) channel mounted on each module. Whilst writing out a triggered event there is a short time-period, known as the dead-time, during which the DAQ is unable to detect or record events. This dead-must be measured for each DAQ configuration separately.

The DAQ embeds the detector state, according to the slow-control, and monochromator motor positions, as retuned by a C++/python server, into the DAQ data stream. The querying of each of these systems was performed on a separate threads to the core MIDAQ process to prevent blocking of the DAQ thread. Both systems were queried at a sufficiently high rate to capture any variation in their reading with slow-control queried once every ten seconds and the monochromator queried every millisecond.

In this work, all calibration and xenon spectra datasets were acquired by triggering on the monochromator PMT. The efficiency in this mode is estimated at close to 100% owing to the high gain of the monochromator PMT. To measure the DAQ dead-time and monitor the electron lifetime several datasets were acquired using a chamber PMT trigger.

### 8.5.3 Dead-time

The DAQ system used for this measurement suffers from non-paralysing dead-time. This leads to the DAQ being unable to trigger for some constant time $\tau_{dead}$ after the previous trigger. Because of this any observed event rate from a random process will be an underestimation of the true event rate. For the case of non-paralysing dead-time, where missed triggers do not reset the dead-time, the true rate can be approximated as

$$n = \left(\frac{1}{1 - m\tau_{dead}}\right) \times m, \tag{8.3}$$

where m is the observed rate and n is the true rate [209]. For low observed rates this correction is minor but for high rates, such as those encountered during calibration, this can lead to a substantial (orders of magnitude) corrections.

The dead-time is a constant proportional to the data quantity and must be measured for each DAQ configuration. To measure the dead-time requires knowledge of the real and observed rate. In proto-Xenia the dead-time was measured by acquiring data triggered on the chamber PMT from $\alpha$-decays. As a random process the time between contiguous events in a random variable sampled from an exponential distribution. By fitting the difference in time between successive events with an exponential the true event rate can be calculated and compared to the observed rate, as seen in Figure 8.8. By inverting Equation 8.3 the dead-time is calculated for all DAQ configurations with the measured dead-time closely matching the observed cut-off in the time difference between events. The dead-time of the DAQ was found to be 141.2 µs for calibration data and 333 µs for xenon spectroscopy data. Whilst 333 µs may at first sound like a long dead-time, taken in context of the peak detected event rate for xenon luminescence, $O$(10 Hz), this is a tiny correction.

### 8.5.4 Data processing

After acquisition this "raw data" is transferred to the Imperial HEP and HPC clusters. Using these two computers provides data redundancy in case of failure at either site and provides a more user-friendly analysis environment than the very stable and utilitarian DAQ and slow-control computers.

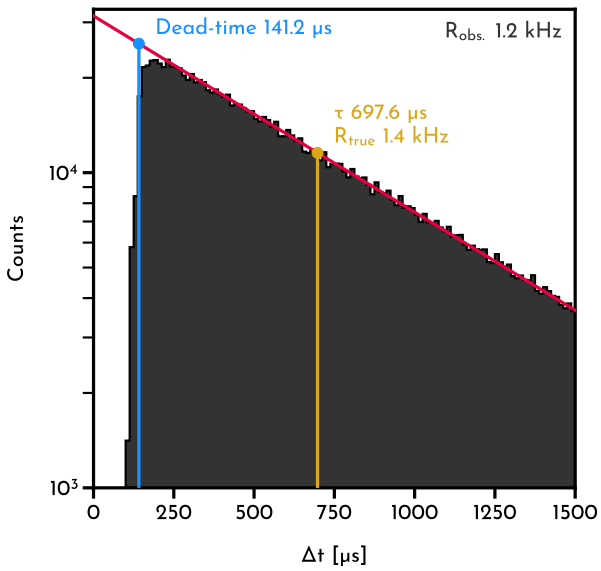



Figure 8.8: The time-separation between contiguous events triggered on the internal α-source. The true event rate is found by inverting the mean time found from fitting the exponential decay of the radioactive decay modelled as a Poisson process. By comparing the true and observed event rate the not-paralysing dead-time of the DAQ has been determined and visually agrees with sharp cut-off observed in the data.

As MIDAQ is only designed to write out the raw data to disk the output is not very "analyser-friendly". To process this raw data into a user analysable format a data processing framework called MIDAS, also part of the MIGDAL project, was used. Using this package unwieldy PMT traces are processed using several algorithms, based on those used in LZ, including: baseline subtraction, pulse finding, pulse parameterisation, and pulse matching between PMTs, to produce output files analogous to LZ RQ files. These processed files can easily be read in Python using the "uproot" package and analysed using the variety of other packages available within the scikit-HEP software stack [210, 211].

The pulse finder setting were efficient at selecting S1/S2 pulses in the chamber PMT and SPE/DPE pulses in the monochromator. In both cases some level of non-signal pulses originating from noise or splitting of genuine pulses were found. These "fake" pulses were dealt with in the specific post-processing analyses as this is preferable to over-tuning the pulse finder which could lead to biases in analysis.

## 8.6 In-situ Calibration Using an LP Hg lamp

To be able to measure wavelengths using the stepper motor controlled monochromator the system must be calibrated. This requires a model relating the stepper motor position, and thus grating angle, to the sampled wavelength and a light source with known spectral lines. The relationship between the motor position and wavelength is known to be linear for the Acton VM-502 monochromator used in this work. As for the calibration source, a low-pressure Mercury (LP Hg) pencil-lamp, discussed previously, was chosen due its strong 184.95 nm spectral line which is in close proximity to xenon's VUV scintillation light.

Calibration was performed before the first xenon spectra dataset and intermittently between subsequent datasets particularly if there was a significant change in the detector conditions or monochromator configuration. During calibration the detector remained in its current state, e.g., grids would remain biased, but with the internal PMT disabled to prevent the large photon flux charging photocathode. It was observed that turning off the internal PMT reduced the temperature of the xenon gas/vapour and by extension the liquid necessitating that the concise calibrations be performed.

Two schemes of moving the monochromator motor were using in this study. The first, known as the sweeping method, uniformly sampled the LP Hg light over the VUV and visible regions in fixed steps. The second, known as the leaping method, used previous calibration results to only sample the observed strong lines of mercury enabling a quicker calibration with higher statistics. In this mode the motor sampled a line uniformly, using the same fixed step size as the first method, and on completion would jump to the beginning of the next spectral line.

Initially the system was calibrated using the first method however the effect of disabling the internal PMT on the thermodynamic state of the system was deemed too large thus requiring the quicker second method of calibration. No difference in calibration result was observed between the two methods.

Figure 8.9 shows the observed (uncorrected) spectrum from Hg calibration for a 0.18 mm slit-width taken in the "sweeping" acquisition mode. The location of several peaks were found within this spectrum using *SciPy's find_peaks* algorithm [212]. The first two peaks, which are also the largest, are the 184.95 nm and 253.7 nm spectral lines. These very bright (high rate) lines suffer significantly from the DAQ dead-time causing a flattening in the observed lines.

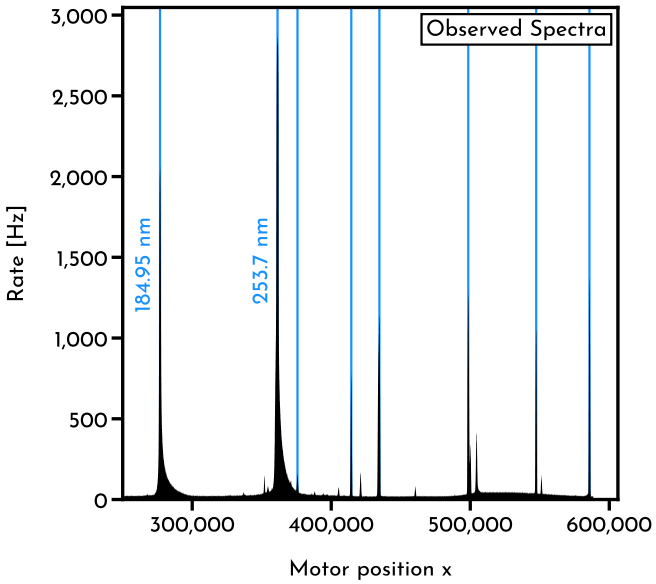



Figure 8.9: The observed spectrum from the LP Hg lamp (black). The blue lines indicate peaks found using SciPy's peak finding algorithm.

To pair the remaining peaks to spectral lines a rudimentary linear calibration model was constructed using the 184.95 nm and 253.7 nm lines. This model was then used to find the closet strong line of mercury from NIST for each observed peak. To better estimate of the mean position of each Hg line the spectra in the region of each peak was dead-time corrected using Equation 8.3 and fit with a Voigt profile. For the 313 nm and 405 nm doublets the weaker lines were missed by the *find_peaks* algorithm and were added by-hand to calibrate and fit with two Voigt profiles.

The corrected spectrum of the 184.95 nm line, the most important calibration point for this work due to its proximity to xenon luminescence, is shown in Figure 8.10 alongside the fitted model. Whist not perfect, this fit does achieve a good estimate of peak detected wavelength. Assuming the 184.95 nm line is infinitesimally narrow the observed shape representing the narrow, slit-width dependant, detection response model of the monochromator close to the xenon wavelengths.

Using these data points (wavelengths and peak motor positions) a linear model was obtained by least-squares fitting, shown in Figure 8.11. In this fit the 253.7 nm line was excluded due to its high rate leading to difficulties in dead-time correction. This linear calibration achieves excellent reconstruction of wavelengths, $\Delta\lambda \lesssim 0.1$ nm, over the entirety of the VUV and into the

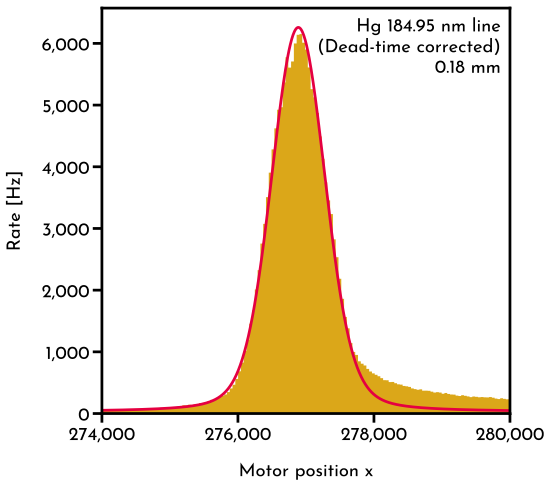



Figure 8.10: Dead-time corrected rate of detected photons as a function of monochromator step position for the LP Hg 184.95 nm line alongside a Voigt profile fit to the data. A tail originating from coma aberration is observed in this line.

visible with no significant systematic offset in the 184.95 nm line as observed in reference [189] which also uses a VM-502 monochromator. The modest ~0.1 nm offset in the 184.95 nm line represents the systematic error in the xenon spectra presented in this work.

Using the above calibration the raw spectrum, Figure 8.9, can be converted into wavelength as shown in Figure 8.12. Below the main spectrum the peaks of several fitted lines are shown alongside their fitted model. Each of these are adequate for this calibration though like the 184.95 nm line are by no means perfect.

From comparing the various calibration performed during this work no significant change in calibration constants (fitted line parameters) were observed. This stability spanned calibrations with different slit-widths and those performed with liquid versus warm gaseous xenon demonstrating the robustness of this method.

The monochromator's resolution was found to be inversely proportional to the horizontal slit-widths as seen in Figure 8.13 which displays fitted Voigt profiles of the 184.95 nm line for 0.1 mm, 0.18 mm, and 0.25 nm slit-widths alongside their respective full-width at half-maximum (FWHM)s.

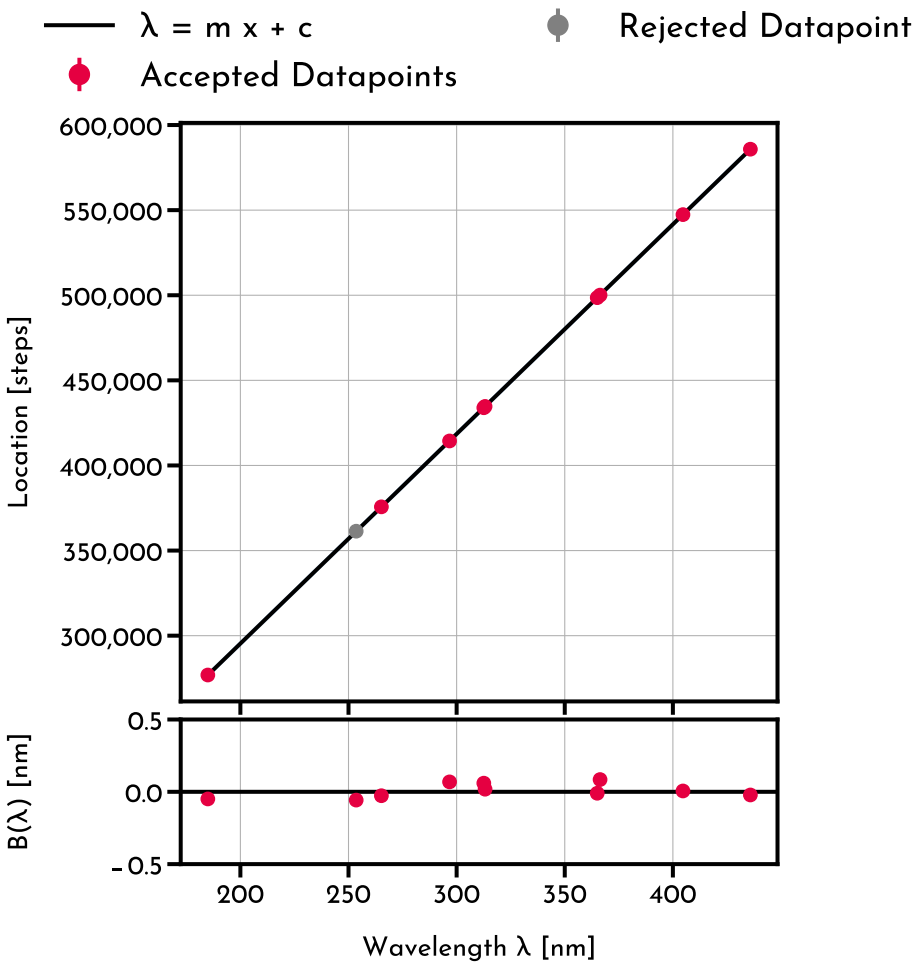



Figure 8.11: Calibration of the monochromator system using a linear model. The top panel shows the calibration points (wavelength vs motor position) whilst the bottom panel shows the residual of the data points to the fitted model. The ~0.1 nm offset observed for the 184.95 nm line defines the systematic error quoted in this work. The 253.7 nm line was not used for this fit due the high photon flux leading to difficulties in dead-time correction affecting the shape of the line.

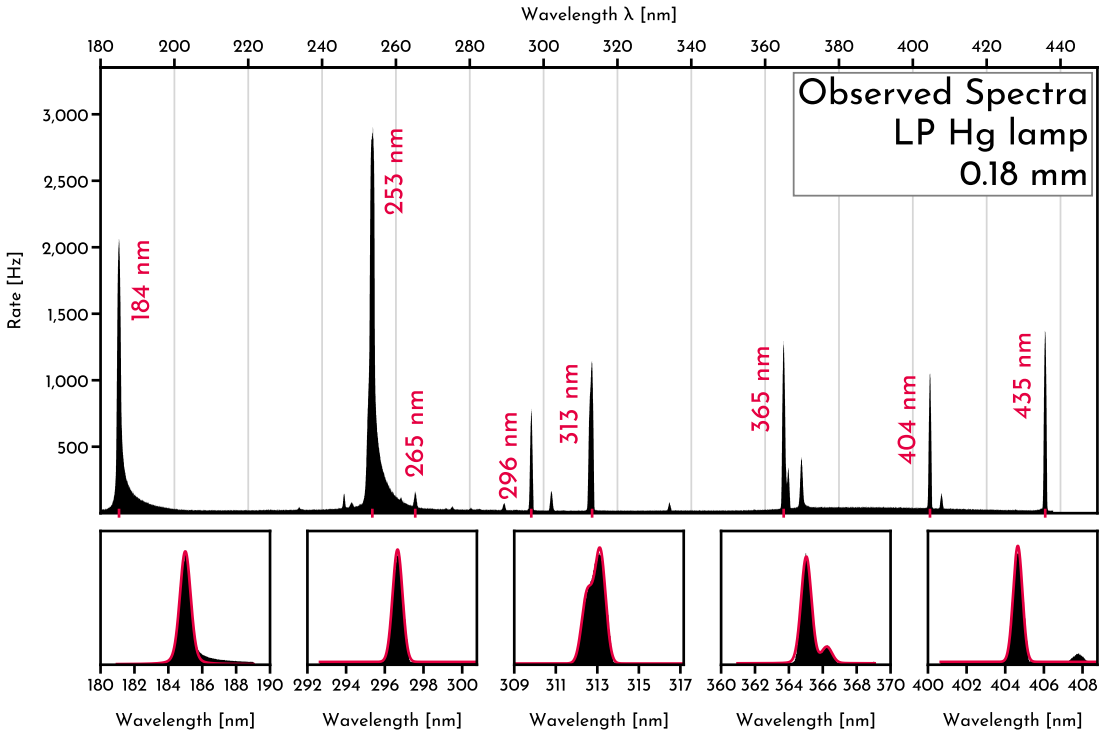



Figure 8.12: Observed LP Hg spectrum converted to wavelength using the calibration values. Several of the dead-time corrected peaks used for calibration are shown in the lower panels alongside their associated fits.

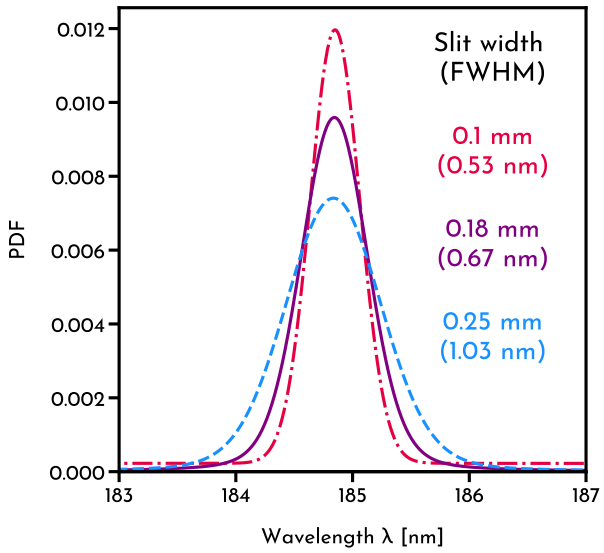



Figure 8.13: Resolution of the 184.95 nm LP Hg line, quantified by the full-width at half-maximum (FWHM), as a function of slit-width

## 8.7 Xenon VUV Luminescence Measurements

Measurements of xenon luminescence spectra were performed at a variety of pressures, both in two-phase equilibrium (GXe/LXe) and warm single phase (GXe) conditions. Two-phase data were acquired at several pressures in the range 1.3 bar to 2.2 bar focusing specifically on 1.3 bar, 1.7 bar, and 2.1 bar. Particular emphasis was put on the 1.7 bar dataset due to its proximity to the conditions found in the LZ and XENONnT experiments, see Figure 8.14.

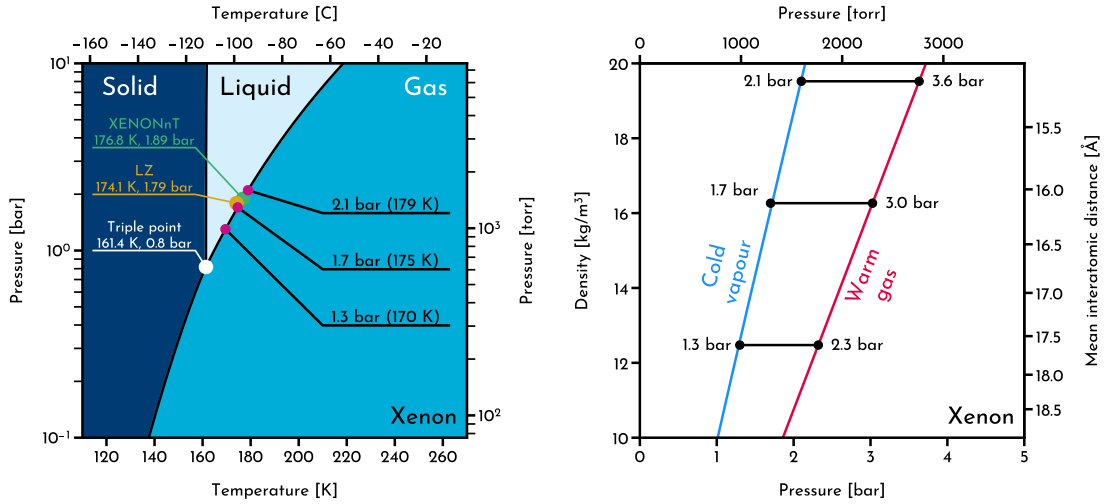



Figure 8.14: (Left) The phase diagram of xenon below the critical point. The operating point of the LZ and XENONnT detectors are shown in yellow and green [45, 153]. The thermodynamic properties of proto-Xenia follow the gas-liquid line of equilibrium. (Right) The density of warm xenon gas and cold xenon vapour. The vapour pressures studied in this work are highlighted alongside the warm gas pressure corresponding to the same density. Figures made using data from Air Liquide [213].

In denser media there is greater facility for collisional relaxation of xenon excimers, this will lead to emission of longer wavelength photons. To study the effect of xenon state (gas v.s. vapour) and density room temperature gas measurements were made at 2.2 bar and 0.3 bar. The former allows comparison between warm gaseous xenon (2.2 bar) and cold saturated vapour (1.3 bar) which have approximatly the same density[1], as seen in Figure 8.14. The latter enables observation of the first continuum which is expected to be absent at higher pressures.

[1]Whilst a 2.3 bar warm gas measurement would have provided a more direct comparison to the 1.3 bar cold vapour measurement we chose to measure the warm gas spectra at 2.2 bar for operational reasons

### 8.7.1 Data selection

Due to the short range of alpha particles produced by $^{228}$Th in LXe and proto-Xenia's compact design the data selection requirements for this measurement are relatively simple, with the four cuts used to select α-decay events, shown in Figure 8.15 for a 1.7 bar dataset. To remove noise and undersized pulses, cuts on the pulse area and width are applied. The remaining "genuine" pulses are then classified as S1-like or S2-like using a binary classifier on pulse width, the time between the 25$^{th}$ and 75$^{th}$ percentiles in integrated area, with pulses wider (narrower) than 100 ns classified as S1-like (S2-like).

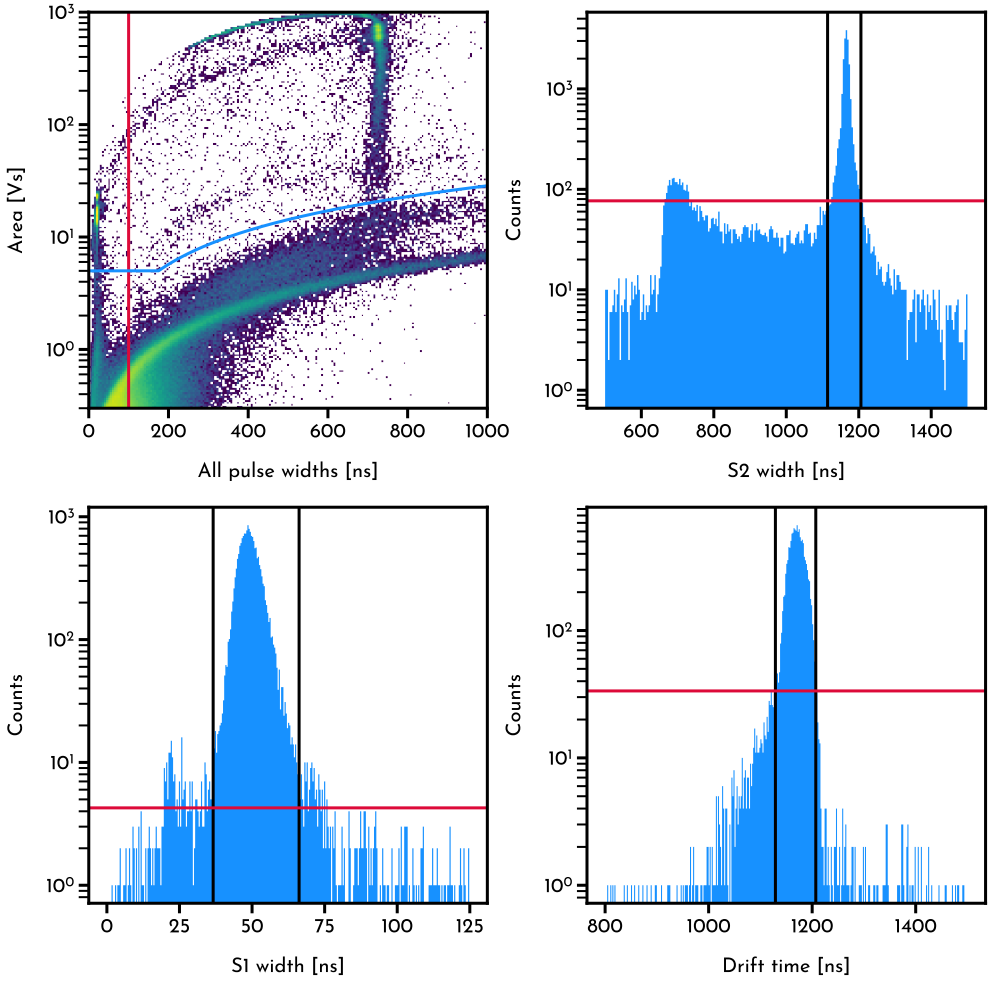



Figure 8.15: Data selection cuts for α interactions. (Top left) events below the blue line are removed and events to the left (right) of the red line are classified as S1-like (S2-like). (Top right) S2-like pulses between the two black lines are classified as S2s from α interactions. (Bottom left) S1-like pulses between the two black lines are classified as S1s from α interactions. (Bottom right) time difference between the S1 and S2 pulses in events with one S1 and one S2. Events with a drift time outside the black lines are removed.

To specifically select α-decay events further cuts are applied to these candidate pulses. The width of well-defined S1 and S2 pulses are very consistent: S1 pulses defined by excimer luminescence from the singlet/triplet states and recombination, and S2 pulse defined by the thickness of the vapour between the liquid surface and anode. Due to the relatively high rate and energy of α-decays the vast majority of detected events are α-particle interactions. To remove anomalous S1 and S2 pulses the tails of the width distribution are rejected at the 1% distribution amplitude level. To remove pile-up events, where multiple interactions occur within one event window, all events without a single S1 and S2 are discarded thereby eliminating events where an S1 can be buried within an S2. Finally, a cut on the drift-time, here defined as the time between the 10% area percentiles of the S1 and S2, was applied again rejecting the distribution tails at the 1% distribution amplitude level

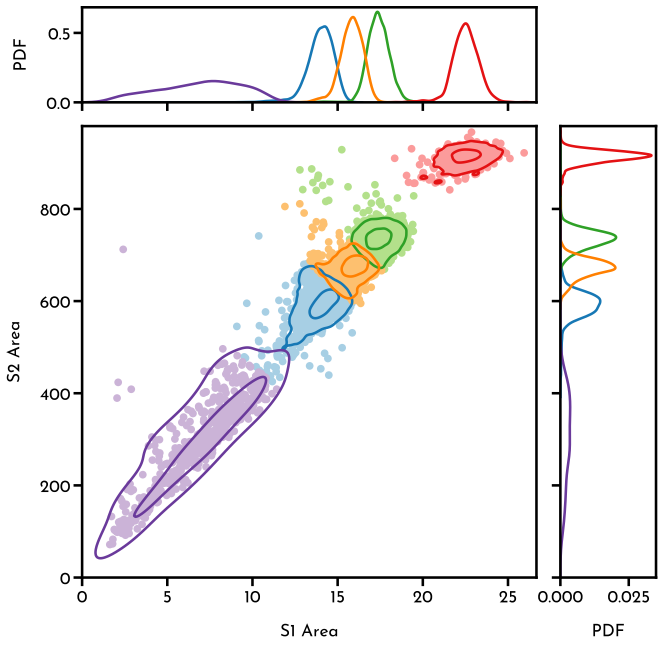



Figure 8.16: S1–S2 distribution of event associated with α-decays. By applying a k-means++ clustering algorithm several peaks associated with α-particle interactions within the liquid are found alongside a continuum of events. Using these classifications the continuum events are moved from spectra analyses.

The S2–S1 distribution from α-particle events is shown in Figure 8.16. In this parameter space several populations can be observed, the long continuum at low energies and several discrete monoenergetic α-decays at high energies. The low-energy continuum is attributed to α-decays directed into the source and associated γ-ray emission. As the foil is very thin, recoils produced within the source are still emitted into the liquid and detected above the detection threshold.

Alternatively, $\gamma$-rays associated with $\alpha$-decay products are also expected to contribute to the continuum with these events producing lower energy point-like interactions.

The $\alpha$-particle events are easily selected using a simple linear cut, however to better understand the detector and this analysis an alternative method using the k-means clustering algorithm, implemented in *scikit-learn*, to select specific $\alpha$-lines was used [214]. Separating out the different lines has advantage of being robust against changes in detector conditions, which would require manual tuning, and allows data quality cuts to be monitored for several monogenetic populations. With each population identified the lowest energy population was removed from the dataset to create a pure $\alpha$-decay dataset.

This population of $\alpha$-particle interactions is used to produce the S1 and S2 spectra. The time-difference between detected monochromator responses and the S1/S2 start time is shown in Figure 8.17. The shape of the two populations follow the S1 and S2 signals measured by the chamber PMT as expected. A small offset in the S2 distribution, where the monochromator appears to detect photons before the chamber PMT, exists due to defining the pulse start-time as the time of 10% integrated pulse-area; this definition provides a more robust timing metric than MIDAS' inbuilt definition. The coincidence windows, where monochromator signals contribute to the spectra, were manually defined for both pulses from these distributions and are highlighted in the figure. This selection procedure was applied for each monochromator signal thereby correctly accounting for the small probability of detecting multiple photons in coincidence with an S1 or S2 pulse.

For the limited number of gas-only datasets, where S2 (S1) datasets were acquired using biased (unbiased) grids, the above pulse-level cuts were applied, assuming slightly wider (150 ns) S1s. These S1 pulses are also present in the S2 datasets but are hidden within the S2 pulse. To remove this contamination monochromator photons within the first 150 ns of the S2 are rejected.

### 8.7.2 Spectra acquisition

Prior to the first run a short dataset from 110 nm to 210 nm was used to establish that no unexpected emission was observed outside the region expected for xenon excimer luminescence. After this initial check, measurements were performed over a narrower 145 nm to 205 nm

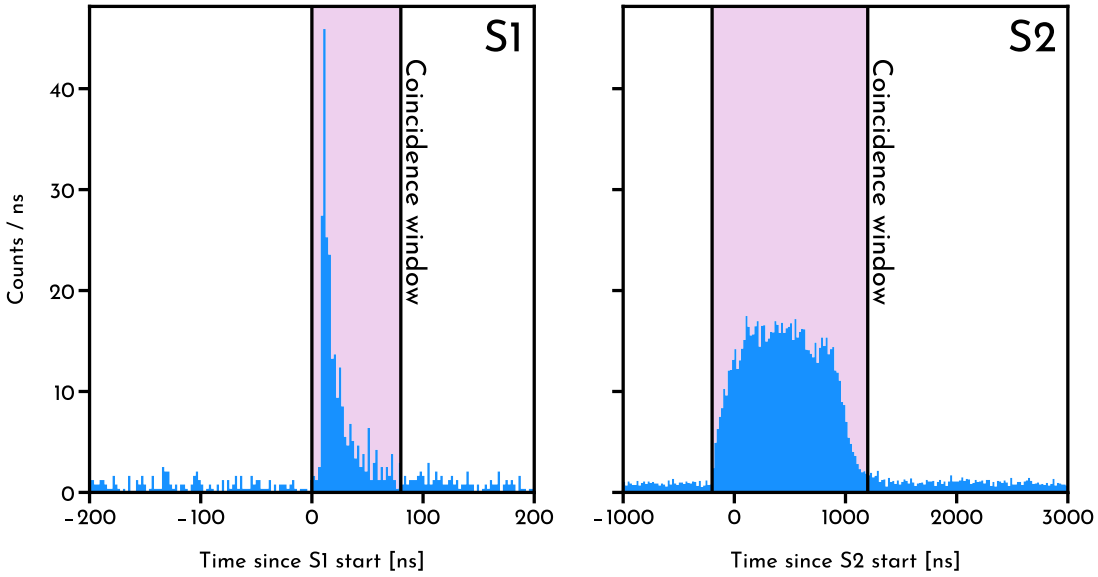



Figure 8.17: The S1 and S2 time coincidence cuts used to measure the luminescence spectra.

window. Xenon spectroscopy data was acquired using a similar methodology to calibration data. The DAQ triggered on the monochromator PMT with the monochromator set to step over the narrower window in equal steps of 0.03 nm (41 motor positions), with a five-second dwell time per step.

The experiment was originally designed for a chamber PMT trigger, with emission spectra measured using the monochromator PMT coincidence rate. However, due to the S1's low coincidence rate in the monochromator (2.1%) this would have proven to be impractical owing to data storage limitations. Instead, the DAQ was triggered on the monochromator PMT, which has a much lower background trigger rate (8 Hz) compared to the $\mathcal{O}$(kHz) chamber trigger rate. As the detection efficiency in both PMTs is approximately 100% this method still observes the same coincident events as a chamber triggered measurement whilst using only ~1% of the disk space.

Two-phase spectroscopy datasets were taken over extended periods, with the longest datasets lasting five days. To make the measurement robust against long timescale systematics, such as the variation in ambient temperature, each dataset traversed the ROI multiple times, with each scan lasting approximately $1\frac{1}{2}$ hours. In this methodology the spectrum from each scan was generated independently and later combined after validating detector stability.

Four two-phase equilibrium states (2.1 bar, 1.7 bar, 1.3 bar, and 1.1 bar) were studied in this work in order of decreasing pressure. The 1.7 bar dataset was of particular interest and studied more carefully due to its proximity to the operation points of several dark matter detectors, as seen in Figure 8.14; this acquisition took 97.8 hrs. The detector was found to be very stable over the length of each acquisition, as seen by the 1.7 bar dataset shown in Figure 8.18. Over this time period almost all detector parameters were found to be extremely stable, minimising systematic effects.

The electron-lifetime, measured by S2 integrated area, was observed to be both high and stable over the 2.1 bar, 1.7 bar, and 1.3 bar datasets. Unfortunately, a sudden drop in purity was observed during the 1.1 bar dataset. This decline, attributed to contamination from electrical discharge within the internal PMT or its voltage divider during operation at low pressure, poisoned the xenon preventing further study of the liquid phase. Whilst limited statistics were acquired at 1.1 bar they are insufficient to perform good measurements of the S1 luminescence.

To acquire further data with warm xenon gas the chamber was emptied of contaminated xenon, flushed with clean xenon, filled with clean xenon gas to a pressure of 2.2 bar, and allowed to warm back up to room temperature. A measurement was performed at 2.2 bar to facilitate the comparison between warm xenon gas and saturated vapour at the same density, whilst a 0.3 bar measurement was expected to observe the emergence of the first continuum, as seen previously in Ref. [215]. For the 0.3 bar GXe dataset the chamber PMT was biased at a reduced voltage of 800 V due to the reduction in breakdown voltage at lower pressures. As this measurement does not specifically require a high gain on the chamber PMT this has no effect on this measurement.

## 8.8 Xenon Spectra Results

The emission spectra of xenon in liquid-vapour equilibrium at 1.7 bar, observed using a 0.18 mm slit-width, is shown in Figure 8.19 alongside the 184.95 nm calibration line observed at the same slit-width. The two spectra form well-defined peaks with a clear offset between the two. By computing splines, shown in black, the peak emission wavelength was found to be $172.86 \pm 0.02(\text{stat.}) \pm 0.1(\text{sys.})$ nm for saturated vapour and $176.4 \pm 0.1(\text{stat.}) \pm 0.1(\text{sys.})$ nm for liquid xenon. All datasets shown in this plot, and all subsequent plots, have already had photon

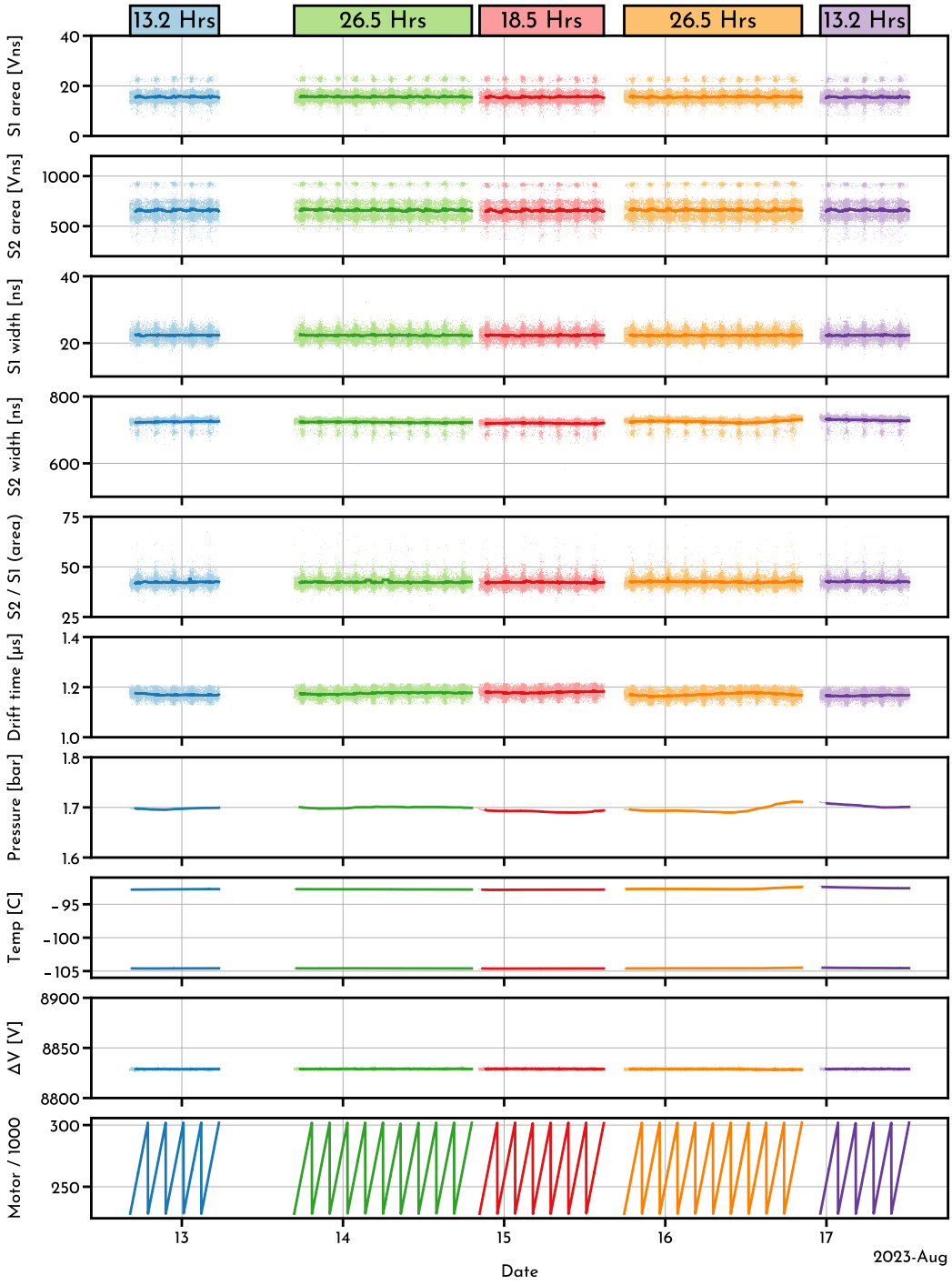



Figure 8.18: The detector state and chamber signal stability during acquisition of two-phase spectra at 1.7 bar. The temperatures indicated are from two thermometers each located 1–2 cm either side of the liquid surface respectively with the warmer (colder) thermometer in the (gas) liquid phase. All detector parameters were found to stable over the entire run.

efficiency corrections applied. No pulse size correction were applied in this and all subsequent plots as they were found to be flat and thus unnecessary. The fine monochromator resolution was found to have negligible effect on the measured FWHM, with the width, quoted at one significant figure of the error, not shrinking after subtraction of the monochromator resolution.

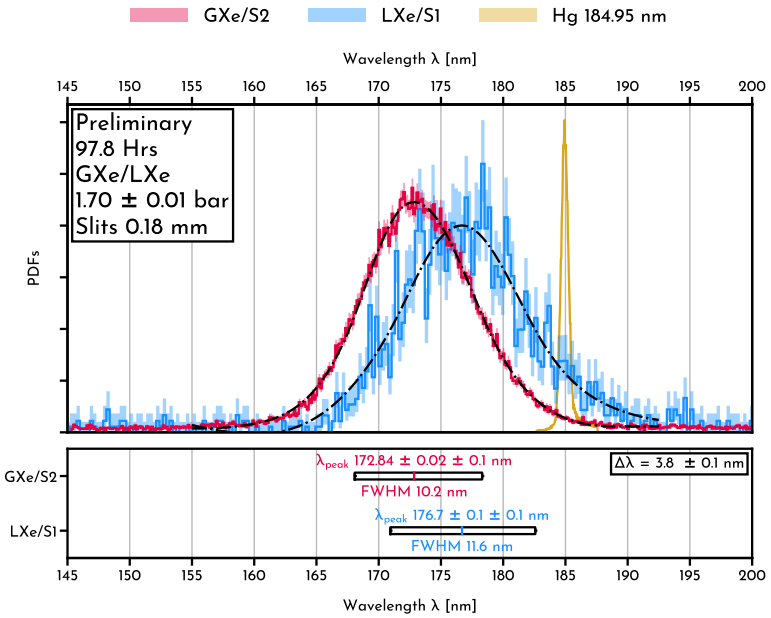



Figure 8.19: (Top panel) The measured luminescence spectra of liquid (blue) and vapourous (red) xenon at 1.7 bar alongside the observed detector response to the monochromatic 185 nm mercury line. The liquid and vapourous datasets were sampled simultaneously from S1 and S2 pulses respectively using a vertical slit-width of 0.18 mm. (Bottom panel) The peak wavelength and FWHM (bar) measured from the smoothed spline.

To evaluate the systematic effect of the temperature gradient and photon path on the S2 emission spectra within the xenon vapour, the spectra were constructed for the beginning and end of the S2 separately, see Figure 8.20. As $\alpha$-particle tracks are effectively point-like in the liquid, photons emitted by the colder vapour nearer to the liquid are detected earlier in the S2 and vice versa. By comparing the peaks of the two datasets, the warmer xenon vapour was found to emit photons with a wavelength 0.19 ± 0.04 nm shorter than that of the colder vapour.

The emission spectra of xenon in liquid-vapour equilibrium at 1.7 bar, observed using a 0.18 mm slit-width, is shown in Figure 8.21. This measurement, the first chronologically, was performed using a wider slit-width of 0.25 mm. At this width the photon acceptance of the monochromator was higher but was more difficult to calibrate informing the decision to move to a 0.18 mm slit-width. This dataset clearly shows two district peaks for S1 and S2 light at 172.68 ± 0.03(stat.) ±

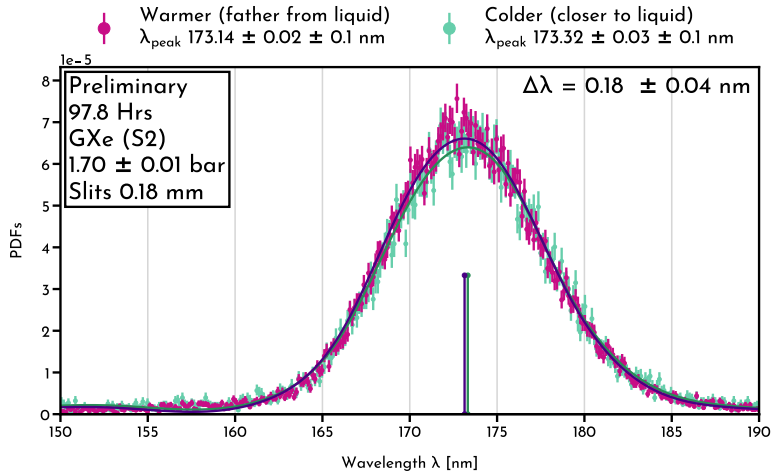



Figure 8.20: Spectra of electroluminescence in xenon vapour at 1.7 bar. The green (violet) histogram and curve correspond to monochromator coincidences from photons emitted from the colder (warmer) xenon vapour found closer to (farther from) the liquid surface.

0.1(sys.) nm and 176.4 ± 0.1(stat.) ± 0.1(sys.) nm respectively.

The observed spectra from two-phase conditions at 1.3 bar with a 0.18 mm slit-width is shown in Figure 8.22. This lower statistics dataset still has two clear and distinct peaks, though the S1 peak is less well-defined due to of lower coincident rate. The peak wavelengths were observed to be 172.89 ± 0.03(stat.) ± 0.1(sys.) nm and 176.3 ± 0.3(stat.) ± 0.1(sys.) nm respectively.

The comparison of warm xenon gas at 2.2 bar and 0.3 bar is shown in Figure 8.24. The peak wavelength of the two spectra were found to be in good agreement demonstrating that the peak electroluminescence wavelength does not strongly depend on pressure. As expected the 0.3 bar dataset clearly observes the first continuum at shorter wavelengths.

## 8.9 Discussion of Observed Xenon Spectra

The measured results described above are collated in Figure 8.25. From this the proportional relationship between peak emission wavelength and density is readily apparent with the gas, vapour, and liquid spectra forming discrete bands. For each state the observed peak wavelength was observed to be constant demonstrating that the peak wavelength is not sensitive to pressure. Liquid luminescence was found to be on average 3.6 nm longer than vapour electroluminescence for all pressures studied and appears constant within quoted

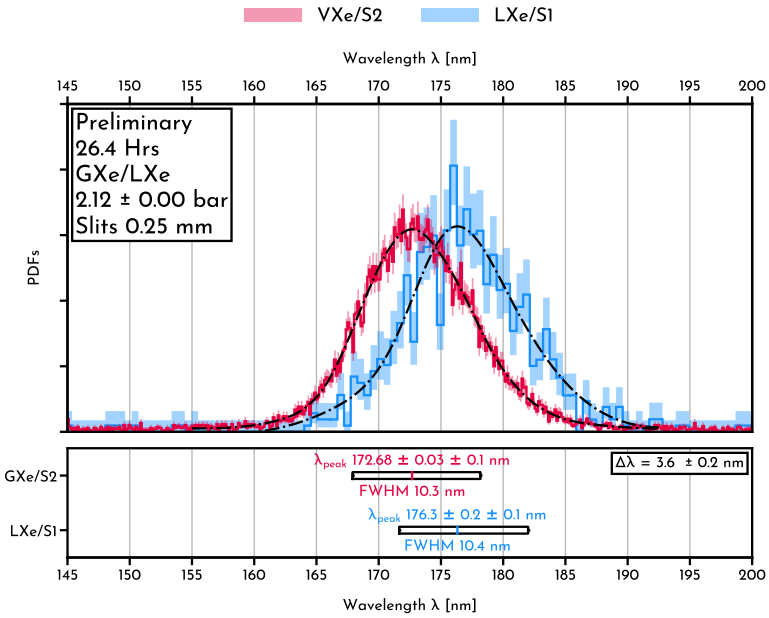



Figure 8.21: (Top panel) The measured luminescence spectra of liquid xenon (blue) and xenon vapour (red) 2.2 bar alongside the observed detector response to the monochromatic 185 nm mercury line. The liquid and vapour datasets were sampled simultaneously from S1 and S2 pulses using a vertical slit-width of 0.18 mm. (Bottom panel) The peak wavelength and FWHM (bar) measured from the smoothed spline.

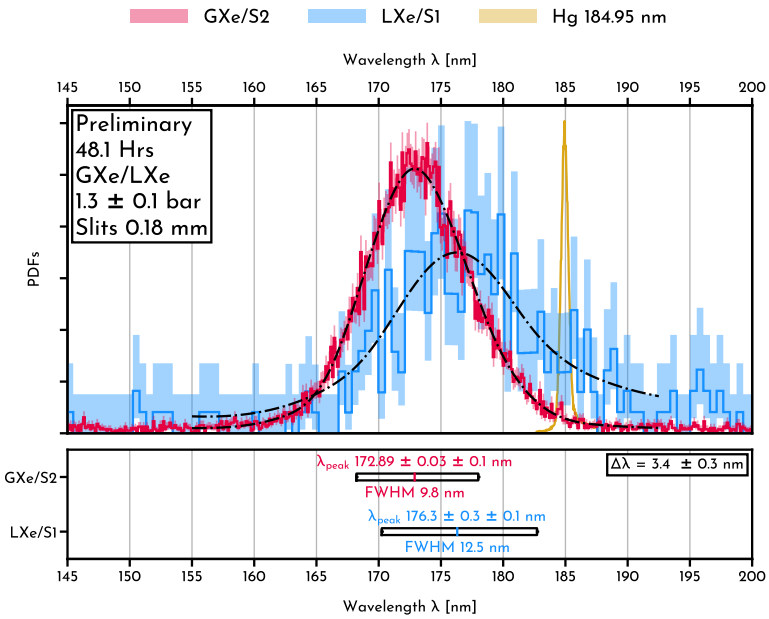



Figure 8.22: (Top panel) The measured luminescence spectra of liquid xenon (blue) and xenon vapour (red) 1.3 bar alongside the observed detector response to the monochromatic 185 nm mercury line. The liquid and vapour datasets were sampled simultaneously from S1 and S2 pulses using a vertical slit-width of 0.18 mm. (Bottom panel) The peak wavelength and FWHM (bar) measured from the smoothed spline.

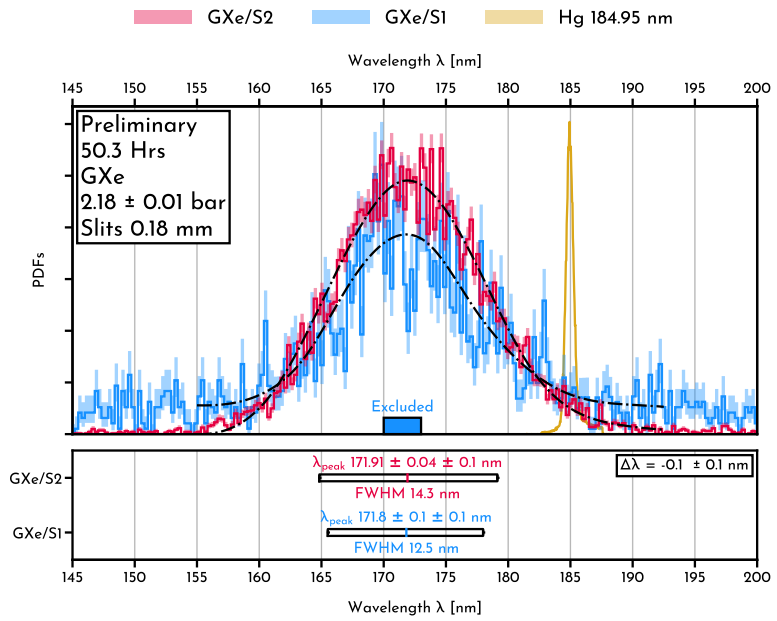



Figure 8.23: Comparison of S1 and S2 light in warm xenon gas. The measured offset in peak emission wavelength, measured using splines, is 0.1 ± 0.1 nm and is consistent with both production mechanisms emitting photons of the same wavelength as expected. The increased background rate observed from this measurement is due to the longer pulse width leading to a higher accidental rate. A small region ≈172 nm was ignored when generating the spline spectra due to a distinct drop in the measured S1 spectrum.

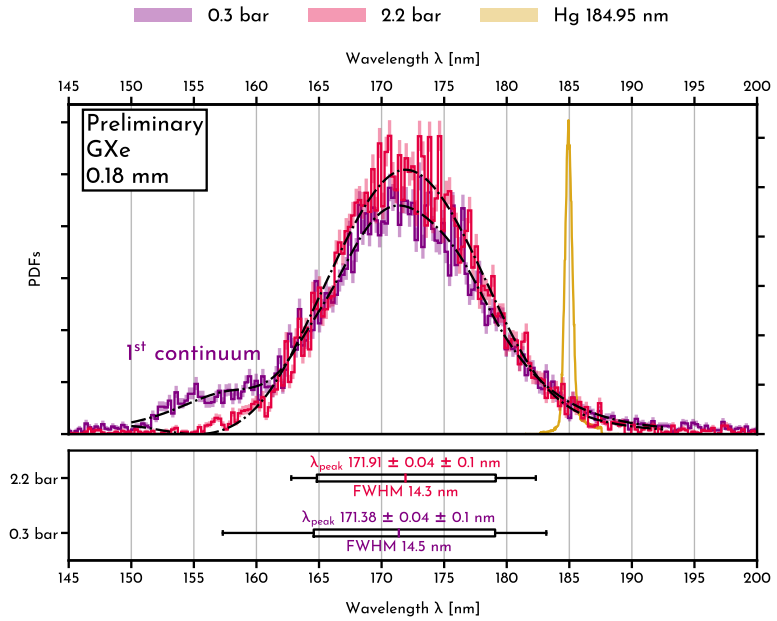



Figure 8.24: (Top panel) Electroluminescence spectra of warm gaseous xenon at 0.3 bar and 2.2 bar. The first continuum can be clearly observed in the 0.3 bar data. (Bottom panel) The peak wavelength and FWHM (bar) measured from the smoothed spline.

uncertainties. Electroluminescence of xenon vapour was found to peak at longer wavelengths than warm xenon gas. A reduction in the FWHM was also observed and is attributed to lower variance in the excimer separation as higher densities.

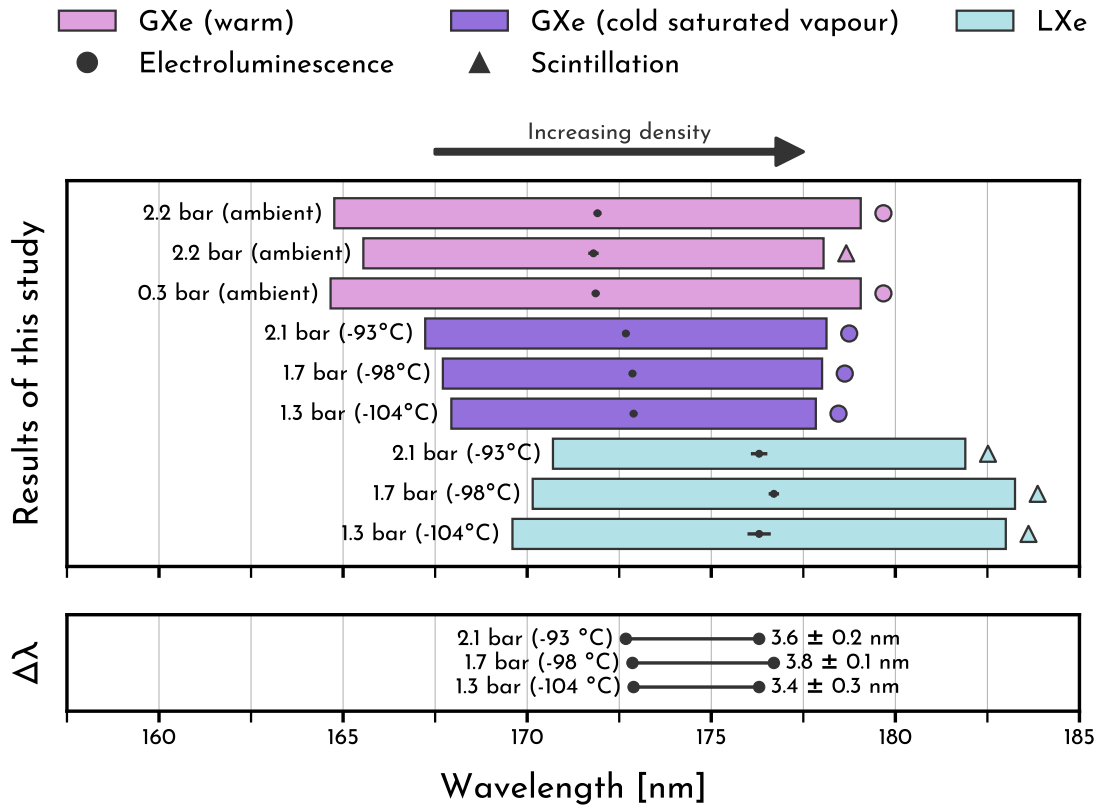



Figure 8.25: Comparison of xenon spectra measured at Imperial College London. (Top panel) The observed peak wavelength and its associated error are shown in black with the FWHM displayed as horizontal bars. The spectra considered by state demonstrate the correlation between peak emission wavelength and density alongside the stability of the spectra as a function of pressure. (Bottom panel) the difference in wavelength between S1 and S2 light was found to be consistent at 3.6 nm.

The results from this study—separated into xenon gas, liquid, and vapour—are displayed alongside results from the literature in Figure 8.26 and tabulated in Table 8.1. Each result is labelled by the light production mechanism (scintillation and electroluminescence), pressure (if available) and temperature. Whilst the peak wavelengths can be directly compared it must be noted not all results account for the detector resolution when quoting the FWHM with only Fujii . unambiguously deconvolving the detector response.

These gas measurements presented here are in good agreement with previous results and

reside approximately at the average of these previous results. The first-of-their-kind xenon vapour spectra measurements have a longer wavelength but are still located within the range of previous results for xenon gas.

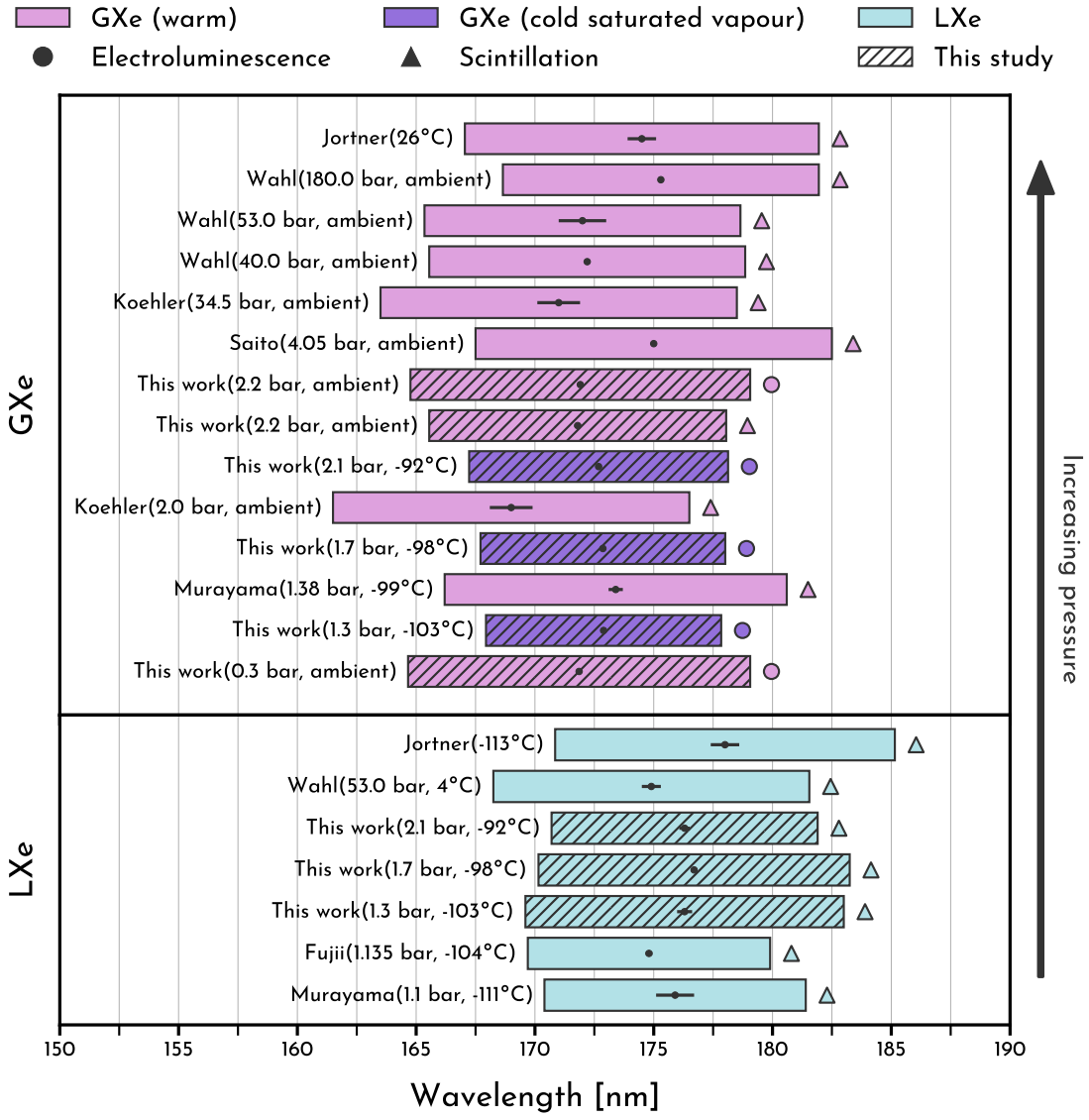



Figure 8.26: Comparison of xenon spectra measurements to results in the literature [189, 216–220].

The newly presented LXe scintillation measurements have some level of tension with recent measurements of the liquid state, particularly with the 174.9 nm measured by Fujii et al. [189]. The measurement presented here simultaneously observe vapour spectra consistent with expectations from previous GXe measurements removing the possibility of most unexpected systematic effects, notably not including geometric effects, affecting the LXe results presented

here. None of the systematic effects either corrected for or otherwise considered could cause a shift significant enough to match Fujii's result. In additions, from comparing the FWHM of all LXe results, Fujii et al. appear to preferably lose their long wavelength. The loss of the long wavelength component could be responsible for the shift between Fujii and the results presented here which are in good agreement with the results by Murayama. The observed offset between liquid and vapour spectra, 3.6 nm, is consistent with the value measured by Wahl, 2.9 ± 1.0 nm, observed over the liquid-gas transition at a constant pressure of 53 bar.

The electroluminescence spectra in the cold saturated vapour (S2) was found to peak at 172.8 nm, approximatly 1 nm longer than warm gaseous xenon's 171.9 nm. This direction of this change is consistent with the expectation that excimers in the vapour undergo greater relaxation towards the potential minimum due to more frequent scattering off neighbouring atoms. By measuring the vapour spectrum at three pressures (1.3 bar, 1.7 bar, 2.1 bar) and the gas spectrum at two very different pressures (0.3 bar and 2.2 bar), we have demonstrated that the difference in luminance between the two states is consistent irrespective of pressure.

The prompt scintillation spectra in the liquid (S1) was found to have a mean modal wavelength of 176.4 nm. This value is within errors of the 175.9 ± 0.8 nm measured by Murayama using a $^{60}$Co source [219]. There is some disagreement with the results from Fujii, the current standard value used in the field, which measured a modal wavelength of 174.8 ± 0.1 nm [189]. Fujii's published FWHM is noticeably curtailed towards longer wavelengths when compared to all other measurement, including those presented here. If Fujii's apparatus contained some spectral inefficiency which selectively removed longer wavelengths, such as absorption on contaminants, it could explain their shorter wavelength compared to Murayama, Jortner [216], and this work, however there is no basis for this hypothesis in their publication.

Very recently, new measurements have been published which measure the luminance spectra across the gas-liquid phase transition [217]. By cooling high pressure (53 bar) gas below the critical temperature (11.8 °C) the modal wavelength was found to redshift by 2.1 ± 0.1 nm from 172.0 ± 1.0 nm in the gas to 174.9 ± 0.4 nm in the liquid. This measured redshift is slightly shorter than the value found here, 3.6 ± 0.4 nm, but is consistent with a change in modal wavelength between the two states.

In the measurements presented here there is some variation in the FWHM of the S1 spectra.

The width of the 1.3 bar and 1.7 bar datasets are consistent but the 2.1 bar spectra is ~2 nm narrower, this effect could arise deficiencies in the spline fitting procedure.

## 8.10 Conclusion

To properly model LXe TPCs requiring a good understanding of the luminance spectra produced by S1 and S2 light. Using the proto-Xenia chamber, we present the first measurements of emission spectra for S2 light from electroluminescence of saturated xenon vapour in liquid equilibrium. To preform this measurement, the proto-Xenia chamber, specifically its monochromator, was calibrated between the VUV and visible using an LP Hg lamp. This calibration achieved excellent spectral reconstruction at all wavelengths with a 0.1 nm systematic offset at the 184.95 nm line most relevant to xenon spectra.

By simultaneously studying the time resolved S1 and S2 signals we also present the first direct comparison between liquid and vapour luminescence. These measurements observe that liquid luminance is 3.6 nm longer than vapour. This result is consistent with denser media, where the inter-nuclear separation is shorter, forming lower energy excimer's which produce luminescence of a longer mean wavelength. Recent measurements performed across the phase boundary at high pressure find a shorter offset between the two states but is nonetheless consistent in its observation of an offset and its direction.

These results are important for properly modelling the propagation and detection of S1 and S2 light in current and future LXe detectors. With regard to currently operating experiments, such as LZ, these results will improve the accuracy of detector response models, specifically reducing the systematic error associated with photon prorogation and the PMT response by allowing the S1 and S2 response to differ. For example, the DPE probability of a PMT is wavelength dependant meaning the detector model should in-principle treat the DPE probability of S1 and S2 light as distinct, though likely very similar, numbers. With regard to future detectors, such as XLZD, the values will inform the design and optimisation of the detector. For instance materials with sharp changes in the spectral response around these regions would have to be reassessed in light of these measurements.

Table 8.1: Measurements of the scintillation spectra of gaseous and liquid xenon.

(a) Gaseous xenon

| Pressure [bar] | Temperature [°C] | Vapour | Source | Type | Wavelength [nm] | FWHM [nm] | Citation |
|---|---|---|---|---|---|---|---|
| 180 | ambient | X | photon excitation | scintillation | 175.3 ± 0.1 | 13.3 | [217] |
| 53 | ambient | X | photon excitation | scintillation | 172.0 ± 1.0 | 13.3 | [217] |
| 40 | ambient | X | photon excitation | scintillation | 172.2 ± 0.1 | 13.3 | [217] |
| 34.5 | ambient | X | Electron beam | scintillation | 171.0 ± 0.9 | 15.0 | [218] |
| 4 | ambient | X | α ($^{241}$Am) | scintillation | 175.0 ± 0.0 | 15.0 | [220] |
| 2.2 | ambient | X | α ($^{228}$Th) | scintillation | 171.8 ± 0.1 (stat.) ± 0.1 (sys.) | 12.5 | This work |
| 2.2 | ambient | X | α ($^{228}$Th) | electroluminescence | 171.91 ± 0.04 (stat.) ± 0.1 (sys.) | 14.3 | This work |
| 2.1 | −92 | ✓ | α ($^{228}$Th) | electroluminescence | 172.68 ± 0.03 (stat.) ± 0.1 (sys.) | 10.9 | This work |
| 2 | ambient | X | Electron beam | scintillation | 169.0 ± 0.9 | 15.0 | [218] |
| 1.7 | −98 | ✓ | α ($^{228}$Th) | electroluminescence | 172.86 ± 0.02 (stat.) ± 0.1 (sys.) | 10.3 | This work |
| 1.4 | −99 | X | γ ($^{60}$C) | scintillation | 173.4 ± 0.3 | 14.4 | [219] |
| 1.3 | −103 | ✓ | α ($^{228}$Th) | electroluminescence | 172.89 ± 0.03 (stat.) ± 0.1 (sys.) | 9.9 | This work |
| 0.3 | ambient | X | α ($^{228}$Th) | electroluminescence | 171.86 ± 0.04 (stat.) ± 0.1 (sys.) | 14.4 | This work |
| – | 26 | X | α ($^{210}$Po) | scintillation | 174.5 ± 0.6 | 14.9 | [216] |

(b) Liquid xenon

| Pressure [bar] | Temperature [°C] | Vapour | Source | Type | Wavelength [nm] | FWHM [nm] | Citation |
|---|---|---|---|---|---|---|---|
| 53 | 4 | – | photon excitation | scintillation | 174.9 ± 0.4 | 13.3 | [217] |
| 2.1 | −92 | – | α ($^{228}$Th) | scintillation | 176.3 ± 0.2 (stat.) ± 0.1 (sys.) | 11.2 | This work |
| 1.7 | −98 | – | α ($^{228}$Th) | scintillation | 176.7 ± 0.1 (stat.) ± 0.1 (sys.) | 13.1 | This work |
| 1.3 | −103 | – | α ($^{228}$Th) | scintillation | 176.3 ± 0.3 (stat.) ± 0.1 (sys.) | 13.4 | This work |
| 1.1 | −104 | – | γ ($^{60}$C) | scintillation | 174.8 ± 0.1 (stat.) ± 0.1 (sys.) | 10.2 | [189] |
| 1.1 | −111 | – | γ ($^{60}$C) | scintillation | 175.9 ± 0.8 | 11.0 | [219] |
| – | −113 | – | α ($^{210}$Po) | scintillation | 178.0 ± 0.6 | 14.3 | [216] |

# 9

# Conclusion

This thesis detailed the motivation for dark matter at astrophysical and Cosmological scales, the search for WIMP dark matter using the LZ experiment, and the measurement of xenon luminescence spectra using a LXe chamber at Imperial.

LZ's first WIMP search, described in Chapter 5, found no evidence of WIMP dark matter using a 5.5 tonne · 60 days exposure; in doing so LZ has set the most stringent upper limits on the spin-independant WIMP-nucleon cross-section to date, with a peak sensitivity of $9.2 \times 10^{-48}$ cm$^2$ for a 36 GeV/c$^2$ WIMP. Obtaining this result using only a short dataset, only 6% of the total 1000 live-day expectation, underlines the potential of LZ to observe or exclude ever more feebly interacting WIMPs as its proceeds towards its design sensitivity of $1.4 \times 10^{-48}$ cm$^2$ for a 40 GeV/c$^2$ WIMP.

To perform the WIMP search analyses, and indeed all analyses in LZ, requires a good understanding of the detector response. Chapter 4 details the in-situ measurement of the DPE probabilities for all TPC PMTs and their comparison to dedicated measurements performed at Imperial. A small systematic offset between the Imperial and LZ measurements was observed with top (bottom) array PMTs having a lower (higher) mean DPE probability than the corresponding Imperial measurements. This offset is attributed to the temperature dependence of the DPE probability and the top (bottom) array PMT being operated at a higher (lower) temperature than the Imperial measurements.

Knowledge of the DPE effect is exploited by the $^8$B sensitivity study contained in Chapter 6. This study uses the "VUV-ness", computed using the DPE probabilities, and time-profile of S1 signals to discriminate between signal-like and background-like interactions, thereby reducing the scintillation threshold of LZ from three-fold to two-fold. The analytic models presented in this chapter both greatly simplify the computation of the signal and background PDFs and trivialises the integration of the full PMT level detector model. By augmenting this analysis with the interaction depth, measured per-array light-detection efficiency, and S2 signal size a $\sim O(30\%)$ improvement in sensitivity was observed using the Asimov dataset.

To use the S1 time-profile in the above study requires time-alignment of all TPC PMTs and the correction of photon TOF. By measuring the photon TOF using waveforms from $\alpha$-decay, we observe a small (7.3 ns) timing offset between the two TPC arrays and a maximum difference in time-of-flight between the two arrays of ~40 ns. This effect, minor for tonne-scale detectors

such as LZ, will be problematic for the 3 m detector proposed by the XLZD consortium which will observe significant distortion of S1 signals emitted from near the top array.

The study of ultra-low energy calibration techniques in Chapter 7 found that photo-nucleus CGES and Compton scattering are impractical for calibrating LXe detectors between 50 eV and 150 eV. In both cases scatters in the range of interest were possible but exceedingly rare: CGES dominated by forwarding scattering for high-energy photons; Compton scattering sub-dominant to photo-ionisation of xenon atoms. The study of $^{127}$Xe electron capture includes predictions of O-shell capture with a probability of $\mathcal{O}$(0.1%). This sub-threshold process should be detectable in LZ via the emission of Auger electrons in coincidence with $^{127}$I $\gamma$-rays. During this study it became apparent that LUX's interpretation of N-shell capture may be incorrect due to their omission of Auger cascades, the dominant reaction process in this regime. By not accounting for the reduction in the cascade energy from Auger ionisation and the presence of Auger electrons, LUX likely overestimated the charge yield and interaction energy in their N-shell yield measurement.

Finally, in Chapter 8 simultaneous measurements of S1 and S2 luminescence spectra are presented. These measurements are the first simultaneous measurements of liquid-vapour luminescence and the first measurements of saturated xenon vapour electroluminescence. The 1.7 bar results, S1 = 176.7 ± 0.1 nm and S2 = 172.8 ± 0.1 nm, are directly applicable to LXe TPC dark matter detectors, enabling more accurate modeling of S1 and S2 signals when simulating the detector response. A clear and consistent 3.6 nm offset is observed between S1 and S2 light during these measurements for all pressures. This offset is consistent with, though slightly larger than, comparisons of isolated measurements of xenon as a warm gas and liquid, and recent measurements of xenon spectra across the phase boundary at high pressure.

# Bibliography


[1] G. Bertone and D. Hooper, 'History of dark matter', Rev. Mod. Phys. **90**, 045002 (2018).

[2] F. Zwicky, 'Die Rotverschiebung von extragalaktischen Nebeln', Helvetica Phys. Acta **6**, 110–127 (1933).

[3] H. Andernach and F. Zwicky, *English and Spanish Translation of Zwicky's (1933) The Redshift of Extragalactic Nebulae*, (5th Nov. 2017) http://arxiv.org/abs/1711.01693, pre-published.

[4] V. C. Rubin, J. Ford W. K. and N. Thonnard, 'Extended rotation curves of high-luminosity spiral galaxies. IV. Systematic dynamical properties, Sa -¿ Sc.', Astrophys. J. **225**, L107–L111 (1978).

[5] K. C. Freeman, 'On the Disks of Spiral and S0 Galaxies', Astrophys. J. **160**, 811 (1970).

[6] T. Prusti et al., 'The Gaia mission', A&A **595**, A1 (2016).

[7] A. Vallenari et al., 'Gaia Data Release 3 - Summary of the content and survey properties', A&A **674**, A1 (2023).

[8] E. L. Wright et al., 'The Wide-field Infrared Survey Explorer (WISE): Mission Description and Initial On-orbit Performance', Astron. J. **140**, 1868–1881 (2010).

[9] S. R. Majewski et al., 'The Apache Point Observatory Galactic Evolution Experiment (APOGEE)', AJ **154**, 94 (2017).

[10] M. F. Skrutskie et al., 'The Two Micron All Sky Survey (2MASS)', Astron. J. **131**, 1163–1183 (2006).

[11] J. Einasto, 'On the Construction of a Composite Model for the Galaxy and on the Determination of the System of Galactic Parameters', Tr. Astrofiz. Instituta Alma-Ata **5**, 87–100 (1965).

[12] X. Ou et al., 'The dark matter profile of the Milky Way inferred from its circular velocity curve', Monthly Notices of the Royal Astronomical Society **528**, 693–710 (2024).

[13] A.-C. Eilers et al., 'The Circular Velocity Curve of the Milky Way from 5 to 25 kpc', ApJ **871**, 120 (2019).

[14] P. F. d. Salas et al., 'On the estimation of the local dark matter density using the rotation curve of the Milky Way', J. Cosmol. Astropart. Phys. **2019**, 037 (2019).

[15] D. Clowe, A. Gonzalez and M. Markevitch, 'Weak-Lensing Mass Reconstruction of the Interacting Cluster 1E 0657–558: Direct Evidence for the Existence of Dark Matter*', ApJ **604**, 596 (2004).

[16] K. Coble, K. McLin and L. Cominsky, *Big Ideas in Cosmology* (LibreTexts).

[17] R. H. Dicke et al., 'Cosmic Black-Body Radiation.', Astrophys. J. **142**, 414–419 (1965).

[18] A. A. Penzias and R. W. Wilson, 'A Measurement of Excess Antenna Temperature at 4080 Mc/s.', Astrophys. J. **142**, 419–421 (1965).

[19] N. Aghanim et al., 'Planck 2018 results - I. Overview and the cosmological legacy of Planck', A&A **641**, A1 (2020).

[20] N. Aghanim et al., 'Planck 2018 results - VI. Cosmological parameters', A&A **641**, A6 (2020).

[21] R. L. Workman et al. (Particle Data Group), 'Review of particle physics', PTEP **2022**, 083C01 (2022).

[22] J. L. Feng, 'Dark Matter Candidates from Particle Physics and Methods of Detection', Annu. Rev. Astron. Astrophys. **48**, 495–545 (2010).

[23] S. D. McDermott, H.-B. Yu and K. M. Zurek, 'Turning off the lights: How dark is dark matter?', Phys. Rev. D **83**, 063509 (2011).

[24] M. Markevitch et al., 'Direct Constraints on the Dark Matter Self-Interaction Cross Section from the Merging Galaxy Cluster 1E 0657–56', ApJ **606**, 819 (2004).

[25] G. Steigman and M. S. Turner, 'Cosmological constraints on the properties of weakly interacting massive particles', Nuclear Physics B **253**, 375–386 (1985).

[26] G. Steigman, B. Dasgupta and J. F. Beacom, 'Precise relic WIMP abundance and its impact on searches for dark matter annihilation', Phys. Rev. D **86**, 023506 (2012).

[27] P. S. B. Dev, A. Mazumdar and S. Qutub, 'Constraining non-thermal and thermal properties of Dark Matter', Front. Phys. **2** (2014).

[28] V. N. Lebedenko et al., 'Results from the first science run of the ZEPLIN-III dark matter search experiment', Phys. Rev. D **80**, 052010 (2009).

[29] C. Collaboration et al., 'First results from the CRESST-III low-mass dark matter program', Phys. Rev. D **100**, 102002 (2019).

[30] R. Bernabei et al., 'The DAMA project: Achievements, implications and perspectives', Progress in Particle and Nuclear Physics **114**, 103810 (2020).

[31] J. B. R. Battat et al., 'Low threshold results and limits from the DRIFT directional dark matter detector', Astroparticle Physics **91**, 65–74 (2017).

[32] W. B. Atwood et al., 'THE LARGE AREA TELESCOPE ON THE FERMI GAMMA-RAY SPACE TELESCOPE MISSION', ApJ **697**, 1071 (2009).

[33] M. G. Aartsen et al., 'Improved limits on dark matter annihilation in the Sun with the 79-string IceCube detector and implications for supersymmetry', J. Cosmol. Astropart. Phys. **2016**, 022 (2016).

[34] J. M. Gaskins, 'A review of indirect searches for particle dark matter', Contemp. Phys. **57**, 496–525 (2016).

[35] T. A. Collaboration et al., 'The ATLAS Experiment at the CERN Large Hadron Collider', J. Inst. **3**, S08003 (2008).

[36] T. C. Collaboration et al., 'The CMS experiment at the CERN LHC', J. Inst. **3**, S08004–S08004 (2008).

[37] O. Buchmueller, C. Doglioni and L.-T. Wang, 'Search for dark matter at colliders', Nature Phys **13**, 217–223 (2017).

[38] A. Boveia and C. Doglioni, 'Dark Matter Searches at Colliders', Annu. Rev. Nucl. Part. Sci. **68**, 429–459 (2018).

[39] J. D. Lewin and P. F. Smith, 'Review of mathematics, numerical factors, and corrections for dark matter experiments based on elastic nuclear recoil', Astroparticle Physics **6**, 87–112 (1996).

[40] A. K. Drukier, K. Freese and D. N. Spergel, 'Detecting cold dark-matter candidates', Phys. Rev. D **33**, 3495–3508 (1986).

[41] L. Necib, M. Lisanti and V. Belokurov, 'Inferred Evidence for Dark Matter Kinematic Substructure with SDSS–Gaia', ApJ **874**, 3 (2019).

[42] N. W. Evans, C. A. J. O'Hare and C. McCabe, *SHM$^{++}$: A Refinement of the Standard Halo Model for Dark Matter Searches in Light of the Gaia Sausage*, (29th Dec. 2018) http://arxiv.org/abs/1810.11468, pre-published.

[43] R. H. Helm, 'Inelastic and Elastic Scattering of 187-Mev Electrons from Selected Even-Even Nuclei', Phys. Rev. **104**, 1466–1475 (1956).

[44] D.-3. Collaboration et al., 'First Results from the DEAP-3600 Dark Matter Search with Argon at SNOLAB', Phys. Rev. Lett. **121**, 071801 (2018).

[45] J. Aalbers et al., *FlamTeam/flamedisx: v2.0.0*, Zenodo, 20th May 2022.

[46] J. Aalbers et al., *JelleAalbers/wimprates: v0.5.0*, version v0.5.0, Zenodo, 13th Feb. 2023.

[47] D. Akimov et al., 'Observation of coherent elastic neutrino-nucleus scattering', Science **357**, 1123–1126 (2017).

[48] C. Collaboration et al., 'First Measurement of Coherent Elastic Neutrino-Nucleus Scattering on Argon', Phys. Rev. Lett. **126**, 012002 (2021).

[49] W. Haxton, R. Hamish Robertson and A. M. Serenelli, 'Solar Neutrinos: Status and Prospects', Annu. Rev. Astron. Astrophys. **51**, 21–61 (2013).

[50] J. Billard, E. Figueroa-Feliciano and L. Strigari, 'Implication of neutrino backgrounds on the reach of next generation dark matter direct detection experiments', Phys. Rev. D **89**, 023524 (2014).

[51] R. L. Platzman, 'Total ionization in gases by high-energy particles: An appraisal of our understanding', The International Journal of Applied Radiation and Isotopes **10**, 116–127 (1961).

[52] V. Chepel and H. Araújo, 'Liquid noble gas detectors for low energy particle physics', J. Inst. **8**, R04001 (2013).

[53] M. Szydagis et al., 'NEST: a comprehensive model for scintillation yield in liquid xenon', J. Inst. **6**, P10002 (2011).

[54] J. Lindhard et al., 'Integral Equations Governing Radiation Effects – Matematisk-fysiske Meddelelser', Mat. Fys. Medd. Dan. Vid. Selsk. **33** (1960).

[55] M. Szydagis et al., *A Review of NEST Models, and Their Application to Improvement of Particle Identification in Liquid Xenon Experiments*, (20th Feb. 2023) http://arxiv.org/abs/2211.10726, pre-published.

[56] M. Szydagis et al., *Noble Element Simulation Technique*, Zenodo, 27th Jan. 2023.

[57] S. Farrell et al., *NESTCollaboration/nestpy: Sync with NESTv2.3.12beta*, Zenodo, 19th Jan. 2023.

[58] L. Collaboration et al., 'Tritium calibration of the LUX dark matter experiment', Phys. Rev. D **93**, 072009 (2016).

[59] D. S. Akerib et al., 'Ultralow energy calibration of LUX detector using $^{127}$Xe electron capture', Phys. Rev. D **96**, 112011 (2017).

[60] L. Collaboration et al., 'Improved measurements of the β-decay response of liquid xenon with the LUX detector', Phys. Rev. D **100**, 022002 (2019).

[61] L. Baudis et al., 'The first dual-phase xenon TPC equipped with silicon photomultipliers and characterisation with $^{37}$Ar', Eur. Phys. J. C **80**, 477 (2020).

[62] L. Collaboration et al., *Low-energy (0.7-74 keV) nuclear recoil calibration of the LUX dark matter experiment using D-D neutron scattering kinematics*, version 2, (26th Oct. 2016) http://arxiv.org/abs/1608.05381, pre-published.

[63] D. Huang, 'Ultra-Low Energy Calibration of the LUX and LZ Dark Matter Detectors' (Brown University, 2020).

[64] B. Lenardo et al., *Measurement of the ionization yield from nuclear recoils in liquid xenon between 0.3 – 6 keV with single-ionization-electron sensitivity*, (1st Aug. 2019) http://arxiv.org/abs/1908.00518, pre-published.

[65] G. J. Alner et al., 'Nuclear recoil limits from the ZEPLIN I liquid xenon WIMP dark matter detector', New Astronomy Reviews, Sources and Detection of Dark Matter and Dark Energy in the Universe **49**, 245–249 (2005).

[66] K. Abe et al., 'XMASS detector', Nuclear Instruments and Methods in Physics Research Section A: Accelerators, Spectrometers, Detectors and Associated Equipment **716**, 78–85 (2013).

[67] X. Collaboration et al., *Direct dark matter searches with the full data set of XMASS-I*, (11th Nov. 2022) http://arxiv.org/abs/2211.06204, pre-published.

[68] B. A. Dolgoshein, V. N. Lebedenko and B. U. Rodionov, 'New Method of Registration of Ionizing-particle Tracks in Condensed Matter', Sov. J. Exp. Theor. Phys. Lett. **11**, 351 (1970).

[69] G. J. Alner et al., 'First limits on WIMP nuclear recoil signals in ZEPLIN-II: A two-phase xenon detector for dark matter detection', Astroparticle Physics **28**, 287–302 (2007).

[70] D. Y. Akimov et al., 'The ZEPLIN-III dark matter detector: Instrument design, manufacture and commissioning', Astroparticle Physics **27**, 46–60 (2007).

[71] R. Linehan et al., 'Design and production of the high voltage electrode grids and electron extraction region for the LZ dual-phase xenon time projection chamber', Nuclear

Instruments and Methods in Physics Research Section A: Accelerators, Spectrometers, Detectors and Associated Equipment **1031**, 165955 (2022).

[72] B. J. Mount et al., *LUX-ZEPLIN (LZ) Technical Design Report*, (27th Mar. 2017) http://arxiv.org/abs/1703.09144, pre-published.

[73] L. Collaboration et al., 'First results from the LUX dark matter experiment at the Sanford Underground Research Facility', Phys. Rev. Lett. **112**, 091303 (2014).

[74] K. Abe et al., 'Radon removal from gaseous xenon with activated charcoal', Nuclear Instruments and Methods in Physics Research Section A: Accelerators, Spectrometers, Detectors and Associated Equipment **661**, 50–57 (2012).

[75] C. Galbiati et al., 'Discovery of underground argon with a low level of radioactive 39Ar and possible applications to WIMP dark matter detectors', J. Phys.: Conf. Ser. **120**, 042015 (2008).

[76] J. Aalbers et al., 'A next-generation liquid xenon observatory for dark matter and neutrino physics', J. Phys. G: Nucl. Part. Phys. **50**, 013001 (2022).

[77] C. A. J. O'Hare, 'New Definition of the Neutrino Floor for Direct Dark Matter Searches', Phys. Rev. Lett. **127**, 251802 (2021).

[78] C. O'Hare, *NeutrinoFog*, (12th Feb. 2023) https://github.com/cajohare/NeutrinoFog.

[79] S. Collaboration et al., 'Search for low-mass dark matter with CDMSlite using a profile likelihood fit', Phys. Rev. D **99**, 062001 (2019).

[80] G. Adhikari et al., 'An experiment to search for dark-matter interactions using sodium iodide detectors', Nature **564**, 83–86 (2018).

[81] R. Bernabei et al., 'First Model Independent Results from DAMA/LIBRA–Phase2', Universe **4**, 116 (2018).

[82] C. Savage et al., 'Compatibility of DAMA/LIBRA dark matter detection with other searches', J. Cosmol. Astropart. Phys. **2009**, 010 (2009).

[83] D. Collaboration et al., 'Low-Mass Dark Matter Search with the DarkSide-50 Experiment', Phys. Rev. Lett. **121**, 081307 (2018).

[84] L. Hehn et al., 'Improved EDELWEISS-III sensitivity for low-mass WIMPs using a profile likelihood approach', Eur. Phys. J. C **76**, 548 (2016).

[85] P. Collaboration et al., 'Improved dark matter search results from PICO-2L Run 2', Phys. Rev. D **93**, 061101 (2016).

[86] P. Collaboration et al., 'Dark Matter Search Results from the $\mathrm{PICO{-}60\ C_3F_8}$ Bubble Chamber', Phys. Rev. Lett. **118**, 251301 (2017).

[87] L. Collaboration et al., 'Results from a Search for Dark Matter in the Complete LUX Exposure', Phys. Rev. Lett. **118**, 021303 (2017).

[88] X. Collaboration et al., 'Dark Matter Search Results from a One Ton-Year Exposure of XENON1T', Phys. Rev. Lett. **121**, 111302 (2018).

[89] P.-I. Collaboration et al., 'Dark Matter Results from 54-Ton-Day Exposure of PandaX-II Experiment', Phys. Rev. Lett. **119**, 181302 (2017).

[90] D. S. Akerib et al., 'The Large Underground Xenon (LUX) experiment', Nuclear Instruments and Methods in Physics Research Section A: Accelerators, Spectrometers, Detectors and Associated Equipment **704**, 111–126 (2013).

[91] L.-Z. Collaboration et al., 'Projected WIMP sensitivity of the LUX-ZEPLIN dark matter experiment', Phys. Rev. D **101**, 052002 (2020).

[92] T. L.-Z. Collaboration et al., 'Projected sensitivity of the LUX-ZEPLIN experiment to the two-neutrino and neutrinoless double $\beta$ decays of $^{134}$Xe', Phys. Rev. C **104**, 065501 (2021).

[93] L.-Z. ( Collaboration et al., 'Projected sensitivity of the LUX-ZEPLIN experiment to the $0\nu\beta\beta$ decay of $^{136}$Xe', Phys. Rev. C **102**, 014602 (2020).

[94] D. S. Akerib et al., 'Projected sensitivities of the LUX-ZEPLIN experiment to new physics via low-energy electron recoils', Phys. Rev. D **104**, 092009 (2021).

[95] D. S. Akerib et al., *Enhancing the sensitivity of the LUX-ZEPLIN (LZ) dark matter experiment to low energy signals*, (21st Jan. 2021) http://arxiv.org/abs/2101.08753, pre-published.

[96] N. Abgrall et al., 'Muon flux measurements at the davis campus of the sanford underground research facility with the majorana demonstrator veto system', Astroparticle Physics **93**, 70–75 (2017).

[97] D.-M. Mei and A. Hime, 'Muon-induced background study for underground laboratories', Phys. Rev. D **73**, 053004 (2006).

[98] D. S. Akerib et al., 'The LUX-ZEPLIN (LZ) radioactivity and cleanliness control programs', Eur. Phys. J. C **80**, 1044 (2020).

[99] F. Neves et al., 'Measurement of the absolute reflectance of polytetrafluoroethylene (PTFE) immersed in liquid xenon', J. Inst. **12**, P01017 (2017).

[100] D. S. Akerib et al., 'The LUX-ZEPLIN (LZ) experiment', Nuclear Instruments and Methods in Physics Research Section A: Accelerators, Spectrometers, Detectors and Associated Equipment **953**, 163047 (2020).

[101] A. Dobi et al., 'Study of a zirconium getter for purification of xenon gas', Nuclear Instruments and Methods in Physics Research Section A: Accelerators, Spectrometers, Detectors and Associated Equipment **620**, 594–598 (2010).

[102] HAMMAMATSU, *Photomultiplier tube R11410-20 — Hamamatsu Photonics*, https://www.hamamatsu.com/eu/en/product/optical-sensors/pmt/pmt_tube-alone/head-on-type/R11410-20.html.

[103] E. Aprile and X. collaboration, *The XENON1T Dark Matter Search Experiment*, (27th June 2012) http://arxiv.org/abs/1206.6288, pre-published.

[104] V. C. Antochi et al., 'Improved quality tests of R11410-21 photomultiplier tubes for the XENONnT experiment', J. Inst. **16**, P08033 (2021).

[105] D. S. Akerib et al., 'An ultra-low background PMT for liquid xenon detectors', Nuclear Instruments and Methods in Physics Research Section A: Accelerators, Spectrometers, Detectors and Associated Equipment **703**, 1–6 (2013).

[106] K. Nakamura et al., 'Latest bialkali photocathode with ultra high sensitivity', Nuclear Instruments and Methods in Physics Research Section A: Accelerators, Spectrometers, Detectors and Associated Equipment, 1st International Conference on Technology and Instrumentation in Particle Physics **623**, 276–278 (2010).

[107] L. Baudis et al., 'Performance of the Hamamatsu R11410 photomultiplier tube in cryogenic xenon environments', J. Inst. **8**, P04026 (2013).

[108] B. López Paredes et al., 'Response of photomultiplier tubes to xenon scintillation light', Astroparticle Physics **102**, 56–66 (2018).

[109] C. H. Faham et al., 'Measurements of wavelength-dependent double photoelectron emission from single photons in VUV-sensitive photomultiplier tubes', J. Inst. **10**, P09010 (2015).

[110] T. M. A. Fruth, 'PMT studies and loop antenna development for the LZ dark matter experiment', DPhil Thesis (University of Oxford, 2019).

[111] C. B. Johnson, L. Bonney and R. F. Floryan, 'Some Ultraviolet Spectral Sensitivity Characteristics of Broadband Multialkali Photocathodes', in Ultrav. Technol. II, Vol. 0932 (16th Aug. 1988), pp. 285–290.

[112] C. H. Faham et al., 'Measurements of wavelength-dependent double photoelectron emission from single photons in VUV-sensitive photomultiplier tubes', J. Inst. **10**, P09010 (2015).

[113] HAMMAMATSU, *PHOTOMULTIPLIER TUBES - Basics and Applications*, 4th Edition (HAMMAMATSU).

[114] K. Lung et al., 'Characterization of the Hamamatsu R11410-10 3-in. photomultiplier tube for liquid xenon dark matter direct detection experiments', Nuclear Instruments and Methods in Physics Research Section A: Accelerators, Spectrometers, Detectors and Associated Equipment **696**, 32–39 (2012).

[115] L. Collaboration et al., 'Improved Limits on Scattering of Weakly Interacting Massive Particles from Reanalysis of 2013 LUX Data', Phys. Rev. Lett. **116**, 161301 (2016).

[116] X. Collaboration et al., 'XENON1T dark matter data analysis: Signal and background models and statistical inference', Phys. Rev. D **99**, 112009 (2019).

[117] D. S. Akerib et al., 'Data acquisition and readout system for the LUX dark matter experiment', Nuclear Instruments and Methods in Physics Research Section A: Accelerators, Spectrometers, Detectors and Associated Equipment **668**, 1–8 (2012).

[118] V. Solovov et al., 'Position reconstruction in a dual phase xenon scintillation detector', in 2011 IEEE Nucl. Sci. Symp. Conf. Rec. (Oct. 2011), pp. 1226–1233.

[119] G. Barrand et al., 'GAUDI — A software architecture and framework for building HEP data processing applications', Computer Physics Communications, CHEP2000 **140**, 45–55 (2001).

[120] T. G. Collaboration et al., 'GridPP: development of the UK computing Grid for particle physics', J. Phys. G: Nucl. Part. Phys. **32**, N1 (2005).

[121] D. Britton et al., 'GridPP: the UK grid for particle physics', Philos. Trans. R. Soc. Math. Phys. Eng. Sci. **367**, 2447–2457 (2009).

[122] A. Dorigo et al., 'XROOTD/TXNetFile: a highly scalable architecture for data access in the ROOT environment', in Proc. 4th WSEAS Int. Conf. Telecommun. Inform. TELEINFO'05 (13th Mar. 2005), pp. 1–6.

[123] A. Tsaregorodtsev et al., 'DIRAC: a community grid solution', J. Phys.: Conf. Ser. **119**, 062048 (2008).

[124] P. Buncic et al., 'A practical approach to virtualization in HEP', Eur. Phys. J. Plus **126**, 13 (2011).

[125] F. Mölder et al., 'Sustainable data analysis with Snakemake', 10.12688/f1000research.29032.2 (2021).

[126] S. (Github), *Snakemake - A framework for reproducible data analysis*, Snakemake (Github), 24th Mar. 2023.

[127] L. Collaboration et al., 'Extending light WIMP searches to single scintillation photons in LUX', Phys. Rev. D **101**, 042001 (2020).

[128] L. W. Kastens et al., 'Calibration of a liquid xenon detector with $^{83m}$Kr', Phys. Rev. C **80**, 045809 (2009).

[129] L. Collaboration et al., '$^{83m}$Kr calibration of the 2013 LUX dark matter search', Phys. Rev. D **96**, 112009 (2017).

[130] F. Jörg et al., 'Characterization of alpha and beta interactions in liquid xenon', Eur. Phys. J. C **82**, 361 (2022).

[131] I. Ahmad et al., 'Half-lives of isomeric states in $^{57}$Fe and $^{83m}$Kr', Phys. Rev. C **52**, 2240–2241 (1995).

[132] L.-Z. Collaboration et al., 'First Dark Matter Search Results from the LUX-ZEPLIN (LZ) Experiment', Phys. Rev. Lett. **131**, 041002 (2023).

[133] L. Collaboration et al., 'Search for new physics in low-energy electron recoils from the first LZ exposure', Phys. Rev. D **108**, 072006 (2023).

[134] T. L.-Z. Collaboration et al., 'Background determination for the LUX-ZEPLIN dark matter experiment', Phys. Rev. D **108**, 012010 (2023).

[135] L. Collaboration et al., *First Constraints on WIMP-Nucleon Effective Field Theory Couplings in an Extended Energy Region From LUX-ZEPLIN*, (4th Dec. 2023) http://arxiv.org/abs/2312.02030, pre-published.

[136] D. S. Akerib et al., 'Simulations of events for the LUX-ZEPLIN (LZ) dark matter experiment', Astroparticle Physics **125**, 102480 (2021).

[137] D. Baxter et al., 'Recommended conventions for reporting results from direct dark matter searches', Eur. Phys. J. C **81**, 907 (2021).

[138] *geant4/CITATION.cff at master · Geant4/geant4*, GitHub, https://github.com/Geant4/geant4.

[139] S. Agostinelli et al., 'Geant4—a simulation toolkit', Nuclear Instruments and Methods in Physics Research Section A: Accelerators, Spectrometers, Detectors and Associated Equipment **506**, 250–303 (2003).

[140] G. Cowan et al., 'Asymptotic formulae for likelihood-based tests of new physics', Eur. Phys. J. C **71**, 1554 (2011).

[141] P. D. Group et al., 'Review of Particle Physics', Phys. Rev. D **98**, 030001 (2018).

[142] W. A. Rolke, A. M. López and J. Conrad, 'Limits and confidence intervals in the presence of nuisance parameters', Nuclear Instruments and Methods in Physics Research Section A: Accelerators, Spectrometers, Detectors and Associated Equipment **551**, 493–503 (2005).

[143] C. Biwer et al., 'Validating gravitational-wave detections: The Advanced LIGO hardware injection system', Phys. Rev. D **95**, 062002 (2017).

[144] M. Aker et al., 'KATRIN: status and prospects for the neutrino mass and beyond', J. Phys. G: Nucl. Part. Phys. **49**, 100501 (2022).

[145] M. Galeazzi et al., 'End-point energy and half-life of the $^{187}\mathrm{Re}$ $\beta$ decay', Phys. Rev. C **63**, 014302 (2000).

[146] F. Fontanelli et al., 'The $\beta$-decay of $^{187}$Re studied with a cryogenic microcalorimeter', Nuclear Instruments and Methods in Physics Research Section A: Accelerators, Spectrometers, Detectors and Associated Equipment, Proceedings of the Sixth International Workshop on Low Temperature Detectors **370**, 247–249 (1996).

[147] X. Zhou et al., 'Erratum: A Search for Solar Axions and Anomalous Neutrino Magnetic Moment with the Complete PandaX-II Data [CHIN. PHYS. LETT. 38 (2021) 011301]', Chinese Phys. Lett. **38**, 109902 (2021).

[148] G. Rischbieter and L.-Z. ( Collaboration, *LUX-ZEPLIN NEST detector model*, Noble Element Simulation Techniques Collaboration, 27th Jan. 2023.

[149] D. S. Akerib et al., 'Investigation of background electron emission in the LUX detector', Phys. Rev. D **102**, 092004 (2020).

[150] P. Sorensen and K. Kamdin, 'Two distinct components of the delayed single electron noise in liquid xenon emission detectors', J. Inst. **13**, P02032 (2018).

[151] T. L.-Z. Collaboration et al., 'Cosmogenic production of $^{37}$Ar in the context of the LUX-ZEPLIN experiment', Phys. Rev. D **105**, 082004 (2022).

[152] G. Cowan et al., *Power-Constrained Limits*, (16th May 2011) http://arxiv.org/abs/1105.3166, pre-published.

[153] X. Collaboration et al., 'First Dark Matter Search with Nuclear Recoils from the XENONnT Experiment', Phys. Rev. Lett. **131**, 041003 (2023).

[154] D. Collaboration et al., 'Search for dark matter with a 231-day exposure of liquid argon using DEAP-3600 at SNOLAB', Phys. Rev. D **100**, 022004 (2019).

[155] J. Aalbers et al., 'Finding dark matter faster with explicit profile likelihoods', Phys. Rev. D **102**, 072010 (2020).

[156] R. S. James et al., 'FlameNEST: explicit profile likelihoods with the Noble Element Simulation Technique', J. Inst. **17**, P08012 (2022).

[157] L. Collaboration et al., 'Liquid xenon scintillation measurements and pulse shape discrimination in the LUX dark matter detector', Phys. Rev. D **97**, 112002 (2018).

[158] H. Dembinski et al., *scikit-hep/iminuit*, version v2.24.0, Zenodo, 15th Aug. 2023.

[159] V. N. Solovov et al., 'Measurement of the refractive index and attenuation length of liquid xenon for its scintillation light', Nuclear Instruments and Methods in Physics Research Section A: Accelerators, Spectrometers, Detectors and Associated Equipment **516**, 462–474 (2004).

[160] A. Hitachi et al., 'New approach to the calculation of the refractive index of liquid and solid xenon', The Journal of Chemical Physics **123**, 234508 (2005).

[161] X. Collaboration et al., 'Light Dark Matter Search with Ionization Signals in XENON1T', Phys. Rev. Lett. **123**, 251801 (2019).

[162] S. C. Roy, L. Kissel and R. H. Pratt, 'Elastic scattering of photons', Radiation Physics and Chemistry **56**, 3–26 (1999).

[163] S. C. Roy, 'Elastic scattering of photons: perspectives and present status', X-Ray Spectrom. **28**, 376–378 (1999).

[164] B. K. Chatterjee and S. C. Roy, 'Tables of Elastic Scattering Cross Sections of Photons in the Energy Range 50–1500 keV for All Elements in the Range 13≤Z≤104', Journal of Physical and Chemical Reference Data **27**, 1011–1215 (1998).

[165] F. Smend and H. Czerwinski, 'Large-angle elastic scattering of 59.54 keV photons by Kr and Xe', Z Phys D - Atoms, Molecules and Clusters **1**, 139–140 (1986).

[166] A. H. Compton, 'A Quantum Theory of the Scattering of X-rays by Light Elements', Phys. Rev. **21**, 483–502 (1923).

[167] O. Klein and Y. Nishina, 'Über die Streuung von Strahlung durch freie Elektronen nach der neuen relativistischen Quantendynamik von Dirac', Z. Physik **52**, 853–868 (1929).

[168] M. Berger et al., *XCOM: Photon Cross Sections Database* (Nov. 2010).

[169] X. Collaboration et al., 'Search for New Physics in Electronic Recoil Data from XENONnT', Phys. Rev. Lett. **129**, 161805 (2022).

[170] A. P. Meshik et al., 'Weak decay of $^{130}$Ba and $^{132}$Ba: Geochemical measurements', Phys. Rev. C **64**, 035205 (2001).

[171] Y. M. Gavrilyuk et al., 'Indications of $2\nu2$K capture in $^{78}$Kr', Phys. Rev. C **87**, 035501 (2013).

[172] E. Aprile et al., 'Observation of two-neutrino double electron capture in $^{124}$Xe with XENON1T', Nature **568**, 532–535 (2019).

[173] L. Meitner, 'Über die Entstehung der β-Strahl-Spektren radioaktiver Substanzen', Z. Physik **9**, 131–144 (1922).

[174] V. A. Sevestrean et al., *Self-consistent calculations for atomic electron capture*, (28th May 2023) http://arxiv.org/abs/2304.10373, pre-published.

[175] W. Bambynek et al., 'Orbital electron capture by the nucleus', Rev. Mod. Phys. **49**, 77–221 (1977).

[176] X. Mougeot, 'Reliability of usual assumptions in the calculation of β and $\nu$ spectra', Phys. Rev. C **91**, 055504 (2015).

[177] X. Mougeot, 'BetaShape: A new code for improved analytical calculations of beta spectra', EPJ Web Conf. **146**, 12015 (2017).

[178] X. Mougeot, 'Towards high-precision calculation of electron capture decays', Applied Radiation and Isotopes **154**, 108884 (2019).

[179] L. Hariasz et al., *First observation of the ground-state electron-capture of $^{40}$K*, (21st Nov. 2022) http://arxiv.org/abs/2211.10343, pre-published.

[180] J. Pradler, B. Singh and I. Yavin, 'On an unverified nuclear decay and its role in the DAMA experiment', Physics Letters B **720**, 399–404 (2013).

[181] P. Auger, 'Sur l'effet photoélectrique composé', J. Phys. Radium **6**, 205–208 (1925).

[182] M. Cardona and L. Ley, eds., *Photoemission in Solids I*, Vol. 26, Topics in Applied Physics (Springer, Berlin, Heidelberg, 1978).

[183] J. A. BEARDEN and A. F. BURR, 'Reevaluation of X-Ray Atomic Energy Levels', Rev. Mod. Phys. **39**, 125–142 (1967).

[184] K. D. Sevier, 'Atomic electron binding energies', Atomic Data and Nuclear Data Tables **24**, 323–371 (1979).

[185] S. Fritzsche, 'A fresh computational approach to atomic structures, processes and cascades', Computer Physics Communications **240**, 1–14 (2019).

[186] S. Fritzsche, P. Palmeri and S. Schippers, 'Atomic Cascade Computations', Symmetry **13**, 520 (2021).

[187] G. W. Rodeback and J. S. Allen, 'Neutrino Recoils Following the Capture of Orbital Electrons in $^{37}$A', Phys. Rev. **86**, 446–450 (1952).

[188] M. Rodrigues et al., 'Standardization of xenon-127 and measurement of photon emission intensities', Applied Radiation and Isotopes, Proceedings of the 19th International Conference on Radionuclide Metrology and its Applications 17–21 June 2013, Antwerp, Belgium **87**, 342–347 (2014).

[189] K. Fujii et al., 'High-accuracy measurement of the emission spectrum of liquid xenon in the vacuum ultraviolet region', Nuclear Instruments and Methods in Physics Research Section A: Accelerators, Spectrometers, Detectors and Associated Equipment **795**, 293–297 (2015).

[190] G. M. Seidel, R. E. Lanou and W. Yao, 'Rayleigh scattering in rare-gas liquids', Nuclear Instruments and Methods in Physics Research Section A: Accelerators, Spectrometers, Detectors and Associated Equipment **489**, 189–194 (2002).

[191] S. Nakamura, Y. Ozaki and K. Saito, 'Proceedings of the Workshop on Ionization and Scintillation Counters and Their Uses (unpublished)', 2007.

[192] M. Piotter et al., 'First time-resolved measurement of infrared scintillation light in gaseous xenon', Eur. Phys. J. C **83**, 482 (2023).

[193] P. M. Morse, 'Diatomic Molecules According to the Wave Mechanics. II. Vibrational Levels', Phys. Rev. **34**, 57–64 (1929).

[194] S. Qadeer et al., 'Vibrational levels of a generalized Morse potential', The Journal of Chemical Physics **157**, 144104 (2022).

[195] J. B. Nee et al., 'Potential energy curves of $Xe_2$ derived from the pressure-dependent fluorescence excitation spectra of the 1st and 2nd continuum', Chemical Physics Letters **318**, 402–408 (2000).

[196] N. Collaboration et al., 'Neutral Bremsstrahlung Emission in Xenon Unveiled', Phys. Rev. X **12**, 021005 (2022).

[197] A. Buzulutskov et al., 'Revealing neutral bremsstrahlung in two-phase argon electroluminescence', Astroparticle Physics **103**, 29–40 (2018).

[198] A. E. Bondar et al., 'Effect of Neutral Bremsstrahlung on the Operation of Two-Phase Argon Detectors', Bull. Lebedev Phys. Inst. **47**, 162–165 (2020).

[199] C. E. Aalseth et al., 'DarkSide-20k: A 20 tonne two-phase LAr TPC for direct dark matter detection at LNGS', Eur. Phys. J. Plus **133**, 131 (2018).

[200] B. Broerman et al., 'Application of the TPB Wavelength Shifter to the DEAP-3600 Spherical Acrylic Vessel Inner Surface', J. Inst. **12**, P04017 (2017).

[201] A. Tomás et al., 'Study and mitigation of spurious electron emission from cathodic wires in noble liquid time projection chambers', Astroparticle Physics **103**, 49–61 (2018).

[202] E. Enterprises, *9406B Series - 30 mm Photomultiplier - ET-Enterprises Ltd*, ET Enterprises, https://et-enterprises.com/products/photomultipliers/product/p9406b-series.

[203] A. Baldini et al., 'Absorption of scintillation light in a 100l liquid xenon γ-ray detector and expected detector performance', Nuclear Instruments and Methods in Physics Research Section A: Accelerators, Spectrometers, Detectors and Associated Equipment **545**, 753–764 (2005).

[204] BatesIsBack and Tosaka, *Diagram showing the different stages of Thorium Decay*, (8th May 2011) https://commons.wikimedia.org/wiki/File:Decay_Chain_of_Thorium.svg.

[205] C. Commons, *Creative Commons — Attribution-ShareAlike 3.0 Unported — CC BY-SA 3.0*, Attribution-ShareAlike 3.0 Unported (CC BY-SA 3.0), https://creativecommons.org/licenses/by-sa/3.0/.

[206] L. primaire des rayonnements ionisants, ed., *Table de radionucléides*, Nouv. éd. (Commissariat à l'énergie atomique, Gif-sur-Yvette, 1999).

[207] M.-M. Bé et al., *Table of radionuclides*, Vol. 8, Monographie BIPM-5 (Bureau International des Poids et Mesures, Pavillon de Breteuil, F-92310 Sèvres, France, 2016).

[208] H. M. Araújo et al., 'The MIGDAL experiment: Measuring a rare atomic process to aid the search for dark matter', Astroparticle Physics **151**, 102853 (2023).

[209] S. Usman and A. Patil, 'Radiation detector deadtime and pile up: A review of the status of science', Nuclear Engineering and Technology **50**, 1006–1016 (2018).

[210] J. Pivarski et al., *Uproot*, (15th Feb. 2023) https://zenodo.org/record/7644351.

[211] E. Rodrigues et al., 'The Scikit HEP Project – overview and prospects', EPJ Web Conf. **245**, 06028 (2020).

[212] P. Virtanen et al., 'SciPy 1.0: Fundamental algorithms for scientific computing in python', Nat. Methods **17**, 261–272 (2020).

[213] A. Liquide, *Xenon — Gas Encyclopedia Air Liquide*, Air Liquide Gas Encyclopedia, https://encyclopedia.airliquide.com/xenon.

[214] F. Pedregosa et al., 'Scikit-learn: Machine learning in Python', J. Mach. Learn. Res. **12**, 2825–2830 (2011).

[215] F. Marchal et al., *Study of Formation and Decay of Rare-Gas Excimers by Laser-Induced Fluorescence* (IntechOpen, 20th Dec. 2017).

[216] J. Jortner et al., 'Localized Excitations in Condensed Ne, Ar, Kr, and Xe', The Journal of Chemical Physics **42**, 4250–4253 (1965).

[217] C. Wahl et al., 'Vacuum-ultraviolet absorption and emission spectroscopy of gaseous, liquid, and supercritical xenon', Phys. Rev. A **103**, 022831 (2021).

[218] H. A. Koehler et al., 'Vacuum-ultraviolet emission from high-pressure xenon and argon excited by high-current relativistic electron beams', Phys. Rev. A **9**, 768–781 (1974).

[219] I. Murayama and S. Nakamura, 'Time profile of the scintillation from liquid and gaseous xenon', Nuclear Instruments and Methods in Physics Research Section A: Accelerators, Spectrometers, Detectors and Associated Equipment **763**, 533–537 (2014).

[220] K. Saito et al., 'Absolute number of scintillation photons emitted by alpha particles in rare gases', IEEE Trans. Nucl. Sci. **49**, 1674–1680 (2002).